

A calorimetric study of plasma based thin film deposition applications

Dissertation

zur Erlangung des Doktorgrades
der Mathematisch-Naturwissenschaftlichen Fakultät
der Christian-Albrechts-Universität zu Kiel

vorgelegt von

Fabian Haase

Kiel, 2018

Erster Gutachter: Prof. Dr. Holger Kersten

Zweiter Gutachter: Prof. Dr. Franz Faupel

Datum der Disputation: 24. August 2018

About this work

This cumulative thesis was prepared within the framework of the project entitled *Untersuchung zur Dynamik schnell-veränderlicher Plasmarandschichten bei der Plasma-Immersion-Ionenimplantation mittels nicht-konventioneller Diagnostik* which is a DFG funded collaborative project of the Leibniz Institute of Surface Modification in Leipzig (IOM) together with the Plasmatechnology Group at the Kiel University. The part of the IOM was supervised by Dr. Stephan Mändl and the Plasmatechnology Group is lead by Prof. Dr. Holger Kersten.

The project was aimed towards diagnostic in plasma-immersion ion implantation systems with a major focus on secondary electron processes and sheath expansion dynamics. The publications presented in this thesis were partly composed within the work of said project. Additionally, experimental results were obtained in measurement campaigns during my time as a PhD student on various experimental setups which are also presented in a form of a scientific publication included in this work.

The introductory part of this thesis (chapter 1) gives a motivation and offers various examples on how plasma physics impacts things we interact with on a daily basis. The second chapter provides the needed theoretical background of plasma physics, including the properties of a plasma and its interaction with surrounding surfaces, as well as different plasma generation methods and coating techniques. The third chapter provides a detailed description of different probes and diagnostic techniques used to monitor a plasma process. This ranges from Langmuir probes, which are capable of determining the basic plasma parameters, calorimetric probes to investigate the integral energy flux as well as deposition rate measurement techniques.

In the fourth chapter, the results which were obtained during internal experiments as well as on national and international measurement campaigns are presented in the form of published articles in different scientific journals.

Kiel, May 2018

Abstract

Nowadays plasma based processes are widely used for surface modification in a great variety of industrial applications. In many cases plasma based deposition techniques are used to tailor functional thin films on an atomic or molecular scale. The ability to control the plasma process opened new ways in material sciences. One key element during plasma coating is the interaction between the plasma itself and the surrounding surfaces, also called plasma-wall interactions (PWI) or plasma-surface interactions (PSI). It dictates the structure and morphology of the deposited film and has been studied extensively in the last decades. The main interaction relies on particle fluxes which may or may not deposit a significant amount of energy once they hit the surface, binding to the film or getting reflected. Therefore, the characterization of the particles as well as the energy flux reaching the surface is of great importance since it helps to understand fundamental mechanisms and may grant opportunities to improve existing processes for surface modification or develop new ones.

In this thesis different plasma based processes used to deposit nanostructured materials are preferably investigated using a calorimetric probe, i.e. a passive thermal probe, which is able to measure the integral energy flux. Combined with additional probe measurements (Langmuir probe, quartz crystal microbalance) and sputter-based simulations (SRIM) a detailed insight of the particle interaction between the plasma and the surface can be obtained. This includes the generation of secondary particles, e.g. secondary electrons which may occur during particle bombardment of a surface.

With knowledge of the energy flux and its components, the mechanisms present in thin film deposition and implantation processes can be better understood, hence, the energy transfer from the plasma to the substrate is studied in detail in this work. Understanding the energy flux and its origin creates the ability to tailor the different processes to the desired outcome and helps to connect key properties of the final product to certain plasma parameters and discharge conditions.

Secondary electron generation and their influence has been studied extensively in plasma-immersion ion implantation where ions are accelerated towards the substrate during a high voltage pulse, using a passive thermal probe. Even in such fast pulsed processes the passive thermal probe was able to detect changes during substrate alteration (sputtering an oxide layer, nitriding a metallic surface) and their influence on the secondary electron yield over several pulses, respectively. Experiments in the plasma systems were performed for various substrate materials (Cu, steel, Al, Mg, AlMg, Ti, Mo, Zn, AZ91) using different process gases (Ar, N₂).

Further investigations in a pulsed magnetron discharge using high-power impulse magnetron sputtering compared the resulting energy flux with the one generated by conventional direct current magnetron sputtering in a reactive gas atmosphere using titanium. The energy flux for the metallic, transition and poisoned target surface regime was compared and backed by Langmuir measurements in the case of direct current magnetron sputtering.

The influence of the process gas during magnetron sputtering of titanium and its impact on the electron energy and density, as well as the resulting integral energy flux have been studied using a combined calorimetric and Langmuir probe. Additionally, the different contributions to the integral energy flux have been calculated using the obtained plasma parameters and deposition rates.

The calorimetric probe was also used to determine the energy flux in a gas aggregation source at elevated pressures of 20 Pa to over 200 Pa. Three different targets, a pure copper and a pure tungsten target, as well as a composite target with 37 tungsten pellets inside a copper disc were investigated. Parameters like the magnetron current, the distance to the target and the pressure were varied. Additional studies with a Langmuir probe and deposition rate measurements were performed as well. The deposited films of selected parameters were also observed ex-situ by scanning electron microscopy.

Further, an extensive study of fifteen gas-target combinations was performed using the passive thermal probe, the Langmuir probe and the quartz crystal microbalance measuring the integral energy flux, plasma parameters and the deposition rate, respectively. Combined with sputter simulations a comprehensive picture of the composition of the energy flux of Ag, Al, Cu, Ti and W targets when sputtered with Ar, Kr and He and the dominant particle mechanisms was obtained.

Kurzfassung

In heutigen Industrieprozessen sind Plasma-gestützte Systeme kaum mehr wegzudenken und man kann sie in einer Vielzahl von Anlagen entdecken. In vielen Fällen werden sie genutzt um Filmabscheideprozesse zu realisieren, da sie das gezielte Steuern der Abscheidung von funktionalen Dünnschichtfilmen auf atomarer und molekularer Ebene erlauben. Die Möglichkeit den Plasmaprozesse gezielt zu steuern ermöglichte neue Wege in der Materialwissenschaft welche zur Erschaffung neuer (Komposit-) Materialien führte. Ein Hauptelement solcher Plasmaprozesse ist die Interaktion des Plasmas mit den umgebenden Oberflächen, was als Plasma-Wand-Wechselwirkung (PWW) oder im Englischen auch plasma-wall interactions (PWI) bekannt ist. Die PWW bestimmen die Struktur und Morphologie der abgeschiedenen Schichten, weshalb sie in den letzten Jahrzehnten intensiv erforscht wurden. Die Interaktion des Plasmas mit den Oberflächen basiert hauptsächlich auf Teilchenflüssen, welche beim Auftreffen auf die Oberfläche Energie deponieren können. Sie können dann entweder als Teil des wachsenden Films an die Oberfläche binden, oder von ihr reflektiert werden. Daher ist die Charakterisierung der verschiedenen beteiligten Teilchen als auch der aus ihnen resultierende Energiefluss auf die Oberfläche essentiell. Sie geben Aufschluss über die vorherrschenden fundamentalen Mechanismen während der Abscheidung und können zur Verbesserung bestehender System als auch der Herstellung von neuen Prozessen führen.

In dieser Dissertation werden verschiedene Plasma-basierende System untersucht, welche zur Abscheidung von nanostrukturierten Schichten und Oberflächenmodifizierung verwendet werden. Hauptsächlich werden die Untersuchungen mit der Kalorimetrischen Sonde, auch Passive Thermosonde, durchgeführt. Diese ist in der Lage den integralen Energiefluss auf ein Substrat zu messen. Die Ergebnisse der Kalorimetrische Sonde, gepaart mit den Ergebnissen aus zusätzlichen Diagnostiken wie der Langmuir-Sonde, oder dem Schwingquartz, welcher die Abscheiderate misst, als auch Simulationen zur Kathodenzerstäubung (SRIM) ermöglichen einen detaillierten Einblick in die Wechselwirkung zwischen den Teilchen aus dem Plasma und der Oberfläche. Dies beinhaltet auch die Produktion von sogenannten Sekundärteilchen, wie z.B. Sekundärelektronen welche beim Auftreffen von energetischen Teilchen auf die Oberfläche entstehen können.

Mit dem Wissen über den Energiefluss und seine einzelnen Komponenten können die Vorgänge, welche in Dünnschichtabscheidungs- und Implantations-Prozessen vorherrschen besser verstanden werden, deshalb wurde der Energietransfer zwischen dem Plasma und dem Substrat in dieser Arbeit umfangreich untersucht. Das Verständnis des Energiestroms und seine Entstehung eröffnet Möglichkeiten den Plasmaprozess gezielt zu steuern um ein gewisses Ergebnis zu erzielen. Dadurch können zudem bestimmte Eigenschaften des Endproduktes mit den vorherrschenden Plasmaparametern und der Entladungsart verknüpft werden.

Die Entstehung von Sekundärelektronen und ihr Einfluss wurden intensiv in einem Plasma-Immersion-Ionenimplantations-System mit Hilfe der Passiven Thermosonde untersucht. In diesem System werden Ionen auf ein Substrat beschleunigt, welches mit Hochspannungspulsen

gepulst wird. Obwohl die Hochspannungspulse auf sehr kleinen Zeitskalen passieren, war die Passive Thermosonde in der Lage Veränderung während des Prozesses, speziell auf der Substratoberfläche (Zerstäuben einer Oxidschicht, Aufbringen einer Nitritschicht) und ihren Einfluss auf den Sekundärelektronenkoeffizienten zu messen. Die Messungen wurden dabei nicht über nur einen sondern über viele kurze Hochspannungspulse durchgeführt und aufintegriert. Dabei wurden eine Vielzahl an verschiedenen Substratmaterialien (Cu, Stahl, Al, Mg, AlMg, Ti, Mo, Zn, AZ91) unter Verwendung von verschiedenen Prozessgasen (Ar, N₂) studiert.

Weitere Untersuchungen beinhalten den Einfluss des Prozessgases während der Kathodenzerstäubung von Titan auf die Elektronenenergie und -dichte, als auch der daraus resultierende Energiefluss. Dies wurde wiederum mit einer Kalorimetrischen Sonde realisiert, welche mit einer Langmuir-Sondenmessung kombiniert wurde. Mit Hilfe der ermittelten Plasmaparameter und den gewonnen Abscheideraten konnte der Energiefluss in seine einzelnen Teile separiert werden.

Des Weiteren wurde die Kalorimetrische Sonde genutzt um den Energiefluss in einer Gas-Aggregationskammer zu untersuchen, welche im höheren Druckbereich von 20 Pa bis über 200 Pa arbeitet und der Herstellung von Nanopartikeln dient. Dabei wurden drei verschiedene Kathodenmaterialien benutzt, eine reine Kupfer- und eine reine Wolframkathode und zudem eine Mischkathode bei der 37 kleine Wolframstifte in eine Kupferkathode eingelassen waren. Parametervariationen im Magnetronstrom, der Distanz zur Kathode und dem Arbeitsdruck wurden durchgeführt. Neben den kalorimetrischen Messungen wurden auch mit einer Langmuir-Sonde die Plasmaparameter bestimmt und Abscheideraten gemessen. Bei ausgewählten Parametern wurden Testabscheidungen hergestellt, welche danach unter einem Elektronenmikroskop untersucht wurden.

Unter anderem wurde auch eine umfangreiche Untersuchung von fünfzehn Gas-Kathoden-Kombinationen mit der Passiven Thermosonde, der Langmuir-Sonde und dem Schwingquartz durchgeführt. Diese gaben wiederum Aufschluss über den intergralen Energiefluss, den Plasmaparametern und der Abscheiderate während der Prozesse. Mit zusätzlichen Simulationen zur Kathodenzerstäubung konnte ein umfangreiches und verständliches Bild über die Komposition des Energieflusses von Ag-, Al-, Cu-, Ti- und W-Kathoden bei der Zerstäubung mit Ar, Kr und He und die vorherrschenden dominanten Teilchenprozesse gewonnen werden.

List of Publications

This thesis is partly based upon the following compilation of peer-reviewed papers which are either already published or submitted for publication in various scientific journals, respectively.

- [I] **F. Haase**, D. Manova, S. Mändl, and H. Kersten, “Evidence of secondary electron emission during PIII pulses as measured by calorimetric probe,” *The European Physical Journal D*, vol. 70, p. 186, 2016.
- [II] **F. Haase**, D. Manova, D. Hirsch, S. Mändl, and H. Kersten, “Dynamic determination of secondary electron emission using a calorimetric probe in a plasma immersion ion implantation experiment,” *Plasma Sources Science and Technology*, vol. 27, p. 044003, 2018.
- [III] **F. Haase**, H. Kersten, and D. Lundin, “Plasma characterization in reactive sputtering processes of Ti in Ar/O₂ mixtures operated in metal, transition and poisoned modes: a comparison between direct current and high-power impulse magnetron discharges,” *The European Physical Journal D*, vol. 71, p. 245, 2017.
- [IV] **F. Haase**, D. Lundin, S. Bornholdt, and H. Kersten, “On the Impact of Electron Temperature in Magnetron Sputtering Benchmarked with Energy Flux Measurements,” *Contributions to Plasma Physics*, vol. 55, pp. 701–713, 2015.
- [V] S. Gauter, **F. Haase**, P. Solar, O. Kylian, P. Kus, A. Choukourov, H. Biederman, and H. Kersten, “Calorimetric investigations in a gas aggregation source,” *Journal of Applied Physics* (submitted), 2018.
- [VI] S. Gauter, **F. Haase**, and H. Kersten, “Experimentally unraveling the energy flux originating from a DC magnetron sputtering source,” *Thin Solid Films* (submitted), 2018.

Contents

Preface	i
Abstract	iii
Kurzfassung	v
List of Publications	vii
1 Introduction	3
2 The plasma state of matter	5
2.1 Fundamentals of Plasma Physics	5
2.1.1 Plasma definition and properties	5
2.1.2 Debye-shielding and plasma frequency	6
2.1.3 Plasma sheath	8
2.2 Plasma-wall interaction and energy balance	9
2.2.1 The total energy flux	10
2.2.2 Contribution of particles	11
2.2.3 Surface processes	17
2.2.4 Conduction and convection	19
2.2.5 Radiation	21
2.2.6 Loss processes	21
2.3 Plasma sources and coating techniques	22
2.3.1 Basics of plasma generation	22
2.3.2 Magnetron sputtering	25
2.3.3 Plasma-immersion ion implantation	29
3 Plasma diagnostics	35
3.1 Calorimetric probing	35
3.2 Passive thermal probe (PTP)	36
3.2.1 Evaluation methods	37
3.2.2 Equilibrium temperature method	39
3.2.3 Probe design	40
3.3 Recent developments in passive thermal probe diagnostics	41
3.3.1 Electron beam calibration	42
3.3.2 Improved probe design	44
3.4 Electrostatic probing	46
3.4.1 Probe design	48
3.4.2 Evaluation of Langmuir probe measurements	49

3.4.3	Recent developments in Langmuir probe diagnostics	50
3.5	Quartz crystal microbalance	52
4	Experimental Results	54
	Publication [I]: Evidence of secondary electron emission during PIII pulses as measured by calorimetric probe	55
	Publication [II]: Dynamic determination of secondary electron emission using a calorimetric probe in a plasma immersion ion implantation experiment . . .	63
	Publication [III]: Plasma characterization in reactive sputtering processes of Ti in Ar/O ₂ mixtures operated in metal, transition and poisoned modes: a comparison between direct current and high-power impulse magnetron discharges	75
	Publication [IV]: On the Impact of Electron Temperature in Magnetron Sputtering Benchmarked with Energy Flux Measurements	83
	Publication [V]: Calorimetric investigations in a gas aggregation source	97
	Publication [VI]: Experimentally unraveling the energy flux originating from a DC magnetron sputtering source	109
5	Conclusion and Outlook	130
	Bibliography	142
	Curriculum Vitae	I
	Acknowledgments	III

1 Introduction

We manage a great portion of our daily life with tools like personal computers, check the weather, approve bank transfers or buy train tickets with our smartphones and watch our favorite TV shows after a hard day's work on giant screens in our living rooms. Airplanes and cars take us anywhere we want in the world within a couple of hours, grandma's new hip implant enables her to walk again and when we return late at night, powerful street lamps lead our way home. If it is just the anti-reflective coating on our new glasses [1], the nanometer sized structures etched into a silicon wafer that represent the basis of a microchip [2], heat and wear resistant components of airplane turbines [3,4] and combustion engines or biocompatible coatings of medical implants [5–7], all these things would not be possible without a world of plasma and plasma based applications.

Plasma is known as the fourth state of matter and in contrast to solids, fluids and gases, it almost does not exist naturally on earth, except in natural spectacles such as lightnings in thunderstorms and auroras near the poles (see figure 1.1).



Figure 1.1: Aurora borealis captured in Iceland. Photograph downloaded from [8]

Although 99 % of the visible universe is still in the plasma state [9], e.g. in stars, on earth it must be artificially generated from neutral gases. One of the biggest challenges in plasma physics is the development of a commercially successful fusion reactor to mimic the processes inside stars like our own sun, where light atoms fuse into heavier elements and release a gigantic amount of energy - nuclear fusion. Since it is impossible to generate the gravitational force that is present inside the stars during the fusion process, nuclear fusion on earth needs to be performed under enormous temperatures (exceeding 100 million degrees

Celsius) [10], resulting in a very hot plasma that pushes the limits on materials used for the reactor walls.

Besides fusion plasmas, one of the well established fields of plasma technology is plasma based material processing. These processes usually do not utilize million degrees hot fusion plasmas but are actually performed under almost room temperature. These kinds of plasmas are called low temperature plasmas (LTP), ranging from around room temperature to a couple of hundred degrees Celsius. Since the requirements for ever shrinking structures etched into a silicon wafer to produce integrated circuits, which are key features of a microchip, could no longer be met by commonly used wet etching techniques in the early 70's, the semiconductor industry was pushing for a new way to accomplish manufacturing these demanding geometries [11]. Plasma based etching processes have the advantage of high selectivity and anisotropy which results in a high aspect ratio of the trenches and has replaced wet etching techniques in many fields. Since then, LTPs have opened up a wide variety of methods and techniques for modification of surfaces of various materials commonly used in the industry today. Besides semiconductor etching, plasma processes are used for modification and activation, as well as cleaning of surfaces. The advantage of the low temperatures during LTP processes enables the possibility to treat heat sensitive materials which was not the case for pure chemical processes. The strength of LTPs is the different nature of its components. While the ionized gas electrons are highly mobile and energetic due to their small mass, the heavy ions are slow resulting in a non-equilibrium of the different plasma components. This non-equilibrium makes it possible to be highly reactive and fuel chemical reactions inside the plasma due to the electrons, but also at a very low temperature. This ability and the fact that LTP processes enable a high level of control have made it the perfect tool for industrial applications.

This has lead to a wide variety of different plasma based thin film deposition techniques. One of the first methods of plasma-enhanced chemical vapor deposition (PECVD) is the direct current magnetron sputtering (DCMS) where cathode material is fragmented by bombardment of plasma ions which are accelerated onto the cathode. The sputtered material can then condense on a substrate surface and create a thin film. Further enhancements of the sputtering applications and the availability of more sophisticated power sources lead to the application of pulsed sputtering techniques like high-power impulse magnetron sputtering (HiPIMS). In contrast to pulsing the cathode, implantation processes apply high voltage pulses to the substrates resulting in implantation of ions into the surface. This is used e.g. in medical implants as well as in doping processes for semiconductors.

Although plasma based surface modifications are widely used in the industry nowadays, many industrial processes are operated in a trial and error approach and lack the fundamental background of the mechanisms present during the different processes. The missing parts necessary to obtain a complete picture of thin film applications can only be obtained by applying extensive diagnostics on these processes, most notably energy flux measurements, to be able to adjust the systems to produce the desired outcome. Additional knowledge may also pave the way for improved modeling of applications allowing for more accurate predictions and simulations. Especially the calorimetric probe has proven itself to be the perfect tool for energy flux measurements. Since its introduction in 1978 [12] it has been applied in many different environments [13–22].

2 The plasma state of matter

2.1 Fundamentals of Plasma Physics

This chapter gives a basic introduction to plasma physics and relevant terms for this work. The term 'plasma' to describe an ionized gas was first introduced by Irving Langmuir in 1928 when he was searching for a way to extend the lifetime of tungsten wires used in light bulbs [23]. Langmuir defined the plasma as a region of 'balanced charges of ions and electrons' and in analogy to a neutral gas, which is characterized by the temperature T and a number density of particles per unit volume n , a plasma is defined by specific parameters, called plasma parameters, and some basic properties.

2.1.1 Plasma definition and properties

A plasma is defined as 'a quasi neutral gas of charged and neutral particles which exhibits collective behavior' [9]. This definition covers the main three properties all plasmas have in common and will be explored in the following.

Quasineutrality

As mentioned earlier, a plasma is described in a similar way than a neutral gas itself through the densities of its charge carriers. Since it is commonly generated from a neutral gas by ionization processes like impact ionization, it consists of positively charged ions and electrons in its most primitive form. The sum of the density of electrons (n_e) and positively (and sometimes negatively) charged ions (n_i) in a plasma equals zero:

$$\sum_k q_k n_{i,k} - e_0 n_e = 0. \quad (2.1)$$

Here, q stands for the different charges of the ions (positive and negative) and e_0 is the elementary charge of an electron. This leads to the fact that a plasma is macroscopically seen as neutral [24]. In many cases it is therefore common to assume $n_i \approx n_e$. However, it is possible that deviations from neutrality can develop on short scales in terms of several Debye lengths (see section 2.1.2), which results in the supplement 'quasi'.

Collective behavior

To further pursue the analogy of a neutral gas, it is crucial to talk about the difference of particle interaction. In a neutral gas, the only way of particles interacting with each other is through collisions. It is a result of the short-range van der Waals forces, which decay with the interparticle distance following r^{-6} . In a plasma this is a whole different story. Like

the term itself suggests, collective behavior is merely a combined action of several particles which results in important properties and characteristic behavior of a plasma. In contrast to a neutral gas, the electrostatic interaction of particles in a plasma can be described with the Coulomb potential, which slowly decays with r^{-2} , making it a long range force in opposition to the aforementioned van der Waals forces. As a result, each plasma particle interacts with a large number of other surrounding particles creating a simultaneous response in the case of an external force. One of the most prominent examples of collective behavior is the Debye-shielding.

2.1.2 Debye-shielding and plasma frequency

The ability to reduce electric fields is one of the key features of a plasma. If one is to release an additional charge Q^+ into the plasma, the trajectories of the electrons and ions respond to its Coulomb potential

$$\Phi_C(r) = \frac{Q}{4\pi\epsilon_0 r} \quad (2.2)$$

where, r is the distance to the positive charge, Q the extra charge itself, and ϵ_0 the vacuum permittivity. As a consequence, the net charge carrier densities around Q^+ change, trying to compensate its presence to ultimately retain the status of quasineutrality. This leads to screening of the electric field of the extra charge, meaning it no longer follows a strict Coulomb potential [24]. The resulting potential is called Debye-Hückel or Yakawa potential, which follows

$$\Phi_D(r) = \frac{Q}{4\pi\epsilon_0 r} e^{-r/\lambda_D} . \quad (2.3)$$

Here, $Q/4\pi\epsilon_0 r$ is the unperturbed Coulomb part and λ_D is the so called Debye length which is a characteristic scale length in a plasma.

The linearized Debye length consists of an electron and ion part and is defined as

$$\lambda_D^{-2} = \lambda_{De}^{-2} + \lambda_{Di}^{-2} . \quad (2.4)$$

The electron Debye length is given by

$$\lambda_{De} = \sqrt{\frac{\epsilon_0 k_B T_e}{n_{e,0} e_0^2}} , \quad (2.5)$$

where k_B is the Boltzmann constant, T_e the electron temperature and $n_{e,0}$ the undisturbed electron density. The ion Debye length is defined in analogy with the ion temperature T_i and density $n_{i,0}$. Especially in LTPs, where $T_i \ll T_e$, the ion term is often neglected and the shielding is mainly performed by the more agile electrons. Figure 2.1 shows a comparison between the Coulomb and Debye potential, where a much faster decay can be seen for values $r > \lambda_D$ in the case of a Debye potential. Therefore, a plasma needs to be at least several Debye lengths in size ($L \gg \lambda_D$) to actually be quasineutral and for the Debye shielding to work.

The time scale at which the plasma can actually react to an external stimulus is given by the inverse plasma frequency and is called response time $\tau_e = \omega_{p,e}^{-1}$. Here, the electron

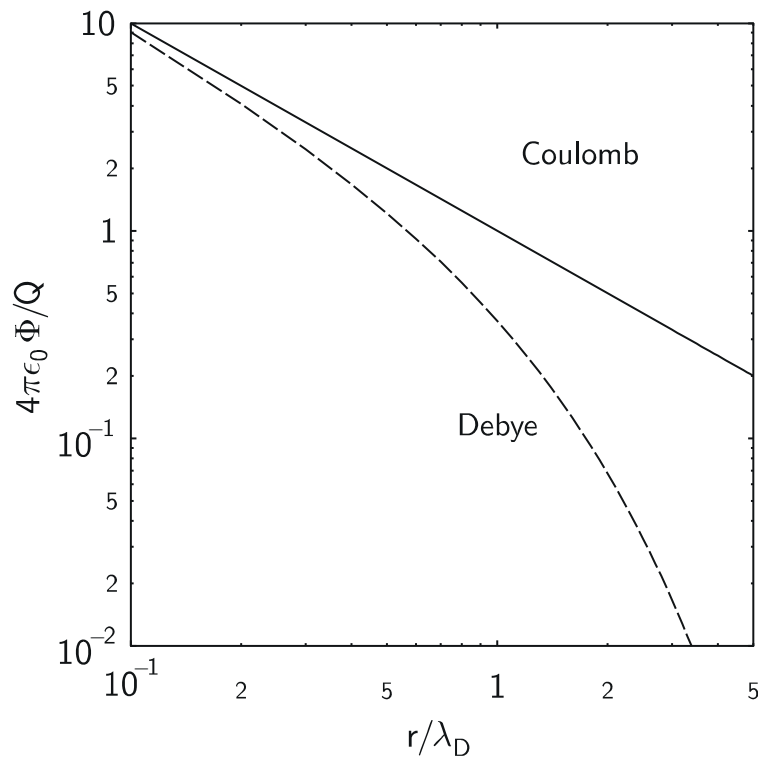


Figure 2.1: Comparison between an unshielded Coulomb potential and the Debye potential. Taken from [24].

plasma frequency is given by

$$\omega_{pe} = \sqrt{\frac{n_{e,0} e_0^2}{\epsilon_0 m_e}}, \quad (2.6)$$

where m_e stands for the electron mass. The ion plasma frequency is given using $n_{i,0}$ and the ion mass m_i , which is usually in the order of four magnitudes higher than those of electrons. This means that only electrons are fast enough to follow disturbances at frequencies of $\omega_{ext} > \omega_{pl,i}$ which is used in many plasma systems with radio frequency (rf) driven discharges. Finally, the amount of electrons shielding the positive charge Q^+ is given by

$$N_{De} = \frac{4}{3}\pi\lambda_{De}^3 n_e. \quad (2.7)$$

Following equation 2.5, electrons and ions exhibit different shielding lengths due to different temperature of the species, leading to $N_{De} \neq N_{Di}$. For the criterion of collective behavior to be true, $N_{De} \gg 1$ must be fulfilled. Hence, if these requirements are fulfilled the plasma species exhibit a fundamentally different behavior from that of gas particles which are bound to interact upon the premise of the short-range van der Waals force through collisions whereas multiple plasma species interact as a 'collective' through the long range Coulomb force.

Further details on the definition of a plasma can be found in introductory textbooks such as [9, 24].

2.1.3 Plasma sheath

In LTPs there is usually an inequality present in terms of thermal velocity of the different plasma species. Electrons usually exhibit a much higher thermal velocity than the much heavier ions, meaning they are more likely to hit a wall and recombine, leaving the plasma with a local net positive charge. This process is even further enhanced due to the fact that the plasma potential Φ_{pl} inside the plasma bulk is positive in reference to the wall potential, increasing the probability of electron wall losses (as shown in figure 2.2). As a consequence, an electric field develops due to the remaining positive charge, leading to trapping of electrons inside the plasma which in turn results in a formation of an equilibrium in which the flux of electrons to surrounding walls is equal to that of ions. The region right in front of a wall, where electrons encounter a repulsive force and ions are attracted is called plasma sheath (see figure 2.2).

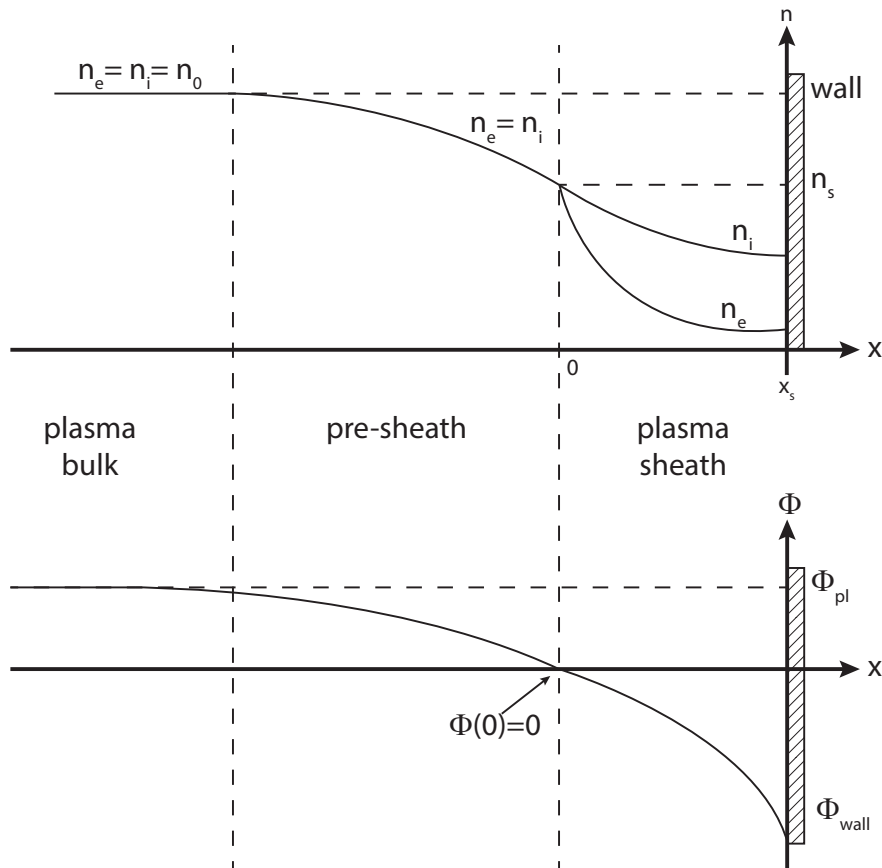


Figure 2.2: Plasma sheath model: The top graph shows the electron and ion densities n_e and n_i , respectively, starting from the bulk plasma across the pre-sheath to the sheath, formed right before the wall. The potential characteristics are shown in the bottom graph. This model works under the assumption of a Maxwellian electron distribution.

The region between the plasma sheath surrounding the surface and the unperturbed plasma is called pre-sheath. The formation of the plasma sheath and pre-sheath is one of the most important properties of a plasma, since it leads to shielding of electrical charges and reduction of electrical fields. Further, it defines the velocity of ions that are able to

escape from the bulk plasma. Said velocity is defined by the Bohm criterion, developed by David Bohm in 1949 [25] stating that every ion at the sheath edge possesses at least the Bohm velocity

$$v_i \geq v_B = \sqrt{\frac{k_B T_e}{m_i}} \quad (2.8)$$

which is equal to the ion sound speed. Hence, the ion flow is supersonic.

2.2 Plasma-wall interaction and energy balance

Every plasma process is spatially confined by some sort of wall. In many cases this can be a grounded electrode, a substrate or a chamber wall. Since plasma processing of materials is one of the fastest growing fields of plasma physics and has been widely adopted in industrial process applications, plasma-wall interactions (PWI) are one of the key fields of study when it comes to low-temperature, low-pressure plasma applications, such as surface modification and deposition of thin films as well as semiconductor etching [14, 20, 26–31]. Even in the thermal plasma research field which includes the field of controlled fusion, plasma-wall interactions are studied extensively [32–34] where the goal is the creation of new compound materials able to withstand the difficult requirements of the highly energetic plasma species.

In all cases, the interaction between the plasma and the surrounding surfaces is of key interest and can be structured into three fundamental categories: First, there is a chemical component which alters the surface due to chemical reactions supported or initiated by the plasma. This includes surface cleaning and activation processes. Second, a physical component describing the physical transformation of the surface by the plasma due to processes like sputtering, implantation and secondary electron emission. And third, the energy transfer to the surface which is caused by the aforementioned chemical and physical processes and their energy flux to the substrate as well as any further process responsible for energy transfer between the plasma and the surface.

In modern plasma applications it is crucial to understand those three key categories and especially the third one can be directly related to important properties of the final product. Understanding the energy transfer between plasma and surface enables a whole new level of process control (e.g. etch rates in semiconductor industry, abrasion and erosion in combustion engines and ion thrusters, film structures in plasma enhanced deposition processes). In the ever growing branch of thin film deposition the properties of the films are highly dependent on the energy transfer during the process itself. It can mean that a rather porous film with specific properties will be deposited in one process, but changing one process parameter, like the power that is fed into the system, will result in a whole different film growth (e.g. a dense, columnar film) with a whole different set of mechanical and chemical properties. To visualize the effect these parameters have on film growth, so called structure zone diagrams (SZD) have been developed, which were first introduced by Movchan and Demshishin [35] in 1969. A rather enhanced version was given by Thornton [27] in 1974 which led to a more recent model by Anders in 2010 [28] which is shown in figure 2.3.

The following sections will explore the most important processes contributing to the energy balance at the surface in greater detail. Starting with a description of the particle balance at the junction between the surface and the plasma, including particles originating from the

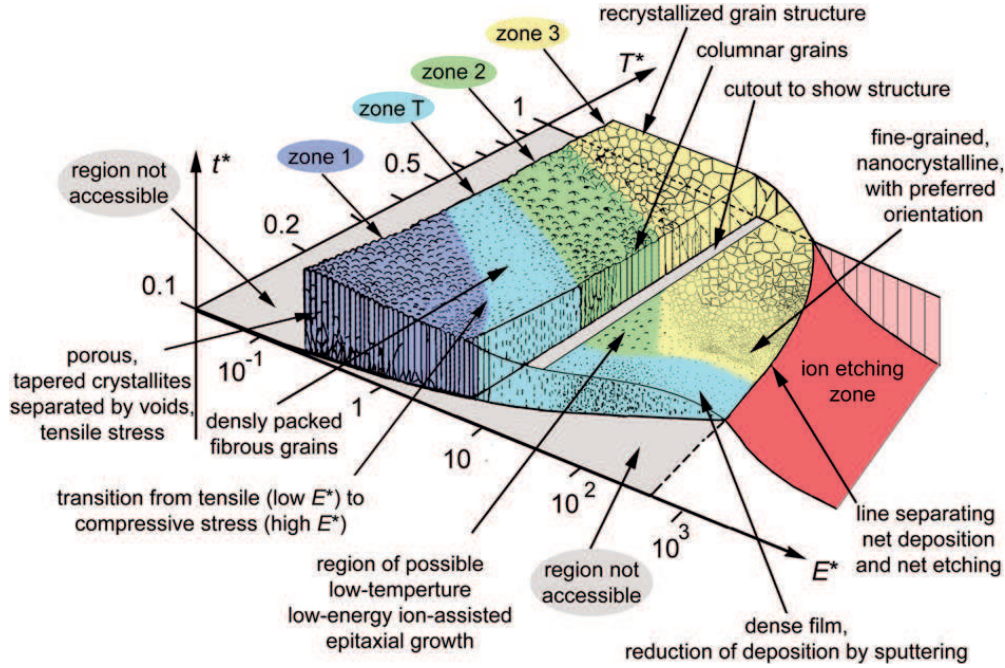


Figure 2.3: Structure zone diagram (SZD) for energetic film deposition, where T^* is a generalized homologous temperature, E^* the normalized energy flux and t^* represents the net thickness. The numbers on the axes are given for simpler orientation only, since the actual values have a strong dependence on the investigated material and many other process conditions. Illustration taken from [28].

plasma such as electrons, ions and neutrals as well as second generation particles such as sputtered particles and secondary electrons.

2.2.1 The total energy flux

The energy transfer between a surface and a plasma is the result of the total energy flux J_{total} which can be divided into different categories. The total energy flux is described in equation 2.9 and consists of the energy flux from particles J_{part} , surface processes J_{surf} , as well as convection and conduction J_{con} and radiation J_{rad} processes in addition to any loss process J_{loss} reducing the energy transfer.

$$J_{total} = J_{part} + J_{surf} + J_{con} + J_{rad} + J_{loss} \quad (2.9)$$

The knowledge about the different contributions allows for calculation of quantitative values. In practice, however, these values must be corrected with certain additional coefficients usually describing the efficiency of a certain process like the probability of sticking of a particle to the surface. In most cases these are probability values ranging from 0 to 1 and in the following a value of 1 was used for all of those cases, meaning that the calculated energy flux is always a maximum value and the real world value is supposedly smaller. Nevertheless, the combination of electrostatic probe measurements (see section 3.4) and SRIM simulations to obtain sputter yields and energy values of sputtered and reflected particles, as well as calorimetric probe data (see section 3.1), which measures the total energy flux, allows for stripping down the total energy flux into its main contributions.

2.2.2 Contribution of particles

Energetic particles hitting a surface have a chance of transferring their kinetic energy to the material they impinge on. Either they stick to the surface and deposit their entire energy or get reflected leaving only a part of it. In the plasma case, these particles can be electrons which are normally fast due to their small mass, ions or (fast) neutrals. As mentioned before, the kinetic energy of heavy particles (ions and neutrals) has an important impact on film growth and structures [20, 27–29].

Assuming that every particle hitting the surface sticks to it, the contribution of particles can be described as

$$J_{part} = \Gamma_{part} \overline{E}_{kin}, \quad (2.10)$$

with Γ_{part} being the particle flux density and \overline{E}_{kin} the mean kinetic energy of the particle stream. Since the energy deposited during film formation is responsible for optical and mechanical properties of the film, high energetic particles can lead to reduction of deposition rate due to a less efficient sticking, unwanted implantation or even sputtering of deposited material. Hence, the tailoring of kinetic energy is crucial for commercial technological plasmas, since it can lead to more efficient, cost reduced processes. Therefore, the contribution of particles to the total energy flux can be written as a sum of its most relevant components leading to

$$J_{part} = J_e + J_i + J_n, \quad (2.11)$$

where J_e is the electron component, J_i the ion component and J_n the energy flux part generated by neutrals. These components are explored in the following sections.

Electrons

Arguably, the most important species in a plasma are the free electrons. They are basically responsible for a majority of key plasma properties like the plasma potential or the degree of ionization. Especially in LTPs they open up the most efficient channel of energy transfer from external sources, e.g. energy transfer through magnetic and electric fields. Further, electrons influence chemical reactions on a major scale, such as molecule fragmentation due to electron impact dissociation. As mentioned before, electrons can be heated very effectively as compared to heavier plasma species due to their small mass, hence, while the electrons are comparatively energetic and possess a high temperature, the background gas resides at a fairly low temperature level. This enables the plasma to be highly reactive at the one hand but being able to do that in a rather low temperature regime on the other, opening up new possibilities to treat a whole different kind of materials (e.g. heat sensitive materials like polymers or biological tissue).

The contribution to the energy flux due to electrons is described by their kinetic energy. Since not all electrons depict the same energy because they lose energy in collisions and other processes, one must assume an electron energy distribution and therefore introduce a mean kinetic energy $\overline{E}_{kin,e}$ for the electrons. The contribution to the total energy flux by electrons is then written as

$$J_e = \Gamma_e \overline{E}_{kin,e}, \quad (2.12)$$

with $\Gamma_e = j_e/e_0$ describing the electron flux density and j_e as the electron current density. The electrons can further be described with the help of an electron energy distribution

function (EEDF). In many cases a Maxwellian energy distribution is assumed [29], leading to

$$J_e = n_e \sqrt{\frac{k_B T_e}{2\pi m_e}} \exp(-\xi) 2k_B T_e = \frac{j_e}{e_0} 2k_B T_e. \quad (2.13)$$

Here, k_B denotes the Boltzmann constant, T_e the electron temperature and m_e the electron mass, whereas $\xi = e_0 V_{bias} / k_B T_e$ describes the ratio between the potential difference of the plasma and the surface and the electron energy. Besides a Maxwellian approach, sometimes electrons are better described by a Druyvesteyn EEDF which leads to an electron energy flux contribution described by

$$J_e = n_e \sqrt{\frac{k_B T_e}{2\pi m_e}} k_B T_e \left(-\xi \exp(-0.25 \xi) + (1.79 + 0.89 \xi^2) \operatorname{erf}(0.5 \xi) \right). \quad (2.14)$$

In case of a mono-energetic EEDF equation 2.12 can be written as

$$J_e = n_e \sqrt{\frac{k_B T_e}{2\pi m_e}} 2\pi (1 - \xi)^2 k_B T_e. \quad (2.15)$$

In the case that the electrons are at a thermodynamic equilibrium the Maxwell distribution applies. However, this is only valid if the degree of ionization is high since the electron-electron collisions drive the EEDF towards a Maxwellian shape. With higher electron energies, however, inelastic collisions of electrons with heavy particles lead to a drop of the EEDF in which case the Druyvesteyn approach gives a more accurate description for a lower ionization degree [36]. A graphical overview of these three EEDFs is given in figure 2.4.

Ions

Alongside electrons, ions are one of the most important species of energetic particles contributing to the total energy flux. They can either be ionized atoms or molecules formed by different processes like electron impact ionization, penning ionization or electron attachment in case of the existence of negative ions such as O^- . Since a plasma is always aiming to retain its status of quasineutrality, the flux of ions and electrons onto a surface can therefore be assumed to be the same at floating potential. The big difference between the electron and ion flux is the fairly isotropic behavior of the electrons due to their high velocity, whereas the ions are much heavier and follow a more directed flux. This is a key feature used in various plasma coating processes since it allows for tailoring of the ion trajectories more easily.

In analogy to the electrons (see equation 2.12) the ion contribution is described by

$$J_i = \Gamma_i \bar{E}_{kin,i}, \quad (2.16)$$

where $\Gamma_i = j_i / e_0$ is the ion flux density and $\bar{E}_{kin,i}$ the mean kinetic energy of the ions. However, Γ_i as well as $\bar{E}_{kin,i}$ are highly dependent on the discharge regime, which alters the

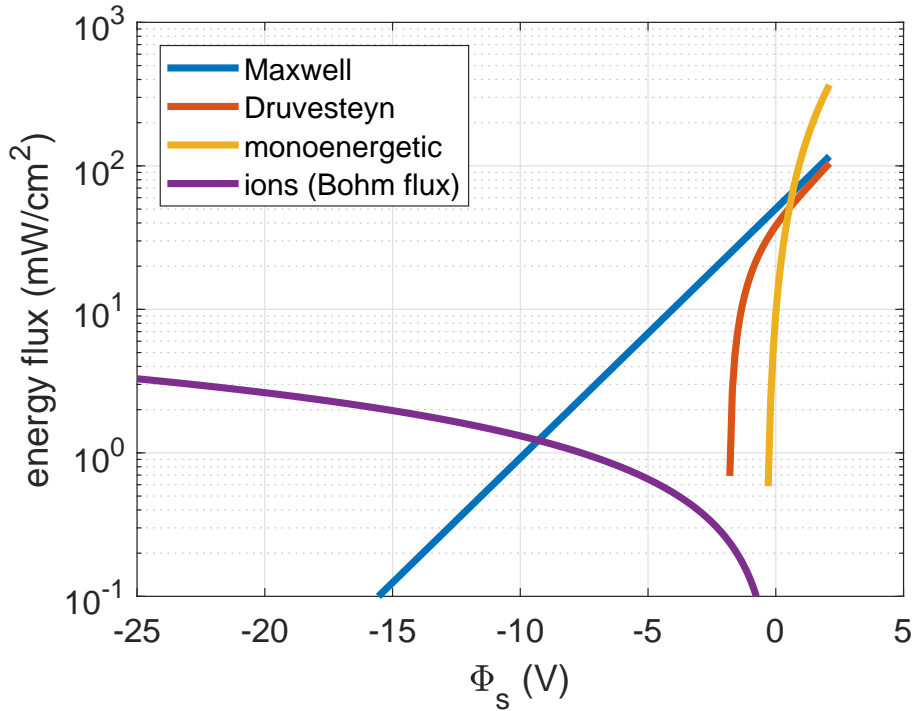


Figure 2.4: Calculated energy flux by electrons as a function of substrate bias for various electron energy distribution functions (EEDF) as well as the ion energy flux as calculated from the Bohm flux. The experimental values origin from a typical DC magnetron sputter system using Ti as target material in an argon discharge at 1 Pa and 50 W resulting in $n_e = 5.5 \times 10^{15} \text{ m}^{-3}$, $k_B T_e = 2.5 \text{ eV}$ and a plasma potential of $\Phi_{pl} = 2.1 \text{ V}$.

ion current density j_i , which can be described by the following expressions [37]:

$$\begin{aligned}
 j_i &= n_e \sqrt{\frac{k_B T_e}{m_u}} \exp(-0.5) && \text{Bohm-flux} \\
 j_i &= \frac{4 \epsilon_0}{9 e_0} \sqrt{\frac{e_0}{m_i}} \frac{\Phi_{sh}^{3/2}}{d_{sh}} && \text{Child-Langmuir (collisionless)} \\
 j_i &= \frac{1}{4} n_i v_i && \text{thermal flux} \\
 j_i &= n_i v_{amb} && \text{ambipolar diffusion}
 \end{aligned} \tag{2.17}$$

Here, n_e is the electron density, k_B the Boltzmann constant, T_e the electron temperature, e_0 the elementary charge and ϵ_0 the vacuum permittivity. Further describes Φ_{sh} the potential drop in the sheath and d_{sh} the corresponding sheath width, v_i and v_{amb} denote the ion velocities. In many plasma applications the typical pressures are in the order of several Pascal or lower, rendering either the Child-Langmuir law inspired equation ($p \leq 1 \text{ Pa}$) or the Bohm equation ($p \leq 10 \text{ Pa}$) as the most adequate form of the ion current. The change in pressure does not only influence the ion current but also their mean kinetic energy, which is also strongly dependent on apparatus geometry, gas mixture and type of gas discharge. The influence of the pressure on the ion energy distribution function (IEDF) is shown in figure 2.5 for an Ar discharge.

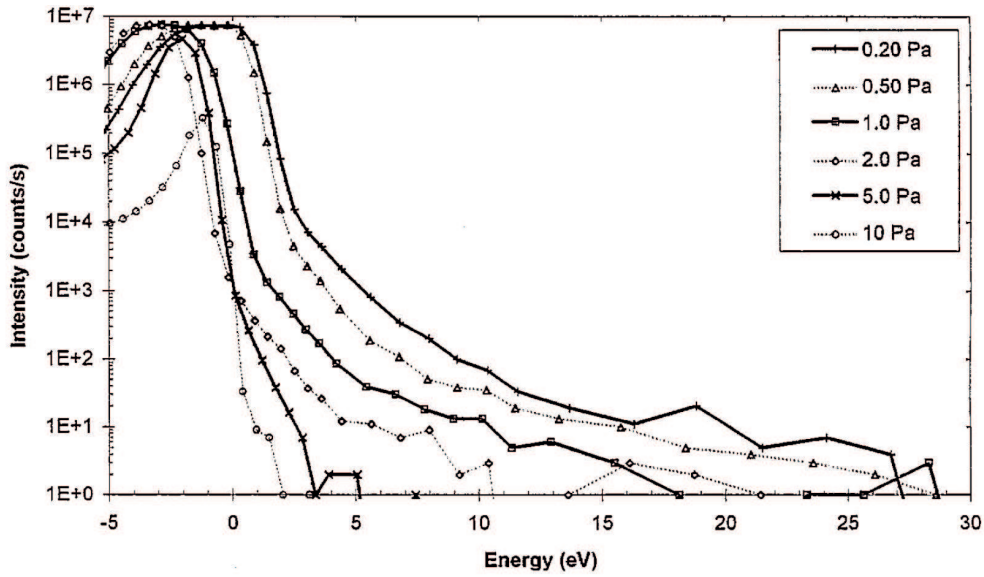


Figure 2.5: Effect of Ar pressure on the ion energy distribution function (IEDF) in a DC magnetron sputtering discharge using a Cu target at a discharge current of about 0.4 A. Image taken from [38].

In basic plasmas it is assumed that the amount of negative ions is negligible and therefore only positive ions exist. They gain their energy due to acceleration in the sheath in front of the surface, meaning their kinetic energy is primarily determined by the voltage drop Φ_{sh} in the sheath. In this case the kinetic energy of the ions can be described by

$$J_i = j_i \Phi_{sh}. \quad (2.18)$$

However, this simple equation fails to describe the ion contribution correctly at higher pressures. In this case the mean free path λ_{mfp} of the ions decreases with increasing pressure. Once it is in the order of the sheath thickness d_{sh} , or even smaller, the effect of collisions is no longer negligible and ions will start losing significant amount of kinetic energy. Thus, the IEDF is no longer monoenergetic as shown in figure 2.5, where the high energy tail is vastly diminishing with increasing pressure.

In addition to positive ions it is necessary to talk about negative ions as they are bound to form in reactive plasma environments with oxygen admixture or in electro-negative plasmas. In contrast to the aforementioned acceleration of positive ions within the sheath, negative ions are decelerated as they pass through the sheath on their way to the most positive region of the plasma (most dense region), resulting in loss of kinetic energy. Due to their relatively low kinetic energies (thermal ions), they reside in the bulk plasma for a long time. It is still possible though, for negative ions to gain high kinetic energies if they are produced close to an electrode, such as a negatively biased target of a magnetron and be accelerated away from it. This way they are able to gain energies in the order of several hundred eV. Although, such negative ions usually have a small current density they can do a lot damage to the surface structure when impinging on the surface with such high energies and alter the film properties in unwanted ways [39,40]. The most commonly occurring negative ions in plasma processing are O^- , O_2^- and SF_6^- .

Neutrals

In theory the description of the contribution of neutral particles is very similar to that of ions and can be written in analogy of equation 2.16 as

$$J_n = \Gamma_n \bar{E}_{kin,n}. \quad (2.19)$$

Since neutrals do not carry any charge, their flux density is not dependent on the substrate potential as it is the case with electrons or ions. However, the detection and investigation of neutrals in a plasma is more complicated since they can not be manipulated with electric fields. The main three source processes for neutrals in technological plasmas are sputtering of target material atoms, reflected neutrals and recombined energetic ions known as fast neutrals.

In general LTPs are characterized by low ion and neutral gas temperatures resulting in low kinetic energies of the neutrals of around several 10 meV up to a few eV [29]. Neutrals which do not contribute to film growth will desorb from the surface as thermal neutrals. The only dependent factors to the energy contributions are the surface temperature T_{surf} and the gas temperature T_{gas} which leads to a more enhanced version of equation 2.19:

$$J_n = \Gamma_n k_B (T_{gas} - T_{surf}) \quad (2.20)$$

It must be noted that due to the energy distribution in the gas, the temperatures are averaged values which is in analogy to the $\bar{E}_{kin,n}$ in equation 2.19. As long as the flux density Γ_n and the energy of the neutrals are small this energy flux is not one of the major contributors to the total energy flux. However, in different plasma systems like atmospheric pressure plasmas the high gas throughput and gas temperatures can lead to a significant amount of energy deposited on the surface leading to substrate heating.

To kick things off with the different source processes the following lines will go a little bit more into detail about sputtered neutrals and sputtering itself. One of the main pillars in today's thin film industry is plasma based physical vapor deposition (PVD). Its main mechanism is called sputtering, a process where accelerated ions or fast neutrals impinge on a surface, triggering a collision cascade inside the solid and eventually leading to a target atom leaving the surface. This technique is not only used in vaporization processes where free material has to be 'generated' but also in semiconductor etching applications where complex geometries are etched into a silicon wafer as a basis for modern microchips. When a particle is sputtered from a surface it possesses an initial energy which is highly dependent on various parameters such as angle of incidence and mass of the impinging particle as well as its energy and further, various surface conditions like the mass of the target material atoms as well as surface temperature and structure [41, 42]. The number of sputtered particles per incident particle may vary and the overall probability is usually described by the so called sputtering yield Y :

$$Y = \frac{\text{number of sputtered particles}}{\text{number of incident particles}} \quad (2.21)$$

In most cases the particles that contribute to the sputter yield are ions, although energetic neutrals may also sputter target material. A visual description of the influence of incident particle energy on the sputter yield Y is given in figure 2.6 which shows the sputter yield of krypton ions in various materials depending on the ion energy.

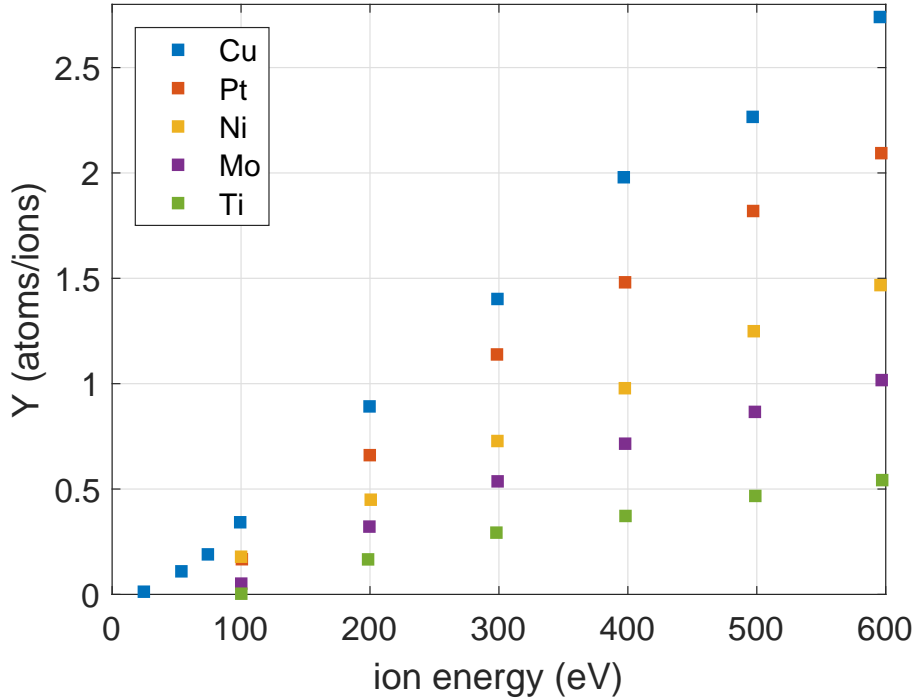


Figure 2.6: Energy dependent sputtering yields for Cu, Pt, Ni, Mo, and Ti in Kr. Data taken from figure 3 in [43].

In typical magnetron sputtering processes the sputter yield is in the range of about 0.1 up to 2, mostly depending on the incident ion energy and mass ratio of incident and target material [44]. The kinetic energy of the sputtered neutrals is usually much higher than the energy of the neutral gas background and is in the order of several 10 eV for typical process plasmas. Besides determination of sputter yields through experimental approaches common simulation models like Stopping Range of Ions in Matter (SRIM) are used to estimate sputter yields [45]. The collision cascades are simulated with the help of the Transport of Ions in Matter (TRIM) package. The software outputs parameters such as number of sputtered particles, sputter yield and energy of sputtered and reflected particles

Another source process of energetic neutrals are reflected neutrals. Reflection of particles always occurs in sputtering processes and gains significant importance if the incident particle mass M_1 is much greater than the target material with mass M_2 , or vice versa. In general, the probability for reflection is rather low as compared to the sputter yield, although, the resulting energy flux can often be in the same range or even surpass it since the reflection leads to the preservation of kinetic energy. The relation between the velocity of a reflected particle v_{refl} and its initial velocity v_{init} is only dependent on the mass ratio and follows

$$v_{refl} = \left(\frac{M_1 - M_2}{M_1 + M_2} \right) v_{init}. \quad (2.22)$$

This equation is another way of expressing the accommodation coefficient α (see equation 2.29) which is introduced in section 2.2.4. Another technique to willingly produce highly energetic neutrals is the utilization of ion beams. In this case ions are created in a source

plasma and then extracted through a grid system. The neutralization can either be happening inside the grid holes or right after passing the grid system due to a neutralizer as well as by charge exchange collisions in the sheath in front of an electrode. These neutrals still exhibit high kinetic energies due to the acceleration at the grid system and depending on the acceleration voltage they can usually range between a few 100 eV of up to several keV [46].

However, there is always the possibility of collisions of energetic ions with neutrals which can either be elastically or with charge exchange. Either way the result of those collisions are fast neutrals with a significant amount of energy. Charge exchange (CXE) occurs when the electron shells of a neutral atom and an ion come into contact, and an electron transfers from the atom to the ion. In this case the energetic ion can be neutralized without losing its kinetic energy. In the case of an elastic collision, some or even all of the momentum of the incident particle is transferred to the collision partner. Anyhow, these two processes do not play an important role in low pressure regimes but gain significance with increasing pressure at around 10^{-2} Pa. The increase of pressure increases the possibility of collisions since the mean free path λ_{mfp} of the particles decreases and reaches values of typical vacuum vessel dimensions. In typical ion beam experiments neutralized particles can make up for roughly 70% [47, 48]. In RF or magnetron discharges, where the nominal pressures are usually higher (several Pa to a few 100 Pa) this effect leads to neutrals with equivalent energies than those of accelerated ions.

2.2.3 Surface processes

This section covers the main processes taking place on the surface that are relevant to the total energy flux. Many process plasmas exhibit complex occurrences that are especially versatile in reactive systems where plasma chemistry plays an important role. However, the complexity of these systems and the qualitative description of every single process would exceed this work, which is why in the following the three main contributions of recombination processes, film formation as well as chemical reactions are described in more detail.

Electron-ion recombination

Ions hitting a surface will recombine with an electron and be neutralized. In order for an ion to actually be able to reach the surface, the surface potential has to be more negative than the plasma potential $\Phi_s < \Phi_{pl}$. In many cases the chamber walls are grounded and conductive substrates are used and can therefore easily provide the electrons necessary for the recombination process. Even if the surrounding walls are at floating potential, which is defined as the potential at which the ion and electron current are equal ($j_e = j_i$), enough electrons are present to recombine with the impinging ions. Since the crucial factor of this process is the amount of ions reaching the surface this process is mainly influenced by the ion flux density Γ_i and follows

$$J_{rec} = \Gamma_i (E_{ion} - E_{ewf}) . \quad (2.23)$$

Here, E_{ion} is the ion energy and E_{ewf} the electron work function. E_{ewf} accounts for the energy an electron has to overcome to be released from the surface. This energy is reducing

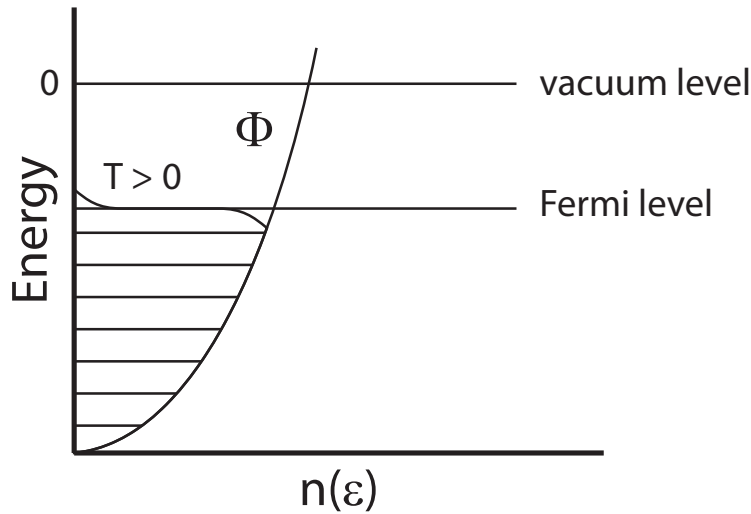


Figure 2.7: Energy diagram of a free electron metal in the conduction band. The density of states $n(\epsilon)$ is shown as a hatched area. Illustration after [49]

the overall energy flux because it is needed to energetically raise the electron from the Fermi level to the vacuum level which is illustrated in figure 2.7.

However, this is only true for metals but does work for semiconductors and dielectrics in a similar manner, where the electron work function is replaced by the minimum binding energy of a valence electron [31].

Film formation

Besides electron-ion recombination, film formation is one of the significant contributors to the energy flux caused by surface processes. When a sputtered particle or precursor fragment hits the surface it is most likely to condense on it. During this process the enthalpy of sublimation E_{subl} is released adding an additional contribution to the energy flux caused by the kinetic neutrals hitting the surface. In analogy to equation 2.23 the contribution of film formation can be written as

$$J_{subl} = \Gamma_n E_{subl}. \quad (2.24)$$

In this equation Γ_n denotes the flux of film-forming neutral particles. In many coating applications the flux of the particles actually contributing to the film can be measured using an in-situ or ex-situ approach. In terms of an in-situ solution devices like a quartz crystal microbalance (QCM) are used to determine the growth rate (see section 3.5) whereas an ex-situ approach would be to determine the film thickness after the process with the help of a profilometer, various microscopy (e.g. laser or SEM) or X-ray techniques.

Chemical reactions

A plasma in its most basic form only consists of ions and electrons generated from the neutral gas. In order to conduct chemical reactions in a plasma, gas admixtures of atomic and molecular gases are introduced into the process. These plasmas are called reactive plasmas and the admixtures can range from plain molecules like H_2 , N_2 and O_2 to complex

precursors such as aluminium triisopropoxide (ATI) or hexamethyldisiloxane (HMDSO). Either way, due to the electrons a plasma can be host to chemical reactions which would normally only occur under very high temperatures at a state of thermodynamic equilibrium. The electrons tend to break up those molecules leaving the plasma with highly reactive radicals and fragments. Depending on the chemical structure and charge of the fragments further reactions like formation of polymeric chains are bound to happen or they will be further dissociated. Due to momentum conservation formation usually happens within a three body collision which is more likely to happen at a chamber wall or a surface rather than in the bulk plasma of low pressure applications, since the mean free path is usually greater than the vacuum vessel dimensions. Therefore, upon re-formation of a molecule the binding energy E_b is released at the surface. For a two atomic molecule like H_2 that is reforming at the surface the transferred energy can be described via

$$J_{mol} = \frac{1}{2} \Gamma_n E_b \quad (2.25)$$

using the neutral flux Γ_n .

2.2.4 Conduction and convection

Especially in laboratory plasmas there will always be contact of the substrate with some kind of heat conductive material, whether it is some kind of substrate holder or the background gas. The physical contact allows energy to be transferred away from the substrate (if the conductor is at a lower temperature), or to be added as an additional energy flux (if the conductor is at a higher temperature). The conductive energy flux can be described with the help of Fourier's law of heat conduction and follows

$$J_{cond} = \frac{1}{A_s} \frac{\lambda_c A_c}{d_c} (T_c - T_s) . \quad (2.26)$$

Here, A_s is the area of the substrate surface and A_c the cross section of the conducting element. λ_c and d_c stand for the heat conductivity and length of the conducting material and T_c and T_s denote the temperatures of the conductor and the substrate surface, respectively. This equation describes a rather simple approach, in reality however, the definition of the heat reservoir is rather complex. The physical contact between the substrate and the conducting material defines the thermal conductivity and in most cases it is hard to define where the reservoir is 'located', since by its definition it is the point where the temperature stays constant during the investigated time period. Therefore, this method is prone to errors.

For most low-pressure plasmas the contribution of convection is of less importance since it describes the interaction with the background gas. The gas pressures in these processes are fairly low, which limits said interaction. However, for higher pressures where the molecular flow is replaced by Knudsen flow or viscous flow it must be taken into account [50].

In the free molecular regime ($p < 10$ Pa), where the Knudsen number is considerably greater than ($Kn \gg 1$), the mean free path of a gas atom λ_{mfp} is in the same order or even greater than the sheath thickness of the boundary layer in front of the substrate ($d_{bl} \leq \lambda_{mfp}$). As a result, the energy flux is highly dependent on the difference between the substrate temperature T_s and gas temperature T_g :

$$J_{conv,mol} = \alpha \chi p (T_g - T_s) . \quad (2.27)$$

Here, α stands for the accommodation coefficient, χ denotes the free molecular heat conductivity and p is the gas pressure. Knudsen [51, 52] describes the free molecular heat conductivity as

$$\chi = \frac{c_p/c_v + 1}{c_p/c_v - 1} \left(\frac{R}{8\pi T_g M_g} \right)^{1/2} \quad (2.28)$$

where c_p/c_v denotes the adiabatic coefficient with c_p and c_v standing for the specific heat at constant pressure and constant volume, respectively. R is the universal gas constant and M_g is the atomic mass of the gas atom. Further, the accommodation coefficient α is given by

$$\alpha = \frac{E_{in} - E_f}{E_{in} - E_s}, \quad (2.29)$$

where E_{in} and E_f are the initial and final energy of the gas atom, respectively. The thermal energy per atom of the substrate is described through E_s .

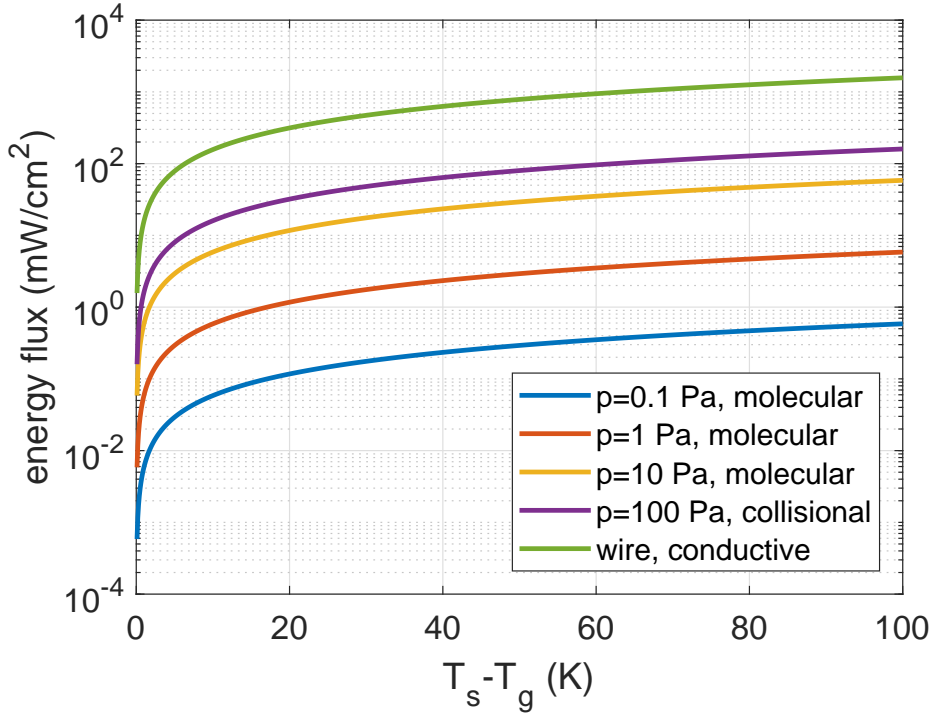


Figure 2.8: Energy flux contribution of conduction and convection as a function of the temperature difference between substrate and background gas or heat reservoir. The values for the free molecular flow were calculated using $\alpha = 0.87$ (Ar on Ti [53]) and a free molecular heat conductivity of $\chi = 0.67 \text{ W}/(\text{m}^2 \text{KPa})$. The adiabatic coefficient was chosen to be $c_p/c_v = 5/3$, the gas temperature was set to room temperature $T_g = 293 \text{ K}$ and the ion mass of argon is $M_g = 39.948 \text{ g/mol}$. For $p = 0.1 \dots 10 \text{ Pa}$ equation 2.27 was used, at $p = 100 \text{ Pa}$ it is no longer valid and the energy flux was calculated using equation 2.30 instead, with $Nu = 1$, $\lambda_g = 1.6 \cdot 10^{-2} \text{ W}/(\text{mK})$ and a thickness of the boundary layer of $d_{bl} = 1 \text{ mm}$ [54]. The conductive curve was calculated using 2.26 with the thermal conductivity of copper $\lambda_c = 380 \text{ W}/(\text{mK})$ for a wire with 1 mm diameter and a length of $d_c = 2 \text{ cm}$ and a probe surface area of $A_s = 9.5 \cdot 10^{-5} \text{ m}^2$ for a $\varnothing = 11 \text{ mm}$ copper platelet.

In systems where $\lambda_{mpf} \ll d_{bl}$ the collisions and interactions between particles and the background gas grow in significance. Therefore, at higher pressures where $Kn \ll 1$ the

system is better described by the collisional regime and the contribution of convection is given by Fourier's law:

$$J_{conv,col} = Nu\lambda_g \frac{T_s - T_g}{d_{bl}} \quad (2.30)$$

Here, Nu stands for the Nusselt number and λ_g is the thermal conductivity of the gas. Figure 2.8 shows the energy flux created by the background gas for different pressures and various $T_s - T_g$. Especially for higher pressures and huge differences in substrate and gas temperature this contribution can gain in significance, although, for most setups the energy flux will be dominated by conductive cooling.

2.2.5 Radiation

One of the most obvious and accessible features of a plasma is its glow. Every element has its distinguished color which is used for lighting devices like street lamps, luminous advertising or plasma screens. However, a plasma does not only emit radiation in the visible light spectrum but also in ultra violet (UV) or infrared (IR). It is therefore no surprise that this kind of radiation contributes to the energy flux onto a surface.

Thermal radiation (IR) may be caused by hot filaments, electrodes or targets as well as by heated chamber walls themselves and can be described using the Stefan-Boltzmann law:

$$J_{rad,IR} = \sigma (\epsilon_{rad} T_{rad}^4 - \epsilon_s T_s^4) \quad (2.31)$$

Where $\sigma = 5.67 \times 10^{-8} \text{ W}/(\text{m}^2\text{K}^4)$ denotes the Stefan-Boltzmann constant, ϵ_{rad} and ϵ_s the emissivities, and T_{rad} and T_s the temperature of the radiating surface and the substrate, respectively. In many cases it is more accurate to account for the geometry of the system with the introduction of a geometry factor $R(A_{rad})$ since equation 2.31 describes the complete energy transfer [37].

Alongside thermal radiation another contribution is caused due to line radiation. Line radiation can range through the whole spectrum starting at UV through the visible spectrum to the infrared. It is dependent on the photon flux Γ_{ph} originating from the plasma and the mean photon energy \overline{E}_{ph} and follows [55]

$$J_{rad,ph} = \Gamma_{ph} \overline{E}_{ph}. \quad (2.32)$$

On paper, this contribution does not look too complicated at all, however, in real environments it is extremely difficult to obtain an absolute measure of the photon flux which gives rise to significant errors.

2.2.6 Loss processes

Sputtering

In one of the previous sections (see section 2.2.2) the idea of heavy particles bombarding a surface and evaporating target material was introduced under the name of sputtering. In contrast to those heavy particles dissipating energy in the solid, particles leaving the surface take energy away and are therefore accounted for with a negative energy flux. In

the description in section 2.2.2 the influence of collisions with the background gas was not discussed although it would lead to a reduction of the energy flux, which is why the same formula applies in the case of sputtered particles leaving the substrate. For this mechanism to really have an impact on the energy flux, the flux of highly kinetic particles needs to be significant. Although the threshold energies for sputtering start at only a few eV, the sputter yields in the case of low energy particles impinging on a surface are fairly low [56], which is why this effect can often be neglected.

Secondary electron emission

Secondary electrons are an ubiquitous nuisance in many plasma process applications necessitating excessive current supplies and shielding for X-rays generated by them. In addition they can hinder plasma processes and deteriorate their outcome. In other cases they are a welcomed and crucial mechanism (e.g. plasma generation, cathode ray tubes, electron multipliers). While sputtering is only observed for heavy particle bombardment (ions, neutrals), secondary electrons are known to be created by impact of electrons and photons as well [57]. The contribution of secondary electrons as an energy loss process (negative sign) is given as the product of the secondary electron flux Γ_{see} leaving the surface and their mean kinetic energy $\overline{E}_{see,kin}$ and follows

$$J_{see} = -\Gamma_{see} \overline{E}_{see,kin}. \quad (2.33)$$

In analogy to the negative energy flux originating from sputtered particles leaving the surface, this contribution will be comparably small and can often be neglected. However, the difficulty of handling secondary electron emission (SEE) at surfaces when current measurements are performed can not be neglected. Secondary electrons tamper with the current measurements in a way that a secondary electron leaving the surface will account for a higher current (positive net current) or decrease the actual value (negative net current). In processes with a high amount of energetic particles bombarding a surface like plasma-immersion ion implantation (see section 2.3.3) this mechanism can result in significant deviations if the energy flux is deduced from electrical current measurements.

2.3 Plasma sources and coating techniques

In contrast to natural plasmas as they occur in space, laboratory plasmas need a constant power input to sustain the discharge and account for energy losses due to charge carriers hitting a wall. Since its early days where discharge tubes were driven with a DC unit, plasma generation has come a long way and is as versatile as its applications [58,59]. In the following sections various plasma sources and coating techniques are presented that are relevant for this work.

2.3.1 Basics of plasma generation

To ignite and sustain a plasma discharge the generation of charge carriers (electrons and ions) is fundamental. The whole process can be described as some sort of avalanche effect. Due to natural radiation (ionizing cosmic radiation) there are always some free charge carriers

available in a neutral gas. Those free electrons need to be accelerated either with the help of electric fields or microwaves. Once they have reached energies above the ionization energy of the neutral gas they are able to ionize the neutrals by electron impact ionization. As an easy example the process can be described by



where an electron e^- collides with an atom A [58]. Now there are two electrons which in turn are again accelerated and after gaining enough energy are able to ionize other atoms and create additional electron-ion pairs. This avalanche effect is best described by the first Townsend coefficient α which follows

$$\alpha = \frac{\nu_{ion}}{v_d}, \quad (2.35)$$

where ν_{ion} is the ionization frequency and v_d the mean drift velocity of the electron. An illustration of the electron avalanche effect can be seen in figure 2.9.

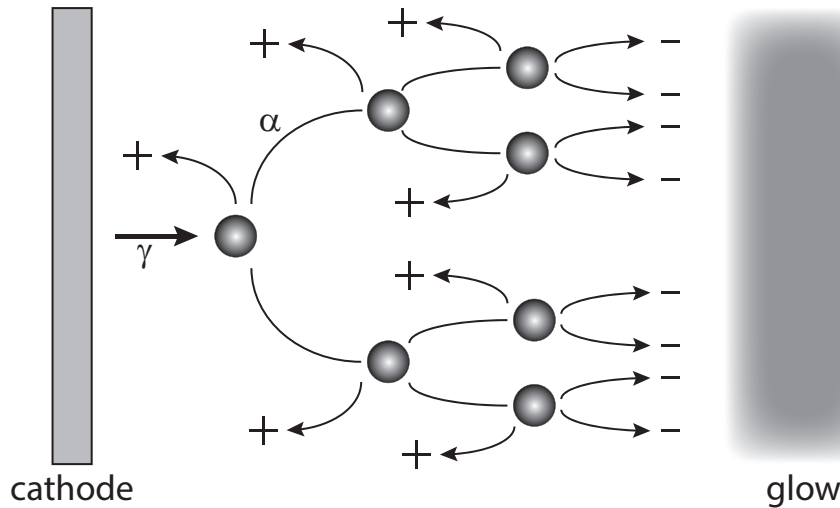


Figure 2.9: Illustration of the electron avalanche effect. An electron accelerated away from the cathode generates an electron-ion pair with the probability α which leads to even more pairs and ultimately to plasma generation. Secondary electrons can be generated due to ion impact at the cathode with the probability γ . After [58].

However, when electrons and ions reach the chamber wall or an electrode they recombine, therefore, there is always the need to generate more electron-ion pairs to sustain the discharge. As described in section 2.2.6 there is always a chance of generating secondary electrons if particles are hitting a surface. For ion induced secondary electron emission the secondary electron yield γ , which is characterized as

$$\gamma = \frac{\text{number of released electrons}}{\text{number of incident ions}} \quad (2.36)$$

is about one order of magnitude higher than that of electron induced secondary electrons. Additionally, there is a chance of electrons generating secondary electrons (δ coefficient) when hitting the anode, but those electrons are immediately accelerated back towards the anode

and are therefore usually neglected. Ultimately, to sustain a stable discharge Townsend's stationary law

$$\gamma (\exp (\alpha d) - 1) = 1 \quad (2.37)$$

needs to be fulfilled, demanding that the number of electron-ion pairs generated by the α -process is sufficiently high enough so that the probability for a γ -process becomes unity.

Townsend developed an empirical law for the dependence of α on the electric field which follows

$$\frac{\alpha}{\lambda_{mfp}} = A \exp \left(-\frac{B}{E/\lambda_{mfp}} \right). \quad (2.38)$$

Here, A and B denote constants that are characteristic for each gas, α/λ_{mfp} stands for the electron multiplication per mean free path and E/λ_{mfp} the energy gain of an electron per mean free path. Hence, equation 2.38 is independent of the gas pressure. The breakdown voltage is defined as $U_{bd} = E_{bd}d$ and combining it with Townsend's stationary law (equation 2.37) yields Paschen's law

$$U_{bd} = \frac{Bpd}{\ln(Apd) - \ln(\ln(1 + 1/\gamma))}. \quad (2.39)$$

It can be seen that the breakdown voltage is dependent on the product of the distance of the electrodes d and the pressure p . Plotting the breakdown voltage against the product of pd results in the characteristic Paschen curves. This was done in figure 2.10 for nitrogen.

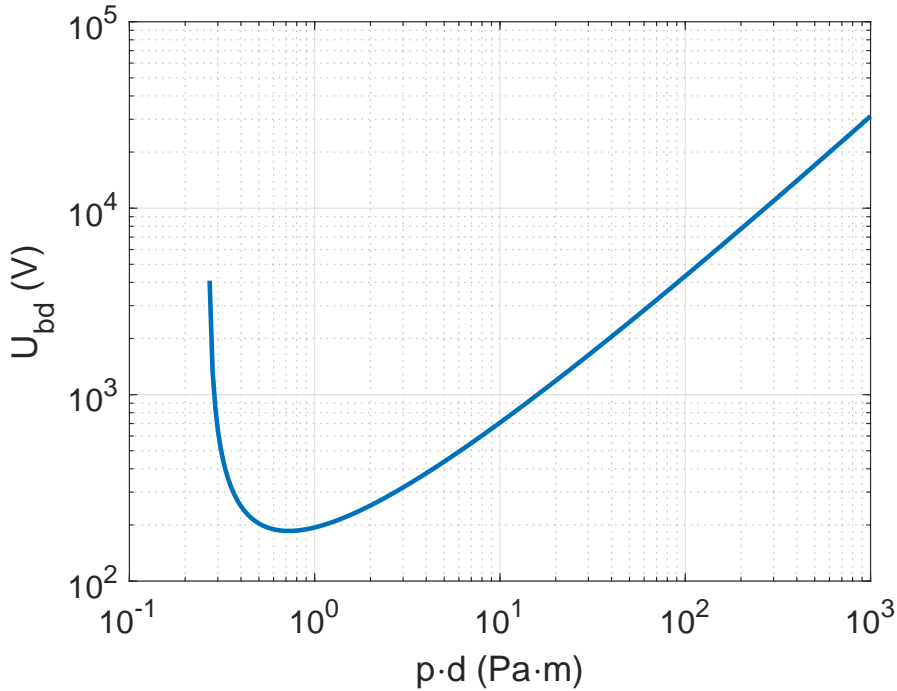


Figure 2.10: Paschen curve for nitrogen with the breakdown voltage U_{bd} plotted versus the product of pressure p and distance d . For the calculations according to equation 2.39 the constants $A = 90 \text{ (kPa}\cdot\text{cm)}^{-1}$ and $B = 2565 \text{ V/(kPa}\cdot\text{cm)}$ [60] and a secondary electron yield of $\gamma = 0.1$ were used.

Every Paschen curve possesses a pronounced minimum. Left of it, the number of atoms is too low for sufficient ionization, right of it the energy gain per λ_{mpf} is not sufficient enough to produce electrons with energies high enough to ionize. Both effects have to be compensated by a higher electric field resulting in a higher breakdown voltage.

However, besides these processes there are some other possibilities to create charge carriers for sustaining the discharge. In addition to the presented collision processes like the aforementioned charge exchange collisions, penning ionization [61, 62] or metastable-metastable ionization can help sustain the discharge. Nevertheless, the process described in this section is fundamental to every plasma generation source, regardless if it is a direct current (DC), radio frequency (RF) or pulsed plasma generation power source like high-power impulse magnetron sputtering (HiPIMS) or plasma immersion ion implantation (PIII).

2.3.2 Magnetron sputtering

Magnetron sputtering is considered as the workhorse in industrial coating processes and can proudly look back on a 40 year old history [63–65]. Therefore, nowadays there is a broad variety of different sputtering techniques available, ranging from different power modes like DC, RF and pulsed magnetron sputtering (e.g. HiPIMS) as well as different geometrical solutions like planar or cylindrical magnetrons. In all cases, the underlying principle of magnetron sputtering (as described in section 2.2.2 and 2.2.6) describes the physical evaporation of target material due to impinging particles. The sputtered atoms condense on a surface forming a thin film whose properties are highly dependent on various process parameters. However, sputtering is not only performed by magnetron sputtering systems but also includes hollow cathode sputtering (or gas flow sputtering) [66, 67], ion beam deposition [68, 69], pulsed laser deposition (PLD) [70] or cathodic arc deposition [71]. For the purpose of this work the following section will concentrate on magnetron sputtering.

A typical magnetron consists of two electrodes whose arrangement is highly depending on the type of power source. A sketch of a planar magnetron is shown in figure 2.11 where a slab of target material is posing as the cathode.

Behind the target is a pair of opposing ring magnets usually embedded in some kind of cooling circuit to cool the magnets and target material since the impinging ions deposit quite an amount of energy, resulting in significant target heating. A cylindrical housing poses as the anode usually set to ground potential. In order to generate a strong electric field the target is negatively biased with several 100 V to attract the plasma ions. There is one main region where the magnetic field lines in front of the target run parallel to it and the electric field lines are perpendicular to the magnetic field. In this region the electrons are efficiently trapped due to the Lorentz force

$$\vec{F}_L = q \left(\vec{E} + \vec{v} \times \vec{B} \right), \quad (2.40)$$

prolonging their residence time and therefore significantly enhancing the possibility of further ionization. Here, q is the charge of the electron, \vec{E} and \vec{B} the electric and magnetic field vectors, respectively, and \vec{v} the velocity of the electron. In this region the plasma densities are higher than in other regions leading to a high ion flux towards the target. Since the planar magnetron is radially symmetric that region can be identified as a bright plasma torus which

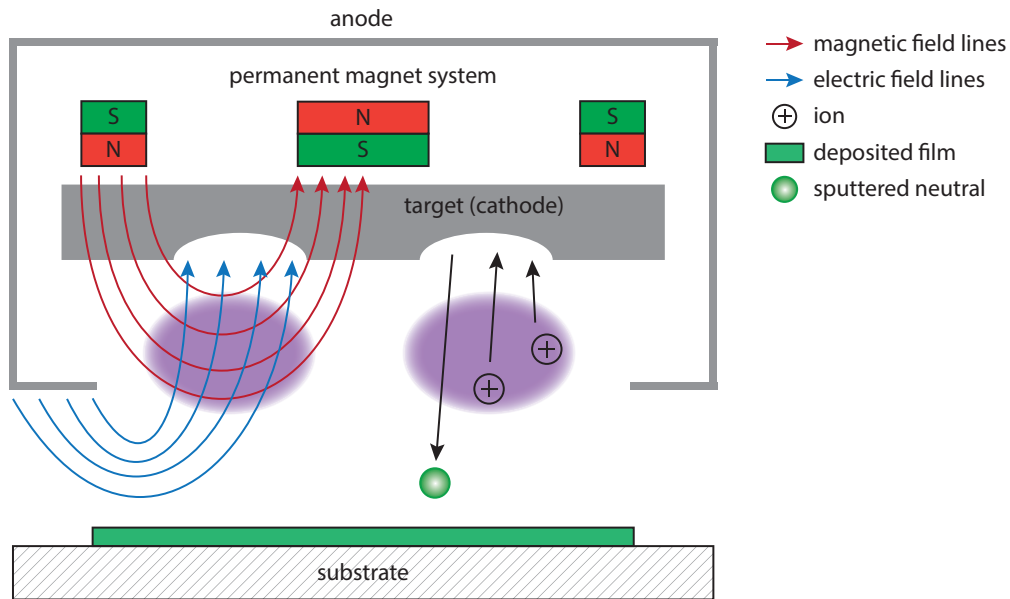


Figure 2.11: Sketch of a typical planar magnetron as used in many plasma coating applications.

produces its cast in the target material - the so called race track. This evaporation trench is a cumbersome nuisance in magnetron sputter deposition since it leads to inhomogeneous abrasion of the target and more frequent target change increasing the production costs. A more homogenous abrasion of the target material has since been an issue which lead to the innovation of the so called rotatables, where the target is not in the form of a simple slab but rather of cylindrical shape rotating during the process. Rotatables were able to raise the exploitation of the targets from around 40-70% to around 85%. However, the costs to melt unevenly used targets and meanwhile replacing them with new ones is common practice and in most cases more economic than an overhaul of the whole production line and investments in new magnetron sputter sources.

Another crucial factor is the arrangement and strength of the magnets inside a magnetron since it greatly affects the type of discharge as well as the particle fluxes of electrons, ions and neutrals to the substrate [72, 73]. There are three basic magnet configurations used in magnetrons which are illustrated in figure 2.12.

In general they can either be in a balanced (type II) or an unbalanced (type I and III) arrangement. Type I uses an inner magnet which is significantly stronger than the outer magnet resulting in unclosed magnetic field lines directed radially to the chamber walls. Hence, the axial component of the magnetic field is basically eliminated, leading to a low density plasma in the substrate area. In configuration type II all magnets exhibit the same strength which is why all magnetic field lines are closed. Type III is the opposite case of type I where the outer magnet is significantly stronger than the inner magnet leading to magnetic field lines not running through the center and reaching the surface. Therefore, ions can easily reach the surface even without additional substrate biasing [74]. It was proven that the ion current density of type III could actually reach values of about 5 mA/cm^2 which is one order of magnitude higher than that of conventional balanced magnetrons (type II) and up to 100 times higher than type I [73, 74]. In addition to higher current densities,

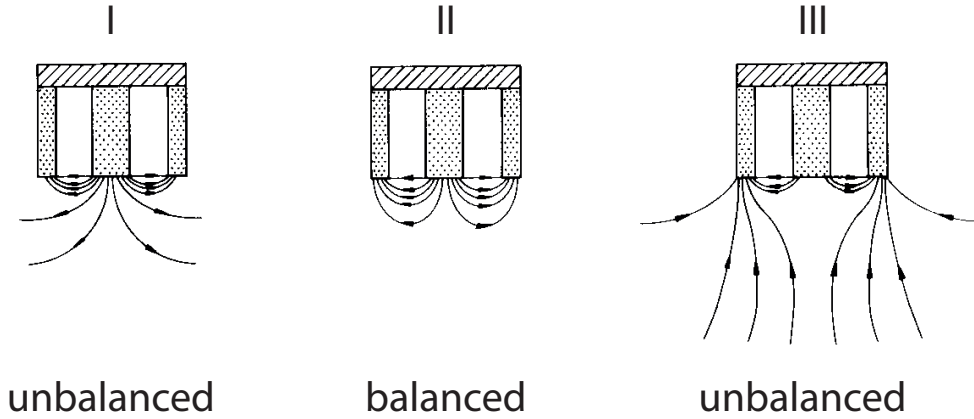


Figure 2.12: Illustration of the three main magnetic field configurations in a magnetron showing an unbalanced (I and III) and balanced (II) magnetron. Taken from [73] and modified.

also higher ion-to-atom ratios were reported, where a ratio of 2:1 was noted for the type III configuration as compared to a 0.00025:1 ratio for type II [73, 75]. In many cases a higher degree of ionization during plasma processing is desired since it allows substantial tailoring of film growth and properties due to the ability of manipulating charged material. Another important influence of magnetic field configuration in thin film deposition is the effect it has on the deposition rate

$$R = \frac{\text{film thickness}}{\text{sputter time}}. \quad (2.41)$$

If the sputtered particles are trapped after emitting from the target surface they cannot participate in film formation leading to increased deposition times for a targeted film thickness. To get a grasp of how unbalanced a magnetron really is, a coefficient [72] can be calculated following

$$K = \frac{\Phi_1}{\Phi_2} = \frac{\int_{S_1} B_{\perp 1} dS}{\int_{S_2} B_{\perp 2} dS}, \quad (2.42)$$

where $B_{\perp 1}$ and S_1 denote the perpendicular component of the magnetic field and the cross section of the outer magnet and $B_{\perp 2}$ and S_2 in analogy the same for the inner magnet, respectively. For $K = 1$ the magnetron is in balanced configuration. For simplification an approximation is usually made using

$$K_G = \frac{Z_{B_0}}{2R_S}. \quad (2.43)$$

Here Z_{B_0} stands for the axial distance to the point in front of the target where the magnetic field is zero and R_S the radial distance from the center of the target to the center of the race track.

There are several ways to control a magnetron discharge in terms of power source. Typically one has to decide whether to operate in voltage, current or power mode. A voltage regulated mode is chosen if the energy of the sputtering ions should be the same, a current regulated mode secures a constant ion flux onto the target whereas a power regulated mode is a trade-off between those two modes. For better comparison of different magnetron systems the

current-voltage-characteristics are usually compared. Thornton [63] described the relation between current and voltage of a magnetron as

$$I \propto U^n, \quad (2.44)$$

where the exponent n describes the efficiency of the electron trapping and is primarily dependent on the working pressure, target material and magnetic field strength. It is typically ranging from values of 5 to 9. This relation can be traced back to the abnormal glow discharge given that the magnetron operates in that regime.

However, all these techniques require conducting target materials. If one is to use insulating materials the deployment of a RF power source is of the essence. The high frequency of the RF cycle is too fast for the heavy ions to follow whereas the electrons can easily keep up and hit the target resulting in a negative net charge on the dielectric surface which in turn accelerates the ions and allows for a sputter process.

High-power impulse magnetron sputtering

One downside of common DC magnetron sputtering (DCMS) is the amount of ionized sputtered material produced [76]. The amount of neutrals usually far exceeds the amount of ionized material limiting the versatility of the process. The desire to improve this factor lead to the innovation of different sputtering techniques. Sometimes the degree of ionized material is improved due to an RF coil post-ionizing material after the initial sputter process. The aforementioned cathodic arc evaporation creates very localized extremely high current discharges, producing regions with a high degree of ionization. Hollow cathode sputtering is a third alternative sputtering technique, where electrons are trapped inside a hollow cylinder accelerated by the electric field. Since the cathode wall is repulsing the electrons are trapped in the more centered region of the cylinder constantly accelerated through the sheath leading to high plasma densities and high degree of ionized material. Another promising technique that merely requires a change of the power supply and can usually be used with the existing equipment is called high-power impulse magnetron sputtering (HiPIMS) first introduced by Kouznetsov et al. [77] in 1999. HiPIMS power sources apply high voltage pulses with pulse widths of about 10-500 μs and pulse repetition frequencies of a few tens of Hz to kHz [78]. Discharge voltages are usually in the range of 500-1000 V leading to current densities at the target of a few A/cm^2 . During the pulse, peak powers in the order of several kW/cm^2 are easily reached, however, the time averaged power is only in the range of a few W/cm^2 due to low duty cycles, preventing damage at the magnetron or target melting. A typical HiPIMS pulse is shown in figure 2.13.

During the pulse the charge carrier density in front of the target is in the order of 10^{18} to 10^{19} m^{-3} as compared to densities of about 10^{15} to 10^{16} m^{-3} in common DCMS processes, decreasing the mean free path of sputtered material from roughly 50 cm (DCMS) to about 1 cm (HiPIMS). The high degree of ionization introduces the possibility of self sputtering [80] where the ionized target material is itself accelerated onto the target surface sputtering new material and induce secondary electron emission making a process gas obsolete and allowing for deposition of extremely pure films [81]. However, in contrast to DCMS, there is a bigger chance in HiPIMS to generate multiply charged ions. If these ions are accelerated towards a biased substrate they can evoke stress in deposited films, since a bias voltage of about

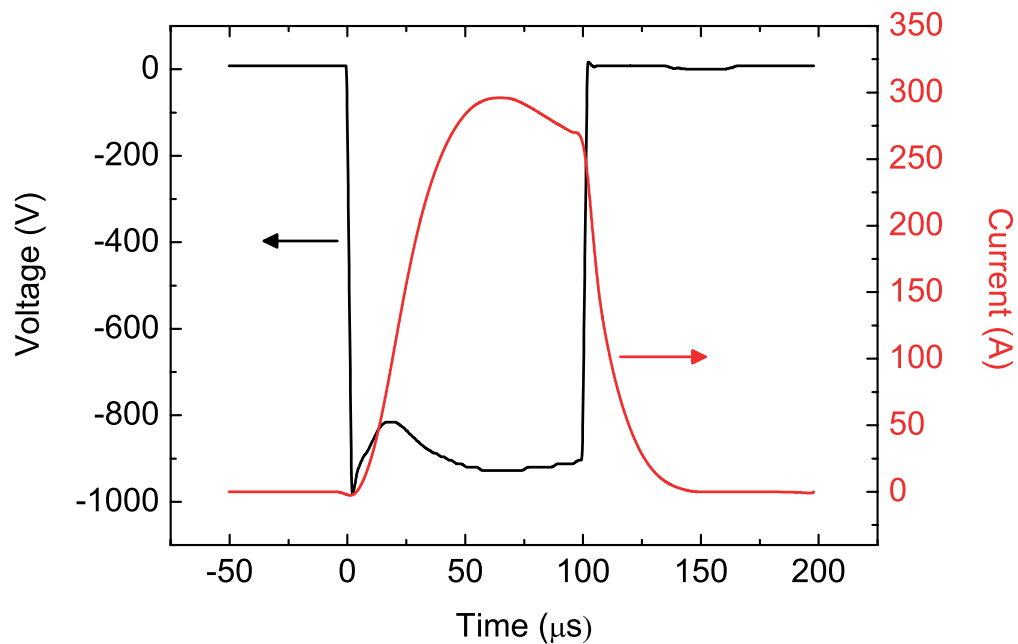


Figure 2.13: Current-voltage-characteristic of a typical HiPIMS pulse using a 6 inch Cu target at a pressure of 1.33 Pa in an Ar discharge. The peak current density is about 1.6 A/cm^2 . Taken from [79].

-50 V leads to a double charged ion gaining energy of about 100 eV depositing a significant amount of energy. Hence, there is even a chance of implanting that ion leading to unwanted problems like film delamination. However, HiPIMS processes enable the deposition of films with superior properties in terms of density, structure and hardness [82].

2.3.3 Plasma-immersion ion implantation

Conventional ion implantation as practiced in the 70's and early 80's has been shown to be quite effective in improving the wear, corrosion, fatigue and friction properties of materials and in modifying their electrical and optical properties [83–85]. It is also a widely used method for doping semiconductors, e.g. adjusting the threshold voltage of a MOSFET. The main advantages of ion implantation can be summarized as follows [86]:

- selective change of surface properties without changing the bulk material properties
- no problems associated with bonding failure or surface layer delamination
- new alloys are not limited by classical thermodynamic properties and diffusion kinetics due to non-equilibrium process
- not a real coating process, hence, no dimensional changes in the work piece
- low temperature process
- implant species concentration can be tailored by changing the implantation energy

However, ion implantation was usually realized as a two step process where the ions were generated in the first stage and then extracted and accelerated onto the substrate [87]. Since this process was a line of sight operation, complex beam rastering and target manipulation was required to achieve uniform implantation. Further drawbacks of conventional implantation include high maintenance of the beam extracting and focusing mechanisms as well as low beam current and nonuniform implantation profiles as well as low-energy efficiency per implanted ion. In 1987 Conrad et al. [86] proposed a plasma source ion implantation (PSII) method, a technique which is nowadays known under the label of plasma-immersion ion implantation (PIII). PIII allows for ion generation right 'in front' of the substrate, purging the necessity of a staged implantation setup. Additionally, due to the plasma sheath forming around the substrate, ions from the bulk plasma are accelerated onto the surface regardless of the geometry and allow for a homogenous implantation without any beam rastering. Hence, the intermediate stages of ion source, beam extraction and focusing as well as beam scanning are obsolete. An illustrative comparison between conventional ion implantation and PIII is given in figure 2.14.

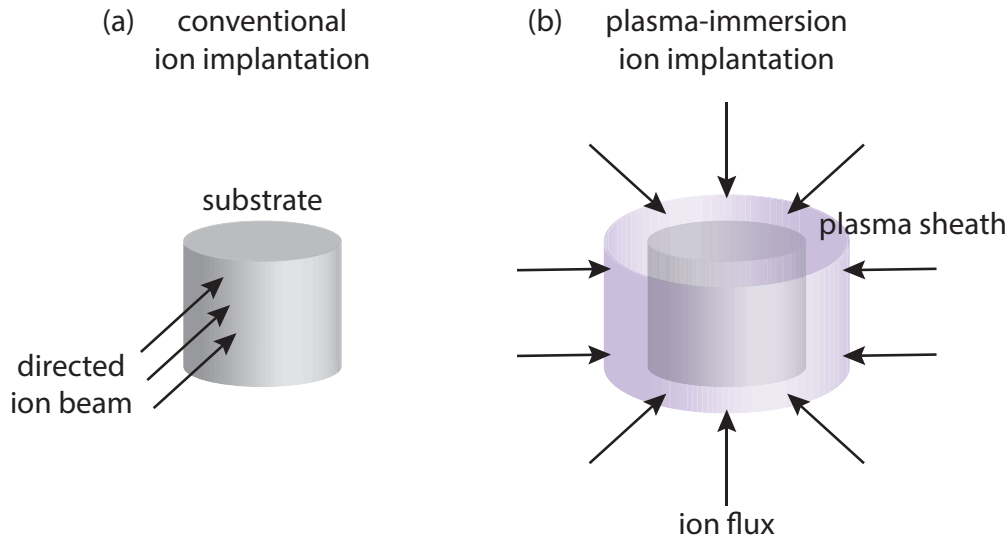


Figure 2.14: Comparison between (a) conventional ion implantation and (b) plasma-immersion ion implantation. In conventional ion implantation a directed beam of ions is hitting a limited surface area of the substrate, whereas the ions in PIII are accelerated in the sheath surrounding the entire substrate.

The main mechanism happening during one pulse can be explained with a model by Lieberman who introduced a basic model for the sheath expansion during PIII [87].

Lieberman model

As explained in section 2.1.2 the time scale in which a plasma can react to an external stimulus is defined by the inverse electron plasma frequency ($\omega_{pe}^{-1} \approx 10^{-9}$ s). When a steep negative pulse is applied to a substrate electrons near the surface are driven away leaving behind the ions which are uniformly scattered, hence, this region is called the ion matrix sheath. On the time scale of the inverse ion plasma frequency ($\omega_{pi}^{-1} \approx 10^{-6}$ s) ions will be accelerated in the plasma sheath eventually hitting the substrate surface. As a consequence

of the ion movement, the sheath edge is driven further away, exposing new ions that are extracted. Ultimately, the system evolves towards a steady-state Child law sheath [88] for longer time scales. However, in PIII the sheath thickness exceeds the plasma size, thus, the voltage drops to zero again before the steady-state is reached. Therefore, the matrix sheath and its time evolution determine the current $j(t)$ and the energy distribution dN/dW of implanted ions.

The further description of the sheath model continues along figure 2.15 and is presented in greater detail in [87].

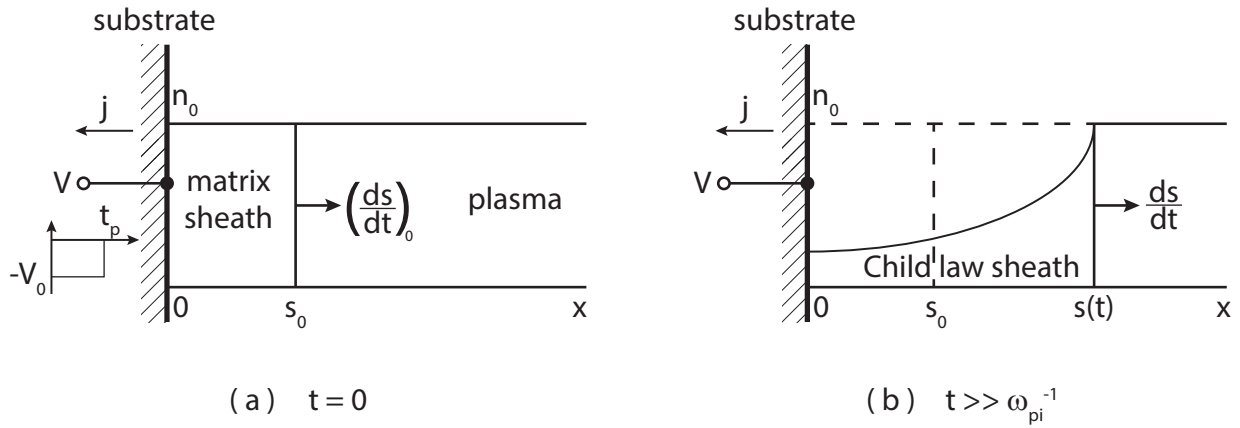


Figure 2.15: Planar PIII geometry just after formation of the matrix sheath (a) and evolving into a quasistatic Child law sheath (b). Illustration after [87].

In figure 2.15 (a) a planar substrate is immersed in a uniform plasma of density n_0 . A voltage amplitude $-V_0$ with pulse width t_p is applied to the substrate at $t = 0$ and the plasma electrons are driven away to form the matrix sheath, with the sheath edge at $x = s_0$. As time evolves (as seen in figure 2.15 (b)), ions are implanted and the sheath edge retreats leading to the formation of a nonuniform, time-varying sheath near the target. The underlying assumptions for the Lieberman model are as follows [87]:

1. The ion flow is collisionless, which is valid for sufficiently low gas pressures
2. The electron motion is more or less instant, which is true due to the characteristic implantation time scales far exceeding ω_{pe}^{-1}
3. The applied voltage amplitude V_0 is much greater than the electron temperature T_e leading to the Debye length $\lambda_D \ll s_0$ and an abrupt sheath edge at s
4. During and after matrix sheath implantation, a quasistatic Child law sheath forms and the demanded current in this sheath is supplied by the uncovering of ions at the moving sheath edge and by the drift of ions towards the target with Bohm velocity $u_B = (qT_e/m_i)^{1/2}$
5. During the motion of an ion across the sheath, the electric field is frozen at its initial value, independent of time, except for the change in field due to the velocity of the moving sheath

Some characteristic parameters can be obtained from the model calculations. The matrix sheath thickness can be calculated using

$$s_0 = \sqrt{\frac{2\epsilon_0 V_0}{qn_0}}. \quad (2.45)$$

Here, ϵ_0 is the vacuum permittivity, V_0 the applied voltage, q the ion charge and n_0 the density of the plasma surrounding the substrate. The characteristic ion velocity can be determined following

$$u_0 = \sqrt{\frac{2qV_0}{m_i}}, \quad (2.46)$$

where m_i denotes the ion mass. Since the ions are in motion, the equation of motion

$$\frac{d^2x}{dt^2} = \omega_{pl}^2(x - s_0) - \frac{2}{9}u_0\omega_{pl}^2t \quad (2.47)$$

needs to be solved for a particle at position x . Here u_0 describes the characteristic ion velocity. The solution results in an expression for the sheath thickness

$$s_0 = (s_0 - x_0) \cosh \omega_{pl}t + \frac{2}{9}s_0 \sinh \omega_{pl}t - \frac{2}{9}u_0t. \quad (2.48)$$

Using this equation, the ion flight time t can be derived. In a time interval between t and $t + dt$, ions from the interval $[x_0, x_0 + dx_0]$ are implanted. Differentiating equation 2.48 leads to an expression for dx/dt and finally the implantation current density. It is described by $j = qn_0 \frac{dx_0}{dt}$ which can be developed into a normalized current density for the ions in the initial matrix sheath ($0 \leq x_0 \leq s_0$) and be written as

$$J = \frac{\sin T}{\cosh^2 T} + \frac{2}{9} \frac{1 + T \sinh T - \cosh T}{\cosh^2 T} \quad \text{for } T < 2.7, \quad (2.49)$$

with the normalized time $T = \omega_{pi}t$. However, a numerical approach of the model shows that this equation solely gives an adequate description for $0 \leq T \leq 2.7$, since at $T \approx 2.7$ all ions in the initial matrix sheath are implanted. Nonetheless, the maximum of the current $J_{max} \approx 0.55$ occurs at $T_{max} \approx 0.95$ which is way before $J(T = 2.7) \approx 0.19$. An illustration of equation 2.49 is shown in figure 2.16 as a solid blue line.

Since for longer pulses there is also a contribution of ions that are not residing in the initial matrix sheath, the current density of those particles needs to be taken into account which alters the original shape of J . For greater time scales the normalized current density is no longer described by equation 2.49 but rather follows

$$J = \frac{1}{\frac{9}{2}(x_0^2/s_0^2) + 3} \quad \text{for } T > 3, \quad (2.50)$$

which is represented in figure 2.16 as a solid red line for pulses longer than $T > 3$. The energy distribution of the matrix ions can be described by

$$\frac{dN}{dW} = \frac{n_0 s_0}{2V_0} (V_0 - W)^{-1/2} \quad \text{for } x_0 \leq s_0, \quad (2.51)$$

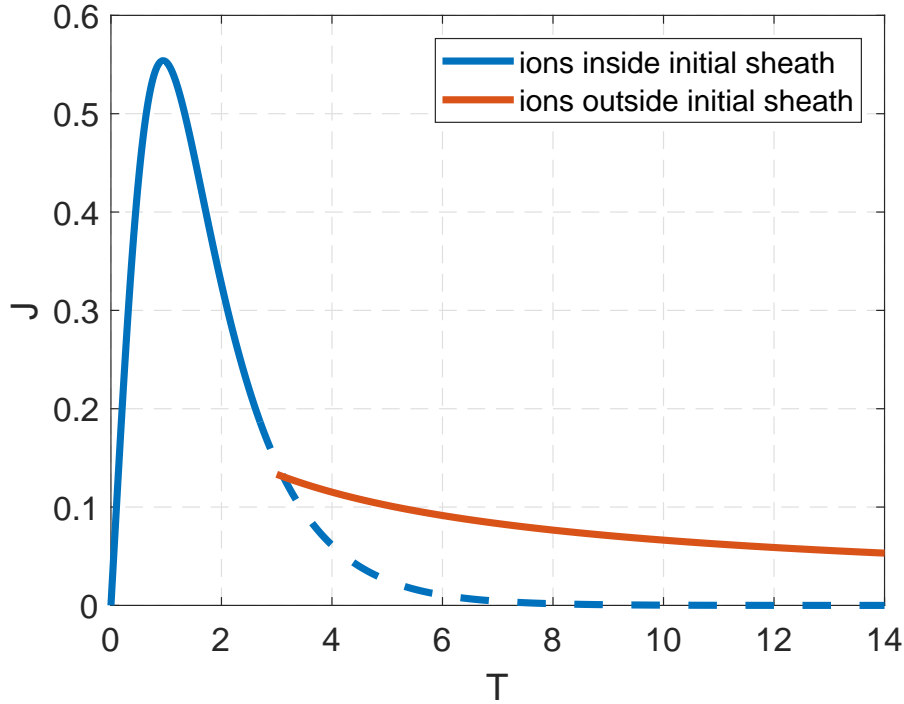


Figure 2.16: Normalized implantation current density $J = j/(qn_0u_0)$ vs normalized time $T = \omega_{pi}t$ (see also equation 2.49). At $T \approx 2.7$ all ions in the initial matrix sheath are implanted. For longer time scales, the ions that are not in the initial sheath have to be taken into account and are represented by the red line.

where W is the energy of the implanted ions and N the number of ions implanted. An illustration of equation 2.51 for an initial ion density of $n_0 = 10^{19} \text{ m}^{-3}$, a voltage pulse of $V_0 = 3 \text{ kV}$ and single charged ions is shown in figure 2.17.

The distribution is quite similar to a δ -function meaning that almost all ions in the initial sheath are implanted with 3 keV. This is not only true for the ions in the matrix sheath, since for a pulse width of $T > 3$ all ions from the interval $s_0 \leq x_0 \leq x_T$ are implanted at full energy due to the fact that they are accelerated through the whole sheath length. Hence, equation 2.51 becomes

$$\frac{dN}{dW} = n_0(x_T - s_0)\delta(W - V_0) \quad \text{for } s_0 \leq x_0 \leq x_T \quad (2.52)$$

and exhibits a δ -peak. Finally, the sheath edge s_T has reached its final position and at the end of the pulse all ions with original positions of $x_T \leq x_0 \leq s_T$ are in transit when the pulse is turned off. Deriving the energy distribution from the Child law sheath just before turnoff leads to an energy distribution of

$$\frac{dN}{dW} = \frac{2}{5} \frac{(s_T - x_T)n_0}{V_0^{2/5}} (V_0 - W)^{-3/5} \quad \text{for } x_T \leq x_0 \leq s_T \quad (2.53)$$

The total energy distribution is the sum of those three intervals and the total dose of implanted ions is n_0s_T .

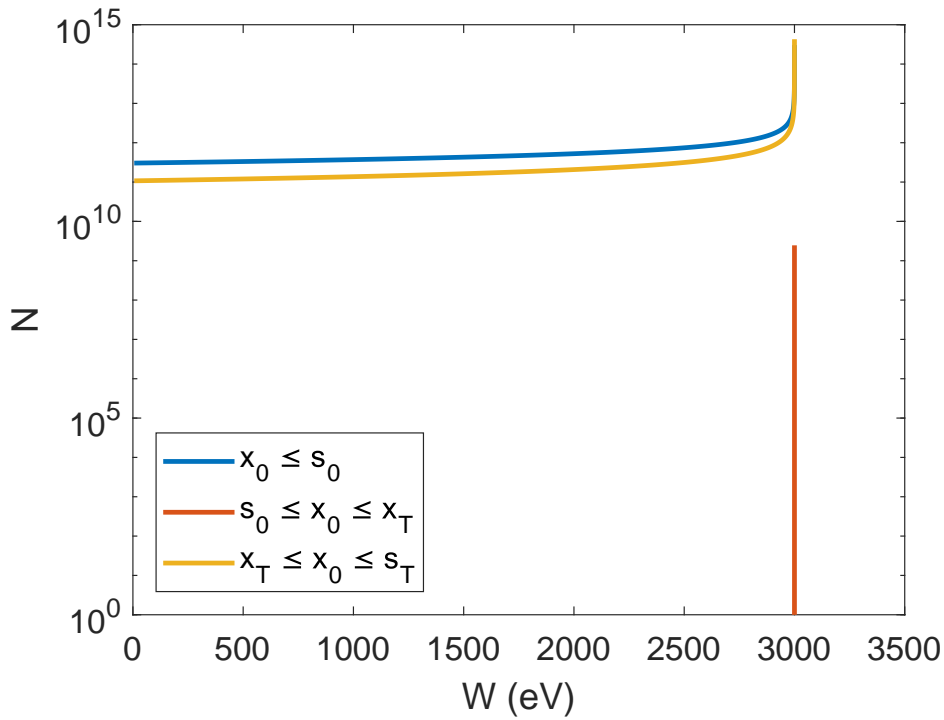


Figure 2.17: Energy distribution of ions in the original matrix sheath (blue line) for an initial ion density of $n_0 = 10^{19} \text{ m}^{-3}$, a pulse voltage of $V_0 = 3 \text{ kV}$ and single charged ions according to equation 2.51. All ions outside the initial matrix sheath within the interval $s_0 \leq x_0 \leq x_T$ are implanted bearing the full energy of the potential drop caused by the pulse voltage, hence a δ -peak at 3 keV can be seen (red line). The rest of the ions, originally residing in the interval $x_T \leq x_0 \leq s_T$, implanted during the pulse are represented by a yellow line exhibiting a similar shape to the initial matrix sheath ions.

3 Plasma diagnostics

3.1 Calorimetric probing

Calorimetric probes such as an active thermal probe (ATP) or a passive thermal probe (PTP) have proven themselves to be a versatile and robust tool for plasma characterization, especially in the detection of energy flux onto a surface during plasma processing. As mentioned in section 2.2 the energy flux is a crucial parameter when it comes to thin film processing. The idea of calorimetric probes originated from the desire to measure the sun's radiation and other radiation sources [89]. Thornton was the one who transferred this method and introduced it to the plasma community in 1978 [12]. Since then, it has been deployed in various plasma environments [13–22]. The difficult requirements of the probe to be able to adapt to different plasma environments lead to a variety of different probe designs. Gardon introduced a probe design in 1935 which determines the energy flux from increased temperature in the center of an exposed membrane [90]. Another technique uses the temperature gradient over a partially exposed substrate [91, 92] which has led to a more refined version which uses cooled PT100 element with an array of 1600 thermocouple junctions [17]. Some of the different probe designs are illustrated in figure 3.1.

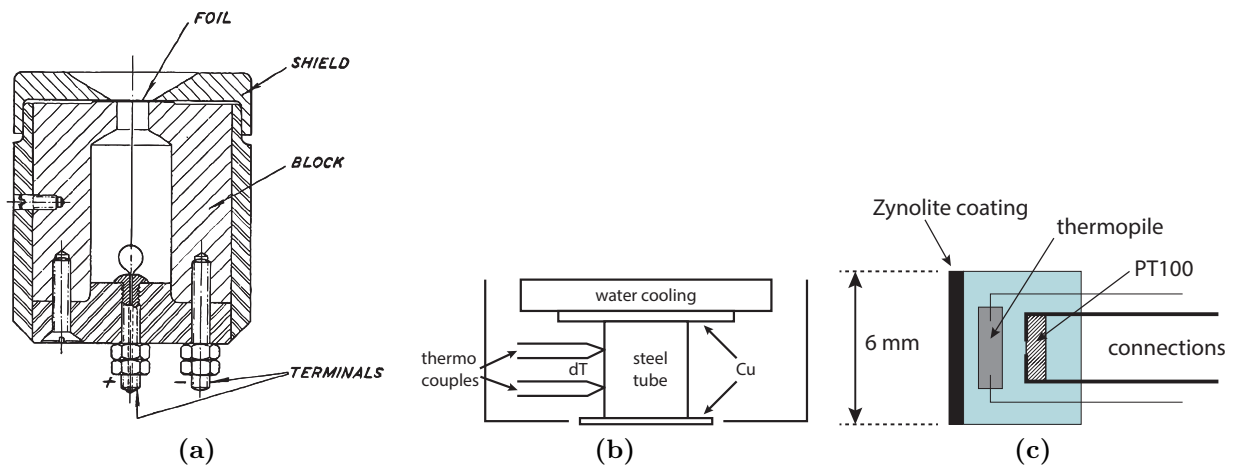


Figure 3.1: (a) Radiometer after Gardon [90] (taken and modified), (b) a probe design using the gradient method [91] (created after figure from citation) and (c) a thermopile sensor as used by Cormier et al. [17] (created after figure from citation).

For this work a slightly redesigned version of Thornton's original probe [12] was used which utilizes a substrate dummy surface and a thermocouple attached to the back of it (see section 3.2). The detection of the energy flux is based on the relation between the net-power to the substrate and the temperature gradient while exposed to a plasma.

3.2 Passive thermal probe (PTP)

In this section a detailed description of the passive thermal probe and its measurement principle is given. The majority of the work presented in this thesis was taken out with a PTP.

Measurement principle

The energy of a thermodynamic system is described by its enthalpy H which is a measure for the total amount of energy stored in said system. In case of a substrate surface, the change of the enthalpy \dot{H}_s is defined as the product of its heat capacity C_s and the time derivative of its temperature dT_s/dt and can be written as

$$\dot{H}_s = C_s \frac{dT_s}{dt} = P_{in} - P_{out}. \quad (3.1)$$

However, the temperature T_s of a surface area A_s connected to a heat reservoir at a constant temperature T_{eq} is dependent on the incoming power P_{in} and the outgoing power P_{out} . The sum of all processes caused by impinging particles, surface processes as well as radiation is represented in P_{in} and all energy loss processes are summarized in P_{out} . Assuming that no additional process inside the substrate leads to a change of enthalpy, a change of it can only be attributed to an interaction with its environment. Now, for better comparison between different systems and probes it is common to normalize these powers with the area of the substrate A_s resulting in the desired energy fluxes as introduced in section 2.2.1:

$$\begin{aligned} J_{in} &= \frac{P_{in}}{A_s} \\ J_{out} &= \frac{-P_{out}}{A_s} \end{aligned} \quad (3.2)$$

The negative sign in front of P_{out} accounts for the fact that the resulting energy flux drains energy from the system. If it is technically feasible to switch off the incoming power at one point the change of enthalpy can be described with two equations where the power is turned on (called heating term) and turned off (called cooling term):

$$\begin{aligned} \text{Heating :} \quad \dot{H}_h &= C_s \dot{T}_h = P_{in} - P_{out,h} \\ \text{Cooling :} \quad \dot{H}_c &= C_s \dot{T}_c = -P_{out,c} \end{aligned} \quad (3.3)$$

For short time frames one can assume that the energy flux leaving the substrate during the heating and cooling phase at same temperatures is equal, therefore these two equations can be combined to determine the incoming power using the temperature gradients as

$$P_{in} = C_s (\dot{T}_h - \dot{T}_c). \quad (3.4)$$

Hence, the measured energy flux is given by

$$J_{meas} = \frac{C_s}{A_s} (\dot{T}_h - \dot{T}_c) \quad (3.5)$$

3.2.1 Evaluation methods

In terms of determination of P_{in} there are three different ways to do it and every method has its upsides and downsides. In most cases the 'kink method' is the element of choice but in certain experimental conditions it may be better to choose one of the other evaluation techniques ('dT method' or 'equilibrium temperature method'), or in some cases a repeated evaluation with a different method will open the door for additional information. This section gives a description of all three evaluation methods and an exemplary data set of an electron beam experiment is evaluated with two of these methods.

Kink method

The 'kink method' is probably the most applicable evaluation technique for a broad variety of plasma environments. It relies only on short time frames which reduces the overall measurement times. However, the 'kink method' requires high sample rates and a good signal-to-noise ratio since the investigated time frames are in fact only a few seconds long.

As mentioned in section 3.2, the temperature curves are composed of two parts. A heating phase, where the power source is turned on and a cooling phase with source off. The curves follow an exponential shape if the conductive cooling of the probe is dominant. Therefore it can be written as:

$$\left. \begin{aligned} T_{s,heat}(t) &= T_{eq} + \frac{P_{in}}{\alpha} \left[1 - \exp\left(-\frac{\alpha}{C_s}t\right) \right] \\ T_{s,cool}(t) &= T_{eq} + (T_{st} - T_{eq}) \exp\left(-\frac{\alpha}{C_s}t\right) \end{aligned} \right\} \text{temperature curve} \quad (3.6)$$

Here, α is a constant describing the efficiency of the conductive cooling process, C_s the heat capacity of the probe and T_{st} gives the probe temperature at the start of the cooling phase. An image of a temperature curve for an electron beam with 1000 eV evaluated with the 'kink method' can be seen in figure 3.2a.

The moment when the the source is turned on and the temperature starts to rise is referred to as 'heating kink', whereas the point when the source is turned off again and the temperature starts to decay is called 'cooling kink'. In the magnified area of the cooling kink it can be seen that for short time frames ($t < 5$ s) the exponential course can be approximated by a linear fit. This linear shape can be developed with the help of a Taylor series and is given by

$$\left. \begin{aligned} T_{s,heat}(t) &= \frac{P_{in}}{C_s}t + T_{eq} \\ T_{s,cool}(t) &= \frac{\alpha}{C_s} (T_{eq} - T_{st})t + T_{eq} \end{aligned} \right\} \text{linear approximation} \quad (3.7)$$

With these equations the time derivative ($\dot{T}_h - \dot{T}_c$) can be calculated for any given point with the same temperature on the heating and cooling curve and no matter where the slope is evaluated it should always yield the same value. An easy way to visually address this is

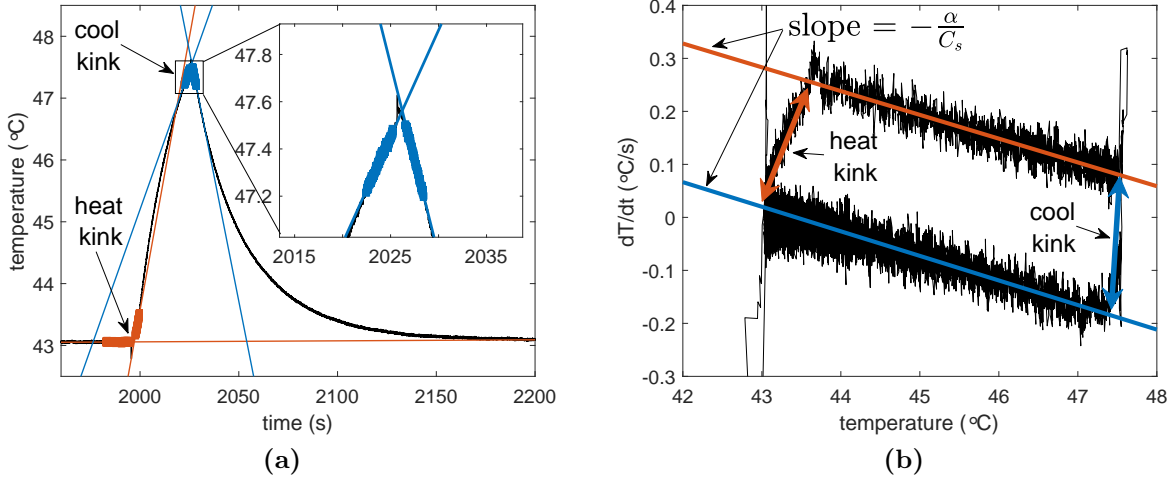


Figure 3.2: Exemplary evaluation of a temperature curve recorded in an electron beam experiment evaluated using the 'kink method'. (a) temperature curve as a function of measurement time. The highlighted areas in red and blue around the kinks are the data points used for the linear fits. The determined energy fluxes are $J_{hk} = 6.77 \text{ mW/cm}^2$ and $J_{ck} = 6.99 \text{ mW/cm}^2$ for the heating and cooling kink, respectively. (b) dT-curve of the measurement presented in (a) with linear fits for the heating and cooling phase. The red and blue arrows indicate the points used to build the difference in derivatives for the heating and cooling kink.

to build the time derivative of equation 3.6 which describes the so called dT-curve:

$$\left. \begin{aligned} \frac{dT_{s,heat}}{dt} &= -\frac{\alpha}{C_s} T_{s,heat} + \frac{\alpha}{C_s} (T_{eq} + P_{in}) \\ \frac{dT_{s,cool}}{dt} &= \frac{\alpha}{C_s} T_{s,cool} + \frac{\alpha}{C_s} T_{eq} \end{aligned} \right\} \text{dT-curve} \quad (3.8)$$

These two equations describe a linear function which should be visible in a plot where the time derivative of the temperature dT is plotted versus the temperature itself. This is illustrated in figure 3.2b. Here, the two phases (heating and cooling) exhibit linear behavior and are indeed parallel to each other. Hence, the value for $(\dot{T}_h - \dot{T}_c)$ is the same for any given point along the temperature axis. However, it must be noted, that the electron beam experiment is a rather simple environment since it only exhibits one type of particle. In more complex plasmas the shape of the dT-curve can somewhat vary from this ideal shape. Additional effects, like warming up effects that are influencing the energy flux due to e.g. a more pronounced cooling or heat radiation term, can falsify the measurements and make the assumption of equal P_{out} for heating and cooling (see section 3.2) less and less accurate. Therefore, minimizing the time frame in which the evaluation is applied allows for the assumption that the temperature of the substrate holder or the vacuum vessel remains constant. This is where the 'kink method' exhibits its greatest strength since it minimizes the measurement time and only requires simple fitting to be applied. Additionally, for every heating and cooling curve two energy flux values are obtained, allowing for a simple statistical error calculation. However, an effective source switching is necessary due to the short evaluation area around the kinks. If the source exhibit some kind of build-up process that has not stabilized within a second or so, the use of a different evaluation method is advised.

dT method

As mentioned in the previous section, the dT-method, also known as the exponential method, determines the energy flux with the help of time derivatives from an exponential function as written in equation 3.6. The coefficients of the exponential shape can either be obtained directly by an exponential fit applied to the heating and cooling part of the temperature curve or indirectly from the linear fits in the dT-curve. This can be seen in figure 3.3a

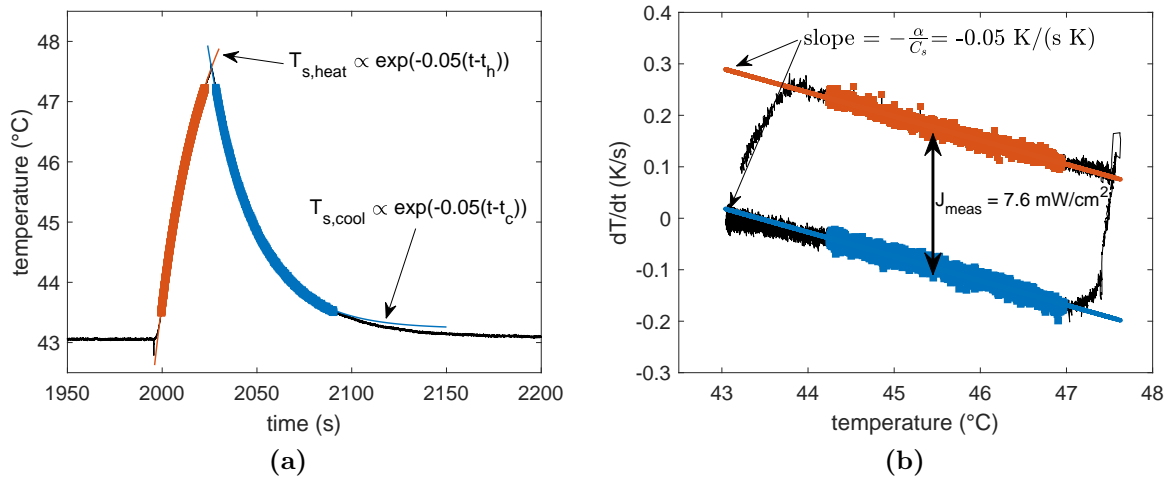


Figure 3.3: Exemplary evaluation of an electron beam experiment using the 'dT method'. **(a)** temperature curve as a function of time with highlighted evaluation areas used for the exponential fit. The determined energy flux is $J_{meas} = 7.6 \text{ mW/cm}^2$. **(b)** dT curve of the data set presented in (a) with linear fits for the heating and cooling phase. The slope of the linear fits follows $m = -\alpha/C_s$ and can be used to determine the coefficients for the exponential fit applied in (a). The points used for the energy flux calculation was chosen to be the middle of the highlighted fitting areas and is indicated by the black double arrow.

In contrast to the 'kink method' the dT method does not require comparably high sample rates since the evaluation time frame far exceeds the one used in the 'kink method'. Therefore, there will be a sufficient amount of data points even with low measurement frequencies. However, the long time frames also demand very stable measurement conditions, meaning no additional significant temperature changes in the probe's vicinity should occur during the measurement apart from the changes created by the investigated source.

3.2.2 Equilibrium temperature method

As a third and last method this paragraph describes the 'equilibrium temperature method'. The main idea is to heat up the probe until a saturated temperature, or a maximum temperature T_{max} is reached. This temperature can be calculated using equation 3.6. For long heating times ($t \rightarrow \text{inf}$) the exponential term strives towards zero and T_{max} can be written as

$$T_{max} = T_{eq} + \frac{P_{in}}{\alpha}. \quad (3.9)$$

By substituting $P_{in} = J_{in} \cdot A_s$ into the equation above the energy flux due to P_{in} can be written as

$$J_{in} = \frac{\alpha}{A_s} (T_{max} - T_{eq}) . \quad (3.10)$$

The downside of this evaluation method is the long measurement time since not only has the probe to be heated to the maximum temperature but also afterward cooled down to reach the equilibrium temperature again. In addition, the conduction coefficient α needs to be determined, which is a difficult thing to do and therefore creates bigger errors. However, the probe design could be adjusted to this method. A smaller overall heat capacity (e.g. through smaller wire diameter, smaller surface area and platelet thickness) and the integration of an active cooling system may bring those time constants down allowing for a more viable application together with utilization of the equilibrium temperature method.

3.2.3 Probe design

The setup of the PTP used for the majority of this work is illustrated in figure 3.4. It consists of a substrate dummy which is realized as a 70 μm thick copper platelet of 2 cm diameter. Spot-welded to the back of the probe surface is a type K thermocouple and an additional copper wire for biasing and current measurements. The whole setup is enclosed in a ceramic housing (Macor[®]) to ensure only the energy flux originating from the upper half space is reaching the surface. The high thermal conductivity of copper $\lambda_c = 380 \text{ W}/(\text{mK})$ ensures for a homogenous heat distribution throughout the whole probe surface and a fast transfer to the back of the platelet where the thermocouple is located. The whole sensor head is mounted on a 6 mm rod which is fed through a KF40 vacuum feedthrough which makes it simple to attach to a variety of vacuum vessels and easily allows for angle and axial variation measurements.

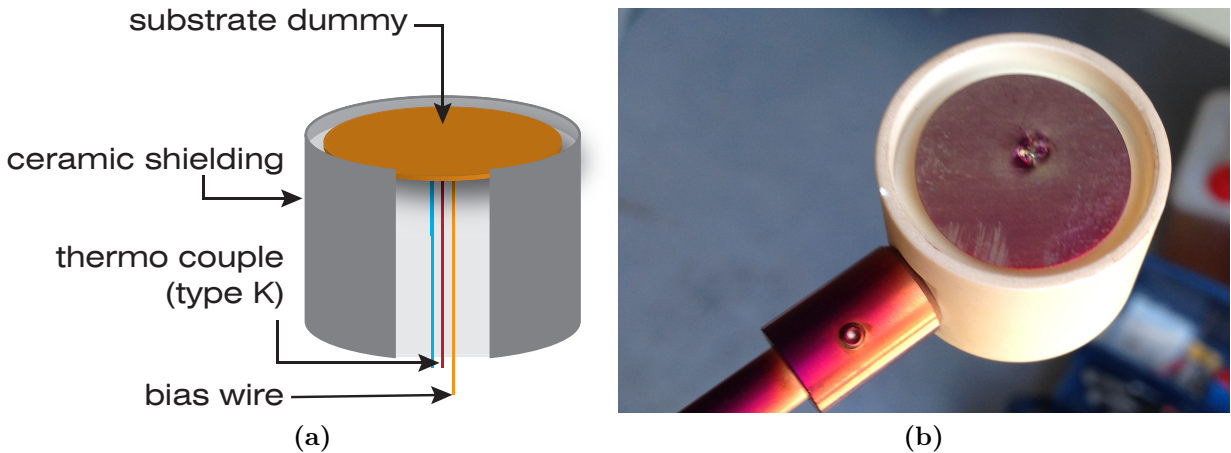


Figure 3.4: (a) Schematic drawing of the PTP sensor head. It consists of a copper platelet with a diameter of 2 cm and a thermocouple and additional copper wire spot-welded to the back of it. The whole setup is enclosed in a ceramic housing. (b) photograph of one of the utilized probe heads. Note the dents on the probe surface due to the spot-welding process.

The type K thermocouple exhibits small voltage differences due to the Seebeck effect in the $\mu\text{V} - \text{mV}$ regime ($41 \mu\text{V}/\text{K}$) requiring sophisticated electronics to measure these

small differences. The main components necessary to transfer the voltage difference at the junction of the type K thermocouple to a temperature value displayed on the PC screen are schematically presented in figure 3.5

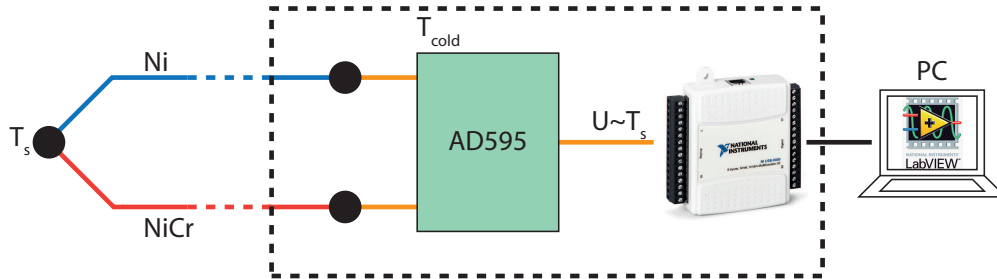


Figure 3.5: Schematic drawing of the main electronic components used for the conversion of the signal from the thermocouple wires to temperature values displayed on a PC screen running *LabVIEW*®.

Outside the vacuum vessel a monolithic thermocouple amplifier with cold junction compensation (AD595 [93]) processes the signal coming from the two thermocouple wires. Although the thermocouple wires are connected to copper wires and only then connected to the AD595, which could generate additional temperature dependent voltages, the cold junction compensation using a PT100 element for junction temperature measurements accounts for these unwanted nuisances. Still, there is room for error in the absolute temperature values, however, the PTP method only considers relative changes and is therefore free of these errors. With the help of an additional amplifier the signal from the AD595 is fed to a National Instruments multifunction I/O device's (USB-6009) analog input. The measurement card has a resolution of 14 bits and is able to record with 48 kHz at its analog input. Due to the inertness of the copper platelet the temperature output is trimmed to 100 Hz. Higher sample rates would not exhibit more information. However, the card is always operated at its maximum sampling rate and every temperature value from the 100 Hz signal is an average value of 480 values to minimize the noise in the temperature signal.

3.3 Recent developments in passive thermal probe diagnostics

As part of this thesis, a revised version of the passive thermal probe was developed in close collaboration with Sven Gauter, who is also a PhD student in the AG Plasmatechnologie lead by Professor Kersten. Starting out with the probe design introduced in section 3.2.3 which was used for the majority of this work, it is necessary to understand the underlying principles. First off, the initial version of the PTP used in our working group was developed in 2010 and was optimized to minimize changes of the temperature of the shielding. The evaluation technique utilized in 2010 was the 'dT method' which was a consequence of low acquisition speeds and any additional heating up effects would falsify the results (see section 3.2.1). Therefore, Sven Gauter and I introduced a completely redesigned and improved acquisition software to record the temperature values of the PTP which allows for much faster and, more importantly, more precise measurements. The luxury of having a high amount of independent data points within a short time frame allowed the transition from the 'dT

method' to the 'kink method'. In the wake of a better understanding and new insights gained from working with the original probe with the new software, many associated experiments (e.g. the calibration chamber) and systematic measurement procedures were altered and lead to the development of an improved version of the PTP.

3.3.1 Electron beam calibration

As mentioned in section 3.2 a precise determination of the heat capacity of the probe is crucial for the accuracy of the probe results when using the 'kink method' or 'dT method'. One way to do that is to study the temperature derivative of the probe measuring the energy flux created by a known power P_{in} . Using equation 3.4, C_s can be determined as

$$C_s = \frac{P_{in}}{\dot{T}_h - \dot{T}_c}. \quad (3.11)$$

Although the known power could be supplied by a variety of different sources (e.g. plasma electrons [14,94] or laser light [95]) for obvious reasons it is recommended to keep the source as simple as possible. For the calibration with an electron beam only voltage and current measurements are needed and no determination of additional parameters is necessary.

Experimental setup

The passive thermal probes used for the work in this thesis were calibrated in an electron beam experiment [93]. The experiment consists of a tube-like vacuum vessel with a diameter of 12 cm and a tube length of about 53 cm. Additionally some ports for the two stage pumping system and insertion of the tungsten wire and probe mounting are present. The chamber is pumped to a pressure level below $p < 10^{-4}$ Pa. The fairly low pressure is necessary so the mean free path of the electrons generated at the wire is greater than the vacuum vessel dimensions ($\lambda_{mfp}(p < 10^{-4} P) > 66$ m for N₂). Collisions between electrons and the background gas can lead to ionization processes and would create an electron energy distribution rather than all electrons having the same energy which would falsify the estimated electron energy used to determine C_s . A schematic overview of the calibration chamber can be seen in figure 3.6.

The electron beam is generated through thermionic emission, described by Richardson's law, from a tungsten wire. The wire is heated by a current of $I_w \approx 1.3$ A and a voltage of $U_w \approx 8$ V. The wire is additionally biased with $U_{w,bias} \approx -70$ V to prevent electrons from accumulating in front of the wire. During the calibration process, for switching the power source on and off a stepwise increased sequential bias to the PTP is used to attract the free electrons. In order to record the heating phase the probe is biased with $U_s \approx 700...1000$ V and after a specific amount of heating time, the bias is set to zero again and the cooling curve is recorded. After another time interval the probe has reached its equilibrium temperature it had before the heating started and the next bias voltage is applied and so on. The relevant voltage for calculation of the energy of the accelerated electrons can be obtained by taking all the different voltages into account and sums up as

$$U_{acc} = \left(U_s - U_{w,bias} + \frac{U_w}{2} \right) \pm \frac{U_w}{2}. \quad (3.12)$$

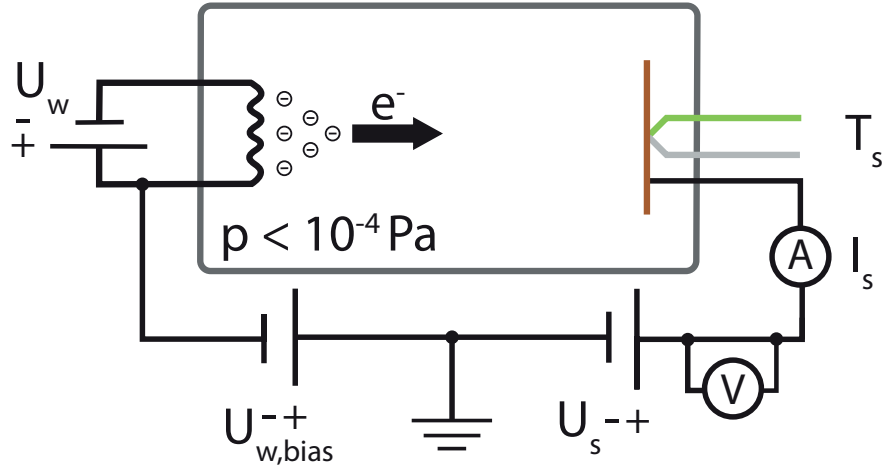


Figure 3.6: Schematic drawing of the electron beam calibration experiment (CPCEX) used to determine the PTP's heat capacity. The electrons are emitted from a tungsten wire due to the Richardson effect and are accelerated onto the sequentially biased probe.

It is in fact difficult to tell how the voltage U_w progresses through the wire since between its both ends a voltage difference of about 8 V is measured. This would also mean that not all of the wire is at the same potential, which is why the term $U_w/2$ is introduced. The bias voltage of the probe U_s and the current I_s arriving at it are measured with digital multimeters (Voltcraft VC820). It must be noted that the current measurement needs to be performed 'after' the voltage measurement since the current going through the resistor of the voltage meter can be in the same order as the measured current and an inverse order would result in false current readings. Using these values an electrical power at the probe surface can be calculated using

$$P_e = I_s (U_{acc} + \Phi_{wf}) . \quad (3.13)$$

The electron work function Φ_{wf} denotes the energy released when an electron recombines at the surface (see section 2.2.3).

Calibration process

In this paragraph the actual calibration process is described in more detail. Combining equations 3.11 and 3.13 yields

$$P_e = C_s (\dot{T}_h - \dot{T}_s) , \quad (3.14)$$

which exhibits the relation between the electrical power and the difference in temperature derivatives. To eliminate any systematic errors in P_e the probe is sequentially biased with increasing bias voltages. The typical bias voltages were ranging from 700 V to 1000 V with a step width of 50 V. Equation 3.14 gives a simple linear relation, hence, a plot of P_e versus $\dot{T}_h - \dot{T}_s$ should result in a linear curve. A typical calibration run is shown in figure 3.7. Figure 3.7a shows the temperature curves for the different probe bias voltages and the corresponding dT-curves and figure 3.7b shows the resulting P_e versus $\dot{T}_h - \dot{T}_s$ as well as the linear fit used to determine the heat capacity C_s .

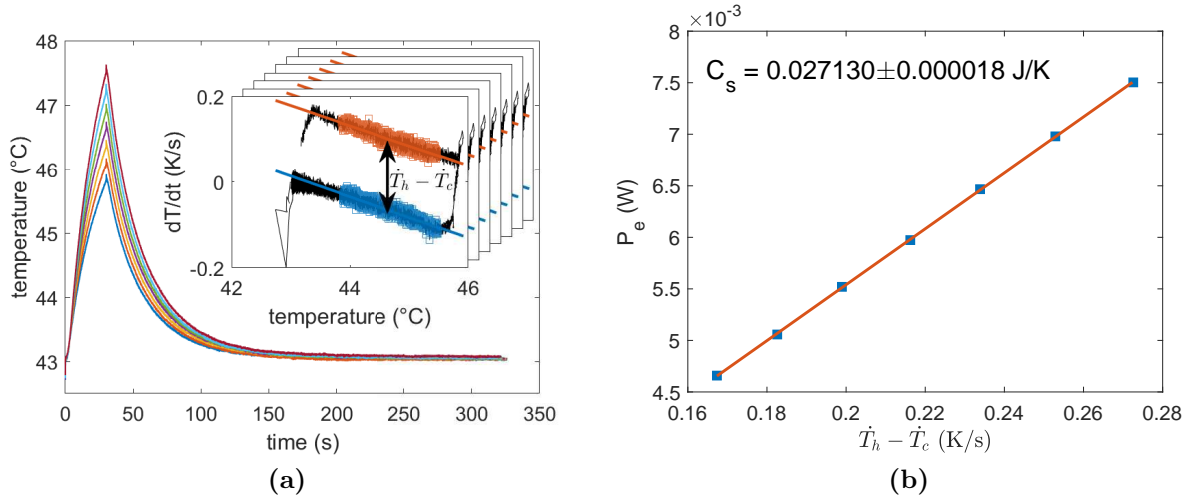


Figure 3.7: Exemplary calibration run for bias voltages ranging from 700 V to 1000 V. The heat capacity is obtained as the slope of the linear relation between P_e and $\dot{T}_h - \dot{T}_s$ according to equation 3.13. P_e is calculated with the help of the recorded voltage and current values.

At first it might be odd that the determination of the heat capacity, which has a big influence on the calculated energy flux and must therefore be determined with great precision, is identified using the 'dT method' although it was argued in section 3.2.1 that for most systems the 'kink method' yields the best results. However, it was also mentioned that the 'kink method' relies on fast switching sources and the power source used to drive the bias on the PTP exhibits fairly flat flanks meaning an instantaneous existence of the full P_e is not feasible. In addition, the multimeters used to record the voltage and current only sample with 2 Hz rendering fast and accurate measurements impossible. For better statistics, every probe is usually not exposed to a single but several calibration runs over a period of more than 12 hours resulting in a minimum of 18 calibrations per probe. The values for the heat capacity are then averaged and a simple statistical error is calculated.

3.3.2 Improved probe design

Continuous experiments have shown, that the probe design which was used for the majority of this work lacked some much needed improvements. Especially the calibration process as presented in section 3.3.1 identified some weak points of the current design with its 2 cm diameter copper platelet and the bulky ceramic housing. Due to electrons accumulating on the ceramic surface, some kind of surface charge developed on the insulator. When the copper platelet is biased during heating phase with up to 1000 V, the electrons residing on the ceramic would somehow reach the platelet due to the strong attracting potential and account for a higher current reading at the digital multimeter. This resulted in a higher calculated electrical power which would falsify the evaluation and ultimately result in a higher heat capacity. Another disadvantage of the ceramic probe design is the difficult transformation of the probe from a 0° orientation to a 90° orientation, or vice versa. The whole probe head has to be disassembled, reconfigured and re-assembled which could take up to half an hour. This could not be done without changing the whole position of the sensor platelet inside

the ceramic housing which often demanded a re-calibration of the probe. In addition, the spatial resolution, which is limited by the relatively big diameter of the copper platelet, was unnecessarily small. Hence, a new probe design was developed in close collaboration with Sven Gauter.

The goal of the new probe design was to obliterate all these disadvantages and make a rather robust diagnostic tool even more robust and ultimately allow for more precise measurements. A CAD drawing of the updated design can be seen in figure 3.8.

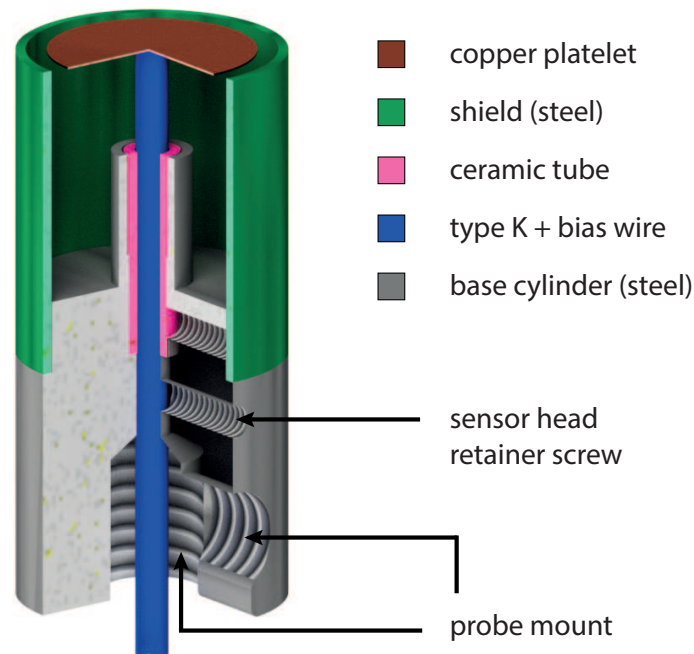


Figure 3.8: CAD drawing of the improved PTP design with a stainless steel housing and a smaller, 11 mm diameter copper platelet.

The platelet diameter was reduced to 11 mm and the copper wire diameter was also slightly reduced to decrease the overall heat capacity of the PTP. The smaller platelet increases the spatial resolution of the diagnostic tool. The ceramic housing was replaced by a steel cylinder with a short ceramic tube inside to isolate the already sleeved wires from the conducting housing.

The platelet is only retained by the stiffness of the wires which are fixed against the base cylinder by a small screw. The whole upper sensor head area (platelet and wires) is protected by a stainless steel shield that sits seamlessly on the base cylinder. The whole sensor head is mounted on a substrate holder in either 0° or 90° configuration. Since the upper parts of the probe are fixed due to the fixed wires, re-configuring the probe to either 0° or 90° is an easy and fast process and does not demand re-calibration of the probe. Additionally, the streamlined process of building the PTP after the new design produces probes that exhibit heat capacities within a very small window, which allows for good estimation of the actual heat capacity of the newly build probe, even before calibration, which was not the case with the old design. Further, probes with an insulating coating on the copper platelet may be calibrated using an additional calibrated probe measuring in parallel in an

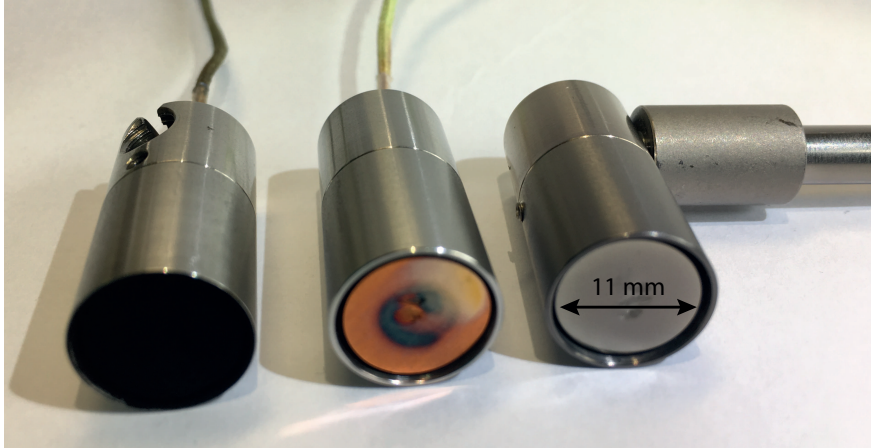


Figure 3.9: The different probe heads of the newly developed PTP design. The copper platelet of the **left probe** is carbon blackened, the **middle probe** exhibits an ordinary copper platelet and the **right probe's** platelet is coated with an Al layer.

ion beam experiment, since the acceleration voltage can not be applied to the insulating platelet surface as is done in the electron beam calibration. An example of a carbon black, a plain copper and an aluminum coated probe platelet is shown in figure 3.9.

3.4 Electrostatic probing

In 1926 Mott-Smith and Langmuir published a study on voltage-current characteristics of small additional electrodes, they called collectors, inserted into a plasma [96]. This study was the foundation of what would later become one of the most successful diagnostic tools for characterization of plasmas, the Langmuir probe.

The principle of operation of these probes is to expose a metallic surface into the plasma bulk and apply a linear voltage sweep while the resulting current onto the probe is recorded. From the resulting I-V-curve fundamental information like the floating potential Φ_{fl} , the plasma potential Φ_{pl} , electron temperature T_e as well as the density n_e can be extracted. Further, using one of the underlying models presented in 2.2.2 the electron energy distribution function (EEDF) can be estimated. A schematic overview of a simple Langmuir probe experiment can be seen in figure 3.10a.

The I-V-curve can be divided into three main regions (see figure 3.10b). First off, at the start of the voltage sweep the probe is negatively biased. All electrons are therefore repelled from the probe and accelerated into an opposing direction. This leads to the formation of a positive space charge region in front of the probe requiring the ions to fulfill the Bohm criterion $v_i \geq v_B$ [25]. At this point only positively charged ions can reach the probe and are dominating the recorded current. This part of the I-V-curve is called ion saturation regime. Ideally the ion current in this regime is constant although in many laboratory plasmas a rather slightly linear decrease of the ion current with increasing positive voltage is seen. The ion saturation current is described by

$$I_{i,sat} = n_i e A_s v_B \approx 0.61 n_{i,0} e A_s \sqrt{\frac{k_B T_e}{m_i}}. \quad (3.15)$$

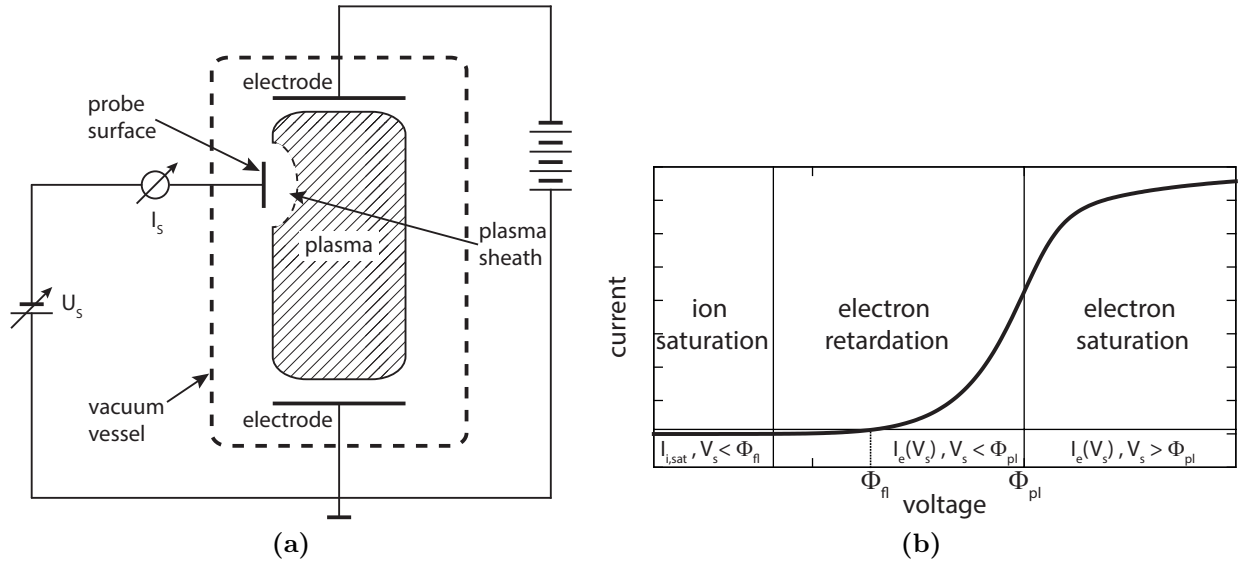


Figure 3.10: (a) Schematic overview of a Langmuir probe measurement. Applying a voltage on a metallic surface will create a plasma sheath around the probe which is indicated by the dashed line in front of it. (b) I-V-characteristics of a cylindrical Langmuir measurement. The negatively biased region is dominated by the ions (ion saturation regime). With increasing positive voltage more and more electrons are able to reach the probe (electron retardation regime) ultimately ending in the electron dominated part of the curve where only electrons (and negative ions) are measured (electron saturation regime).

Here, n_i is the ion density, e the electron charge, A_s the probe surface area, v_B the Bohm velocity, k_B the Boltzmann constant, T_e the electron temperature and m_i the ion mass. The assumption is made that the ion density at the sheath edge has decayed to a value of $n_i \approx n_{e,0}/\sqrt{\exp}$ compared to the electron density in the quasi neutral plasma bulk. The factor $0.61 \approx \exp(1/2)$ is given by the Bohm criterion stating the ions gained the energy $E = k_B T_e / 2$ in the presheath. Note that the ion current is displayed with a negative sign and the electron current is deemed positive. With increasing positive voltage, energetic electrons start to reach the probe increasing the current. The voltage point $V(I = 0)$ is known as the floating potential Φ_{fl} . It is the point where the electron and ion current are equal resulting in a net current of zero. An insulated object that is immersed in the plasma will charge itself up to the floating potential due to the electron and ion bombardment and is therefore called 'floating'. Further increasing the bias voltage will result in an ever growing electron current until the bias voltage reaches the plasma potential Φ_{pl} . It is visible as the inflection point of the current curve. The regime for $V_s > \Phi_{pl}$ is called the electron saturation regime exhibiting a constantly increasing electron current which is only limited by the probe's geometry (see figure 3.11a). The electron saturation current is described by

$$I_{e,sat} = -\frac{1}{4} n_e A_s e \sqrt{\frac{8k_B T_e}{\pi m_e}}, \quad (3.16)$$

where m_e denotes the electron mass. The overall current is the sum of ion and electron current $I_{tot} = I_i + I_e = (j_i + j_e) A_s$ and is written as

$$I_{tot}(V_s) = n_e e A_s \sqrt{\frac{k_B T_e}{2\pi m_e}} \left(0.61 \sqrt{\frac{2\pi m_e}{m_i}} - \exp\left(\frac{-e(\Phi_{pl} - V_s)}{k_B T_e}\right) \right) \quad (3.17)$$

with the probe potential V_s . For further information on Langmuir probe diagnostics it is referred to typical textbooks such as [97] at this point.

3.4.1 Probe design

In general there are three different types of Langmuir probes depending on their electrode geometry. In many cases, the probe only consists of a thin tungsten wire (typical $r_p = 100\mu m$) with an exposed wire tip with length L of a few millimeter. The wire runs through a ceramic tube to shield the rest of the wire to make sure the current is only collected by the wire tip with its well known surface area A_s . This type of probe is called a cylindrical probe and can be seen in figure 3.11a.

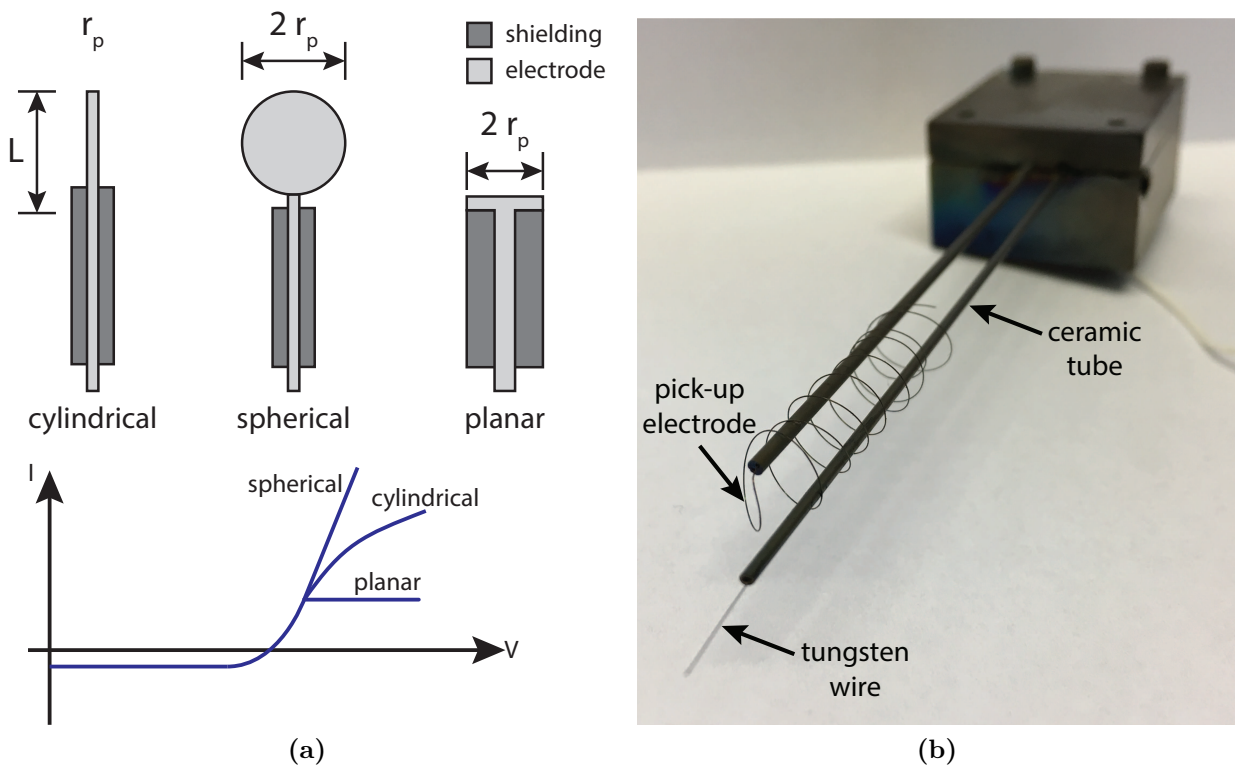


Figure 3.11: (a) Different Langmuir probe geometries and their influence of the I-V-curve shape in the electron saturation regime. (b) Photograph of a cylindrical Langmuir probe with a tungsten wire, ceramic shielding and an additional pick-up electrode for RF compensation.

Instead of using a simple tungsten wire, some probe designs exhibit an electrode of spherical shape. These probe designs are especially popular in space applications, e.g. Langmuir probes attached to scientific rockets [98]. A third option of electrode geometry is the planar probe. In its basic design it is similar to the cylindrical and spherical probe except it exhibits a plane surface at the end. In some measurements presented in this thesis, the sensor platelet of a passive thermal probe was used as a planar Langmuir probe due to a voltage sweep applied to the bias wire. Utilizing one of the presented probe designs, more sophisticated setups like Langmuir probe arrays or probes with additional RF compensation (as shown in figure 3.11b) have emerged and are widely used [99, 100].

In any case, a good approach to Langmuir probe measurements is to always restrict the overall size of the probes since they can greatly effect the plasma itself and will therefore measure an entire different plasma if the probe dimensions are considerably large compared to the plasma dimensions.

3.4.2 Evaluation of Langmuir probe measurements

This section will give a brief introduction of how Langmuir curves are evaluated and the developed software components are explained. First of all, requirements for a Langmuir probe measurement process can vary greatly. There are plasma processes that are stable over long periods of time and a Langmuir measurement is allowed to take minutes, in other experiments fast changing processes are investigated longing for very fast acquisition speeds or time-resolved solutions.

First of all, an I-V-curve is recorded using the *LabVIEW*[®] software developed in our working group, which can be seen in figure 3.12a where an exemplary data set of a DC magnetron discharge of $P = 30\text{ W}$ at a pressure of $p = 2.00\text{ Pa}$ using a Mg target is presented.

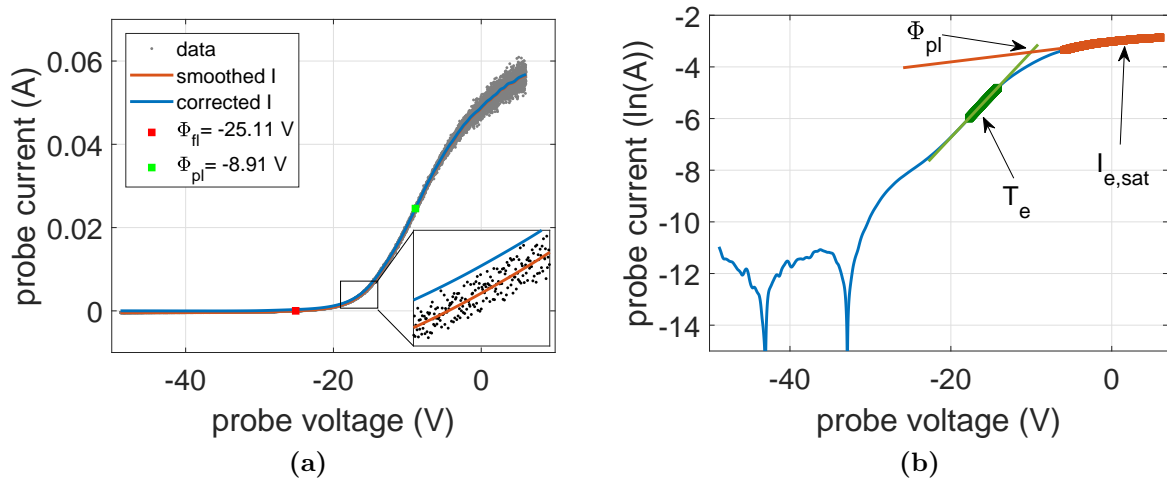


Figure 3.12: Exemplary evaluation of a Langmuir I-V-curve taken from a DCMS experiment using a Magnetron target. (a) shows the typical I-V-curve with determined floating and plasma potential, respectively. (b) Semi-logarithmic plot of the data set used to determine the electron temperature T_e (through slope of green line), electron saturation current $I_{e,sat}$ (red line) and an additional value for the plasma potential Φ_{pl} (intersection of green and red line).

An additional offset file is measured with the electronics while the plasma is off to correct the current from an offset due to the electronics. The offset current is then subtracted from the original current values and the data set is plotted in the typical probe current versus probe voltage manner (black data points). At the point where the current, coming from the negative half space, is exceeding 0 the floating point is determined ($\Phi_{fl} = -25.11\text{ V}$). In a next step the ion current $I_{i,sat}$ is determined in the ion saturation regime using a linear fit. The ion current is then subtracted from the current values. This can be seen in the magnified area in figure 3.12a where the data points have been smoothed, represented by

the red line and the ion corrected current is shown as a blue line, slightly running on top of the original data points. The plasma potential $\Phi_{pl} = -8.91 V$ is determined as the inflection point of the data set. It can be determined using the second derivative as the point where d^2I/dV^2 exhibits a zero crossing. If the assumption is made, that the electron distribution is of Maxwellian shape one can determine the electron temperature T_e with the help of a semi-logarithmic plot. Since the electron current is determined as

$$I_e = I_{e,sat} \exp\left(\frac{eV_s}{k_B T_e}\right), \quad (3.18)$$

logarithmizing this equation leads to

$$\ln(I_e) = \ln(I_{e,sat}) + \frac{eV_s}{k_B T_e}. \quad (3.19)$$

Therefore, a semi-logarithmic plot should exhibit the slope $S = eV_s/(k_B T_e)$ in the electron retardation regime. Using equation 3.19 the electron temperature can be calculated by

$$T_e = \frac{e}{k_B S}. \quad (3.20)$$

Figure 3.12b shows the logarithmic current $\ln(I_s)$ versus the probe voltage V_s . The area used for the linear fit to determine T_e is highlighted in green. The electron saturation current $I_{e,sat}$ is determined by a linear fit of the plateau-like end of the curve (highlighted in red). In addition to the determination of the plasma potential Φ_{pl} through the inflection point of the rising electron current, there is another method to determine the potential using the semi-logarithmic plot. The voltage point where the linear fit of the exponential increase of the current (T_e fitting region) intersects with the linear fit of the electron saturation current $I_{e,sat}$ does also yield the plasma potential. However, it must be noted that in many cases it is hard to determine the exact region of the exponential rise of the current (linear region in the semi-log plot), since there are often two different slopes detected. This can hint at two different electron populations with different energies yielding two different T_e . Finally, the electron density can be calculated as

$$n_e = -\frac{4I_{e,sat}}{A_s e} \left(\frac{8k_B T_e}{\pi m_e}\right)^{-1/2}. \quad (3.21)$$

Recapitulating that all this information on characteristic plasma parameters can be obtained from a fairly simple measurement by just changing the voltage and recording the resulting current makes it easy to understand why this probe is so successful. However, as always, the devil is in the details and Langmuir probe measurements is one of those easy-to-learn-hard-to-master techniques since it can get quite complicated (e.g. RF compensation, dielectric coating of the probe during reactive plasma probing, etc.) and the description of these occurrences are beyond the scope of this work.

3.4.3 Recent developments in Langmuir probe diagnostics

With the evaluation technique presented in the previous section, which automatically determines the presented plasma parameters, it is also possible to transfer the method to evaluate

cylindrical probes to other probe designs. This was realized during the course of this work which came with one particular advantage: The substrate dummy of the PTP, which is connected to a bias wire, can be used as a planar probe, therefore rendering the insertion of an additional cylindrical Langmuir probe obsolete. This fact does not only save time when performing complex measurements with a lot of parameter variations, it also minimizes the errors in terms of probe construction where unwanted connections may occur resulting in a time consuming search for errors.

Similar to the PTP acquisition it is important that the hard- and software to acquire Langmuir data are well coordinated. In close collaboration with Sven Gauter an acquisition software was developed in *LabVIEW*[®] to take full advantage of the Langmuir electronics and measurement card. As mentioned in the previous section, the requirements for Langmuir measurements may vary greatly, however, a high resolution and fast acquisition speed for recording I-V-curves are always desired. Since the current rises extremely fast once the electrons start reaching the probe it is crucial to have enough data points, especially in the exponential rise of the current, since it also greatly affects the semi-log plot and the determination of T_e . The more data points are acquired during the steep rise the more data points are available for the linear fit resulting in a more accurate determination of the electron temperature.

In analogy to the PTP electronics, the measurement card made by National Instruments is the heart of the Langmuir electronics used in our group. For this purpose, a model USB-6211 Digital I/O measurement card was chosen, with a sampling rate of 250 kHz and a resolution of 16 bits at the analog output. The *LabVIEW*[®] based software is designed in a way that it takes full advantage of the fast acquisition speed of the measurement card and its good bit resolution. The power source system inside the Langmuir electronics is capable of producing voltages between $V_{out} = -150 V \dots 150 V$. This means the 16 bits are equally divided between a voltage span of 300 V resulting in a minimal step width of $\Delta V = 4.6 mV$. So whatever the desired start and end values for the voltage sweep are, the step width is always set to the minimum to get as big as a voltage resolution as possible. Besides start and end voltage, another user input required is the desired time span of one measurement. To get as much data points as possible, the software dictates the card to always operate on full speed, meaning it will take 250,000 data points per second.

As an example, if one wants to do a full voltage sweep from -150 V to +150 V, the software will measure 65,536 data points which would take the card roughly 0.25 s. If the user decided to do that sweep in one second, the card is able to measure four times at every bias voltage point, resulting in 65,536 data points in the I-V-curve where every data point is an averaged value of four separately recorded measurements. As long as the card can keep up with the desired voltage span in the given time set by the user, it will use the averaging technique. However, for very fast measurements, e.g. a desired measurement time of 25 ms, the card would not be able to measure every of the 65,536 data points within the desired time. In these cases the software adapts to the problem and raises the step width. In this particular case, a ten times higher step width of $\Delta V = 46 mV$ is used by the software resulting in an I-V-curve which exhibits 6,553 data points (one tenth of the original amount) in total with no averaging at all.

In a nutshell, the software only requires three simple inputs (start voltage, end voltage and measurement time) from the user and will configure the measurement card to obtain the

maximum amount of data points (in most cases averaged ones) which minimizes errors and provides high accuracy data sets for the evaluation resulting in more precisely determined plasma parameters.

3.5 Quartz crystal microbalance

One of the key parameters for coating processes is the deposition rate. Usually described in nanometer per minute (nm/min) it determines the rate of film growth on the substrate during sputter processes. One way to measure the deposition rate includes the application of so called quartz crystal microbalance (QCM) devices, which utilizes a certain type of crystal to monitor the growth rate. Quartz crystals belong to the family of piezoelectric crystals where a mechanical deformation results in a voltage and vice versa. This property lead to application of piezo-active crystals in precise motor controls, sensors and actuators as well as frequency generating devices. If a crystal is operated with an alternating current (AC) it will begin to oscillate. If the AC is tuned correctly and fed into the crystal through its electrodes, it is possible to generate a standing shear wave. The frequency at which this is happening is called the resonance frequency. However, this may happen for a variety of frequencies determined by the bandwidth. For measurement purposes a very small bandwidth is desired to create a high accuracy. The higher the ratio between frequency and bandwidth (called Q-factor) of the crystal, the more stable it is enabling a high accuracy when determining the resonance frequency of the crystal. Usually crystals with resonance frequencies of $f = 4 - 6$ MHz are utilized which leads to a resolution of 1 Hz. If the mass of the crystal is changed due to film deposition, the resonance frequency will change to lower values. Utilizing the Sauerbrey equation [101] the frequency change can be written as

$$\Delta f = \frac{2f_0^2}{A\sqrt{\rho_q\mu_q}}\Delta m \quad (3.22)$$

with the resonance frequency f_0 , the mass change Δm , the crystal area A , the density of the quartz ρ_q and the shear modulus μ_q . This equation clearly showcases the relation between the change in mass evoking a change in frequency.

For this work a 6 MHz crystal was used, connected to a commercially available IL150 measurement electronics by *Intellectrics Global Ltd.* The crystal itself is a plano-convex plate, approximately 14 mm in diameter and 3 mm thick, which is excited into thickness shear mode vibrations by an external oscillator. A plano-convex shape of the crystal induces most of the oscillations to occur in the central exposed region. This increases the sensitivity of the crystal to deposited material. Sauerbrey's original assumption that the effect of depositing a quartz crystal with a film material is equivalent to depositing an equivalent mass of quartz is arguable. Therefore, the IL150 uses a different approach of determining the mass change. A more rigorous acoustic analysis of the loaded crystal as a one dimensional composite resonator of quartz and the film material leads to

$$T_f = \frac{D_q N_q T Z_f}{D_f 3.14 Z_q} \arctan \left(\frac{Z_q}{Z_f} \tan \left(3.14 \left(1 - \frac{T_q}{T} \right) \right) \right). \quad (3.23)$$

Here, T_f is the film thickness (in cm), D_q and D_f the density of the quartz crystal and film (in g/cm^3), respectively, N_q the frequency constant for an 'AT' cut quartz crystal oscillating

in thickness shear mode (in Hz/cm), T and T_q the period of the loaded and unloaded crystal, respectively. The acoustic impedance of the quartz and of the film material is described by Z_q and Z_f , respectively. However, for crystals that do not exhibit a high load this equation can be reduced to a rather simpler form

$$T_f = \frac{N_q D_q}{D_f} (T - T_q), \quad (3.24)$$

which is adequate for a majority of applications. Nonetheless, it must be noted that many parameters have to be chosen with great care. For the determination of the film thickness the density of the deposited film has to be considered, which can vary greatly from that of the density of a solid of that material and is in fact dependent on parameters such as substrate temperature and other deposition conditions. A photograph of the utilized QCM sensor head and an exemplary data set showing the deposition rate and thickness of Cu in Ar is shown in figure 3.13.

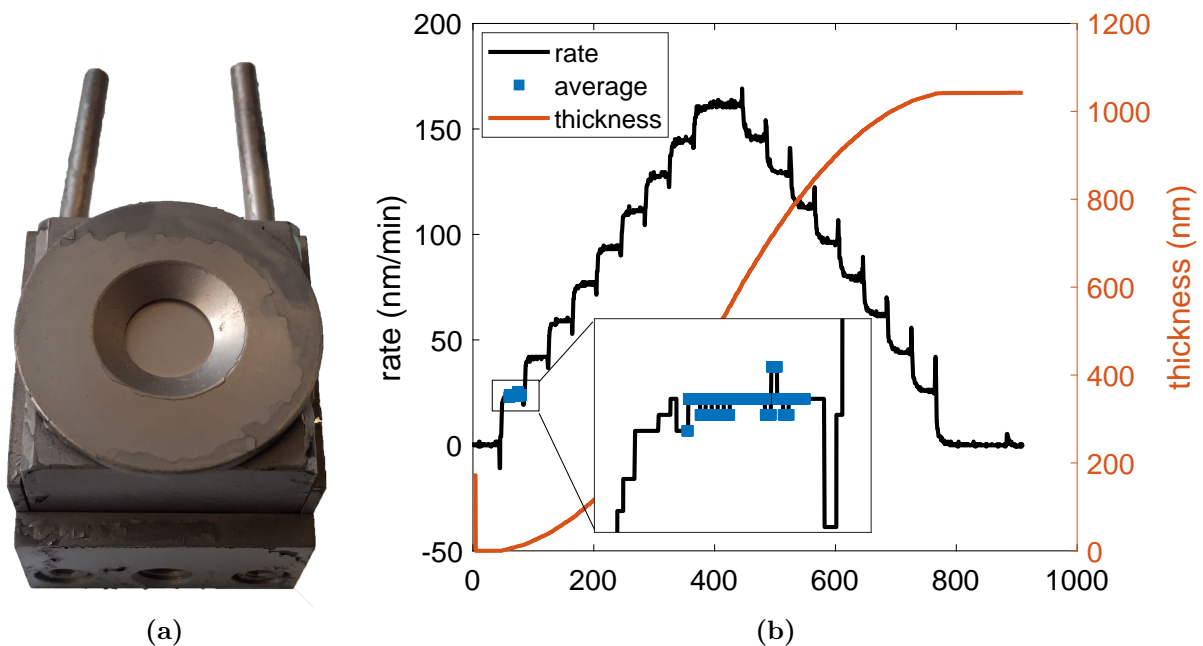


Figure 3.13: (a) Photograph of the QCM sensor head after deposition with copper. The 14 mm diameter crystal is mounted in the center of the probe and is shielded by a cap which exhibits a cone-shaped entry hole to the crystal. The two cooling tubes can be seen on the top of the image. (b) Exemplary data set of Cu sputtered in Ar using during DCMS at a pressure of 2 Pa. The data was obtained during a magnetron power variation from 30 W up to 190 W and back again, hence the step-like shape of the deposition rate (black curve). The thickness is shown as a red line. The value of the deposition rate is determined by averaging over a fairly horizontal interval, highlighted here in blue and shown in detail in the zoomed in box for the first value of 30 W ($R = 23.9$ nm/min).

4 Experimental Results

The following results were obtained in various plasma experiments used for different implantation and coating processes. In all cases the investigation of the resulting energy flux during the process was of key interest. In magnetron sputtering systems the energy flux greatly affects the stoichiometry and growth structure of the deposited films dictating the properties of the final product. During the investigations in the PIII system, the energy flux was used to determine the influence of secondary particles generated during the pulses.

The results are presented in form of published (or submitted) papers and are ordered by their underlying plasma generation principle. Every publication is preceded by an 'about page' which summarizes the title of the publication, the names of the co-authors, the name of the scientific journal it was (or is bound to be) published in, as well as the investigated coating (implantation) technique and utilized probes and observation methods. Further, it highlights the motivation for the presented investigation as well as the main results.

Publication I

Evidence of secondary electron emission during PIII pulses as measured by calorimetric probe

Authors: F. Haase, D. Manova, S. Mändl, and H. Kersten

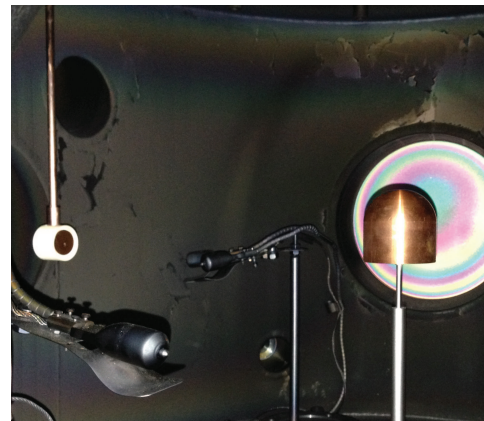
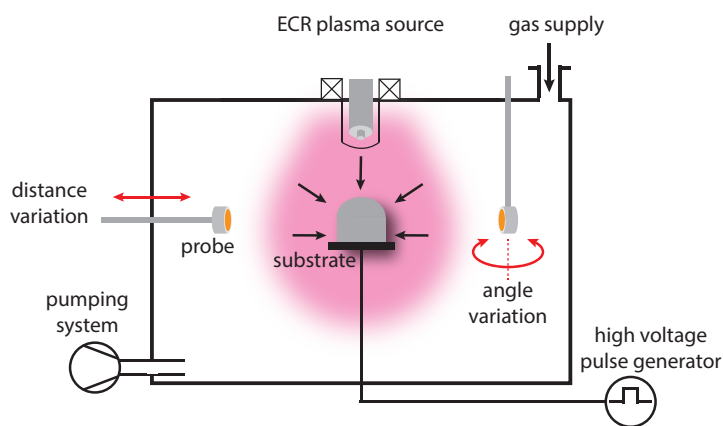
Journal: The European Physical Journal D

Technique: Plasma-immersion ion implantation (PIII)

Utilized Probes: Passive thermal probe (PTP)

Own contribution: approx. 60%

Experimental Setup:



Motivation:

The goal of this investigation was to answer three questions: Is the passive thermal probe, whose measurements typically take a few seconds, able to measure processes occurring during PIII pulses which last around $15 \mu\text{s}$? Is the differential measurement of a PTP able to detect the energy flux originating from the pulsed substrate and can that energy flux be attributed to secondary electrons by means of elimination?

Main results:

This work has shown the applicability of the passive thermal probe in a plasma-immersion ion implantation experiment. Although the pulses are on the μs time scale and PTP measurements take a few seconds, good results were obtained over the time span of several pulses. The resulting energy flux was observed to have a clear orientation, originating from the substrate. Parameter as well as substrate material variations strengthened the assumption that the resulting energy flux is mainly created by secondary electrons.

Evidence of secondary electron emission during PIII pulses as measured by calorimetric probe

Fabian Haase¹, Darina Manova^{2,a}, Stephan Mändl², and Holger Kersten¹

¹ Institut für Experimentelle und Angewandte Physik, Christian-Albrechts-Universität zu Kiel, Germany

² Leibniz-Institut für Oberflächenmodifizierung, Permoserstr. 15, 04318 Leipzig, Germany

Received 1 April 2016 / Received in final form 4 July 2016

Published online 8 September 2016 – © EDP Sciences, Società Italiana di Fisica, Springer-Verlag 2016

Abstract. Secondary electrons are an ubiquitous nuisance during plasma immersion ion implantation (PIII) necessitating excessive current supplies and shielding for X-rays generated by them. However, additional effects – especially at low pulse voltages – can include interactions with the plasma and transient increases in the plasma density. Here, it is shown that the transient thermal flux associated with secondary electrons emitted from the pulsed substrate can be directly measured using a passive calorimetric probe mounted near the chamber wall away from the pulsed substrate holder. A small increase of a directed energy flux from the substrate towards the probe is consistently observed on top of the isotropic flux from the plasma surrounding the probe, scaling with pulse frequency, pulse voltage, pulse length – as well as depending on gas and substrate material. A strong correlation between voltage and substrate-probe distance is observed, which should allow further investigation of low energy electrons with the plasma itself.

1 Introduction

Plasma immersion ion implantation is a fast and convenient technique for ion implantation or energetic coating processes into complex shaped 3D substrates or for large area wafer doping [1,2]. However, a crucial drawback compared to conventional beamline ion implantation is the rather high emission rate of secondary electrons (SE) created by the impinging primary ions. As the acceleration of the ions towards the substrate and of the SEs from the substrate is occurring within the plasma sheath in close vicinity of the substrate, no suppression at their origin is possible. Thus, the maximum voltage for PIII is limited to 100 kV or less as these SEs will in turn create energetic X-rays when they hit any chamber wall [3,4]. While containment inside the PIII chamber – similar to a balanced magnetron configuration – has been tried [5], no effective solution is available at present. At the same time, the secondary electron coefficient increases with the momentum of the impinging ions and can reach values of 10 for pulse voltages near 50 kV, thus leading to values for the energy efficiencies down to 5% [6,7].

The mean free path of these SEs is energy dependent and does increase for higher energies [8], similar to the mean free path for the accelerated ions [9]. However, these two quantities should not be confused while the range for the electrons is in general larger than for the ions. Several investigations have shown that the total emission of secondary electrons is well behaved and can be described

using a only few key parameters, i.e. ion energy, ion species and substrate material [10,11]. Nevertheless, the standard technique consists of measuring the total substrate current and correcting for ion current and displacement current.

For low energy SEs in the range of 1–10 keV, a considerable interaction with the plasma is expected, leading to a gradual increase of the plasma density during the pulse, as measured with a Langmuir probe near the plasma sheath [12]. In this study, the suitability of a calorimetric probe inserted away from the substrate inside the plasma for SE measurements is evaluated and the obtained results are compared with theoretical predictions. While such a calorimetric probe is generally suited for measuring energy and particle fluxes inside a plasma or a continuous ion beam, the separation of a continuous plasma background from short, repetitive pulses has not been attempted previously.

2 Experimental

An Electron Cyclotron Resonance (ECR) plasma was ignited using either nitrogen or argon gas at a pressure of 0.5 Pa (N₂ gas flow 150 sccm, purity 5.0; Ar gas flow 100 sccm, purity 5.0) with a rather low electron temperature of about 1.0–1.5 eV and corresponding low self-bias. The plasma density near the substrate is about $6 \times 10^9 \text{ cm}^{-3}$ [13]. As substrates, cylinders with a height of 50 mm and diameter of 50 mm, capped with a hemispherical top made of stainless steel 304, aluminium and copper respectively, were inserted into the centre of the vacuum

^a e-mail: darina.manova@iom-leipzig.de

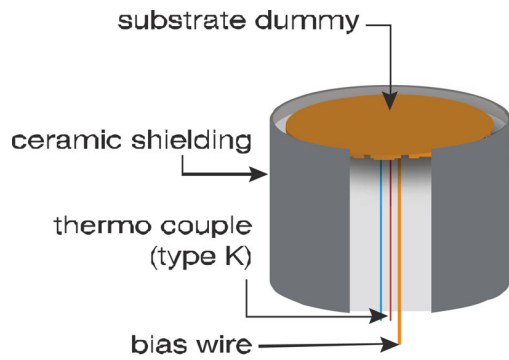


Fig. 1. Calorimetric probe setup – The type K thermocouple is spot welded to a substrate dummy (Cu) with a diameter of 20 mm and a thickness of 100 μm . An additional copper wire for probe biasing and current measurements is also spot welded to the probe area which itself is shielded in a ceramic cylinder.

chamber. Thus, the substrates are surrounded by the homogenous plasma forming a plasma sheath. The negative high voltage (HV) pulses were applied using a tetrode switch with a rise time of 10 ns/kV. The total pulse length was varied between 2.5 and 30 μs with a voltage of 2–5 kV and a pulse repetition rate of 1–5 kHz.

The energy flux measurements were obtained with a calorimetric probe using a substrate dummy made of copper (diameter 20 mm). The sensor area was shielded by a ceramic Macor[®] block mounted at the backside of the copper disc, which was spot welded to a thermocouple (type-K) for temperature recording and an additional copper wire for biasing and current measurements, although all measurements presented here were performed with a grounded probe. A schematic drawing of the probe is presented in Figure 1.

The energy influx was determined by evaluating the time evolution according to the procedure described in reference [14]. For every data point, a heating and a cooling curve is recorded. The calculation of the energy flux is based on the rate of change in the temperature of the sensor area and follows:

$$\dot{H}_S = C_S \frac{dT_S}{dt}, \quad (1)$$

where C_S is the effective heat capacity of the calorimetric probe and H_S the enthalpy of the substrate. The energy balance during the heating and the cooling phases are given by $\dot{H}_{S,\text{heat}} = P_{\text{in}} - P_{\text{out}}(T_S)$ and $\dot{H}_{S,\text{cool}} = -P_{\text{out}}(T_S)$, respectively. This leads to a total incoming power (P_{in}) at the substrate area of:

$$P_{\text{in}} = C_S \left[\frac{dT_{S,\text{heat}}}{dt} - \frac{dT_{S,\text{cool}}}{dt} \right]. \quad (2)$$

The effective heat capacity of the calorimetric probe is a key parameter for the correct determination of the measured energy influx at the probe surface. Since each component of the probe (thermocouple, substrate dummy, copper wire) has its own heat capacity, a calibration of the probe is essential. The calibration is done in a separate electron beam experiment which is described in detail by Stahl et al. [15].

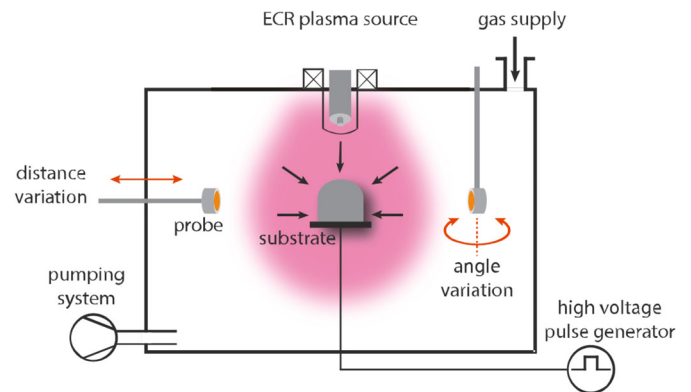


Fig. 2. Schematic experimental setup with an ECR ion source mounted on the top centre position for plasma generation. Substrate holder is mounted in the centre of the chamber from the bottom for applying HV pulses to the substrate. For most measurements the calorimetric probe was in a top mounted position 26 cm away from the substrate. The distance dependency measurements were performed with a probe mounted on a load lock system in line with the substrate.

As can be seen from Figure 1, the acceptance angle is a hemisphere, albeit reduced by the effective probe area when accepting non-normal incidence particles. Nevertheless, by rotating the probe, a distinction between an isotropic energy flux and a flux emanating from a point source can be obtained. Initially, the response of the probe to the plasma was recorded, waiting for a thermal equilibrium to be obtained. After that, in-situ recording of heating and cooling curves during and after PIII pulses, respectively, was performed.

Two different measurement geometries have been employed (cf. Fig. 2) with one probe mounted at 90° to the holder inserted from the top of the chamber to record additionally the angular flux variation and another probe mounted parallel to the holder at a variable distance from the substrate. No significant differences have been observed between the measurements of the probes. In the following, all results except for the distance variation are obtained by the rotating probe (fixated to face the substrate directly unless otherwise noted) at a distance of 26 cm from the substrate surface (i.e. 28.5 cm from the centre of the chamber).

Unfortunately, no experiments at a lower pressure of 0.3 Pa were possible as the reduced plasma density lead to a penetration of the microwave and the wires acting as an antenna with stray heating leading to unreliable read-outs of the probe. For pressures lower than 0.3 Pa, no stable operation of the ECR plasma source is possible. Ignition of the plasma had to be performed near 2 Pa. At higher pressures, the transport of the plasma from the resonance region at the top of the vacuum chamber towards the substrate is restricted, leading to much lower plasma densities near the substrate in addition to collisions in the plasma sheath, leading to a deviation from the monoenergetic ion energy distribution, i.e. the secondary electron emission coefficient becomes apparently pressure dependent. As the combination of PIII and ECR plasma source

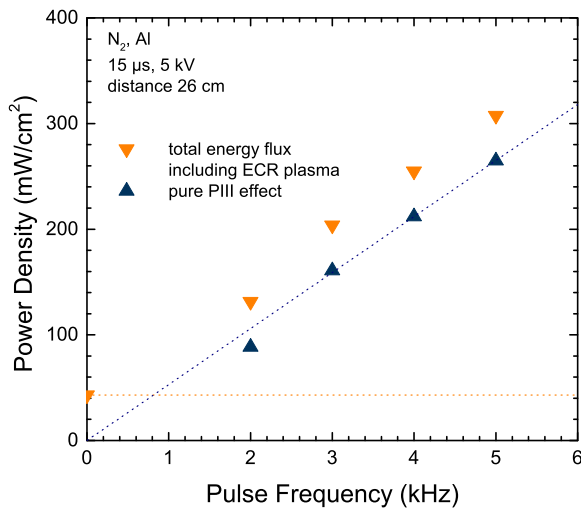


Fig. 3. Time averaged measurements of the additional energy during HV pulses before and after correcting for offset by plasma background.

allows only a small range of accessible pressures [16], changing the mean free path in this way is ineffective.

3 Results

Figure 3 presents data for nitrogen gas and Al substrate (at a fixed distance of 26 cm) when varying the pulse frequency from 0 to 5 kHz for a fixed 15 μs pulse length and 5 kV pulse amplitude. The downward triangles present the total measured energy power density by the probe and the upward triangles the PIII data when corrected for the plasma background of 43 mW/cm². Fitting these datapoints yields an additional flux density at the calorimetric probe of 53 mW/(cm² kHz). Hence, the time-averaged energy flux during the pulses exceeds the background plasma even at a pulse frequency of 1 kHz. Nevertheless, a direct comparison is futile as the interaction of these fast electrons with the plasma is rather weak and the energy flux is normally deposited only on the chamber walls (far) away from the plasma. In the following figures, the background flux is already deducted from the measured data, i.e. the values present only the additional energy flux during the HV pulses.

To ascertain that the additional energy flux is actually caused by the secondary electrons emitted from the substrate (neutral secondary particles or negative secondary ions are either less energetic or less numerous), Figure 4 shows the orientation dependent excess energy flux, i.e. corrected for the background, for nitrogen gas and steel substrate. As can be clearly seen, the measured flux is arriving directly from the direction of the substrate with the angular dependence following a cosine function. Thus, any energy flux arriving not directly from the substrate is rather weak (5 mW/cm² or less) and could be well within variations of the local plasma environment. The plasma is generated at the top of the chamber above the substrate and is diffusing out from there, creating local density gradients which will translate into a variation of

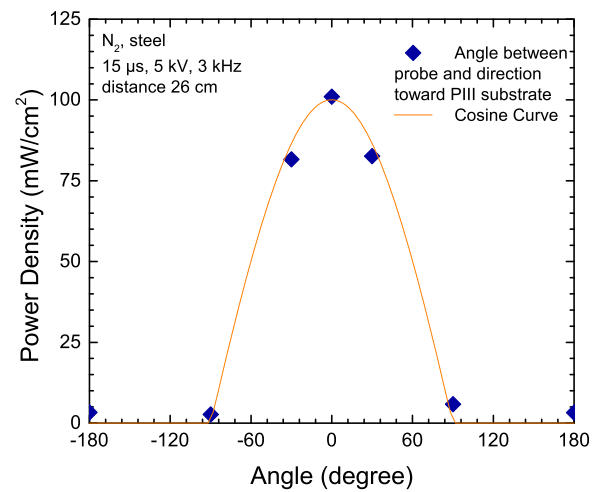


Fig. 4. Power density during the HV pulses as function of angle for probe rotation. 0° implies the probe facing directly the substrate. The directed energy flux originating from the substrate was measured in a nitrogen discharge using a stainless steel substrate with 15 μs pulses at 5 kV and 3 kHz.

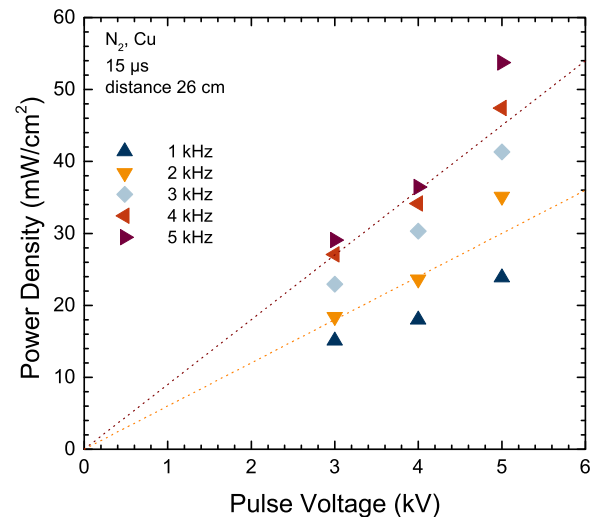


Fig. 5. Power density during the HV pulses as function of pulse voltage and frequency; the dashed lines are meant as guides for the eye only. The data was recorded in a nitrogen discharge using a copper substrate applying 15 μs pulses.

directional, local energy flux from the plasma. Rotating the probe without HV leads to a similar variation of the baseline intensity by 5–10%.

As a next step, the variation of the pulse voltage for different pulse frequencies (nitrogen, Cu substrate) was performed, with the results presented in Figure 5. A faster increase than linear is observed for the increasing pulse voltage, especially for the highest voltage of 5 kV. To establish that this is not due to a substrate or gas effect, the data for four different gas-substrate combinations are shown in Figure 6 with the identical effect being observed except for Al, where a slight decrease is present at 5 kV instead of a further increase of the already exceptionally high energy flux (corresponding to about nine times the baseline of the plasma).

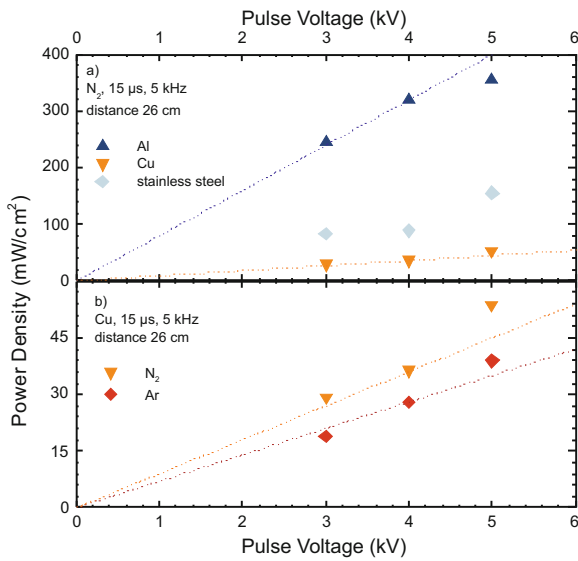


Fig. 6. Power density for different gases and substrate materials; as a guide for the eye, straight lines representing a linear dependency are indicated. The measurements were performed with 15 μs pulses at 5 kHz.

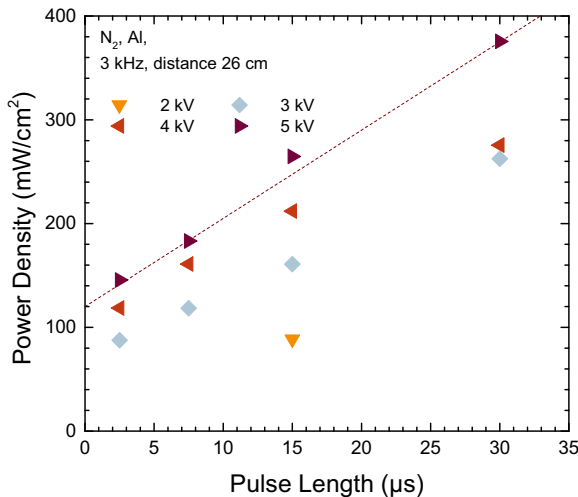


Fig. 7. Power density as function of pulse length; please note that the guideline which would implicate a linear behaviour does not start at the origin. The data were recorded in a nitrogen discharge using an Al substrate with 3 kHz pulses.

Remaining with the Al substrate, the pulse length variation leads to another dependency of the total, time averaged energy flux due to secondary electrons from the substrate: an already high value for short pulses of 2.5 μs with a slower increase to values about two times higher for 30 μs pulses is depicted in Figure 7. Finalising the presentation of the experimental results, Figure 8 shows the influence of the distance of the calorimetric probe from the substrate on the measured energy flux. While the flux is decreasing rapidly with distance d this effect is more pronounced for lower voltages than for higher ones. Thus, the values for 2 kV pulses are nearly zero already at a distance of 30 cm.

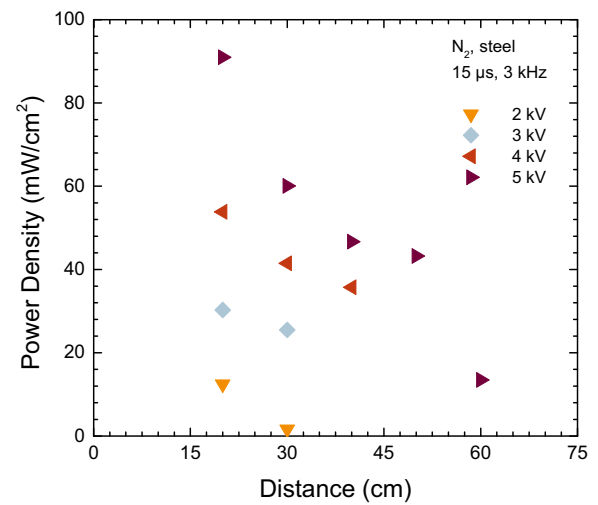


Fig. 8. Power density on the probe as function of distance and pulse voltage. The energy flux decreases with increasing distance. The measurements were performed in a nitrogen discharge using 15 μs pulse length and a frequency of 3 kHz.

4 Discussion

While only selected data sets have been shown here, the general tendencies and quantitative behaviour as a function of the investigated parameters (gas, substrate material, pulse voltage, pulse length, pulse frequency, distance) are unequivocal. In the following section, these dependencies are now discussed in detail. For comparison, a theoretical calculation using the simple Lieberman model without presheath dynamics is employed [17,18] with the sheath expansion, current evolution and integrated ion flux for a spherical geometry and 1 or 5 kV pulses plotted in Figure 9. A fast expansion followed by a new equilibrium is obtained for 1 kV with a wider sheath width becoming stationary at a later time for 5 kV. The current and time integrated ion fluence mirror exactly this behaviour with the initial supersonic expansion and following steady state.

The orientation dependence (Fig. 4) clearly points towards the substrate as the origin of the additional energy flux registered by the calorimetric probe with energetic SEs as the only viable candidate, given that energetic neutral atoms or negative ions are unlikely due to the rather low sputter yield, ionisation probability and very low initial kinetic energy [19]. Cu is known to exhibit a higher sputter yield than either steel or Al while Ar should be more efficient for sputtering heavy metals than the lighter nitrogen ions [20]. When comparing the qualitative dependency of the energy flux on the substrate material, the correlation with data from Szapiro and Rocca [6] is excellent with Al showing a much higher SE emission at identical ion energies than either steel or Cu. The weak gas dependency when changing Ar by N₂ is also known from literature. The energy dependence is more complex as additional factors arising from the sheath expansion have to be included with this discussion elaborated on further below.

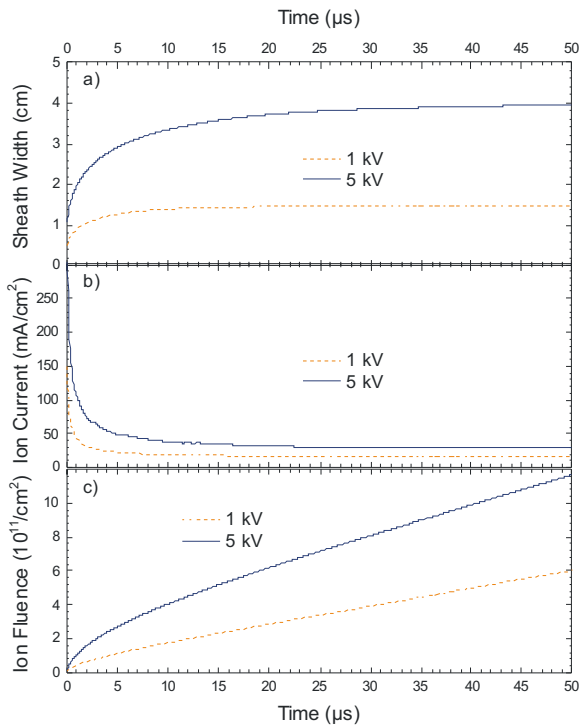


Fig. 9. Calculated (a) plasma sheath width, (b) ion current density and (c) integrated ion flux for nitrogen plasma and 1 or 5 kV pulses in cylindrical geometry.

The incident ion current towards the substrate is determined by the plasma sheath expansion during the high voltage pulses. The rise time of 10 ns/kV is sufficiently fast to allow a computation of the sheath expansion according to the Lieberman model [17] assuming square pulses (the finite fall time is not relevant as fast neutralisation of the substrate leads to a reduction of the sheath potential to values near the floating potential very rapidly [12]). The calculation for the sheath expansion was performed using a 2D model with the calorimetric probe located in the same geometric plane as the cylindrical part of the substrate, thus necessitating an additional geometric factor in the calculation [21] compared to the purely 1D Lieberman model. The 1D calculation could be sufficient for 1 kV pulse voltage, 5 kV certainly require a 2D model [22].

As a result, the supersonic sheath expansion is slowing considerably and reaching a stationary state again during the first 10 μ s – or even earlier for lower pulse voltages. On a long timescale, one Child-Langmuir sheath is replaced by a second one with a larger bias [23]. As a consequence, the ion flux per unit time for the stationary sheath is constant, being supplied only from the presheath and hence the integrated ion flux increases linearly with pulse length in this regime. This corresponds to the secondary emission reverting to a linear increase with the pulse time again, resulting – however – in a finite offset corresponding to the ion flux during the actual sheath expansion (cf. Fig. 9 and dashed line in Fig. 7 for 5 kV).

Similarly, the time averaged measurements of the secondary electron emission is directly linear with the pulse frequency without any offset, as seen in the experimental

results (Fig. 3). Likewise, the 5 kV data in Figure 7 show a stronger increase with pulse length than the 3 kV data as the sheath for 5 kV is larger than for 3 kV. A combination of larger sheath width with increasing pulse voltage and increasing SE coefficient with ion energy should be responsible with detailed calculations still necessary.

However, the 5 kV, 5 kHz data point for Al in Figure 6 does not follow this straightforward explanation. It has been observed previously that for high repetition rates a plasma depletion is occurring as the ion current to the substrate has to be provided by additional plasma generation in the whole plasma volume with diffusive transport to the near substrate region [24]. However, more detailed investigations are necessary to identify the specific involved mechanisms.

A more nuanced situation is encountered when looking at the distance dependence shown in Figure 8. A simple explanation would assume an isotropic distribution of secondary electrons (at least in the plane of the substrate and probe), thus, a decrease proportional to the inverse distance d should be expected, assuming a real 3D-geometry would lead to a $1/d^2$ relation. However, in contrast to the sheath edge expansion where the ions are originating, the SEs are always starting at the substrate surface with the acceleration being highest in the vicinity of the substrate. The sheath edge will lead only to minor focusing or defocusing effects as the electric field is smaller at the sheath edge and the velocity is already high. The effects leading to a more homogeneous implantation for larger plasma sheath extensions observed in PIII simulations are thus not applicable for the emission of SEs from the substrate.

At the same time, inelastic collisions with the background gas will lead to a decrease in the SE flux with increasing distance, starting for lower pulse voltages, i.e. kinetic energy, as the interaction cross sections are smaller for lower ion energies [8]. However, a local increase in the plasma density due to the energy loss will automatically be registered by the calorimetric probe. Here, additional work is necessary – and is in progress – for a clear delineation of the mean free path, energy loss and interaction of SE with the original plasma, albeit beyond the scope of the manuscript. A tentative fit to the data should thus include a geometric factor and an energy dependent exponential decay $d^{-(2\pm\delta)} \times e^{-\alpha(E)}$.

5 Conclusions

Using a calorimetric probe, a clear, orientation dependent energy influx emanating from the PIII substrate was observed. These measurements correlate directly with gas, substrate material, pulse length, pulse frequency and pulse voltage, exhibiting excellent qualitative agreement with standard PIII sheath expansion theory. Thus, an unequivocal identification with secondary electrons is proposed.

Moreover, tentatively observed effects include an interaction of the SEs with the plasma for an increasing plasma density to be dominant at low voltages and high repetition rates with higher cross sections and more secondary electrons, especially for the Al substrate. At high pulse

frequencies and voltages a plasma depletion not caused by the SEs could be observable.

Unfortunately, current measurements by the calorimetric probe have not been successful up to now. At the same time the temporal resolution of the calorimetric probe cannot be reduced enough to allow the observation of the SE flux during single pulses as the integrated heating-cooling-curve is analysed. A reduced acceptance angle could be envisaged for a more direct observation and ascribing of the energy flux to the substrate where high energy ions are impinging. Absolute quantification of the thermal flux is in progress. As a summary, it is easily possible to employ such a probe successfully for diagnostics during PIII treatments without interfering with the ion implantation process.

This work was supported by Deutsche Forschungsgemeinschaft (Project MA 2054/17-1 and KE 574/4-1).

References

1. J.R. Conrad, J.L. Radtke, R.A. Dodd, F.J. Worzala, J. Appl. Phys. **62**, 4591 (1987)
2. R.B. Liebert, S.R. Walther, S.B. Felch, Z. Fang, B.O. Pedersen, D. Hacker, *Plasma doping system for 200 and 300 mm wafers, in Ion Implantation Technology*, edited by H. Ryssel (IEEE Press, Piscataway, NJ, 2000), pp. 472-475
3. B.P. Wood, I. Henins, R.J. Gribble, W.A. Reass, R.J. Faehl, M. Nastasi, D.J. Rej, J. Vac. Sci. Technol. B **12**, 870 (1994)
4. D.J. Rej, R.J. Faehl, J.N. Matossian, Surf. Coat. Technol. **96**, 45 (1997)
5. J.N. Matossian, J.D. Williams, U.S. Patent 5498290, 1996
6. B. Szapiro, J.J. Rocca, J. Appl. Phys. **65**, 3713 (1989)
7. A. Anders, G.Yu. Yushkov, Surf. Coat. Technol. **136**, 111 (2001)
8. Y. Itikawa, M. Hayashi, A. Ichimura, K. Onda, K. Sakimoto, K. Takayanagi, M. Nakamura, H. Nishimura, T. Takayanagi, J. Phys. Chem. Ref. Data **15**, 985 (1986)
9. A.V. Phelps, J. Phys. Chem. Ref. Data **20**, 557 (1991)
10. M.M. Shamim, J.T. Scheuer, R.Pl. Fetherston. J.R. Conrad, J. Appl. Phys. **70**, 4756 (1991)
11. B.P. Cluggish, C.P. Munson, J. Appl. Phys. **84**, 5945 (1998)
12. S. Mändl, R. Günzel, W. Möller, J. Phys. D **31**, 1109 (1998)
13. S. Mändl, B. Rauschenbach, J. Appl. Phys. **88**, 3323 (2000)
14. S. Bornholdt, H. Kersten, Eur. Phys. J. D **67**, 176 (2013)
15. M. Stahl, T. Trottenberg, H. Kersten, Rev. Sci. Instrum. **81**, 023504 (2010)
16. S. Mändl, J. Brutscher, R. Günzel, W. Möller, J. Vac. Sci. Technol. B **14**, 2701 (1996)
17. M.A. Lieberman, J. Appl. Phys. **65**, 4186 (1989)
18. I. Langmuir, K.B. Blodgett, Phys. Rev. **22**, 347 (1923)
19. A. Wucher, H. Oechsner, Surf. Sci. **199**, 567 (1988)
20. J.F. Ziegler, M.D. Ziegler, J.P. Biersack, Nucl. Instrum. Methods B **268**, 1818 (2010)
21. I. Langmuir, K.B. Blodgett, Phys. Rev. **22**, 347 (1923)
22. S. Mändl, Plasma Proc. Polymers **4**, 23 (2007)
23. C.D. Child, Phys. Rev. **32**, 492 (1911)
24. D. Manova, S. Mändl, B. Rauschenbach, Plasma Sources Sci. Technol. **10**, 423 (2001)

Publication II

Dynamic determination of secondary electron emission using a calorimetric probe in a plasma immersion ion implantation experiment

Authors: F. Haase, D. Manova, D. Hirsch, S. Mändl, and H. Kersten

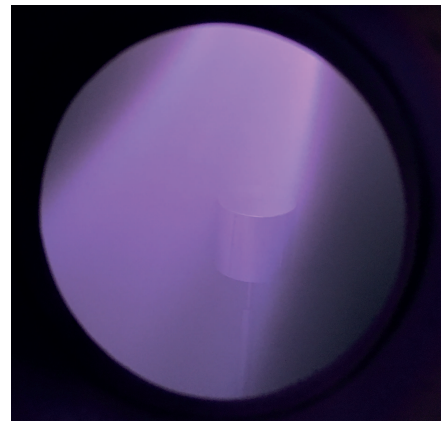
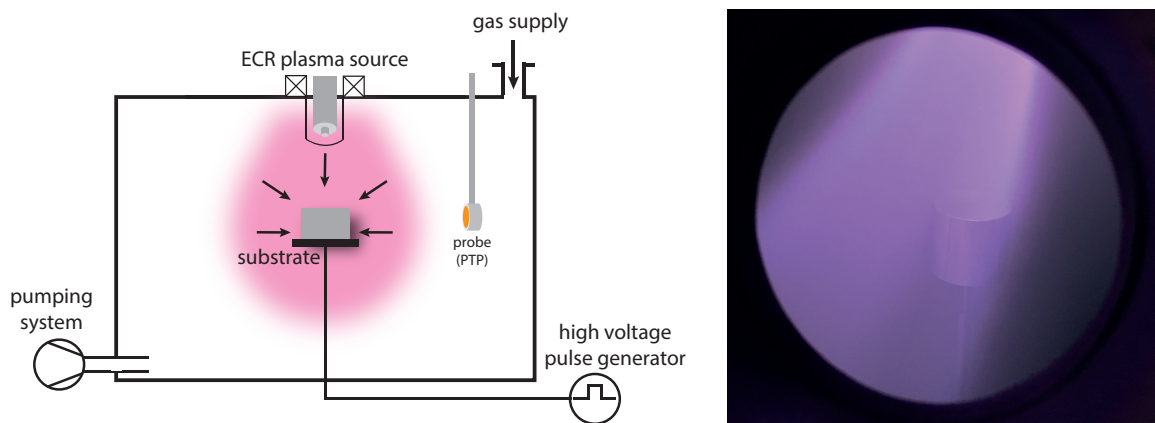
Journal: Plasma Sources Science and Technology

Technique: Plasma-immersion ion implantation (PIII)

Utilized Probes: Passive thermal probe (PTP)

Own contribution: approx. 60%

Experimental Setup:




Motivation:

The main topic of this investigation was to monitor surface changes of different substrates by investigating the resulting energy flux during the high voltage pulses. Seven different substrate materials (Al, Mg, AlMg, Ti, Mo, Zn and AZ91) were oxidized in a furnace and then sputtered with argon gas. Later, the metallic surfaces were exposed to high voltage pulses using nitrogen as process gas. Intermittent short measurements with the PTP should be able to determine changes in the surface composition and changing secondary electron coefficient.

Main results:

This publication has shown the possibility of detecting time dependent changes in the surface composition of substrates during sputtering processes using argon and a nitrogen plasma by means of the PTP. The 'poisoned' and metallic states of the substrates have been observed as well as the evolution of the transition between them. Following a simple model, time dependent secondary electron coefficients were calculated for all seven investigated materials and normalized to be able to compare the trends with other works. Especially Al, Mg and AlMg exhibited strong changes in the SEE depending on the surface composition.

Dynamic determination of secondary electron emission using a calorimetric probe in a plasma immersion ion implantation experiment

Fabian Haase^{1,3} , Darina Manova², Dietmar Hirsch², Stephan Mändl² and Holger Kersten¹

¹Institut für Experimentelle und Angewandte Physik, Christian-Albrechts-Universität zu Kiel, Germany

²Leibniz-Institut für Oberflächenmodifizierung, Permoserstr. 15, D-04318 Leipzig, Germany

E-mail: fhaase@physik.uni-kiel.de

Received 6 March 2018

Accepted for publication 3 April 2018

Published 25 April 2018



CrossMark

Abstract

A passive thermal probe has been used to detect dynamic changes in the secondary electron emission (SEE). Oxidized and nitrided materials have been studied during argon ion sputtering in a plasma immersion ion implantation process. Identical measurements have been performed for the metallic state with high voltage pulses accelerating nitrogen ions towards the surface, supposedly forming a nitride layer. Energy flux data were combined with scanning electron microscopy images of the surface to obtain information about the actual surface composition as well as trends and changes during the process. Within the measurements, a direct comparison of the SEE within both employed ion species (argon and nitrogen) is possible while an absolute quantification is still open.

Additionally, the nominal composition of the investigated oxide and nitride layers does not always correspond to stoichiometric compounds. Nevertheless, the oxides showed a remarkably higher SEE compared to the pure metals, while an indistinct behavior was observed for the nitrides: some higher, some lower than the clean metal surfaces. For the aluminum alloy AlMg3 a complex time dependent evolution was observed with consecutive oxidation/sputtering cycles leading to a very rough surface with a diminished oxide layer, leading to an almost black surface of the metal and non-reproducible changes in the SEE. The presented method is a versatile technique for measuring dynamic changes of the surface for materials commonly used in PVD processes with a time resolution of about 1 min, e.g. magnetron sputtering or HiPIMS, where changes in the target or electrode composition are occurring but cannot be measured directly.

Keywords: PIII, plasma-immersion ion implantation, calorimetric probe, passive thermal probe, plasma diagnostics, secondary electron emission

1. Introduction

Secondary electron emission (SEE) from surfaces upon energetic ion impingement is an important and crucial factor in low pressure plasma discharges [1–3]. They are accelerated and gain high kinetic energy when transiting through the plasma sheath, leading to either impact ionization by inelastic

collisions with atoms or ions, or alternatively heating of the less energetic electrons by elastic collisions. Furthermore, changes in the chemical composition or topography of the electrodes can lead to a modified SEE coefficient, e.g. as encountered during the ageing of plasma TV screens. Another nuisance is occurring when surfaces at ground potential, isolators or feedthroughs are bombarded by energetic electrons or ions, which are not accounted for in the plasma discharge model. Thus, a temporal potential variation coupled

³ Author to whom any correspondence should be addressed.

with a varying incident current on such surface will lead to additional secondary electrons—whose current density is changing and thus can influence the plasma process. In any case, glow-like discharges as used in reactive magnetron sputtering and high-power impulse magnetron sputtering (HiPIMS) applications depend on the SEE.

Measuring the SEE directly in a plasma discharge is very indirect as the only indication of change is hidden in the discharge voltage and current and one has to be sure which surfaces are modified or charged in the plasma. Target poisoning, due to dielectric layers forming on the target surface during a plasma process, or plasma impedance variations could mask or imply a change in the SEE. Using directed ion beams may work for conductive materials [4, 5] but will lead to surface charging for insulators aggravated by the SEE. Adjustment and control of the surface potential can either be performed by electron bombardment using a flood gun or, otherwise, using a plasma discharge. An alternative method for measuring the SEE include modeling of I - V measurements [6, 7].

Plasma immersion ion implantation (PIII) is a versatile technique to modify surface properties of materials and to form new compounds, without the limitations of conventional implantation. It enables altering the surface near layers of a component due to homogenous implantation of ions. This is accomplished by applying negative high voltage (HV) pulses to the component during the process, which leads to formation of a sheath around it, drawing ions onto the component. Using PIII [8] with a separate plasma source and a low electron temperature, almost no surface sputtering or electron emission is occurring for a grounded substrate potential. However, during the highly negative voltage pulse at the substrate for ion implantation, these effects surely occur. Thus, the SEE is directly coupled to the energetic ions during the pulses. At sufficiently low pressures and fast pulse rise times, a mono-energetic bombardment can be realized, albeit presenting a mixture of atomic and molecular ion species for molecular gas precursors such as N_2 or O_2 [9]. Since the emitted electrons are accelerated in the plasma sheath due to the potential drop caused by the pulse voltage, the higher energy allows for a more efficient detection, e.g. using electron induced scintillation [10] compared to the initial energy distribution at the surface. Concurrently emitted negative ions are only a small fraction of the sputtered material and should impose an error of less than 0.1% on the results. While it has been established that the static SEE can be measured in such an experiment using a passive thermal probe (PTP) [11], the open question is whether a dynamic recording of the changes induced by the impinging ions, which could lead to a time dependent SEE, is possible. This study tries to answer this question using either Ar bombardment of oxidized metallic substrates or nitrogen bombardment of metallic surfaces while measuring the energy flux correlated with the secondary electrons using a passive calorimetric probe for determining the related energy flux.

During the last decades, a variety of probes have been developed to gain a better understanding of plasma-based systems. In terms of plasma characteristics, Langmuir probes have proven to be the workhorse of electrostatic probing [12, 13].

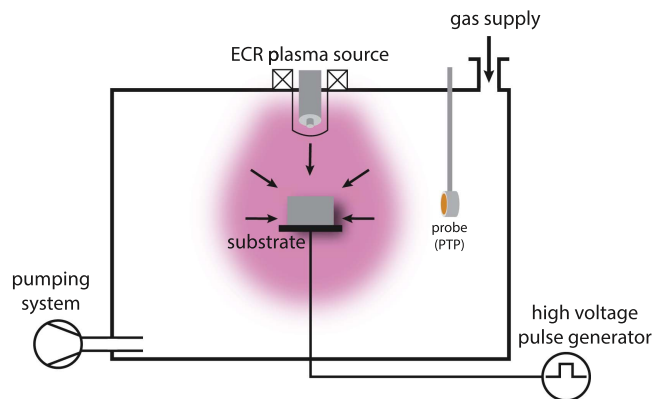


Figure 1. Schematic drawing of the discharge chamber and the utilized probe. The ECR ion source is mounted on the top center position for plasma generation, the substrate holder is placed underneath it and connected to a HV pulse generator. The PTP is top mounted at a radial distance of 26 cm to the substrate.

However, when it comes to plasma-wall interactions present in a variety of plasma process applications, such as film deposition, etching and surface modification, calorimetric probes are essential for a fundamental understanding of energy transfer to the substrate. In these processes, thermal effects are playing a dominant role in terms of adsorption, desorption, diffusion as well as chemical reactions [14–17]. Furthermore, the energy transfer during thin-film coating processes is crucial to the structure and morphology of the deposited film.

A calorimetric probe, such as a PTP, was already introduced by Thornton in 1978 [18] and has since that time been successfully used in a variety of plasma environments [11, 19–23]. The simple and robust design of the probe enables a flexible integration into existing experiments. The design can effortlessly be upscaled or downscaled and allows for spatially resolved measurements. The area of application ranges from investigations in rf-systems [24, 25], simple DC magnetron sputtering [11, 26, 27] and more advanced pulsed sputtering techniques like HiPIMS [21, 28, 29] or PIII [30, 31].

The energy transfer between plasma species and the solid is a complex mechanism and the experimental study due to heat transfer requires suitable measurement techniques. In low pressure (non-equilibrium) plasma applications the thermal conditions at the substrate surface are characterized by a detailed energy balance, which considers the different source and loss mechanisms [32, 33].

2. Experimental setup

The experiments were performed in a vacuum chamber (165 l) with a two stage pumping system for a base pressure of 10^{-7} mbar. A schematic drawing is shown in figure 1. The plasma was generated by an ECR ion source at a pressure of 0.5 Pa (N_2 gas flow 150 sccm or Ar gas flow 100 sccm, respectively). For lower pressures, no stable plasma discharge could be obtained, while increasing the pressure by a factor of 10 or more resulted in the beginning of a pulsed DC discharge

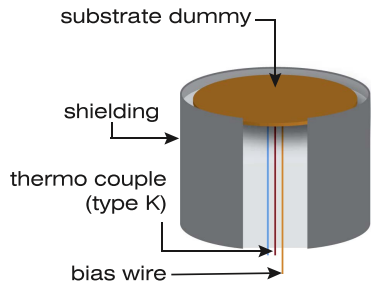


Figure 2. Schematic drawing of a passive thermal probe (PTP).

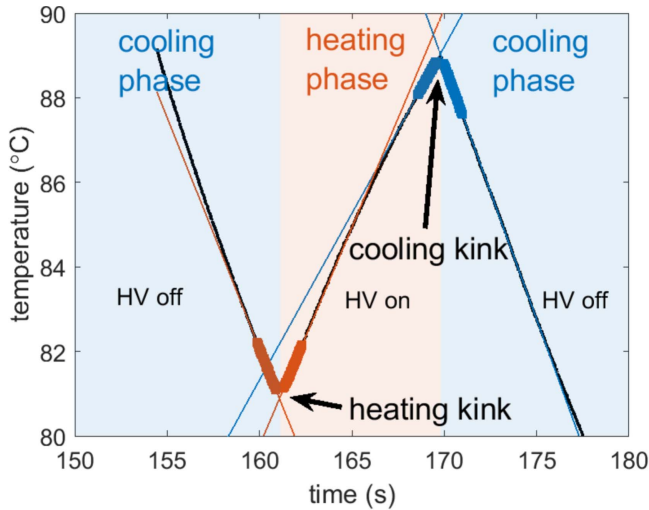


Figure 3. Evaluation of a temperature curve for an oxidized AlZ91 substrate in the sputtering phase using Ar ions after 1 min of sputtering. The pressure is 0.6 Pa and a 3 kV pulse with a frequency of 5 kHz and 15 μ s pulse width is applied to the substrate. A single data set consists of three phases (two phases with the source being switched off and a phase in between with the energy source is turned on) which yields two measurement values for the energy flux.

originating at the substrate during the negative HV pulses. The plasma density near the substrate was measured in an earlier investigation to be $6 \times 10^9 \text{ cm}^{-3}$ with a rather low electron temperature of about 1.0–1.5 eV [34]. The substrates used had a cylindrical shape with a height h of 25 mm and a radius R of 25 mm mounted at the center of the discharge chamber.

Thus, the substrates were surrounded by the homogenous plasma glow forming a plasma sheath. The negative HV pulses were applied using a tetrode switch with a rise time of 10 ns kV^{-1} . By opening this switch, a capacitor is discharged. The pulse length was kept constant at 15 μ s with a voltage of 3 kV and a pulse repetition rate of 5 kHz for the present experiments. Between the pulses, the capacitor was recharged by a capacitor charging power supply whose time-averaged current has been recorded during experiments. This primary current is directly proportional to the pulse frequency and integrated current during the pulses supplied by the HV pulse generator.

For energy flux measurements caused by the emitted secondary electrons during the HV pulses a PTP was top mounted at a distance of 26 cm to the substrate and facing the substrate. The center of the probe is facing the center of the height of the substrate.

A detailed description of this probe and the evaluation of the measurement is presented here as the understanding of the effects is important for discussing the results shown in section 3.

The probe employed in the experiments consists of a sensor plate (substrate or probe dummy) made out of copper with a diameter of 2 cm and a thickness of 100 μ m. Attached to the back of it is a type K thermocouple and an additional copper wire for biasing and current readings [35]. The sensor plate is placed into a ceramic or metallic shielding to make sure, that only contributions hitting the sensor area from the top are measured. A schematic drawing is shown in figure 2.

The basic idea of the PTP is the ability to observe and calculate the change in the enthalpy H . The energy flux can be determined due to the relation between the time derivative of the enthalpy \dot{H} and the time derivative of the temperature \dot{T} during the heating T_h (energy source on, i.e. HV pulses on) and the cooling T_c (energy source off, i.e. HV pulses off) phases at the substrate dummy which yields:

$$\text{Heating: } \dot{H}_h = C_p \dot{T}_h = P_{\text{in}} - P_{\text{out,h}}, \quad (1)$$

$$\text{Cooling: } \dot{H}_c = C_p \dot{T}_c = -P_{\text{out,c}}. \quad (2)$$

Here, C_p is the heat capacity of the probe, P_{in} gives the energy flux from the source, $P_{\text{out,h}}$ and $P_{\text{out,c}}$ compensate for the energy losses of the probe during heating and cooling respectively. Assuming that the energy flux leaving the dummy during the heating phase equals the energy flux leaving the probe during cooling at the same temperatures, equations for heating and cooling can be combined to calculate the energy flux J_{in} :

$$J_{\text{in}} = \frac{P_{\text{in}}}{A_p} = \frac{C_p}{A_p} (\dot{T}_h - \dot{T}_c). \quad (3)$$

Here, A_p stands for the probe area. For the assumption $P_{\text{out,h}}(T_h) = P_{\text{out,c}}(T_c)$ for equal temperatures $T_h = T_c$ to be valid, any heat flux originating from secondary heat sources has to be constant for the monitored time period. As the ECR plasma source is operating at the same power and interactions of the emitted secondary electrons are nearly negligible, the heat flux from the plasma is provided as a constant background. This background has been measured by plasma on/plasma off measurements [31] and is of no interest for the current investigations on the influence of the HV pulses. Nevertheless, a short measurement time is useful to avoid any potential drift, e.g. encountered by a slow heating of the chamber walls. However, a time resolution in the micro-second range commensurable with single HV pulses is not feasible. Hence, the measured temperature increase of the probe and the determined energy flux is a result of many HV pulses occurring during tens of seconds. To obtain the changes in a relatively short time frame the temperature around the kinks that occur during transition from HV off to HV on (heating kink) and HV on to HV off (cooling kink) are evaluated. This method is graphically demonstrated in figure 3. Additionally, the figure shows the determination of the temperature derivative by linear fits, which yields a

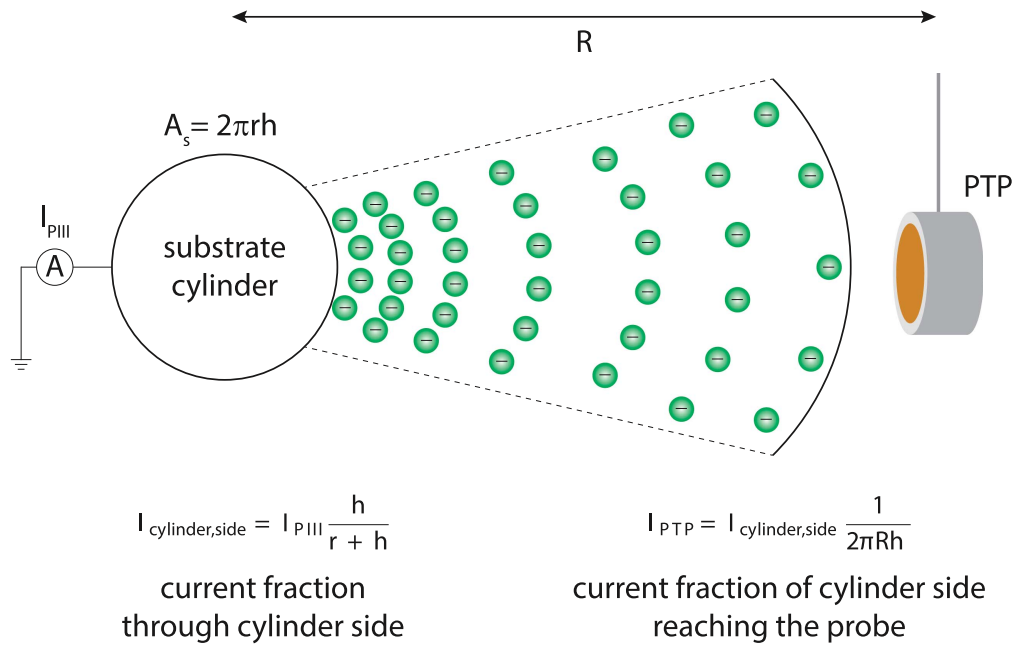


Figure 4. Schematic drawing of the current model that connects the PTP and current readings with the SE yield.

sufficiently good approximation of the exponential slope of the probe temperature for short time intervals.

With the knowledge of the energy flux and additional current readings from the HV pulse generator, these values can be combined to make a simple estimation for the secondary electron coefficient. Although it is very difficult to estimate the absolute secondary electron yield and compare it with studies from others (since it seems to be very dependent on the surface properties and discharge parameters), a simple model shall be presented here.

Assuming the measured current at the substrate during the negative HV pulse is the sum of the secondary electron current and the ion current $I_{\text{PIII}} = I_{\text{SE}} + I_{\text{ion}}$ and $I_{\text{SE}} = \gamma_{\text{SE}} I_{\text{ion}}$, the secondary electron current can be written as

$$I_{\text{SE}} = I_{\text{PIII}} \left(1 + \frac{1}{\gamma_{\text{SE}}} \right)^{-1}$$

with the secondary electron coefficient γ_{SE} . Since the energy flux measured with the PTP primarily results from secondary electrons (as argued in earlier works [31]), the energy flux can be written as

$$J_{\text{PTP}} = \frac{F_{\text{area}} I_{\text{SE}} U_{\text{PIII}}}{2\pi R h}$$

Here, $F_{\text{area}} = 1/(1 + A_{\text{tb}}/A_{\text{s}})$ is a geometry factor to compensate for the fact that the target is of cylindrical shape, where only the part that leaves the side is assumed to reach the probe. A_{tb} denotes the surface area of the top and bottom of the cylinder and A_{s} is the area of the cylinder side. R is the distance between substrate and the PTP ($R = 26$ cm), h the height of the cylindrical substrate, and I_{SE} the secondary electron current. Combining the current and PTP readings we

can calculate the secondary electron yield γ_{SE} as:

$$\gamma_{\text{SE}} = \left(\frac{I_{\text{PIII}}}{I_{\text{SE}}} - 1 \right)^{-1} = \left(\frac{F_{\text{area}} I_{\text{PIII}} U_{\text{PIII}}}{2\pi R h J_{\text{PTP}}} - 1 \right)^{-1}.$$

It must be noted that this is a rather simple model and will probably overestimate the secondary electron yield, however, it is a valid basis for discussion. A schematic overview of the presented model can be seen in figure 4.

3. Results

3.1. Sputtering of oxide layer

The existence of secondary electrons in PIII as measured by the PTP has been introduced in [31]. It is well known that the secondary electron yield γ_{SE} is highly dependent on the substrate material and its surface properties [36–38]. Before showing the recent results, an overview of the existing literature is given.

Depla *et al* [36] performed a detailed determination of the secondary electron yield for seventeen different metals with an oxide or nitride layer monitoring the discharge voltage of a magnetron sputtering system. Especially in the case of Mg and Al the SEE was much higher with an oxidized or nitrided surface compared to the sole metal surface, whereas for most other metals like Ti, Cu and Mo the SEE was lower compared to the pure metal. While the discharge characteristics have been used to derive the electron emission, another set of recent experiments employed an electrical SE collector. Corbella *et al* [4, 37, 38] investigated the SEE of Al and Ti foils using a secondary electron collector for an ion source which posed as a magnetron sputtering source. They were

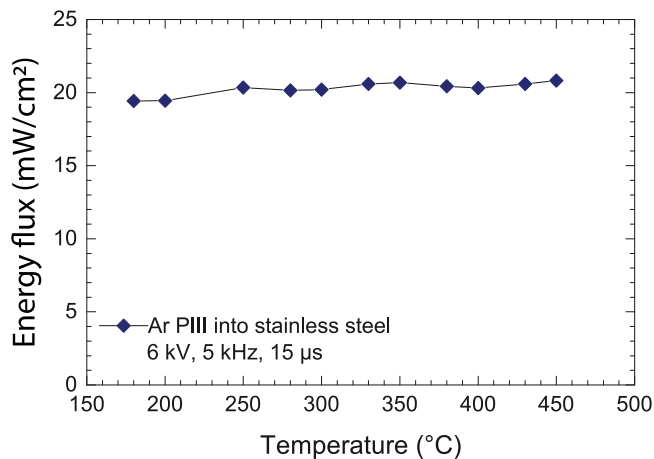


Figure 5. Energy flux as measured by PTP for secondary electrons originating on stainless steel as function of surface temperature.

able to detect an increase of γ_{SE} of up to one magnitude for Al_2O_3 .

How does the PIII setup with a PTP compare to these experiments? The typical PIII experiment with ion energies in the kV range and pulse repetition rates of a few kHz leads to gradual heating of the substrate and integrated ion fluences of 10^{17} – 10^{18} cm^{-2} during one experiment. Consequently, the influence of the substrate temperature and the substrate roughness has been investigated. The commercial laser profiler system μ Scan was used to determine the surface roughness. The laser is driven at a NIR wavelength of 780 nm. The surface characteristic was measured at a scan field size of $200 \mu m \times 200 \mu m$ spatial resolution. Based on the obtained data the isotropic power spectral density was calculated by the commercial SPIP software.

As shown in figure 5 for Ar bombardment of stainless steel, no influence of the substrate temperature on the measured energy flux is observed. On the other hand, surface roughening of a Cu substrate could lead to a slightly higher energy flux (see figure 6) due to a more efficient SEE, however, the difference is still within the error bar.

Returning to the dynamic measurement, different substrate materials (Al, Mg, AlMg, Ti, Mo, Zn, AlZ91, steel and Cu) were oxidized in a thermal furnace at a temperature of 400 °C for 4 h before the measurements. For each measurement with the PTP, 3 kV pulses with a frequency of 5 kHz and a length of 15 μs were applied to the substrate for a short time of about five seconds and then turned off again for about 15 s. After the measurement was done, the HV pulses were turned on again for a certain time (ranging from 1 to 5 min) to allow a continuation of the sputtering process with Ar ions. During the sputtering period, no measurements with the PTP were conducted. After each sputtering phase the PTP measurements were repeated.

Typical results for the primary current through the pulse generator used to apply the PIII voltage pulses to the substrate, the measured energy flux due to the secondary electrons and the substrate temperature are shown in figure 7 for the magnesium alloy AZ91. The primary current and the energy flux show a nearly constant plateau after an initial

phase, followed by a nearly instantaneous drop after 45 min. The original surface could be characterized by a mixture of hydrocarbons and hydroxides, which recede after sputtering (of about 15 min) to reveal the thermal oxide layer, which is removed with time. It has to be noted that the energy flux is indicative of a small substrate area facing the PTP while the primary current is integrating across the substrate and includes primary ions, secondary electrons and displacement currents due to the moving sheath edge. The transition from oxide to metal at about $t = 45$ min is completed within 60–90 s.

An exemplary result for commercially pure Mg can be seen in figure 8 where the oxide layer is removed between 10 and 15 min. The observed transition period is limited by the sampling rate. The actual transition from sputtering the oxide to sputtering the metal could be faster. The oxidized substrate yields power densities of around 90 mW cm^{-2} for the first 10 min of sputtering and produces a steep drop in the energy flux to a steady level of about 10 mW cm^{-2} . The steep drop is due to transitioning from an oxidized surface to a metallic surface when sputtered with Ar ions. This behavior is fairly present for all investigated materials and is emphasized especially for AZ91 and Mg. The change in the energy flux during sputtering is shown in figure 9 for all investigated materials.

3.2. Formation of nitride layer

As an additional investigation, the substrates investigated in section 3.1 were exposed to a nitrogen atmosphere to form a nitride layer on the substrate surface using the same pulse parameters. The pulsing was periodically interrupted for short measurements with the PTP and then continued. Figure 10 illustrates the change in the energy flux during the nitriding.

Again, Mg and AZ91 have the highest yields when bombarded with nitrogen ions, which was the same case in the investigations during sputtering with argon. When comparing the power densities, the change in primary ion current density as well as the molecular/atomic ratio should be considered in addition to the exchange of the precursor gas. For the plasma composition, about 90% N_2^+ ions and 10% N^+ ions are present. Molecular ions accelerated to 3 keV separate into 1.5 keV nitrogen atoms immediately upon impinging onto the surface. Thus, the measured SEE for nitrogen is a mixture of the values at 3 and 1.5 keV with the lower energy ions clearly dominating.

When using the magnesium substrate the measured energy flux from the emitted secondary electrons starts from roughly 25 mW cm^{-2} , staying fairly constant for about 25 min after which it starts to rise to a value of about 63 mW cm^{-2} for the nitride. Anyhow, for most materials there is but a slight change in the energy flux measured by the PTP and primary current of the HV pulse generator over the investigated time span. Al, AlMg, Ti, Mo and Zn all exhibit a slight decrease in the energy flux when exposed to a nitrogen atmosphere.

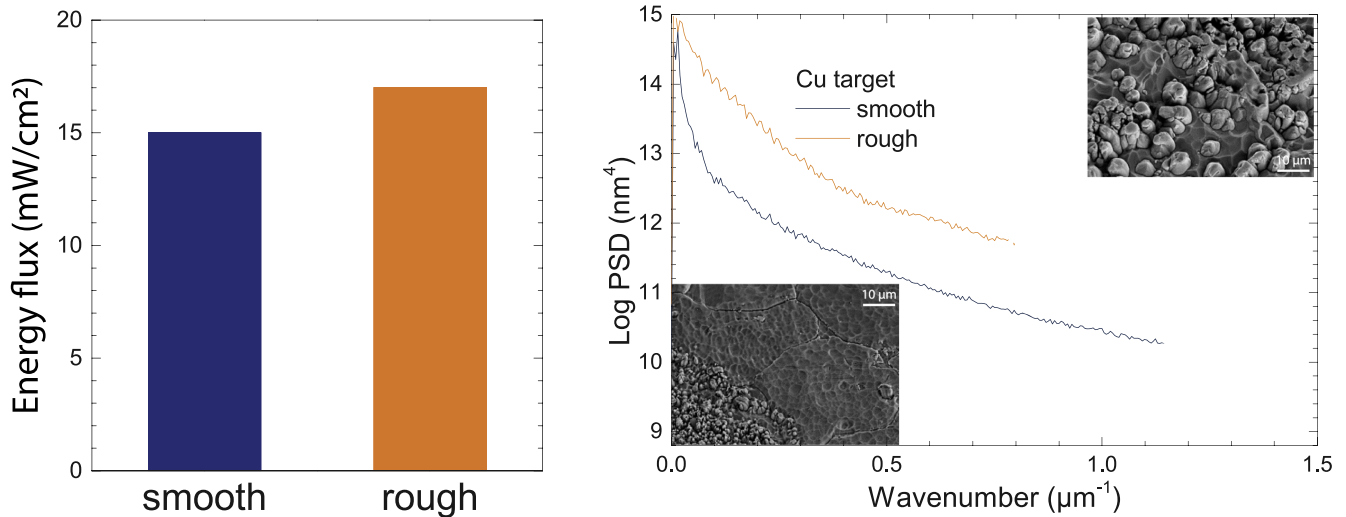


Figure 6. Energy flux as measured by PTP for copper with smooth and rough surface (left side) and power spectral density with SEM images of the respective surface (right side).

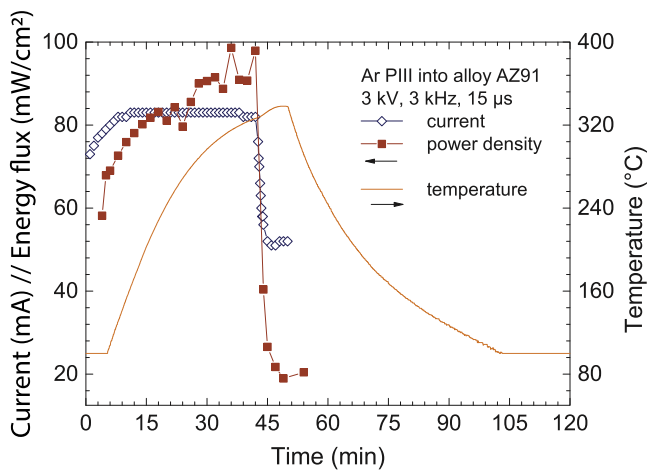


Figure 7. Temporal evolution of primary current, energy flux and sample temperature for oxidized alloy AZ91 during sputtering with Ar ions in a 3 kV, 5 kHz, 15 μs PIII pulse. At roughly 52 min the measurement was done, no further experiments were performed and the substrate was cooling off without any PIII or background plasma.

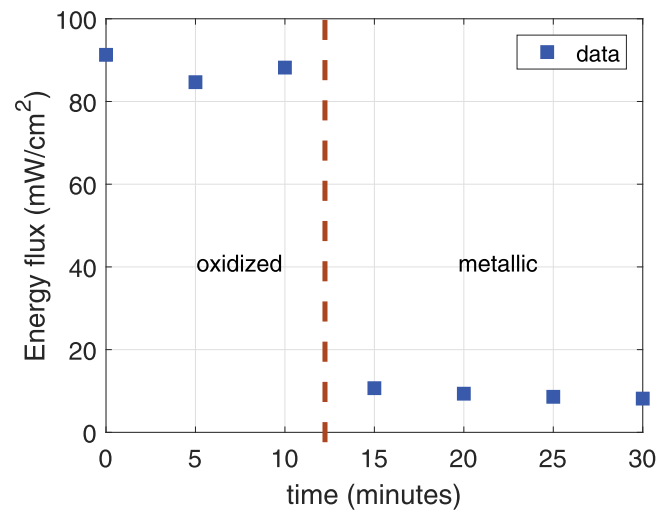


Figure 8. Exemplary results of the change in the energy flux for oxidized Mg during sputtering with Ar ions in a 3 kV, 5 kHz, 15 μs PIII pulse.

4. Discussion

The presented data is excellent for a comparison within each gas species between different materials whereas comparison for argon and nitrogen is more qualitatively at the present state. However, extreme care has to be taken upon identifying the surface condition as oxidized, metallic and nitrided. While the metallic condition after sufficient Ar sputtering should correspond to an uncontaminated metallic surface, the nitride formed after nitrogen implantation is more questionable. However, nitrogen ion implantation will lead to an equilibrium nitrogen content—especially when reactive nitrogen is available as radicals or ions between the HV pulses—where at least the immediate surface will consist of a continuous nitrogen containing layer, albeit with an *a priori* unknown surface concentration. Comparison with low energy nitrogen

ion implantation experiments from the literature will help for absolute calibration of the SEE coefficients.

One main feature that needs to be investigated is the characterization of the oxidized surface obtained in the thermal furnace, since it could have a great effect on SEE. Figure 11 shows some interesting effects of the oxidized surface. While the commercially pure Mg shows a reasonable oxide layer with a fast decay towards the metal, the Cu surface is immediately sputtered from oxide to metal. Furthermore, the aluminum alloy AlMg3 shows a non-reproducible behavior for the SEE. These two points will be discussed now in detail.

For copper, the difference between the oxidic and the metallic state is rather small and concurrent scanning electron microscopy (SEM) and energy-dispersive x-ray spectroscopy investigations (as shown in figure 12) explain why this difference is so small and less than expected from the literature.

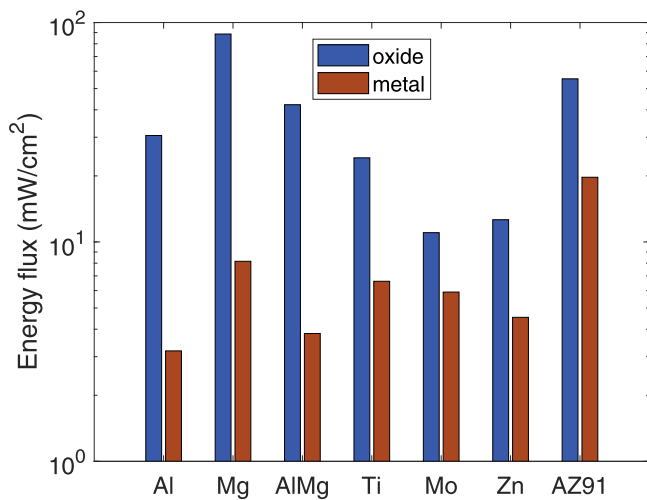


Figure 9. Sputtering of various oxidized materials with Ar in a 3 kV, 5 kHz and 15 μ s PIII pulse. The energy flux values at the end of the treatment (metal) are plotted in red to visualize the change in the energy flux.

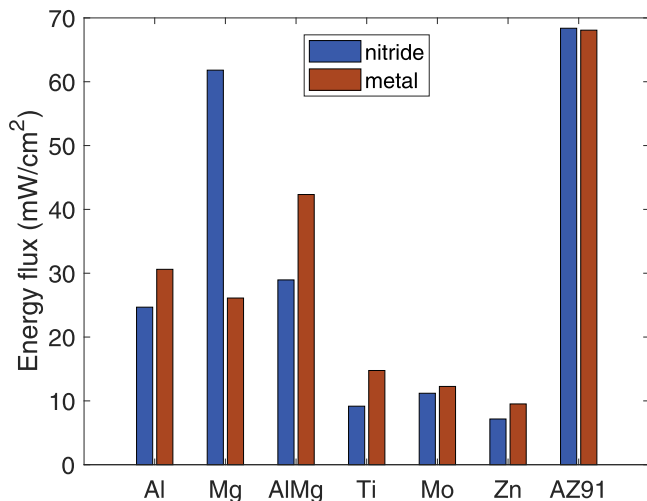


Figure 10. Nitriding of various materials with N₂ in a 3 kV, 5 kHz and 15 μ s PIII pulse. The energy flux values at the beginning of the treatment (metal) are plotted in blue to visualize the change in the energy flux.

The oxide at the beginning is consisting of uniformly sized, small crystallites scattered across the surface. With increasing sputter time, they are removed and a surface roughening due to the ion bombardment is observed. Indeed, the black oxide layer formed in the furnace exhibits a very weak adhesion so that upon handling the substrate, the oxide layer is flaking off.

For the alloy AlMg₃, a completely different effect is observed. The SEM images in figure 13 start after a 3rd oxidation (reoxidizing the surface after the 2nd sputter experiment used to obtain the data shown in figure 11), showing an inhomogeneous, non-continuous oxide layer which explains the reduced SEE compared to the 1st oxidation (using pristine, polished material as obtained from the supplier before any ion bombardment). While the oxide layer

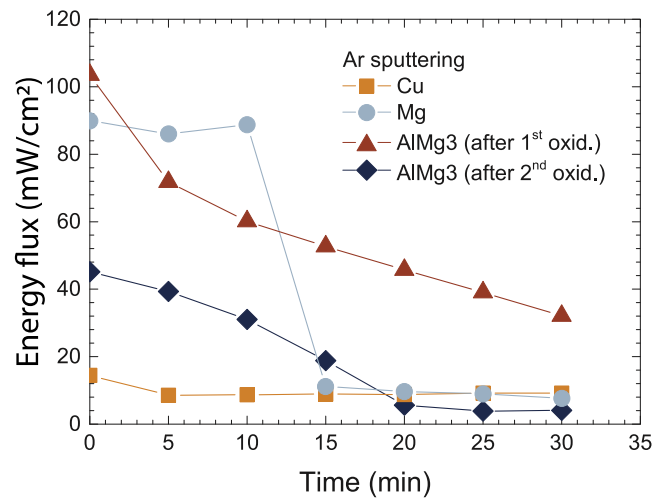


Figure 11. Comparison of time evolution for different Ar sputtering experiments.

with a varying thickness is subsequently removed, the surface is progressively roughening and developing a chemical segregation. This sputtering and oxidation procedure is creating some kind of feedback loop, thus, leading to the formation of a completely black metallic surface without any oxygen contamination at the end (excluding the native oxide formed spontaneously when venting the vacuum chamber at room temperature).

Perfect SEE measurements can be performed on such surfaces, with the oxidic and metallic states as the beginning and the end of the experiment. However, the reproducibility and comparability of such experiments appears to be far from ideal. Nevertheless, the surface state of targets in magnetron sputtering or HiPIMS experiments should experience a similar, convoluted history so that the assumption of SEE coefficients identical to those of virgin materials directly procured from a supplier should be equally questionable. A critical and comprehensive characterization of any surface where SEE coefficients are published should be included in such work.

Using the simple model introduced in the end of section 2, simplified time dependent secondary electron yields for the investigated materials have been calculated and can be seen in figure 14. It has to be noted that the influence of the displacement current is ignored and a perfect, directed emission of the secondary electrons normal to the surface is assumed. Both effects change the following values in opposite directions so that the presented values are only maximum estimates.

Taking a look at figure 14, a striking feature is obvious for materials with high γ_{SE} : especially for AZ91 and Mg, a steep decrease from high to low γ_{SE} is visible, indicating a rapid removal of the oxide layer within a few minutes of sputtering. This effect is also visible for Al, albeit not observed for AlMg₃. First, this indicates an extremely sharp interface between the oxide and the metal. Second, only here a clear distinction between oxide and metal is possible. For

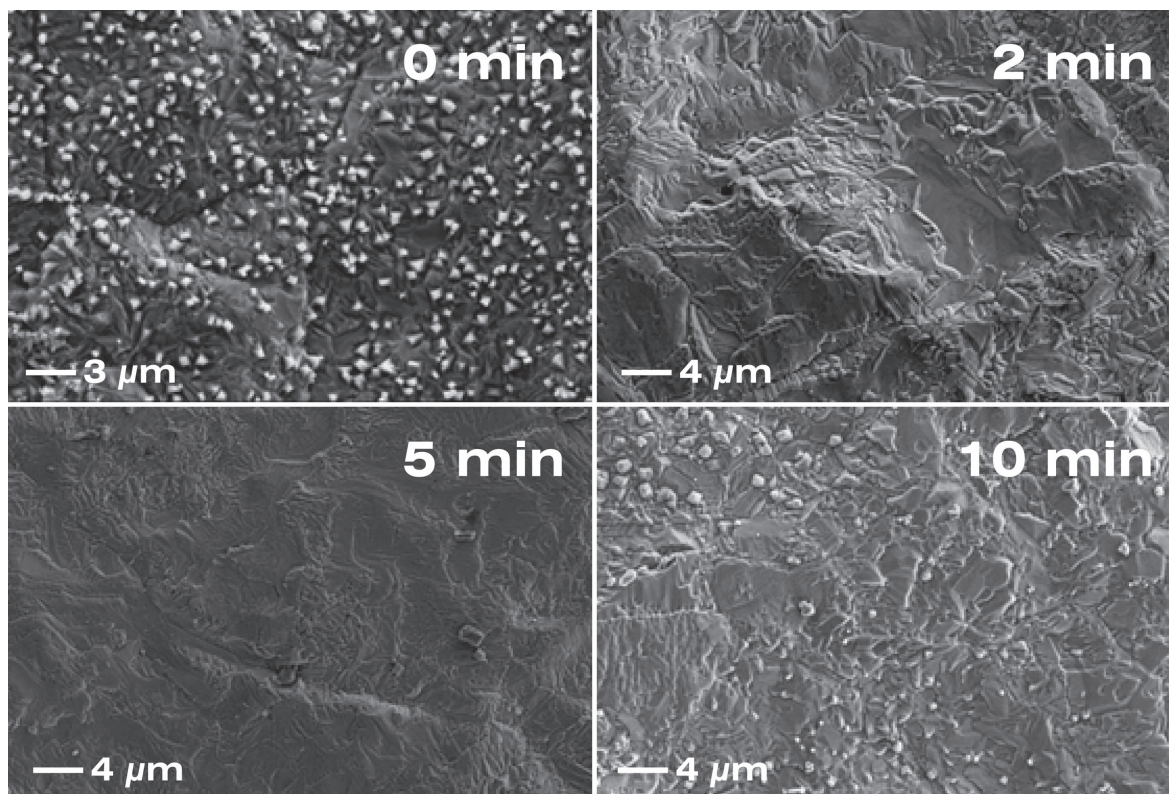


Figure 12. Time evolution of surface topography with sputter time. The white crystallites in panel (a) consist of copper oxide with the rest of the surface consisting of metallic copper.

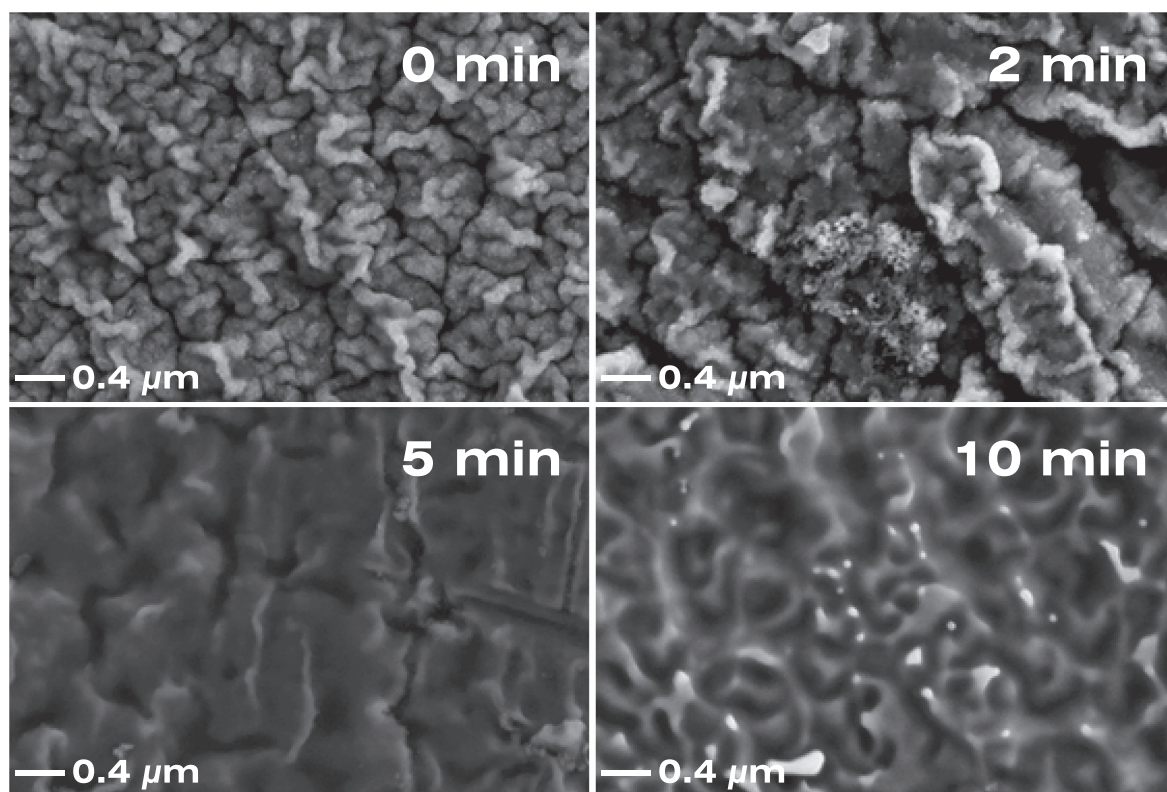


Figure 13. Surface topography of alloy AlMg3 changing with sputter time.

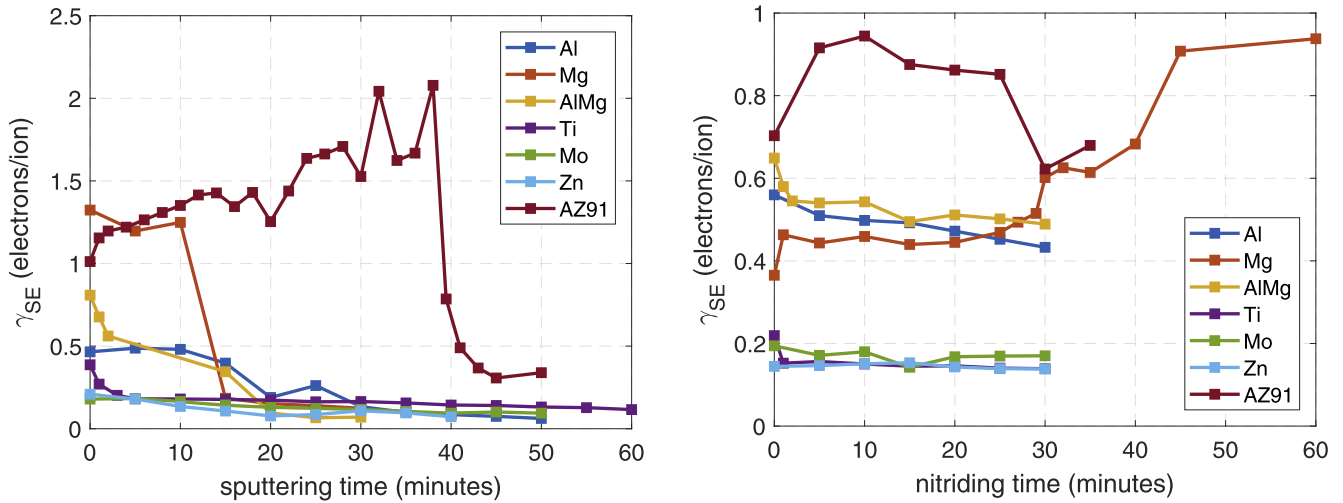


Figure 14. Calculated absolute secondary electron yield during sputtering of the oxide (left) and nitriding (right).

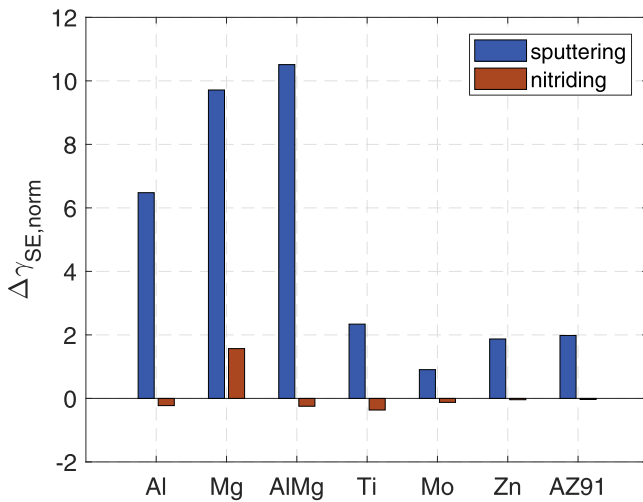


Figure 15. Normalized secondary electron yields of the investigated materials for argon and nitrogen ion bombardment.

smoother and more gradual transitions, the corresponding (partial) changes in the surface composition may lead to subliminal errors.

For better comparison, the calculated SEE yields have been normalized to their metallic values following

$$\Delta\gamma_{norm} = \frac{\gamma_{ox, nit} - \gamma_{met}}{\gamma_{met}}, \quad (4)$$

where $\gamma_{ox, nit}$ is the calculated value at the start of the sputtering phase, where the substrate is in its most oxidized state or at the end of the nitriding phase, respectively. The value for the metallic state of the substrate is given by γ_{met} . The normalized yields for the several materials are plotted in figure 15.

For all oxidized substrates, there is an increase in γ_{SE} for all materials present, whereas after the treatment with nitrogen, only Mg shows an increase in γ_{SE} . All other materials emit fewer secondary electrons when implanted with nitrogen compared to their pure metal state. This contradicts with the findings of Depla *et al* [36], where they saw an increase for Al in both cases but a decrease for Ti for an oxidized and nitrided

substrate. However, the work of Corbella *et al* [37] supports the results presented here, since they also see an increase of γ_{SE} for both Al and Ti in the case of an oxidized substrate surface.

However, it should be noted that comparison with other experiments performed by other groups is rather difficult due to the varying experimental setups and different operating regimes (e.g. pulse voltage). At the same time, a clear definition of the ‘metallic’ and ‘oxidic’ state has to be provided.

Before ending the discussion, some aspects of the ongoing quantification of energy flux into a value of secondary electrons per impinging ions will be mentioned. The transit of the high energy secondary electrons through the plasma towards the PTP is nearly collisionless as the initial acceleration to the 3 keV used in the present experiments occurs in the plasma sheath with a width of less than 1 cm. At the same time, the collision cross sections decrease considerably with increasing ion energy, however still depending on the gas species. The incident ion flux composition is well known and established from flux measurements including retained fluence, sputter yield and thermal balance of the substrate while the ion species composition for molecular gases is accessible from direct plasma measurements, e.g. employing a plasma monitor, without HV pulses. Using the current to the substrate for the short pulses with a fast rise time is actually not permissible as the value of the displacement current, needed for correction, is not accessible.

In a first approximation, the incident energy flux should scale inversely with the ratio of the probe distance to the center of the vacuum chamber and the radius of the substrate assuming a geometric relation for the flux of secondary electrons. However, here a pure perpendicular emission of the secondary electrons has been assumed, which does not correspond to the physical reality [39, 40]. On the other hand, a drastically changing angular emission distribution during the experiments is highly unlikely. Thus, only a correction factor—still to be determined—is necessary to account for the off-normal emission of some secondary electrons and the finite size of the PTP.

5. Conclusions

Using a calorimetric probe in a PIII system, it is possible to detect time dependent changes in the surface composition of the substrates during sputtering processes using argon and nitrogen plasma. The metallic and ‘poisoned’ states of the substrates have been observed as well as the evolution of the transition between them for seven different materials. Care has to be taken to identify the correct surface state corresponding to the actual measured secondary electron yield concerning chemistry and topography. Absolute quantification of the relative values is still in progress.

The advantages of the present method is (i) direct access to dynamic changes induced by the impinging ions or the plasma, (ii) no surface charging for insulating materials, (iii) no artefacts from other materials near the substrate, (iv) a fast measurement time with a time resolution of 1 min or even less, and (v) a large accessible energy range from 0.1 to 20 keV. Disadvantages of eventual loss of secondary electrons in the plasma, a mixture of molecular and atomic ions or the reduced acceptance angle are minor. Thus, the evaluated experimental setup is ideally suited for fundamental SEE measurements of materials prone to target poisoning or imprinting the history of target evolution. While relative measurements are immediately possible, the absolute quantification is still in progress.

Acknowledgments

This work was supported by Deutsche Forschungsgemeinschaft (Projects MA 2054/71-1 and KE 574/4-1). J Bauer (IOM) is acknowledged for the roughness measurements.

ORCID iDs

Fabian Haase  <https://orcid.org/0000-0002-6334-1414>

References

- [1] Anders A, Andersson J and Ehasarian A 2007 High power impulse magnetron sputtering: current–voltage–time characteristics indicate the onset of sustained self-sputtering *J. Appl. Phys.* **102** 113303
- [2] Lieberman M A and Lichtenberg A J 2005 *Principles of Plasma Discharges and Materials Processing* (Hoboken, NJ: Wiley)
- [3] Depla D and Mahieu S 2008 *Reactive Sputter Deposition* ed D Depla and S Mahieu vol 109 (Berlin: Springer)
- [4] Marcak A, Corbella C, de los Arcos T and von Keudell A 2015 Note: ion-induced secondary electron emission from oxidized metal surfaces measured in a particle beam reactor *Rev. Sci. Instrum.* **86** 106102
- [5] Baragiola R A, Alonso E V and Florio A O 1979 Electron emission from clean metal surfaces induced by low-energy light ions *Phys. Rev. B* **19** 121–9
- [6] Depla D, Heirwegh S, Mahieu S, Haemers J and De Gryse R 2007 Understanding the discharge voltage behavior during reactive sputtering of oxides *J. Appl. Phys.* **101** 13301
- [7] Böhm C and Perrin J 1993 Retarding field analyzer for measurements of ion energy distributions and secondary electron emission coefficients in low pressure radio frequency discharges *Rev. Sci. Instrum.* **31** 31–44
- [8] Anders A 2000 *Handbook of Plasma Immersion Ion Implantation and Deposition* (New York: Wiley)
- [9] Barradas N P, Maas A J H, Mändl S and Günzel R 1997 Alpha-elastic recoil detection analysis of the energy distribution of oxygen ions implanted into silicon with plasma immersion ion implantation *J. Appl. Phys.* **81** 6642
- [10] Nakamura K, Mändl S, Brutscher J, Günzel R and Möller W 1997 Incident ion monitoring during plasma immersion ion implantation by direct measurements of high-energy secondary electrons *Surf. Coat. Technol.* **93** 242–6
- [11] Bornholdt S, Itagaki N, Kuwahara K, Wulff H, Shiratani M and Kersten H 2013 Characterization of the energy flux toward the substrate during magnetron sputter deposition of ZnO thin films *Plasma Sources Sci. Technol.* **22** 25019
- [12] Hutchinson I H 2002 *Principles of Plasma Diagnostics* vol 44 (Cambridge: Cambridge University Press)
- [13] Bradley J W, Bäcker H, Aranda-Gonzalvo Y, Kelly P J and Arnell R D 2002 The distribution of ion energies at the substrate in an asymmetric bi-polar pulsed DC magnetron discharge *Plasma Sources Sci. Technol.* **11** 165
- [14] Thornton J A 1974 Influence of apparatus geometry and deposition conditions on the structure and topography of thick sputtered coatings *J. Vac. Sci. Technol.* **11** 666
- [15] Deutsch H, Kersten H and Rutscher A 1989 Basic mechanisms in plasma etching *Contrib. Plasma Phys.* **29** 263–84
- [16] Hussla I, Enke K, Grunwald H, Lorenz G and Stoll H 1987 *In situ* silicon-wafer temperature measurements during RF argon-ion plasma etching via fluoroptic thermometry *J. Phys. D: Appl. Phys.* **20** 889
- [17] Deutsch H, Kersten H, Klagge S and Rutscher A 1988 On the temperature dependence of plasma polymerization *Contrib. Plasma Phys.* **28** 149–55
- [18] Thornton J A 1978 Substrate heating in cylindrical magnetron sputtering sources *Thin Solid Films* **54** 23–31
- [19] Kersten H, Deutsch H, Steffen H, Kroesen G M W and Hippler R 2001 The energy balance at substrate surfaces during plasma processing *Vacuum* **63** 385–431
- [20] Kersten H, Rohde D, Berndt J, Deutsch H and Hippler R 2000 Investigations on the energy influx at plasma processes by means of a simple thermal probe *Thin Solid Films* **377–378** 585–91
- [21] Lundin D, Stahl M, Kersten H and Helmersson U 2009 Energy flux measurements in high power impulse magnetron sputtering *J. Phys. D: Appl. Phys.* **42** 185202
- [22] Cormier P A, Balhamri A, Thomann A L, Dussart R, Semmar N, Mathias J, Snyders R and Konstantinidis S 2013 Measuring the energy flux at the substrate position during magnetron sputter deposition processes *J. Appl. Phys.* **113** 13305
- [23] Welzel T, Kellermeier M, Harbauer K and Ellmer K 2013 Development of a compact combined plasma sensor for plasma surface engineering processes *Appl. Phys. Lett.* **102** 15–9
- [24] Cormier P A, Stahl M, Thomann A L, Dussart R, Wolter M, Semmar N, Mathias J and Kersten H 2010 On the measurement of energy fluxes in plasmas using a calorimetric probe and a thermopile sensor *J. Phys. D: Appl. Phys.* **43** 465201
- [25] Kersten H, Stoffels E, Stoffels W W, Otte M, Csambal C, Deutsch H and Hippler R 2000 Energy influx from an rf plasma to a substrate during plasma processing *J. Appl. Phys.* **87** 3637–45

- [26] Cormier P A, Balhamri A, Thomann A L, Dussart R, Semmar N, Lecas T, Snyders R and Konstantinidis S 2014 Titanium oxide thin film growth by magnetron sputtering: total energy flux and its relationship with the phase constitution *Surf. Coat. Technol.* **254** 291–7
- [27] Abadias G, Leroy W P, Mahieu S and Depla D 2013 Influence of particle and energy flux on stress and texture development in magnetron sputtered TiN films *J. Phys. D: Appl. Phys.* **46** 55301
- [28] Haase F, Lundin D, Bornholdt S and Kersten H 2015 On the impact of electron temperature in magnetron sputtering benchmarked with energy flux measurements *Contrib. Plasma Phys.* **55** 701–13
- [29] Čada M, Bradley J W, Clarke G C B and Kelly P J 2007 Measurement of energy transfer at an isolated substrate in a pulsed dc magnetron discharge *J. Appl. Phys.* **102** 63301
- [30] Gauter S, Fröhlich M, Garkas W, Polak M and Kersten H 2017 Calorimetric probe measurements for a high voltage pulsed substrate (PBII) in a HiPIMS process *Plasma Sources Sci. Technol.* **26** 65013
- [31] Haase F, Manova D, Mändl S and Kersten H 2016 Evidence of secondary electron emission during PIII pulses as measured by calorimetric probe *Eur. Phys. J. D* **70** 186
- [32] Rapakoulias D E and Gerassimou D E 1987 Simulation of energy transfer from a glow discharge to a solid surface *J. Appl. Phys.* **62** 402–8
- [33] Nimmagadda R and Bunshah R F 1971 Temperature and thickness distribution on the substrate during high-rate physical vapor deposition of materials *J. Vac. Sci. Technol.* **8** VM85–94
- [34] Mändl S and Rauschenbach B 2000 Anisotropic strain in nitrided austenitic stainless steel *J. Appl. Phys.* **88** 3323
- [35] Stahl M, Trottenberg T and Kersten H 2010 A calorimetric probe for plasma diagnostics *Rev. Sci. Instrum.* **81** 1–5
- [36] Depla D, Li X Y, Mahieu S and De Gryse R 2008 Determination of the effective electron emission yields of compound materials *J. Phys. D: Appl. Phys.* **41** 202003
- [37] Corbella C, Marcak A, de los Arcos T and von Keudell A 2016 Revising secondary electron yields of ion-sputtered metal oxides *J. Phys. D: Appl. Phys.* **49** 16LT01
- [38] Corbella C, Marcak A, von Keudell A and de los Arcos T 2017 Electric potential screening on metal targets submitted to reactive sputtering *J. Vac. Sci. Technol. A* **35** 21307
- [39] Nickles N, Davies R E and Dennison J R 2000 Applications of secondary electron energy- and angular-distributions to spacecraft charging *Proc. 6th Spacecraft Charging Technology Conf.* pp 275–80
- [40] Willis R F, Fitton B and Painter G S 1974 Secondary-electron emission spectroscopy and the observation of high-energy excited states in graphite: theory and experiment *Phys. Rev. B* **9** 1926–37

Publication III

Plasma characterization in reactive sputtering processes of Ti in Ar/O₂ mixtures operated in metal, transition and poisoned modes: a comparison between direct current and high-power impulse magnetron discharges

Authors: F. Haase, H. Kersten, and D. Lundin

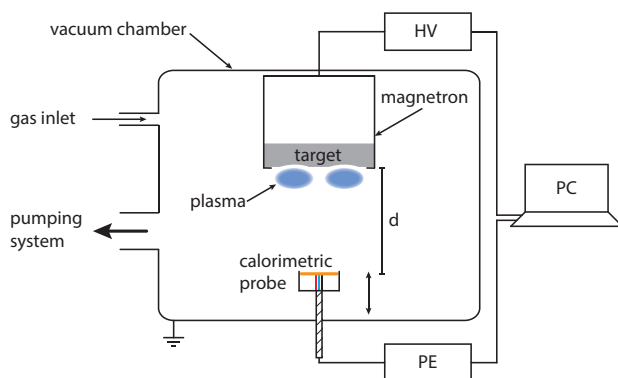
Journal: The European Physical Journal D

Technique: DC and High-power impulse magnetron sputtering (HiPIMS)

Utilized Probes: Passive thermal probe (PTP), Quartz crystal microbalance (QCM),
Langmuir probe

Own contribution: approx. 50%

Experimental Setup:



Motivation:

This publication aimed towards a comparison of reactive sputtering of titanium between common direct current magnetron sputtering (DCMS) and high-power impulse magnetron sputtering (HiPIMS). The goal was to investigate the energy flux in the different target surface states (metallic, transition, poisoned) dependent on the reactive gas admixture (O₂) using either DCMS or HiPIMS, respectively.

Main results:

The results show a generally higher energy flux for HiPIMS. In pure Ar, the energy flux was about 1.48 times higher for HiPIMS than for DCMS, but this ratio gradually decreased with increasing oxygen gas flow to about 1.26 in the poisoned mode. A large reduction of deposition rate was observed for both DCMS and HiPIMS (factor 10 vs 14) when transiting from the metal to the poisoned mode. However, this was not accompanied by a significant change in the energy flux for DCMS but a slight decrease for HiPIMS (<20%) was visible. This effect was attributed to the increasing effective electron temperature.

Plasma characterization in reactive sputtering processes of Ti in Ar/O₂ mixtures operated in metal, transition and poisoned modes: a comparison between direct current and high-power impulse magnetron discharges

Fabian Haase^{1,a}, Holger Kersten¹, and Daniel Lundin^{1,2}

¹ Institute of Experimental and Applied Physics, Kiel University, Leibnizstrasse 11-19, 24098 Kiel, Germany

² Laboratoire de Physique des Gaz et des Plasmas – LPGP, UMR 8578, CNRS – Université Paris-Sud, 91405 Orsay, France

Received 15 February 2017 / Received in final form 20 April 2017

Published online 3 October 2017 – © EDP Sciences, Società Italiana di Fisica, Springer-Verlag 2017

Abstract. Two reactive sputtering techniques have been studied: direct current magnetron sputtering (DCMS) and high-power impulse magnetron sputtering (HiPIMS), operated in various Ar/O₂ gas mixtures using a Ti target. The processes were characterized during different modes of operation including pure argon, metallic, transition and compound mode. Energy flux data as well as data on electron density and temperature were combined to obtain knowledge about the trends and changes in the investigated internal process plasma properties for the different modes investigated. Although there is a large reduction of the mass deposition rate (a factor 10 in DCMS and a factor 14 in HiPIMS), when transiting from the metal to compound mode, we detect no significant decrease of the total energy flux in DCMS and only a minor decrease in HiPIMS (<20%). Such a result is surprising considering that the neutral flux contribution to the total energy flux is known to be significant. Instead, we find that the reduction of the neutral component is compensated by an increase in the electron and ion flux components, which is experimentally detected as an increase of the effective electron temperature and a slightly increasing (DCMS) or essentially constant (HiPIMS) electron density with increasing oxygen flow rate.

1 Introduction

Deposition of thin films by physical vapor deposition (PVD) techniques, such as magnetron sputtering, is today employed for a wide range of applications within many industrial sectors. Direct current magnetron sputtering (DCMS) is a common method, although various ionized physical vapor deposition (IPVD) methods [1], such as high-power impulse magnetron sputtering (HiPIMS) [2,3], have shown great promise, due to the possibility to ionize a substantial fraction of the sputtered material. An ionized deposition flux can, unlike neutrals, be accelerated by applying a substrate bias, which has opened up new ways to engineer thin films with improved properties [3]. In general, these techniques allow the deposition of metals, alloys, ceramic, and polymer thin films onto various substrate materials. A large fraction of these coatings are compound films consisting of at least one metal (e.g. Al, Ti) or a non-metal (e.g. C, B) and a reactive gas (e.g. O₂, N₂). The deposition of these thin films by reactive magnetron sputtering is an intensively studied field during the last three decades [4].

However, the addition of a reactive gas raises the question of changes in the plasma chemistry and the internal plasma parameters. For example, variations in density and energy of the electron, ion, and neutral populations affect the energetic material flux to the substrate, which in turn determine elementary processes like adsorption, diffusion and chemical reactions, as well as microstructure and stoichiometry during film growth [5,6]. It is well known that the momentum per incoming particle and the particle flux can greatly affect the intracolumnar as well as intercolumnar porosity of thin films [7].

So far, few reports devoted to experimentally investigating the internal process plasma parameters in reactive magnetron sputtering exist [8–11], although it is known that there are significant changes in the secondary electron emission yield [12], the sputter yields [13], ion flux composition [8], and electron density n_e and temperature T_e [10] when sputtering from a clean and poisoned (compound) target, respectively. In particular, there are, to our knowledge, no systematic studies on the energy flux for the different modes of operation: metallic, transition, and compound mode in reactive HiPIMS, although such investigations have been carried out in the non-reactive case for DCMS [14,15] as well as for HiPIMS [15,16]. Experimental investigations of the energy flux in reactive DCMS

^a e-mail: phaase@physik.uni-kiel.de

have been carried out by Thomann et al. [17] sputtering Al in Ar/O₂. They focused on coupling the energy flux with the properties of the deposited film. However, plasma properties, such as electron density and temperature, were not investigated. In addition, Bornholdt et al. [18,19] have characterized the energy flux in radio-frequency (rf) magnetron discharges operated in Ar/N₂ and Ar/O₂ reactive gas mixtures. Those discharges were, strictly speaking, not pure reactive magnetron sputtering discharges, since compound targets (h-BN and ZnO targets, respectively) were used.

Due to the strong interest in energetic bombardment of the growing film, we have therefore studied the process plasma during HiPIMS deposition of TiO_x using a Ti target in various Ar/O₂ mixtures, which is a promising method to deposit crystalline TiO₂ thin films [20,21]. For comparison, we also carried out the same type of characterization in DCMS under equivalent deposition conditions. The processes were characterized in pure argon as well as metallic, transition and compound modes. Energy flux, measured by a passive thermal probe (PTP), deposition rate, measured by a quartz crystal microbalance (QCM), as well as electron density and temperature, measured by a Langmuir probe, were combined to obtain knowledge about the trends and changes in the investigated internal process plasma properties for the different reactive modes investigated.

2 Experimental setup

2.1 Deposition system

A standard planar circular magnetron with a target diameter of 0.05 m (2 in.), equipped with a Ti (99.9%) target mounted in a cylindrical vacuum chamber (height 0.50 m, diameter 0.45 m) was used in the present work, see Figure 1. The chamber was pumped by a two stage pumping system (turbo-molecular pump and membrane pump) to a residual pressure $< 2 \times 10^{-6}$ Torr (2.7×10^{-4} Pa), after which the working gas (Ar (N5)) was let into the chamber at a constant mass flow rate of 7.80 sccm. The argon pressure was set to 7.5 mTorr (1.0 Pa). Oxygen (99.995% purity) was fed into the chamber at various mass flow rates through the same gas inlet as for the Ar. The oxygen flow rate was varied in the range 0.0–2.0 sccm. The magnetron was either operated in DCMS mode or in HiPIMS mode. In both cases, a constant discharge power of 50 W (2.5 W/cm^2 , calculated using the entire target area) was applied to the sputter target. The DC discharge was generated by an MDX 500 power supply (Advanced Energy, USA), and the discharge current and voltage characteristics of the magnetron were recorded on the unit's display. The voltage and current values varied depending on O₂ flow rate. At 0 sccm O₂ the recorded DC voltage and current were 390 V and 0.130 A, respectively. With increasing O₂ flow rate, the voltage gradually increased to about 470–480 V and the current gradually decreased to 0.107 A at 2.0 sccm O₂.

For the HiPIMS mode, the DC power supply was connected to a HiPSTER 1 HiPIMS pulser (Ionautics AB,

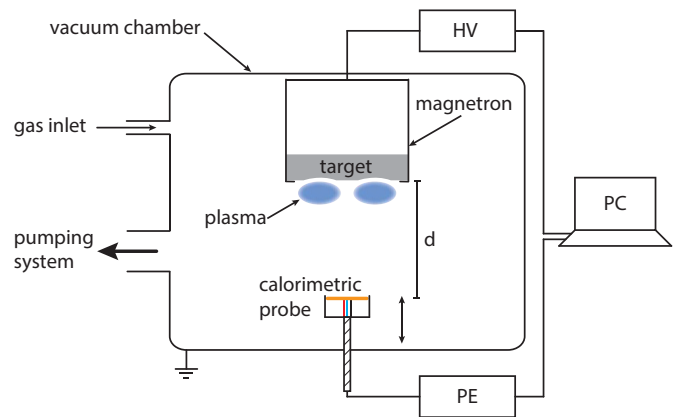


Fig. 1. Schematic of the cylindrical deposition chamber used in the experiments, displaying the cathode mounted in the lid of the chamber (top) and the calorimetric probe head placed below at a typical distance of $d = 0.04$ m from the target surface. HV denotes the computer-controlled high voltage power supply (DCMS or HiPIMS). PE denotes the probe electronics, which was also computer controlled. Note that the different objects are not drawn to scale.

Sweden). In this case, $35 \mu\text{s}$ square voltage pulses were applied to the cathode at a pulse frequency of 500 Hz. Typical discharge voltage and current waveforms are shown in Figure 2. Operating in pure Ar gas resulted in peak currents of about 7 A, which correspond to a peak current density over the target of 0.35 A/cm^2 . Operating in an Ar/O₂ mixture increased the peak current to about 13 A for 2.0 sccm O₂, which correspond to a peak current density of 0.65 A/cm^2 . We note that the HiPIMS discharge current becomes distinctly triangular with increasing O₂ flow, which has also been reported in other works [22] and is discussed in more detail elsewhere [23].

2.2 Plasma probes

The passive thermal probe (PTP), or sometimes referred to as a calorimetric probe [24,25], consists of a sensor plate (Cu) with a diameter of 2 cm and a type K thermocouple, which is spot welded to the back of a $100 \mu\text{m}$ thick sensor plate. An additional copper wire, which is also spot welded to the back of the sensor plate, allows for biasing and current measurements. The entire device is shielded by a ceramic housing (Macor) to make sure we solely detect the energy influx that is reaching the front of the sensor plate. A schematic view is presented in Figure 3. Detailed information on the probe design is given by Stahl et al. [25]. A description on the PTP data evaluation is provided by Gauter et al. [26]. The probe was mounted on a rod at a distance of 4 cm below the center of the target surface. For every parameter set we recorded a heating (plasma on) and cooling curve (plasma off) to determine the energy flux onto the probe.

For detailed investigations of the contributions of the different species present in the plasma, time-averaged Langmuir probe measurements were performed at the same location. A cylindrical probe consisting of a tungsten wire ($100 \mu\text{m}$ in diameter) surrounded by a ceramic

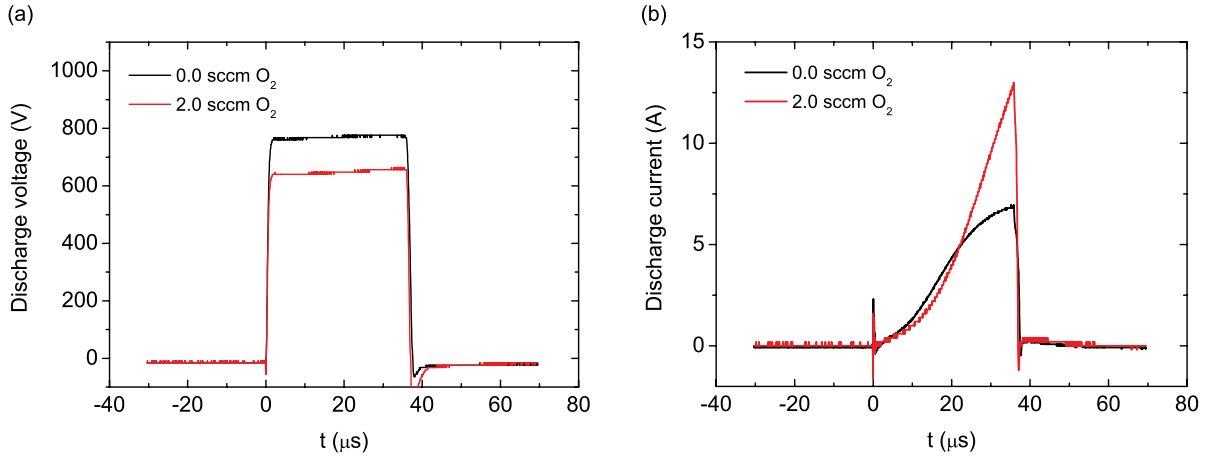


Fig. 2. Experimental (a) discharge voltage and (b) current characteristics recorded at 1.0 Pa Ar pressure for 0.0 and 2.0 sccm O_2 gas flows, using $35 \mu s$ long HiPIMS discharge pulses at 500 Hz. The average power was kept constant at 50 W.

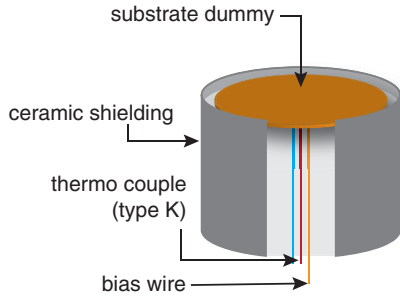


Fig. 3. Schematic of the thermal probe used in the experiments.

tube with an exposed wire area (probe tip) of about $9.4 \times 10^{-7} \text{ m}^2$ was used to record the I - V characteristics of the plasma. The electron temperature T_e was obtained from a semi-logarithmic plot of the probe current versus the probe bias using

$$\ln \left(\frac{I_e}{I_{e0}} \right) = \frac{eV_{\text{probe}}}{k_B T_e},$$

where I_e is the measured electron current and I_{e0} the electron saturation current [27]. Using the electron temperature and the ion saturation current the plasma density n_e was calculated. For our measurements, we assumed a Maxwellian electron energy distribution, which has been shown to be valid for low pressure DCMS processes around 1 Pa [28], and also verified in one of our previous works [29]. In the HiPIMS case, the Langmuir probe curves were recorded in the same manner as in DCMS, i.e. time-averaged data acquisition. It means that each data point on the probe characteristics constitute an average over typically a few hundred HiPIMS discharge pulses. The time-averaged values were required in order to compare with the time-averaged output from the PTP.

In order to study the deposition rate versus O_2 flow rate, a quartz crystal microbalance (QCM) system (Intelmetrics Global Ltd, UK) was installed at the same distance to the target as the PTP. The mass flow rate converted to

mass deposition rate was recorded when stepwise increasing the O_2 flow rate from 0.0 to 2.0 sccm and successively decreasing again to 0.0 sccm. The deposition rate was also used to calculate the energy flux contributions of neutrals to the surface as well as film condensation that dissipates energy on the substrate using

$$J_n = \frac{\rho_{\text{TiO}_x} R}{m_{\text{TiO}_x}} \bar{E}_{\text{kin}} \quad \text{and} \quad J_{\text{cond}} = \frac{\rho_{\text{TiO}_x} R}{m_{\text{TiO}_x}} E_{\text{bind}},$$

respectively. Here ρ_{TiO_x} is the mass density and m_{TiO_x} the mass of the film forming species, which depend on the oxygen flow rate (mode of operation). R is the deposition rate, \bar{E}_{kin} the averaged kinetic energy of the sputtered neutrals (obtained from SRIM calculations) hitting the probe, and E_{bind} the binding energy.

3 Results and discussion

3.1 Hysteresis study

It is well known that for low O_2 flow rates, in the metal mode, the reactive TiO_x deposition process is characterized by a high mass deposition rate and low O_2 partial pressure resulting in a substoichiometric composition of the deposited coating [30]. With increasing O_2 flow rate, a transition from the high rate metal mode to the poisoned (compound) mode, with substantially lower mass deposition rate, occurs. In the poisoned mode, the target surface is covered by a compound layer (target poisoning), and it remains in the poisoned state until the oxygen flow is sufficiently reduced. This transition, from metal mode to compound mode for the two different magnetron discharges, was studied using the QCM, and the mass deposition rates are shown in Figure 4. The recorded deposition rate versus O_2 flow rate values also allow us to identify the different modes of operation, which are indicated by vertical lines in the same figure. The required O_2 flow rates for these modes have also been summarized in Table 1. From hereon we use the name of the

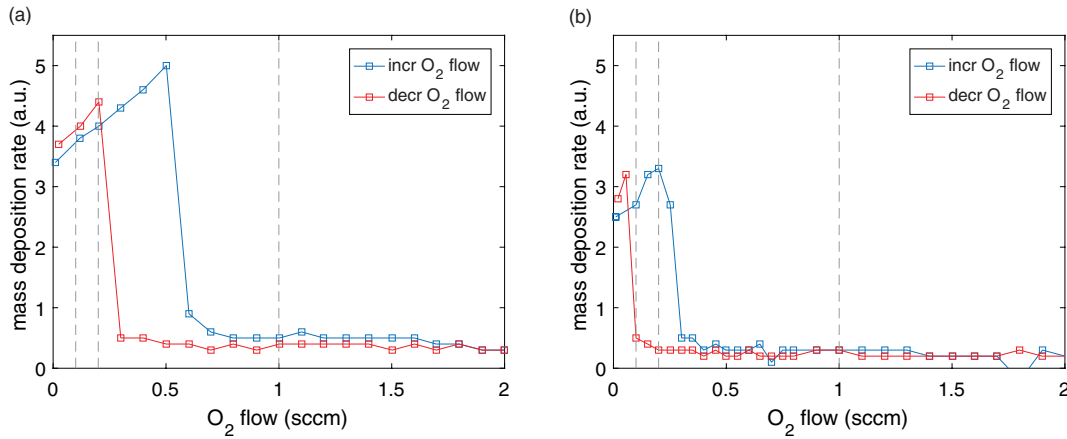


Fig. 4. Deposition rate as a function of O_2 gas flow for (a) DCMS discharges and (b) HiPIMS discharges operated at an average power of 50 W. Vertical lines indicate the chosen process points of interest for the metal, transition, and poisoned modes, which are defined in Table 1.

Table 1. Identified O_2 gas flow rates in sccm for the different operating regimes in the reactive magnetron discharges investigated: metal mode, transition mode, and poisoned (compound) mode. Please note that two different process points in the poisoned regime were selected.

Discharge	Pure Ar	Metal mode	Transition mode	Poisoned mode 1	Poisoned mode 2
DCMS	0	0.11	0.2	1.0	2.0
HiPIMS	0	0.11	0.2	1.0	2.0

mode of operation and the corresponding O_2 flow rate interchangeably.

Note that there is commonly a hysteresis observed in the process parameters (i.e. target voltage, deposition rate, and reactive gas partial pressure) in reactive sputtering [31], which makes it difficult to operate the process in the desired transition region, where stoichiometric coatings at high deposition rates can be obtained. We also observe a hysteresis in the measured deposition rate, see Figure 4, although it is somewhat reduced in the HiPIMS case. For the DCMS case, it was difficult to record repeatable and consistent values for the energy flux when operating inside the transition region. A slightly lower flow rate (0.2 sccm) for the transition region had to be chosen as indicated by the second vertical dashed line in Figure 4a. This was not an issue in the HiPIMS case.

Lundin et al. [11] have previously reported on a hysteresis-free TiO_x HiPIMS process, where it was possible to reach stable operating points also in the transition region. We note that, although the magnetron size and the process gas pressure were almost the same as in the present case, the pulse peak currents achieved here were smaller compared to [11]. In addition, Kubart et al. [32] did experience hysteresis during TiO_2 deposition for different HiPIMS pulsing frequencies. We therefore agree with the conclusion of Aiempnakit et al. [33] that reduction/elimination of hysteresis in reactive HiPIMS is likely system dependent and governed by the process conditions, such as target size, pumping speed, gas pressure, and HiPIMS pulse characteristics.

From the QCM measurements we also find that the mass deposition rate changes by a factor 14 between

the metal mode and the poisoned mode in HiPIMS. For DCMS there is a reduction of a factor 10. However, unlike previous reports of strong reduction in the deposition rate in HiPIMS compared to DCMS when depositing pure metal coatings [34], we here find a rate difference between HiPIMS and DCMS of about 0.75 in pure Ar. This is a considerably higher value compared to $rate_{HiPIMS}/rate_{DCMS} \approx 0.30$ reported by Samuelsson et al. [34]. Mishra et al. [35] reported a six fold increase in the deposition rate of Ti for HiPIMS by weakening the B-field of the magnetron by up to 33%. It is likely that the main reason for the increased $rate_{HiPIMS}/rate_{DCMS}$ in our study is due to the magnetic field strength and configuration of the magnetron. Further investigations of this topic are beyond the scope of the present work.

3.2 Energy flux

The total energy flux J_{tot} for the identified modes of operation for increasing O_2 flow rate in DCMS and HiPIMS are shown in Figure 5. The overall trend is that the HiPIMS discharge generates a more energetic flux with values around $J_{tot} = 150\text{--}180\text{ mW/cm}^2$ as compared to the DCMS discharge with $J_{tot} = 115\text{--}125\text{ mW/cm}^2$. Both Lundin et al. [16] and West et al. [36] have previously reported a lower total energy flux in HiPIMS compared to DCMS when running in pure Ar at the same average power. However, the main reason was found to be a substantially lower deposition rate in HiPIMS, which is not the case in the present work, see also Section 3.1. In addition, for a rotating cylindrical magnetron sputtering discharge with a Ti target in Ar, Leroy et al. [37]

find that the total energy flux arriving at the substrate is slightly lower for HiPIMS than for DCMS for the same average power. We therefore conclude that $J_{\text{tot,HiPIMS}}/J_{\text{tot,DCMS}} \approx 1.48$, found in the present work in pure Ar, is likely a result of more energy per deposited particle in HiPIMS, as previously reported [16], in combination with a relatively high deposition rate for this discharge configuration, as discussed in Section 3.1.

Looking closer at the energy flux results for the HiPIMS discharges, we also find that $J_{\text{tot,HiPIMS}}$ decreases as the O_2 flow rate increases and the discharge switches from metallic mode to poisoned mode. Bornhold et al. [18] reported an opposite trend when depositing c-BN using an addition of O_2 gas to the conventional Ar/ N_2 mixture in rf magnetron sputtering. In their case the energy influx increased from about 60 mW/cm^2 to 90 mW/cm^2 as the O_2 flow rate increased from 0 sccm to 20 sccm. Due to the differences in material system and operating conditions, it is, however, difficult to make any direct comparisons with our results. For the present HiPIMS experiment, the decrease in energy flux is rather limited, less than 20%. We believe that the main reason for this behavior is the reduction of the deposition rate seen in Figure 4b, which reduces the energy flux by neutrals J_n . However, looking only at the mass deposition rate, one would expect a much stronger and more abrupt reduction in the energy flux with increasing O_2 flow rate (see also Sect. 3.1). This effect is either minor or compensated by an increase of energy flux by some other contribution(s). On the other hand, it is known that the neutral flux contribution can carry a significant part of the total energy flux in at least non-reactive magnetron discharges [16], sometimes even the dominating part [29]. Instead, based on recent modeling of HiPIMS TiO_x processes by Gudmundsson et al. [23] and Lundin et al. [38], we suggest that there is an increase of the energy flux by ions J_i and by electrons J_e , when the discharge is operated in the poisoned mode. The reason is that recycling of mainly Ar^+ -ions (ions impinging on the cathode and then returning to the plasma volume and becoming ionized again) has been found to dominate the discharge current in this mode [23]. The recycling leads to increased discharge currents in the poisoned mode, which we also observe in Figure 2b, as well as increased ionic densities [23]. One indication of such process gas recycling is an increase of the electron temperature T_e . We therefore carried out Langmuir probe measurements at the same location as the thermal probe. T_e was indeed found to increase from about 0.8 eV to about 1.7 eV as the O_2 flow was varied from 0.0 sccm to 2.0 sccm, whereas the time-averaged n_e did not exhibit any significant change. These results are also in line with results from Čada et al. [39], who carried out time-resolved Langmuir probe measurements during the HiPIMS discharge pulse in TiO_x processes at the same distance from the target and using the same target size as in the present investigation. We therefore conclude that the increase in T_e will likely increase J_e , since $J_e = 2 \frac{j_e}{e_0} k_B T_e$, where j_e is the electron current and k_B the Boltzmann constant. Indeed, by calculating the electron contribution to the total energy flux, we find that J_e/J_{sum} increases from about 10% in pure Ar to 18% in the poisoned mode. J_{sum}

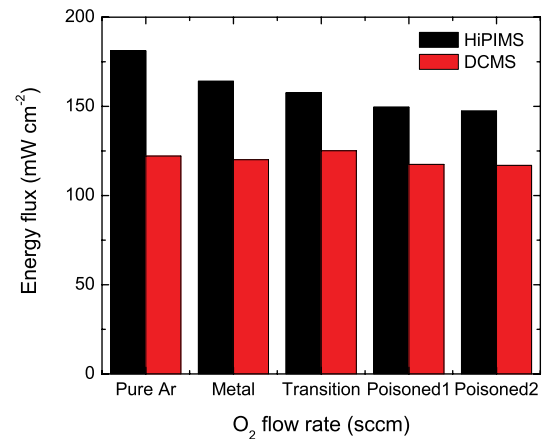


Fig. 5. The total energy flux measured at 4 cm from the target with the probe facing the target surface. The energy flux was measured for increasing O_2 flow rate at the chosen process points of interest for the pure Ar, metal, transition, and poisoned modes, which are defined in Table 1.

is the calculated total contributions to the energy influx from electrons, ions, sputtered neutrals, film condensation, and recombination of electrons and ions at the probe surface, discussed elsewhere [29]. It also supports the idea of an increased J_i , since $J_i = \frac{j_i}{e_0} (\Phi_{\text{pl}} - V_{\text{probe}})$, where j_i is the ion saturation current described by the Bohm flux and thereby proportional to $\sqrt{T_e}$. $(\Phi_{\text{pl}} - V_{\text{probe}})$ is the potential drop between the plasma and probe potential. We find that the calculated ion contribution, J_i/J_{sum} , increases from about 24% in pure Ar to 38% in the poisoned mode.

It should be noted that we did not include any contribution from negative ions in our calculations above, such as O^- created at the target surface. Typically 90% of the negative ions are created by volume reactions and therefore not accelerated over the cathode potential to high energies [40]. Modeling of the TiO_x system in HiPIMS has shown peak densities of O^- of less than 10^{15} m^{-3} [23]. If 10% are high-energy ions then we can assume densities on the order of 10^{14} m^{-3} , i.e. well below typical particle densities of Ar (10^{19} – 10^{20} m^{-3}), Ti (10^{17} – 10^{18} m^{-3}), or O_2 (10^{18} m^{-3}) for the same discharge conditions [23].

We now turn to the $J_{\text{tot,DCMS}}$ results in Figure 5. What is striking here is that $J_{\text{tot,DCMS}}$ does not change significantly although the mass deposition rate is found to substantially decrease (Fig. 4a). Thomann et al. [17] show a decrease of the total energy flux in DCMS when sputtering Al in Ar/ O_2 for increasing O_2 flow rates by more than 30% (between metal mode and poisoned mode). In addition, they report a strong increase in the energy flux around the transition, where the energy flux exhibits a 100% increase as compared to the poisoned mode. Thus, their results are clearly very different from what is reported here. In addition, Mahieu and Depla [41] investigated reactive sputter deposition of TiN by DCMS, and calculated the energy flux with increasing N_2 flow rate. They found that the energy flux per incoming metal particle increased with increasing N_2 flow rate. For this nitride there is, however, not a strong reduction in the deposition rate when transiting into the poisoned mode. Our

own investigations of TiN (not shown) shows a decrease of the mass deposition rate by a factor 2 with increasing N_2 flow (compared to our finding of a factor 10 in DCMS and a factor 14 in HiPIMS for the TiO_x system). Direct comparisons are therefore difficult, in particular, since no measurements were carried out to benchmark the calculations in [41].

Unfortunately, no plasma process modeling of the TiO_x reactive process in DCMS has been performed. It should also be noted that the discharge current decreases with increasing O_2 flow rate, in contrast to the HiPIMS case, see Section 2.1. The reason for the discharge current decrease is claimed to be a reduction of the effective secondary electron yield as the target becomes oxidized. Depla et al. [42] have estimated the Ar^+ induced effective secondary electron yield in a DC discharge with a Ti target to $\gamma_{Ti,metal} = 0.114$ and $\gamma_{Ti,poisoned} = 0.080$ for the metal and the poisoned modes, respectively. Since we are running at a fixed discharge power, we also observe an increase in the DC discharge voltage with increasing O_2 flow rate from about -390 V to -480 V, see also Section 2.1. An increase of 90 V means that the secondary electrons are more energized in the poisoned mode, independent of whether these electrons are accelerated in the cathode sheath or by Ohmic heating in the near-cathode region [43]. Such an increase in energy, results in increased probability for electron impact ionization of the process gas, which is mainly Ar in the present case, $e + Ar \rightarrow Ar^+ + 2e$. This process also generates new electrons, which can continue the ionization sequence. From our Langmuir probe measurements we find that the electron density n_e increases in the DCMS case from about $1.8 \times 10^{15} \text{ m}^{-3}$ at 0.0 sccm O_2 to $7.0 \times 10^{15} \text{ m}^{-3}$ at 2.0 sccm O_2 , i.e. by almost a factor 4, which we attribute to the above increased electron impact ionization. Further evidence of increased electron energization with increasing O_2 flow rate is found when measuring T_e , which is found to increase from about 1.3 eV to 3.3 eV when transiting from the metal mode to the poisoned mode. Also Petrov et al. [8] found an increase of T_e , when carrying out Langmuir probe measurements in reactive DCMS in Ar/ N_2 with a Ti target. Calculating the electron contribution to the total energy flux, we find that J_e/J_{sum} increases from about 8% in pure Ar to 19% in the poisoned mode. For the ion contribution, it is found that J_i/J_{sum} increases from about 20% in pure Ar to 38% in the poisoned mode. Our overall conclusion for $J_{tot,DCMS}$ is therefore that the strong drop in sputtered particles and thereby deposition rate, as the target becomes oxidized, is compensated by an increase in J_e , which is also supported by our Langmuir probe measurements. Furthermore, the observed increase in T_e and n_e also suggests an increase in J_i , since the ions are assumed to arrive at the probe with the Bohm flux, which is directly proportional to $n_e\sqrt{T_e}$ [18]. In the present setup and for the above given discharge conditions, we believe that J_n and $J_i + J_e$ cancel each other out and thereby $J_{tot,DCMS}$ remains unchanged as the O_2 flow rate increases.

Finally we would like to add a comment on the possibility of using the PTP for reactive process control, since

there is currently a strong interest in this topic, in particular for HiPIMS [11,44]. By reactive process control, we here refer to a technique, which allows the user to identify/characterize the transition from metal mode to compound mode, and use that input as some type of feedback for stable operation in the transition region over long periods of time. From the results presented in Figure 5, we conclude that only minor changes in the energy flux can be detected at best, when such a transition occurs. We are also concerned about the long-term stability of the probe in such an environment, since a significantly coated probe head will have a different heat capacity as compared to the clean Cu sensor plate. We therefore conclude that although it is possible to record the energy influx, the PTP is not a suitable tool for identifying the operating regime during a reactive deposition process.

4 Conclusions

Reactive DCMS and HiPIMS processes using a Ti target in various Ar/ O_2 mixtures were characterized during different modes of operation including pure argon, metallic, transition and compound mode. The energy flux was generally higher in the HiPIMS case with values around $J_{tot} = 150\text{--}180 \text{ mW/cm}^2$ as compared to the DCMS discharge with $J_{tot} = 115\text{--}125 \text{ mW/cm}^2$. In pure Ar $J_{tot,HiPIMS}/J_{tot,DCMS} \approx 1.48$, but the ratio gradually decreased with increasing O_2 flow rate and reached $J_{tot,HiPIMS}/J_{tot,DCMS} \approx 1.26$ in the compound mode. Although there is a large reduction of the mass deposition rate (a factor 10 in DCMS and a factor 14 in HiPIMS), when transiting from the metal to compound mode, we detect no significant decrease of the total energy flux in DCMS and only a minor decrease in HiPIMS ($<20\%$). We find that the reduction of the neutral component is compensated by an increase in the electron and ion flux components, which is experimentally detected as an increase of the effective electron temperature of at least a factor 2, and a slightly increasing (DCMS) or essentially constant (HiPIMS) electron density with increasing oxygen flow rate.

This work was supported by the Deutsche Forschungsgemeinschaft under SFBTR24/B13 and the French National Center for Scientific Research (CNRS). D.L. gratefully acknowledges the hospitality of Kiel University (CAU), Germany, where most if this study was conducted.

Author contribution statement

D.L. planned the study. F.H. and D.L. carried out the experiments. Data analysis and interpretation were jointly performed by all the authors. D.L. wrote the manuscript. All the authors contributed to the discussion of the results and reviewed the manuscript.

References

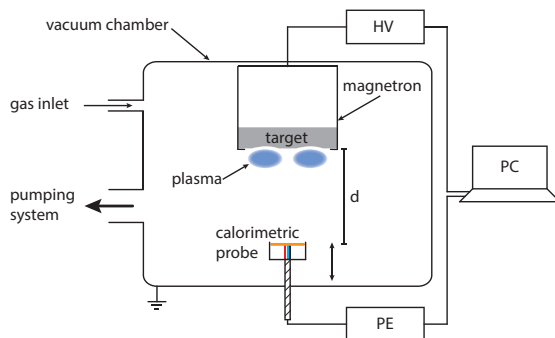
1. U. Helmersson, M. Lattemann, J. Bohlmark, A.P. Ehi-asarian, J.T. Gudmundsson, *Thin Solid Films* **513**, 1 (2006)
2. J.T. Gudmundsson, N. Brenning, D. Lundin, U. Helmersson, *J. Vac. Sci. Technol. A: Vac. Surf. Films* **30**, 30801 (2012)
3. D. Lundin, K. Sarakinos, *J. Mater. Res.* **27**, 780 (2012)
4. J. Musil, P. Baroch, J. Vlcek, K.H. Nam, J.G. Han, *Thin Solid Films* **475**, 208 (2005)
5. J.A. Thornton, *J. Vac. Sci. Technol.* **11**, 666 (1974)
6. H. Kersten, H. Deutsch, H. Steffen, G.M.W. Kroesen, R. Hippler, *Vacuum* **63**, 385 (2001)
7. I. Petrov, F. Adibi, J.E. Greene, L. Hultman, J. Sundgren, *Appl. Phys. Lett.* **63**, 36 (1993)
8. I. Petrov, A. Myers, J.E. Greene, J.R. Abelson, *J. Vac. Sci. Technol. A: Vac. Surf. Films* **12**, 2846 (1994)
9. M. Čada, Z. Hubicka, P. Adámek, J. Kluson, L. Jastrabík, *Surf. Coat. Technol.* **205**, S317 (2011)
10. V. Stranák, Z. Hubicka, P. Adámek, J. Blažek, M. Tichý, P. Špatenka, R. Hippler, S. Wrehde, *Surf. Coat. Technol.* **201**, 2512 (2006)
11. D. Lundin, M. Čada, Z. Hubicka, *J. Vac. Sci. Technol. A: Vac. Surf. Films* **34**, 41305 (2016)
12. D. Depla, S. Mahieu, R. De Gryse, *Thin Solid Films* **517**, 2825 (2009)
13. I. Safi, *Surf. Coat. Technol.* **127**, 203 (2000)
14. S.D. Ekpe, S.K. Dew, *J. Vac. Sci. Technol. A: Vac. Surf. Films* **20**, 1877 (2002)
15. P.-A. Cormier, A. Balhamri, A.-L. Thomann, R. Dussart, N. Semmar, J. Mathias, R. Snyders, S. Konstantinidis, *J. Appl. Phys.* **113**, 013305 (2013)
16. D. Lundin, M. Stahl, H. Kersten, U. Helmersson, *J. Phys. D: Appl. Phys.* **42**, 185202 (2009)
17. A.L. Thomann, P.A. Cormier, V. Dolique, N. Semmar, R. Dussart, T. Lecas, B. Courtois, P. Brault, *Thin Solid Films* **539**, 88 (2013)
18. S. Bornholdt, J. Ye, S. Ulrich, H. Kersten, *J. Appl. Phys.* **112**, 123301 (2012)
19. S. Bornholdt, N. Itagaki, K. Kuwahara, H. Wulff, M. Shiratani, H. Kersten, *Plasma Sources Sci. Technol.* **22**, 25019 (2013)
20. V. Stranák, M. Quaas, H. Wulff, Z. Hubicka, S. Wrehde, M. Tichý, R. Hippler, *J. Phys. D: Appl. Phys.* **41**, 055202 (2008)
21. J. Alami, K. Sarakinos, F. Uslu, C. Klever, J. Dukwen, M. Wuttig, *J. Phys. D: Appl. Phys.* **42**, 115204 (2009)
22. F. Magnus, T.K. Tryggvason, S. Olafsson, J.T. Gudmundsson, F. Magnus, T.K. Tryggvason, S. Olafsson, *J. Vac. Sci. Technol. A: Vac. Surf. Films* **30**, 50601 (2012)
23. J.T. Gudmundsson, D. Lundin, N. Brenning, M.A. Raadu, C. Huo, T.M. Minea, *Plasma Sources Sci. Technol.* **25**, 65004 (2016)
24. J.A. Thornton, *Thin Solid Films* **54**, 23 (1978)
25. M. Stahl, T. Trottenberg, H. Kersten, *Rev. Sci. Instrum.* **81**, 1 (2010)
26. S. Gauter, M. Fröhlich, W. Garkas, M. Polak, H. Kersten, *Plasma Sources Sci. Technol.* **26**, 65013 (2017)
27. A. Piel, *Plasma physics: an introduction to laboratory, space, and fusion plasmas* (Springer, Berlin Heidelberg, 2010)
28. I. Ivanov, S. Statev, V. Orlinov, R. Shkevov, *Vacuum* **43**, 837 (1992)
29. F. Haase, D. Lundin, S. Bornholdt, H. Kersten, *Contrib. Plasma Phys.* **55**, 701 (2015)
30. P. Baroch, J. Musil, J. Vlcek, K.H. Nam, J.G. Han, *Surf. Coat. Technol.* **193**, 107 (2005)
31. S. Berg, T. Nyberg, *Thin Solid Films* **476**, 215 (2005)
32. T. Kubart, M. Aiempakit, J. Andersson, T. Nyberg, S. Berg, U. Helmersson, *Surf. Coat. Technol.* **205**, S303 (2011)
33. M. Aiempakit, U. Helmersson, A. Aijaz, P. Larsson, R. Magnusson, J. Jensen, T. Kubart, *Surf. Coat. Technol.* **205**, 4828 (2011)
34. M. Samuelsson, D. Lundin, J. Jensen, M.A. Raadu, J. Gudmundsson, U. Helmersson, *Surf. Coat. Technol.* **205**, 591 (2010)
35. A. Mishra, P.J. Kelly, J.W. Bradley, *Plasma Sources Sci. Technol.* **19**, 45014 (2010)
36. G. West, P. Kelly, P. Barker, A. Mishra, J. Bradley, *Plasma Process. Polym.* **6**, S543 (2009)
37. P. Leroy, S. Konstantinidis, S. Mahieu, R. Snyders, D. Depla, *J. Phys. D: Appl. Phys.* **44**, 115201 (2011)
38. D. Lundin, J.T. Gudmundsson, N. Brenning, M.A. Raadu, T.M. Minea, *J. Appl. Phys.* **121**, 171917 (2017)
39. M. Čada, D. Lundin, Z. Hubicka, *J. Appl. Phys.* **121**, 171913 (2017)
40. M. Bowes, J.W. Bradley, *J. Phys. D: Appl. Phys.* **47**, 265202 (2014)
41. S. Mahieu, D. Depla, *J. Phys. D: Appl. Phys.* **42**, 53002 (2009)
42. D. Depla, S. Heirwegh, S. Mahieu, J. Haemers, R. De Gryse, *J. Appl. Phys.* **101**, 013301 (2007)
43. N. Brenning, J.T. Gudmundsson, D. Lundin, T. Minea, M.A. Raadu, U. Helmersson, *Plasma Sources Sci. Technol.* **25**, 65024 (2016)
44. T. Shimizu, M. Villamayor, D. Lundin, U. Helmersson, *J. Phys. D: Appl. Phys.* **49**, 1 (2016)

Publication IV

On the Impact of Electron Temperature in Magnetron Sputtering Benchmarked with Energy Flux Measurements

Authors:	F. Haase, D. Lundin, and H. Kersten
Journal:	Contribution to Plasma Physics
Technique:	DC magnetron sputtering (DCMS)
Utilized Probes:	Passive thermal probe (PTP), Quartz crystal microbalance (QCM), Langmuir probe
Own contribution:	approx. 50%

Experimental Setup:



Motivation:

This publication dealt with the influence of different process gases (Ne, Ar, Kr) on the electron energy, resulting in a higher degree of ionization and ultimately affecting the deposited thin film. Combined PTP and Langmuir probe measurements paired with QCM investigations would also open the possibility to measure the total integral energy flux, as well as its main contributions.

Main results:

Using a combined Langmuir and calorimetric probe a comparison of n_e , T_e , the total energy flux and its main contributions was possible. It was found that the first ionization potential of the process gas has a considerable impact on the probability of ionizing the sputtered neutrals, where plasmas of gases with a high ionization potential (Ne) exhibited a significantly higher electron temperature. This results in a shorter mean free path for ionization which, given the right admixture, could be used to tune the process to fulfill the needs of certain applications. However, changing the sputtering gas also comes with changes in the deposition rate and the energy flux at the substrate. Different substrate biasing will also result in a different composition of the energy flux which was investigated at different probe bias voltages.

On the Impact of Electron Temperature in Magnetron Sputtering Benchmarked with Energy Flux Measurements

F. Haase^{1*}, D. Lundin^{1,2}, S. Bornholdt¹, and H. Kersten¹

¹ Institute of Experimental and Applied Physics, Kiel University, Leibnizstrasse 11-19, D-24098 Kiel, Germany

² Laboratoire de Physique des Gaz et des Plasmas – LPGP, UMR 8578, CNRS – Université Paris-Sud, 91405 Orsay, France

Received 30 March 2015, revised 13 November 2015, accepted 24 November 2015

Published online 23 December 2015

Key words Magnetron sputtering, calorimetric probe, Langmuir probe.

In this work we have investigated the effect of increasing the electron energy as a way to increase the ionization probability of the sputtered metal (Ti) by measuring the impact of three different process gases (Ne, Ar, and Kr). Using a combined Langmuir and calorimetric probe we were able to compare the electron density n_e , the electron temperature T_e , the total energy influx, as well as the different energy flux contributions from charge carriers, neutrals and surface processes for various discharge conditions. The results show that the electron temperature can be increased by up to a factor of 3 by using Ne instead of Ar (or Kr). Furthermore, it was also found that by using Ne the mean free path for electron impact ionization was decreased by at least 50 %, and for higher pressures even more. In addition, we show that the contributions from sputtered neutrals and film formation represent a large fraction of the total energy influx, whereas the energy flux from ions is very low due to low n_e in this type of discharge. However, by investigating changes in the electron energy flux, it was possible to study the effects of using Ne. These results may provide a way to tune the degree of ionization in sputtering processes.

© 2015 WILEY-VCH Verlag GmbH & Co. KGaA, Weinheim

1 Introduction

Plasma-wall interactions are important in several areas of plasma processing, e.g. etching, surface treatment and deposition of thin films. The conditions at the substrate are affected by the incoming energetic flux, such as electrons, ions, and neutrals, which determine elementary processes like adsorption, diffusion and chemical reactions, as well as microstructure and stoichiometry during film growth [1,2]. The energy per incoming particle and the particle flux can greatly affect the intracolumn as well as intercolumnar porosity [3], making these quantities highly important for thin film deposition. Furthermore, the dissipation of particle energy by collisions with the process (buffer) gas leading to a more thermalized deposition flux is of importance when synthesizing metastable materials [4].

With the introduction of various ionized physical vapor deposition (IPVD) methods [5], such as high-power impulse magnetron sputtering (HiPIMS) [6, 7], the possibility to ionize and accelerate a substantial fraction of the deposition flux [8] has opened up new ways to engineer thin films with improved properties. The key to these beneficial deposition conditions lies in the ionization reactions of the sputtered material, which typically occurs through electron impact ionization [9].

The probability of having an electron impact ionization event for sputtered metal atoms can be described by using the ionization mean free path, λ_{miz} , which depends on the velocity of the sputtered neutrals ν_s , the rate coefficient for such an event k_{miz} , and the electron density n_e , through the following expression [10]:

$$\lambda_{miz} = \frac{\nu_s}{k_{miz} n_e}. \quad (1)$$

In Eq. (1) k_{miz} can be approximated by [10]:

$$k_{miz} = k_0 \exp(-E_0/k_B T_e), \quad (2)$$

* Corresponding author. E-mail: fhaase@physik.uni-kiel.de

where k_0 and E_0 are material dependent constants, which can be extracted from experiments or computer simulations [10–12]. k_B denotes the Boltzmann-constant. A closer inspection of Eqs. (1) and (2) shows that T_e , residing in the exponential expression of Eq. (2), provides a more efficient way for increasing the ionization probability (decreasing λ_{miz}) as compared to the linear term. The main factor that determines T_e in magnetron plasmas is the process gas; at least in the gas-dominated sputtering regime, such as for steady-state DC magnetron sputtering (DCMS) and short HiPIMS pulses ($t_{pulse} \lesssim 100 \mu s$) [13]. The reason is that there must be a sufficient number of electrons with energies above the first ionization potential of the process gas in order to generate the required ionization to sustain the plasma [14].

This implies that gases with a high first ionization potential, such as Ne ($E_i = 21.56$ eV), possess the potential to increase T_e beyond what is found in for example an Ar discharge ($E_i = 15.76$ eV) or Kr discharge ($E_i = 14.00$ eV) [15]. Aijaz et al. [16] explored this possibility in the case of a HiPIMS process depositing ta-C, where it was indeed verified that adding Ne to the Ar/C process increased the C^{1+} flux towards the substrate. However, due to noisy plasma conditions it was not possible to perform Langmuir probe measurements during plasma-on (only in the afterglow), which meant that it was not possible to quantitatively assess changes in both n_e and T_e during the plasma discharge. Earlier measurements by Petrov and co-workers [17] in DCMS comparing Ne/C and Ar/C discharges revealed indeed that T_e increases. Although no detailed investigations were carried out related to changes in the ionization of sputtered carbon as well as no information on the changes of the energy flux, the total ion current increased in the Ne/C discharge for process gas pressures larger than 1 Pa [17]. However, in another investigation by Petrov et al. [18] no difference in the total ion current was observed when changing to a vanadium (V) target. For the latter case no n_e and T_e data are available. In addition, Thornton and Lamb [19] investigated the total energy flux to the substrate in a cylindrical magnetron source with a molybdenum (Mo) target operated in Ne, Ar, Kr, and Xe. They found that the energy flux in the Ne/Mo discharge was considerably larger as compared to the other discharges using noble gases with lower first ionization potential. It was speculated that this was due to energetic reflected ions, but no deconvolution of the various energy contributions was made.

In this work we have therefore carried out measurements of n_e and T_e for different process gases (Ne, Ar, and Kr) in magnetron sputtering of titanium (Ti) using a combined Langmuir and calorimetric probe, which was recently developed [20]. The results have been compared with the energy flux, which was monitored simultaneously, in order to investigate the total energy influx as well as the different contributions from charge carriers, neutrals and surface processes.

Focus has been on the steady-state DCMS discharge in order to eliminate any transients that commonly arise in pulsed discharges. Different process gas pressures have been investigated as well as two different regions: the denser plasma region halfway between the cathode and the substrate as well as the substrate region. The paper is organized as follows: in section 2 the experimental magnetron system and the probe setup are described. Section 3 treats the electron density and temperature. The energy flux measurements and the deposition rate are covered in section 4. Conclusions and an outlook are given in section 5.

2 Experimental setup and data acquisition

2.1 Deposition apparatus

A standard planar circular magnetron with a target diameter of 0.05 m (2 inch), equipped with a Ti (99.9 %) target mounted in a cylindrical vacuum chamber (height 0.50 m, diameter 0.45 m) was used in the present work, see Figure 1. The magnetron was operated in direct current mode at a constant power of 100 W unless otherwise stated. Discharge current and voltage characteristics of the magnetron were recorded directly from the DC power supply (Advanced Energy, MDX 500). The chamber was pumped by a two stage pumping system (turbo-molecular pump and membrane pump) to a residual pressure $< 2 \times 10^{-6}$ Torr (2.7×10^{-4} Pa), after which the working gas (Ar (N5), Ne (N5), Kr (N48), respectively) was let into the chamber. The pressure was set to 10 mTorr (1.3 Pa), 18 mTorr (2.5 Pa) or 30 mTorr (4.0 Pa), respectively.

2.2 The transient calorimetric probe

For electrostatic probing and energy flux measurements, a calorimetric probe with a sensor made of copper was used (diameter of 10mm). The sensor area was shielded by a Macor® block mounted at the backside of the

copper disc, which was connected to a thermo couple (type-K) for temperature recording and a copper wire for biasing and current measurements. Detailed information on the probe design is given by Stahl et al. [21]. The probe was mounted on a rod at a distance of 0.06 or 0.12 m, respectively, below the center of the target surface.

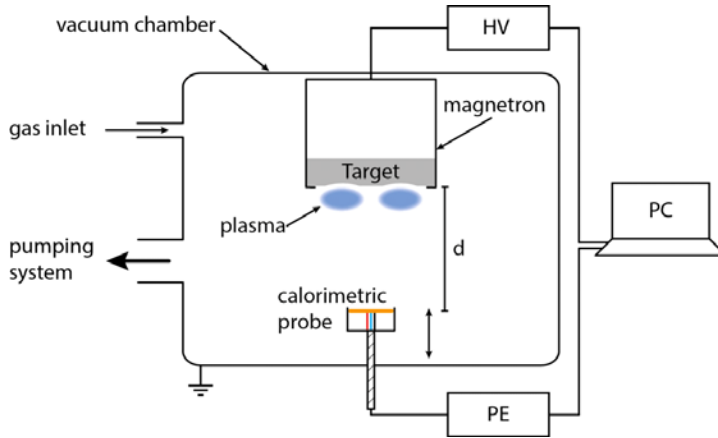


Fig. 1 Schematic of the cylindrical deposition chamber used in the experiments, displaying the cathode mounted in the lid of the chamber (top) and the combined Langmuir/thermal probe head placed below at either $z = 0.06$ m or $z = 0.12$ m from the target surface. HV denotes the computer-controlled DC high voltage power supply. PE denotes the probe electronics, which was also computer controlled. Note that the different objects are not drawn to scale.

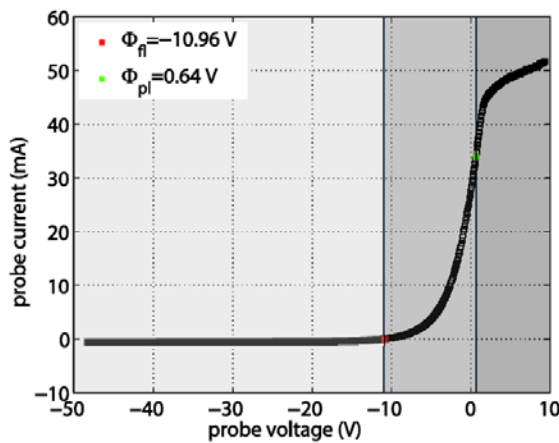


Fig. 2 Typical I-V characteristics measured with the calorimetric probe. The experimental parameters were $P = 20$ W DC power, operating at a pressure of $p = 1.0$ Pa. Also the three typical regions: ion saturation (left), electron acceleration (middle), and electron saturation (right) are indicated by different greyscale backgrounds.

The magnetron power supply and the probe electronics were synchronized in order to control the data recording during plasma-on as well as plasma-off. The measurement procedure was as follows: During plasma-on the probe bias was swept from -50 V to $+10$ V in about 50 s by the probe electronics and an $I_{probe} - V_{probe}$ curve was recorded, here denoted $I - V$ characteristics. A typical curve is shown in Figure 2. The electron temperature T_e was obtained from a semi-logarithmic plot of the probe current versus the probe bias using

$$\ln\left(\frac{I_e}{I_{e0}}\right) = \frac{eV_{probe}}{k_B T_e}, \quad (3)$$

where I_e is the measured electron current and I_{e0} the electron saturation current. The plasma density n_e was calculated using the electron temperature and the ion saturation current. For these calculations we assumed a Maxwellian electron energy distribution function (EEDF), which has been shown to be valid in DCMS for total gas pressures above ~ 1 Pa [22]. The recorded EEDF:s for the different discharges support this assumption. An example can be seen in Figure 3 for the Ar case in a pressure of $p = 1.3$ Pa using a DC discharge power of $P = 100$ W. The fairly straight line in the semi logarithmic plot indicates a Maxwellian distribution and therefore justifies our calculations.

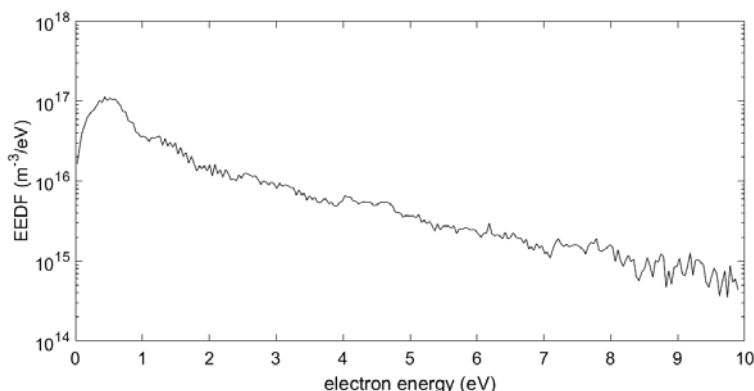


Fig. 3 Calculated electron energy distribution function (EEDF) for an Ar discharge at a pressure of $p = 1.3$ Pa and a DC discharge power of $P = 100$ W. The semi logarithmic plot shows a fairly straight line indicating a Maxwellian distribution.

The naturally present noise on the measured probe characteristics introduces an error on the investigated EEDF:s. Although we used averaging to reduce this error, it should be noted that some noise still remained of the recorded electron current for the high-energy tail even after smoothing. Such noise introduces errors in the calculations of the plasma parameters. However, the error contribution is estimated to 10 % - 15 % or less, since the high-energy tail only constitutes a minor part of the EEDF in our case. When plotting n_e and T_e we have therefore added error bars. Note however, that n_e is plotted on a logarithmic scale, which means that the error bars are on the same scale or smaller than the plotted symbols. It should be noted that the probe did not seem to affect the DC plasma discharge during biasing, and we saw no signs of the probe starting to act as an anode in the electron saturation mode when collecting the $I - V$ characteristics.

After the voltage sweep the plasma was turned off and the probe cooled down for 300 s. During the combined plasma-on and off periods the probe temperature characteristics ($T - t$) were recorded by the calorimetric probe electronics. Details of the measurement procedure for acquiring the $T - t$ characteristics are given by Bornholdt et al. [20]. A typical $T - t$ plot is shown in Figure 4. This procedure was repeated for the different gases and pressures when the probe was placed at $z = 0.12$ m. The temperature behavior was used for calculating the total energy influx.

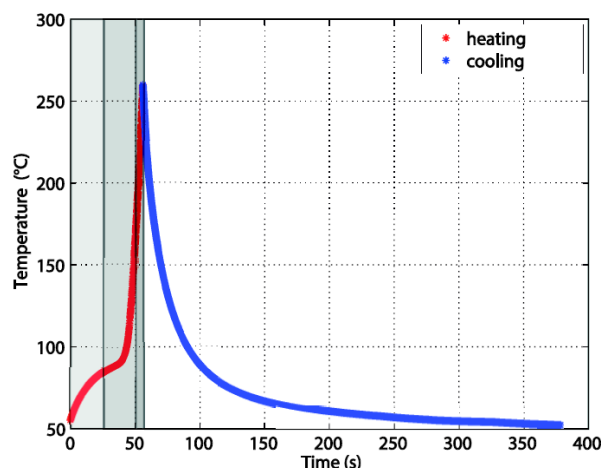


Fig. 4 Typical temperature behavior of the probe during a transient measurement. The process parameters were the same as in Figure 2. In the beginning the heating is fast due to the high voltage accelerating the ions. This region corresponds to the ion saturation region in Figure 2 (light grey). When the probe potential is approaching floating potential the heating is only moderate, due to the low acceleration voltage. For the electron acceleration (middle grey) and electron saturation (dark grey) regions the heating is the strongest due to the high electron current.

2.3 Energy flux contributions

The $T - V$ characteristics recorded by the calorimetric probe were also used to calculate the various contributions to the total energy influx. In this work we have taken into account contributions caused by electrons J_e , ions J_{ion} , electron-ion recombination J_{rec} , impact of sputtered neutrals J_n , and film growth J_{cond} . The procedure for these

calculations is described in [2,23], but will here be summarized for increased clarity when interpreting the energy flux results.

The first three contributions are related to charge carriers, thus their portions can be determined from the $I - V$ characteristics obtained with the Langmuir electronics. The contribution by electron impact (assuming a Maxwellian electron energy distribution function) is calculated using the electron current density j_e and the electron temperature T_e :

$$J_e = 2 \frac{j_e}{e_0} k_B T_e, \quad (4)$$

where e_0 is the elementary charge. The ion current density j_i and plasma potential Φ_{pl} is used for the calculation of ion impact:

$$J_i = \frac{j_i}{e_0} (\Phi_{pl} - V_{probe}). \quad (5)$$

The third contribution, which can be calculated from the plasma parameters, is the recombination of electrons and ions (ionization potential Φ_{ion}) at the probe surface with the electron work function Φ_{ewf} . This is given by

$$J_{rec} = \frac{j_i}{e_0} (\Phi_{ion} - \Phi_{ewf}). \quad (6)$$

Furthermore, the deposition rate was investigated in order to calculate the contributions from impinging sputtered neutrals (deposition flux) J_n and the energy released by film condensation J_{cond} to the total energy influx, since they cannot be determined from the current measurements. The growth rate was investigated for the various conditions by utilizing a quartz crystal micro balance (QCM), which was mounted at the same position as the probe (only at 0.12 m from the target).

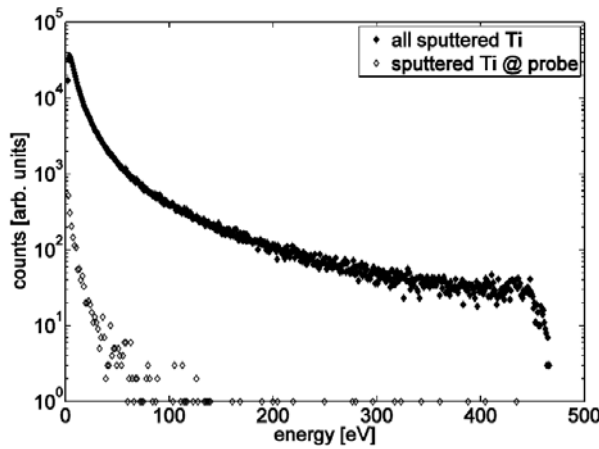


Fig. 5 Calculated energy distributions of sputtered neutral Ti atoms during Ar ion bombardment. The energy distribution of those atoms which hit the probe (open symbols) differs from the overall distribution (filled symbols). The data was generated with SRIM calculations.

The determination of J_n and J_{cond} is based on SRIM simulations [24] and growth rate measurements. SRIM is a Monte Carlo based code simulating many features of the transport of ions in matter. This includes sputtering events for various target materials and projectiles. A detailed description of the physics used in the SRIM code is given by Ziegler et al. [25]. Again, like for all contributions, they are given by the particle flux times the mean energy delivered by each particle. The procedure is as follows: First off, SRIM simulations were performed by using the target potential taken from the experiments in order to obtain the angular energy distribution of sputtered Ti atoms for the different process gases used. For the calculation of the mean kinetic energy \bar{E}_{kin} only those particles hitting the probe were used, see Figure 5. The particle flux of the neutrals Γ_n can easily be extracted from measurements of the growth rate R by using $\Gamma = \rho R/m$, where m and ρ denote the mass of the atom and the density of the film, respectively. \bar{E}_{kin} and R have been summarized in Table 1. For increased clarity we have also plotted the normalized deposition rates compared to R_{Ar} . They are displayed in Figure 12 and are further discussed in section 4.

Table 1 Mean kinetic energy and growth rate for the three investigated pressure regimes using Ar, Kr, and Ne.

Pressure (Pa)	Ar		Kr		Ne	
	\bar{E}_{kin} (eV)	R (nm/min)	\bar{E}_{kin} (eV)	R (nm/min)	\bar{E}_{kin} (eV)	R (nm/min)
1.3	17.2	65.0	12.1	44.6	22.7	50.4
2.5	16.6	55.3	11.7	31.5	22.1	46.4
4.0	16.6	42.8	11.7	23.5	21.1	41.7

Thus, the contribution by impinging sputtered neutrals (deposition flux) can be calculated as

$$J_n = \Gamma_n \bar{E}_{kin} \quad (7)$$

The contribution by film formation (film condensation) is estimated from

$$J_{cond} = \Gamma_n \alpha E_{bind} \quad (8)$$

where E_{bind} is the surface binding energy between the metal atom and the film and α the sticking coefficient. Here $\alpha = 1$ is assumed, which is typically used for sputtering metal onto metal. For the binding energy of Ti a value $E_{bind} = 4.89$ eV [26] was used.

3 Electron temperature and density

3.1 Measurements at the substrate position and close to the ionization region

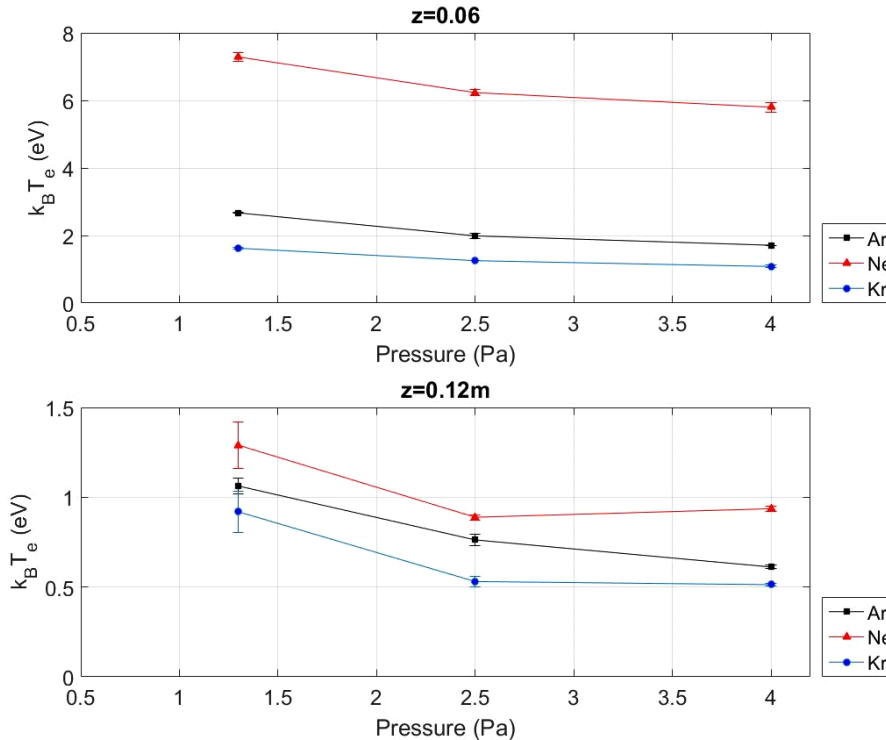


Fig. 6 Electron temperature plots for the near-cathode region at $z = 0.06$ m (top) and substrate position at $z = 0.12$ m (bottom) vs. process gas pressure. The DC discharge power was in all cases fixed at 100 W. Note that the scale for T_e in the bottom plot is not the same as in the top plot, due to large differences between the two regions investigated.

The Langmuir probe results for the two positions investigated are shown in Figure 6 and Figure 7 for the region at $z = 0.06$ m and for the substrate position at $z = 0.12$ m. In general, it is seen that both n_e and T_e exhibit larger values closer to the cathode, as expected, since this region exhibits stronger electron trapping giving rise to the well-known dense plasma torus above the target race track (see for example [27]). Furthermore, the electrons are mainly accelerated in the cathode sheath and extended pre-sheath [14, 28] before successively being slowed down as they traverse the magnetic field lines of the magnetron out into the plasma bulk (larger z distances), which explains the changes in T_e . From Figure 6 it is also seen that T_e increases with decreasing process gas pressure. Similar observations were made by Petrov et al. [17]. It is likely a consequence of the plasma trying to sustain itself with fewer seed gas atoms available, and therefore T_e increases to increase the probability of ionization.

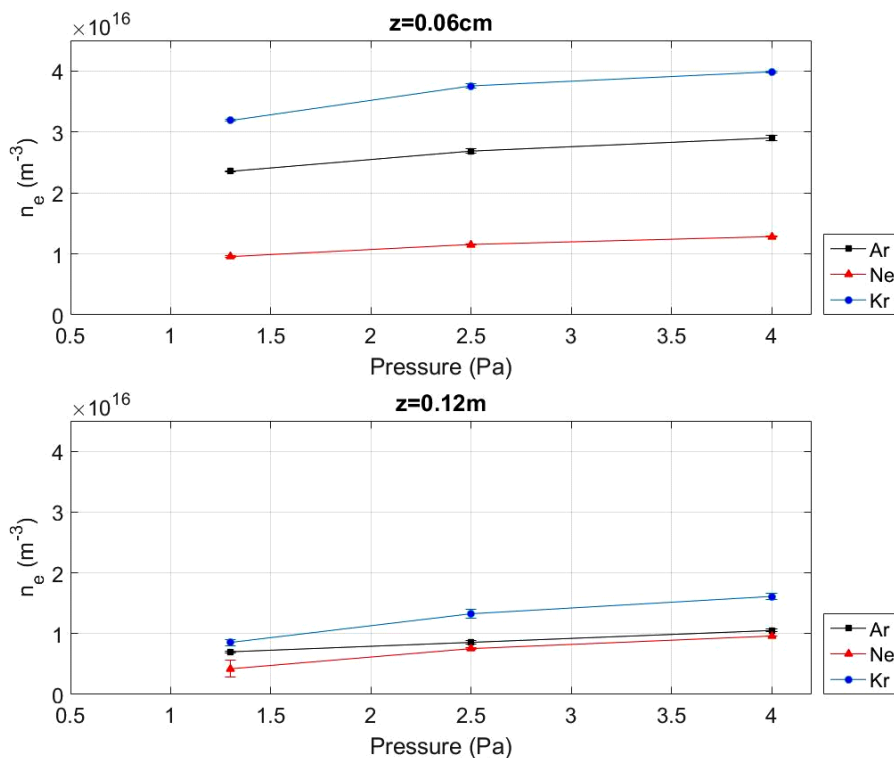


Fig. 7 Electron density plots for the near-cathode region at $z = 0.06$ m (top) and substrate position at $z = 0.12$ m (bottom) vs. process gas pressure. The DC discharge power was in all cases fixed at 100 W.

However, what is remarkable is the strong increase in electron temperature in the Ne/Ti case with $T_e \sim 5 - 7$ eV as compared to the other process gases used, where $T_e \sim 1 - 3$ eV, see Figure 6. This is most striking for $z = 0.06$ cm, where $T_{e,Ne}$ consistently is a factor 3 larger over the entire pressure range investigated as compared to Ar/Ti and Kr/Ti. At the same time $n_{e,Ne}$ shows 2-3 times lower values as compared to $n_{e,Ar}$ and $n_{e,Kr}$ (Figure 7, top). For the substrate position ($z = 0.12$ m) the same trends can be seen, although the differences in plasma parameters between the different process gases are smaller. T_e is here in the range 0.5 – 1.4 eV with Kr/Ti giving rise to the lowest values and Ne/Ti generating the highest values. In all cases n_e is fairly constant around 1×10^{16} m⁻³ (Figure 7, bottom).

It should be noted that the Langmuir probe characteristics in all cases exhibited a Maxwellian distribution of the plasma electrons. A small hot electron component could sometimes be discerned at probe bias voltages of around -20 V to -30 V, which did skew the current-voltage trace somewhat. For the present investigation we chose to focus on the cold plasma electron population.

3.2 Conditions for increased ionization probability of the sputtered material

To quantify the above presented plasma characteristics with respect to increased probability of electron impact ionization we have below calculated the ionization mean free path λ_{miz} for the sputtered Ti based on Eq. (1) for the different process gases as well as the pressure range investigated.

For the calculations, an averaged velocity of the sputter-ejected Ti, ν_s , was used based on experimental measurements of the velocity distributions at different pressures and under different angles of view relative to the target surface by Britun et al. [29] using Fabry-Perot interferometry in the near-cathode region. These values are summarized in Table 2. Note that these are estimations based on Ar discharges.

Table 2 Estimated average velocity of sputtered neutrals in Ar, after [28], used to calculate λ_{miz} .

Pressure (Pa)	Velocity of sputtered neutrals ν_s (m/s)
1.3	550
2.5	320
4.0	250

The rate coefficient for electron impact ionization of Ti, $k_{miz}(T_e)$, has been estimated by Hopwood [10] to $k_{miz}(T_e) = 2.34 \times 10^{-13} \exp(-7.25/k_B T_e)$. Using this input together with our presented values for n_e and T_e (Section 3.1) we calculated λ_{miz} for our two regions of interest. The results are plotted in Figure 8 for $z = 0.06$ m and $z = 0.12$ m. Note that λ_{miz} has, for each investigated pressure, been normalized to $\lambda_{miz,Ar}$ for increased clarity and easier comparison. It should be noted that λ_{miz} in typical DCMS discharges is on the order of several tens of cm in the dense plasma zone above the target surface due to the limited plasma density (see also Figure 7), which was also found in the present study. This is further discussed in section 4 concerning the ionic flux contribution. However, we will first discuss the changes in the probability of electron impact ionization based on the measured n_e and T_e data.

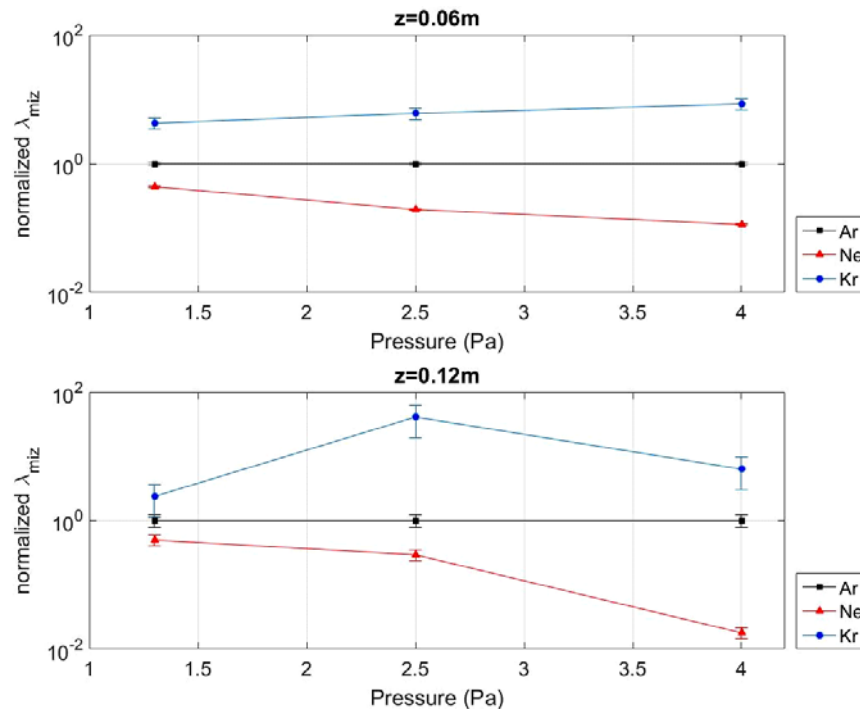


Fig. 8 The mean free path for electron impact ionization of Ti, which, for each investigated pressure, has been normalized to the Ar case, $\lambda_{miz,Ar}$. These results are calculated based on the Langmuir probe measurements in the near-cathode region (top) and substrate region (bottom), which are shown in Figure 6 and Figure 7.

It is evident from Figure 8 that the overall effect of using Ne instead of Ar or Kr results in a great increase of the ionization probability for the sputtered Ti over the whole pressure range investigated. For the denser plasma region at $z = 0.06$ m we find that the mean free path in the case of Ne decreases to about 25 – 44 % of the corresponding λ_{miz} for Ar depending on pressure. For our purposes these results are very important, since generally the near-cathode region is expected to generate most of the ionization of sputtered material, as described by Brenning et al [30] in their modeling of magnetron discharges. Here is also clearly shown the greater importance of the electron temperature for the investigated inelastic collisions. We find that, although $n_{e,Ne}$ shows 2-3 times lower values as compared to $n_{e,Ar}$ and $n_{e,Kr}$ (Figure 7, top), this only plays a minor role in the overall reaction kinetics when ionizing Ti. For the Kr/Ti discharge, it is found that λ_{miz} increases by approximately 42-99 % as compared to Ar/Ti. It is therefore concluded that the first ionization potential of the sputtering gases has a considerable impact on the probability of ionizing the sputtered neutrals.

Also in the substrate region ($z = 0.12$ m) the same trends are still valid. The mean free path in the case of Ne decreases to about 0.03 – 59 % depending on pressure as compared to the Ar/Ti discharge. Since n_e was fairly constant at about $1 \times 10^{16} \text{ m}^{-3}$ independent of pressure and process gas type, this increased ionization is more or less entirely due to an increased electron temperature. For the Kr/Ti discharge, it is found that λ_{miz} increases by approximately 250-1700 % as compared to Ar/Ti.

4 Energy flux and deposition rate

The energy balance at the substrate is a key factor for film structure and morphology, because the resulting surface temperature influences surface processes like diffusion, ad-atom mobility etc. In addition, it is also reported that different contributions have different impact, depending on if the energy transfer is connected to momentum transfer by kinetic impact of ions and fast neutrals or if it is caused by surface processes like recombination, molecule formation and film growth. Especially ion bombardment is known to be crucial for optimizing the film properties [31, 32]. Since the energy balance depends on the process gas, because plasma parameters and sputter yields vary, we have also taken a closer look at the different contributions caused by electrons, ions, electron-ion recombination, impact of sputtered neutrals, and film growth, as previously described in section 2.3.

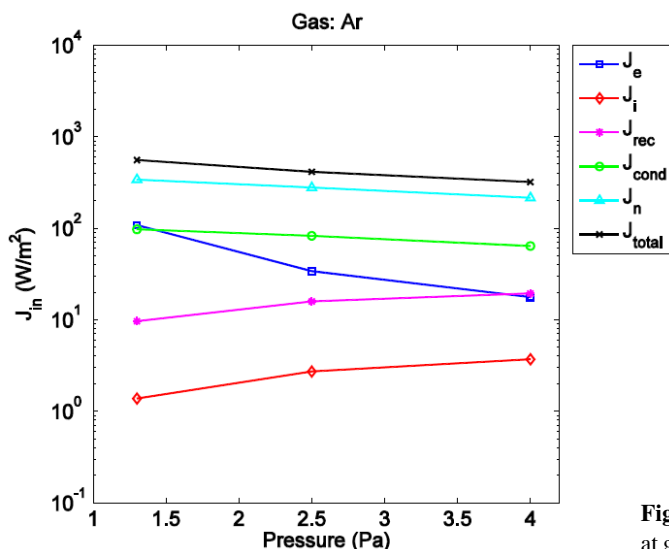


Fig. 9 Evolution of the different energy flux contributions at ground potential for the substrate position $z = 0.12$ m vs. argon pressure.

We will first focus on the measured total energy influx J_{tot} for the three different gases and compare it to the calculated contributions. From Figures 10–12 it is seen that there is not a great difference in J_{tot} , when changing process gas. The general trend is however that $J_{tot,Ne} > J_{tot,Ar} > J_{tot,Kr}$. Note that there is a good qualitative agreement between the measured and calculated energy fluxes. However, the differences, which are most obvious at the electron acceleration and saturation regions (not shown), may be attributed to resistive heating of the bias wire due to relatively high currents. The differences between calculation and experiment in the ion saturation

regime have been measured in different experiments [23] and are attributed to the fact that collisions of ions are not accounted for in this treatment. For all investigated sputter gases there is only a slight reduction of the total energy flux with increasing pressure. The small pressure effect seen is likely an effect of the increasing collision frequency as the pressure increases. It leads to a reduction of the particle flux perpendicular to the target and an increase of the flux parallel to the target surface, i.e. a more isotropic flux at higher pressure. This effect was also verified using the OMEGA code [33], which showed that the mean kinetic energy was reduced to 0.65 – 1.0 eV at the probe surface (see also Table 1). However, these simulations were only performed for the Ar/Ti discharge, since Ne and Kr has not yet been implemented in the code.

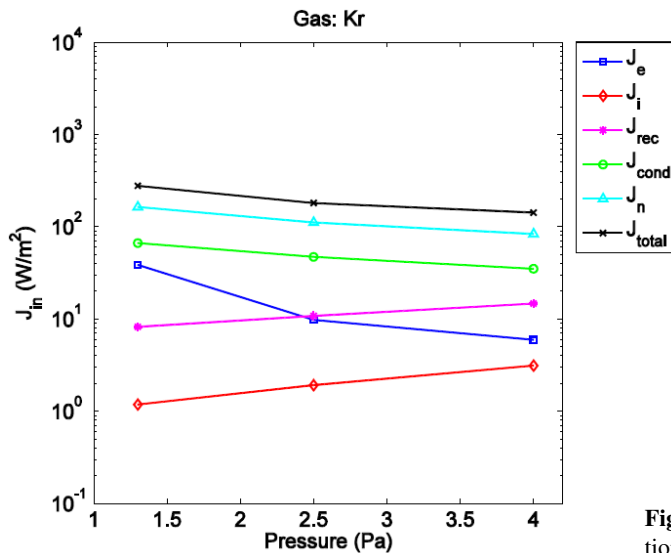


Fig. 10 Evolution of the different energy flux contributions at ground potential for the substrate position $z = 0.12$ m vs. krypton pressure.

From the calculated contributions it is seen that the largest fraction comes from kinetic impact of neutral metal atoms J_n originating from collisions cascades at the target. In addition it is seen that J_n exhibits a steep increase from Kr to Ar. Changing process gases from Ar to Ne only slightly increases J_n , which is due to increased \bar{E}_{kin} for the Ne case (Table 1), since $R_{Ne} < R_{Ar}$. A similar trend has been reported by Thornton and Lamb using a Mo target [19], although they noticed the greatest difference going from Ar to Ne.

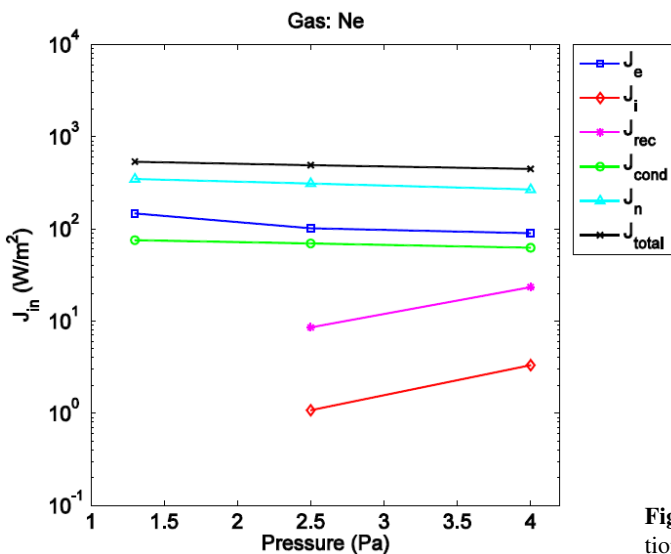


Fig. 11 Evolution of the different energy flux contributions at ground potential for the substrate position $z = 0.12$ m vs. neon pressure.

We now turn towards the question of increased charged particle contribution to the energy flux for process gases with higher first ionization potential, such as Ne. Comparing only the ion contribution J_i in Figures 10–12 we do not find a significant difference between the three different gases investigated. Typically $J_i \approx 1 - 3 \text{ W/m}^2$ and increases somewhat with increasing pressure. This result is in line with previous ion flux measurements by Petrov et al. [18] on a V target using Ne, Ar, Kr, and Xe. In case of substrates which are more negative than the plasma potential the positive ions reaching the surface can only escape from the surface if they are neutralized. Thus, there is a second contribution by the ions due to recombination, J_{rec} . From Figures 10–12 it can be seen that there is indeed a slightly higher contribution of J_{rec} in the case of Ne/Ti with a maximum reaching $\sim 25 \text{ W/m}^2$. We believe that the reason for these small changes in the ionic contribution is due to the low degree of ionization of sputtered material for DCMS discharges with typical ionization mean free paths around 0.50 m or more resulting in a degree of ionization of a few percent or less. It is therefore extremely hard to detect any changes even though a clear change in T_e is observed. We conclude that the calculated total ionic contribution to the energy flux is not sufficient to determine if there are any significant changes in the ionization and transport of sputtered Ti. However, it may still be possible to detect an increase of the ionization of the sputtered (metal) atoms by performing mass spectrometric measurements under the same conditions. Such measurements are planned to be carried out in the near future. Also, ongoing investigations using HiPIMS will result in increased n_e due to the higher instantaneous power density on the cathode, which will effectively decrease λ_{mfp} to only a few centimeters and, thereby, amplify the ionic contribution, as suggested by earlier measurements [34].

If we instead consider the electron energy flux, J_e , which is the third and final contribution to the charged particle flux, the situation is quite different. Here a strong increase is detected in the Ne/Ti case with values around 90–150 W/m^2 as compared to 20–100 W/m^2 for Ar/Ti and 6–40 W/m^2 for Kr/Ar, which is most likely an effect of the more energetic electrons (higher T_e). Note that this is not an obvious result since J_e is proportional to T_e as well as indirectly proportional to n_e (through the electron current density j_e). Even though the lowest electron densities were measured in the Ne/Ti discharge, we still find a higher J_e for this case due to more energetic electrons. The same can also be said when looking at the pressure dependence, where J_e is generally found to decrease with increasing pressure. This is an effect of the measured T_e , which slightly decreases with increasing pressure, although n_e exhibits the opposite trend, see Figure 6 (bottom) and Figure 7 (bottom).

Changing the sputtering gas however, will result in different deposition rates on the substrate. To quantify these changes, quartz crystal microbalance (QCM) measurements were performed with all three gases under all three pressure configurations respectively. For a better understanding these values have been normalized to the Ar rates for each pressure regime, which is shown in Figure 12. It can be seen that both Ne and Kr yield lower deposition rates than Ar.

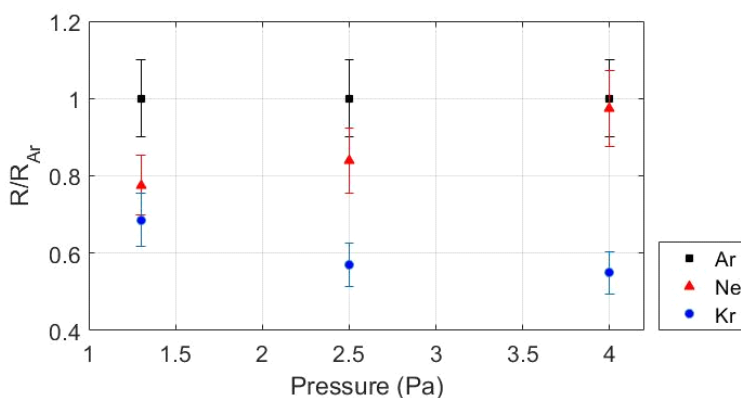


Fig. 12 Normalized deposition rates compared to the commonly used Ar case for all pressures investigated (1.3, 2.5, and 4.0 Pa) and all process gases (Ar, Ne, Kr). These measurements were taken at the substrate position ($z = 0.12 \text{ cm}$). The DC discharge power was in all cases fixed at 100 W. The exact values are found in Table 1.

At low pressure the difference in the deposition rate between Ne and Ar is related to the slightly higher sputter yield of Ar, which was also verified in our SRIM runs. However, with increasing pressure this difference is almost eliminated. This is likely due to increased scattering of the sputtered Ti at higher pressure, in which Ti is more

scattered in a collision with Ar (mass 39.95 u) than with Ne (20.18 u) due to Ar being heavier. Less Ti will thereby reach the QCM head.

In the case of Kr (83.80 u), the trend is the opposite as compared to Ne, with an increasingly lower deposition rate as compared to Ar for higher pressures. This is also due to increased scattering of sputtered Ti, since Kr is the heaviest element of the three gases investigated. At low Kr pressure this effect is less important. However, the flux of ions sputtering the target is also considerably lower for the Kr case, which is reflected by a lower discharge current (170 mA for Kr compared to about 220 mA for Ar and Ne at 1.3 Pa).

5 Conclusions

In this study we have investigated the effect of increasing the electron energy as a way to increase the ionization probability of the sputtered metal by measuring the impact of three different process gases (Ne, Ar, and Kr). Using a combined Langmuir and calorimetric probe we were able to compare n_e , T_e , the total energy influx, as well as the different energy flux contributions from charge carriers, neutrals and surface processes for various discharge conditions.

It was found that the first ionization potential of the process gas has a considerable impact on the probability of ionizing the sputtered neutrals, where plasmas of gases with a high ionization potential, such as Ne, were shown to have a significantly higher electron temperature, and thereby a shorter ionization mean free path, as compared to plasmas of gases with a low ionization potential, such as Kr. Thus, the degree of ionization can be somewhat tuned in order to fulfill the needs of the application. However, changing the sputtering gas also changes the deposition rate and the energy flux at the substrate. This was verified by calorimetric measurements and modeling of the different contributions of the energy influx. It was shown that in the case of DCMS the contributions from sputtered neutrals and film formation represent a large fraction of the total energy influx. At ground potential the energy flux from ions is very low due to low n_e in this type of discharge, but may exceed the contribution by neutrals at negative substrate bias. Still, by investigating changes in the electron energy flux J_e , it was possible to see the effect of the increased electron energy.

Acknowledgements This work was supported by the Deutsche Forschungsgemeinschaft under SFB TR 24/B13, the Swedish Research Council (VR), and the French National Center for Scientific Research (CNRS). DL would like to acknowledge Kiel University (CAU) for the Scandinavian Visiting Professorship.

References

- [1] J.A. Thornton, *J. Vac. Sci. Technol.* **11**, 666 (1974).
- [2] H. Kersten, H. Deutsch, H. Steffen, G.M.W. Kroesen, and R. Hippler, *Vacuum* **63**, 385 (2001).
- [3] I. Petrov, F. Adibi, J.E. Greene, L. Hultman, and J. Sundgren, *Appl. Phys. Lett.* **63**, 36 (1993).
- [4] R.E. Somekh, *J. Vac. Sci. Technol. A Vacuum, Surfaces, Film.* **2**, 1285 (1984).
- [5] U. Helmersson, M. Lattemann, J. Bohlmark, A.P. Ehiasarian, and J.T. Gudmundsson, *Thin Solid Films* **513**, 1 (2006).
- [6] J.T. Gudmundsson, N. Brenning, D. Lundin, and U. Helmersson, *J. Vac. Sci. Technol. A Vacuum, Surfaces, Film.* **30**, 030801 (2012).
- [7] D. Lundin and K. Sarakinos, *J. Mater. Res.* **27**, 780 (2012).
- [8] T. Kubart, M. Čada, D. Lundin, and Z. Hubička, *Surf. Coatings Technol.* **238**, 152 (2014).
- [9] M.A. Raadu, I. Axnäs, J.T. Gudmundsson, C. Huo, and N. Brenning, *Plasma Sources Sci. Technol.* **20**, 065007 (2011).
- [10] J.A. Hopwood (Ed.), *Thin Films: Ionized Physical Vapor Deposition* (Academic Press, San Diego, CA, 2003).
- [11] M.-H. Lee and C.-W. Chung, *Phys. Plasmas* **12**, 073501 (2005).
- [12] R.S. Freund, R.C. Wetzell, R.J. Shul, and T.R. Hayes, *Phys. Rev. A* **41**, 3575 (1990).
- [13] C. Huo, D. Lundin, M. a Raadu, A. Anders, J.T. Gudmundsson, and N. Brenning, *Plasma Sources Sci. Technol.* **23**, 025017 (2014).
- [14] C. Huo, D. Lundin, M. a Raadu, A. Anders, J.T. Gudmundsson, and N. Brenning, *Plasma Sources Sci. Technol.* **22**, 045005 (2013).
- [15] C. Nordling and J. Östermalm, *Physics Handbook for Science and Engineering*, 6th ed. (Studentlitteratur, Lund, Sweden, 1999).
- [16] A. Aijaz, K. Sarakinos, D. Lundin, N. Brenning, and U. Helmersson, *Diam. Relat. Mater.* **23**, 1 (2012).
- [17] I. Petrov, I. Ivanov, V. Orlinov, and J. Kourtev, *Contrib. Plasma Phys.* **30**, 223 (1990).
- [18] I. Petrov, I. Ivanov, V. Orlinov, and J.E. Sundgren, *J. Vac. Sci. Technol. A Vacuum, Surfaces, Film.* **11**, 2733 (1993).

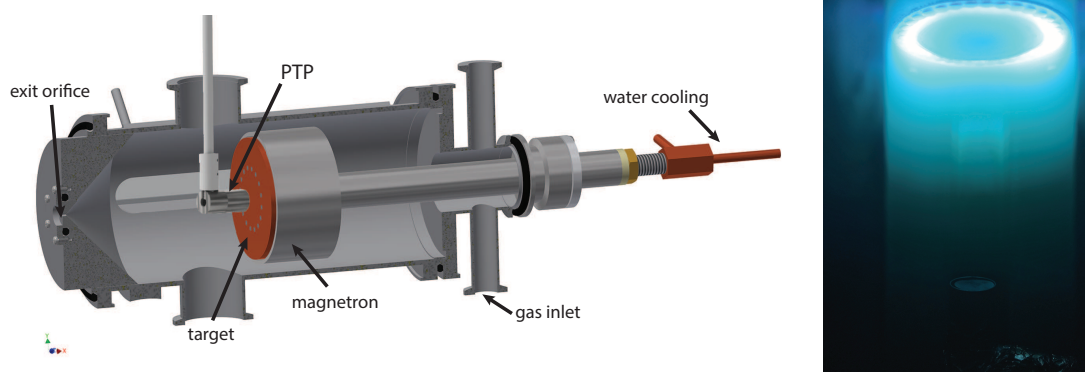
- [19] J.A. Thornton and J.L. Lamb, *Thin Solid Films* **119**, 87 (1984).
- [20] S. Bornholdt and H. Kersten, *Eur. Phys. J. D* **67**, 176 (2013).
- [21] M. Stahl, T. Trottenberg, and H. Kersten, *Rev. Sci. Instrum.* **81**, 023504 (2010).
- [22] I. Ivanov, S. Statev, V. Orlinov, and R. Shkevov, *Vacuum* **43**, 837 (1992).
- [23] S. Bornholdt, J. Ye, S. Ulrich, and H. Kersten, *J. Appl. Phys.* **112**, (2012).
- [24] SRIM, Stopping Range of Ions in Matter, available at www.srim.org.
- [25] J. F. Ziegler, J. P. Biersack, and U. Littmark, *The Stopping and Range of Ions in Solids* (Pergamon, New York, 1985).
- [26] R.C. Weast, *CRC Handbook of Chemistry and Physics*, 48th ed., (Chemical Rubber Company, Cleveland, OH, 1968).
- [27] D. Lundin, S. Al Sahab, N. Brenning, C. Huo, and U. Helmersson, *Plasma Sources Sci. Technol.* **20**, 045003 (2011).
- [28] J.A. Thornton, *J. Vac. Sci. Technol.* **15**, 171 (1978).
- [29] N. Britun, J.G. Han, and S.-G. Oh, *Appl. Phys. Lett.* **92**, 141503 (2008).
- [30] N. Brenning, C. Huo, D. Lundin, M.A. Raadu, C. Vitelaru, G.D. Stancu, T. Minea, and U. Helmersson, *Plasma Sources Sci. Technol.* **21**, 025005 (2012).
- [31] K. Ellmer and T. Welzel, *J. Mater. Res.* **27**, 765 (2012).
- [32] S. Bornholdt, N. Itagaki, K. Kuwahara, H. Wulff, M. Shiratani, and H. Kersten, *Plasma Sources Sci. Technol.* **22**, 025019 (2013).
- [33] D. Lundin, C. Vitelaru, L. De Poucques, N. Brenning, and T. Minea, *J. Phys. D. Appl. Phys.* **46**, 175201 (2013).
- [34] D. Lundin, M. Stahl, H. Kersten, and U. Helmersson, *J. Phys. D. Appl. Phys.* **42**, 185202 (2009).

Publication V

Calorimetric investigations in a gas aggregation source

Authors:	S. Gauter, F. Haase, P. Solar, O. Kylian, P. Kus, A. Choukourov, H. Biederman, and H. Kersten
Journal:	Journal of Applied Physics (submitted)
Technique:	DC magnetron sputtering (DCMS)
Utilized Probes:	Passive thermal probe (PTP), Quartz crystal microbalance (QCM), Langmuir probe
Own contribution:	approx. 40%

Experimental Setup:



Motivation:

The goal of this work was the investigation of a gas aggregation source (GAS), which operates a DC magnetron in fairly high pressures (20 Pa up to 210 Pa) and aims to produce nanoparticles. The composition of the energy flux and its evolution during parameter variation (distance, magnetron current, pressure) was of key interest. Additionally, the influence of a composite target (W in Cu) as compared to pure W and Cu targets should be studied, since it opens up new ways of creating composite nanoparticles.

Main results:

The studies in this publication exhibited comparable basic mechanisms contributing to the energy flux for the higher pressure regimes the GAS operates in, as compared to low pressure regimes of conventional DCMS. Contributions from charged particles (electrons and ions) and radiation have comparably small influences on the integral energy flux. Similar to conventional DCMS the energy flux is mainly composed of the contribution of film condensation and reflected neutrals. The contribution of reflected neutrals is highly dependent on the gas-target mass ratio.

Calorimetric investigations in a gas aggregation source

Sven Gauter,¹ Fabian Haase,¹ Pavel Solař,² Ondřej Kylián,² Peter Kúš,³ Andrei Choukourou,² Hynek Biederman,² and Holger Kersten¹

¹*Institute of Experimental and Applied Physics, Kiel University, Kiel, Germany*

²*Department of Macromolecular Physics, Faculty of Mathematics and Physics, Charles University, Prague, Czech Republic*

³*Department of Surface and Plasma Science, Faculty of Mathematics and Physics, Charles University, Prague, Czech Republic*

(Dated:)

A gas aggregation source based on DC magnetron sputtering was investigated using a passive thermal probe and supplementary diagnostics (Langmuir probe and quartz crystal microbalance). Parameter variations of pressure, axial distance and magnetron current have been performed for three different targets (pure Cu, pure W, composite Cu/W) in argon discharge. The measurements showed the energy flux to be significantly higher for the case of the pure tungsten and the composite target compared to the copper target, which is likely a result of the strongly increased amount of neutrals being reflected from the heavier targets. Furthermore, gas rarefaction by the sputtered atoms was found to be essential for the understanding of the observed energy flux and that the dominant contributors to the energy flux in the higher pressure regime are comparable to those observed in the conventional lower pressure regime. Selected deposited films have been investigated ex-situ by scanning electron microscopy, which allowed to gain insight into the nanoparticle formation in relation to the observed energy conversion.

I. INTRODUCTION

Metal nanoparticles (NPs) produced by means of gas aggregation cluster sources (GAS) represent an ever growing field in nanoscience¹⁻⁵. In the past, the major focus was laid upon construction of GAS themselves^{6,7}, to understand the basic principles of the nanoparticle formation process^{1,2,8,9}, the properties of single-phase particles and their transport to substrates¹⁰⁻¹². Recent developments shift the focus from single material to composite nanoparticles, which resulted in a variety of different approaches to achieve complex nanoparticle formation. Some methods employ multiple steps such as in-flight coating or subsequent coating of single-metal NPs by a thin film of another material^{13,14}. Although the formation of the core is in this case completely decoupled from the deposition of the shell the produced shell is usually very thin (typically several nm). Another method utilizes simultaneous sputtering of two or more metals from several magnetrons in one aggregation chamber¹⁵ allowing for the production of multi-component NPs. Although control of the component ratio can be well achieved with this method, the control of the overall homogeneity is not straightforward. The same problem arises when a single magnetron is used with a target composed from two halves consisting of two different metals^{16,17}. Other studies with different forms of composite targets like a silver target with a concentric thin gold wire inserted in the erosion track¹⁸ or various alloyed targets¹⁹⁻²¹ were found to reliably produce nanoparticles with varying results regarding particle size distribution, composition and structure. A similar approach, which is investigated in this study is based on small pellets of different material located in the erosion track. Although the possibility to produce core-shell NPs using this method was already demonstrated²², the formation and growth of such NPs

is still not well-understood. This is partially due to insufficient knowledge of the processes occurring inside the aggregation chamber, such as heating/cooling of growing NPs. To gain insight on the energy flux inside the aggregation chamber and, thus, also on the energy conversion relevant for the formation process of the particles, energy flux measurements using a passive thermal probe (PTP) were performed for different settings of discharge power, gas pressure and distance to target. Supplementary to the measurement of the power density (energy flux) with the PTP, the deposition rate was measured using a quartz crystal microbalance (QCM) and plasma parameters were monitored with a Langmuir probe (LP). To correlate the obtained experimental values to the formation process of the particles, these test films were deposited for selected parameter sets and analyzed using a scanning electron microscope (SEM).

II. EXPERIMENTAL SETUP OF THE GAS

The investigated system represents a typical gas aggregation cluster source consisting of an indirectly cooled 3 inch magnetron inserted on the axis of a cylindrical vacuum chamber of 100 mm diameter. The distance between the target and the exit orifice (2 mm diameter) was 131 mm for the standard magnetron position (distance magnetron to PTP: 16 mm). To allow extraction of particles, the aggregation chamber is connected to the main, differentially pumped vacuum chamber ($p < 1$ Pa, 210 l/s from turbo pump). The operation pressures of 20 - 210 Pa inside the aggregation chamber were obtained with a gas flow of 2 - 40 sccm of argon introduced at the top of the chamber (see figure 1). Differential pumping creates a pressure gradient directed from the gas input of the aggregation chamber towards its exit orifice, allow-

ing efficient transport of clusters and particles. Both the magnetron and the chamber walls were cooled with water. The position of the magnetron in the chamber was adjustable via a sliding vacuum feedthrough, see figure 1. The magnetron was powered by an *Advanced Energy MDX500* DC power supply operated in constant current mode. The magnetron voltage, current and power were continuously recorded to monitor the process. Pure Ar was used as a process gas.

For all measurements, the probes were side-mounted to the aggregation chamber facing the magnetron target. Since the probes could not be moved along the vertical axis of the magnetron, the distance variation was performed by moving the magnetron to the most distant position ($d_{max} = 66$ mm) and then successively moving it closer to the probes with intermittent measurements until reaching the minimum distance of $d_{min} = 16$ mm.

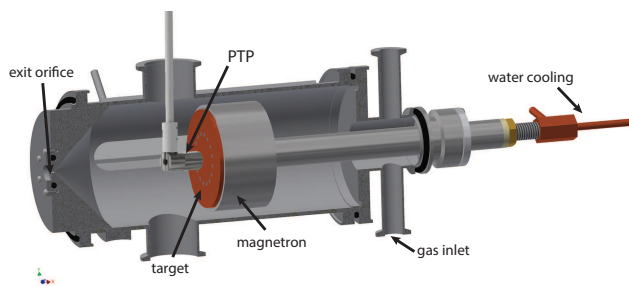


Figure 1: Schematic drawing of the aggregation chamber. The probes were mounted inside the aggregation chamber at a standard distance of 16 mm from the magnetron.

Identical parameter variations as summarized in table I have been performed for three different targets: a pure tungsten target, a pure copper target and a composite target made from copper with 37 tungsten pellets of 3 mm diameter distributed over the race track (see figure 2). All targets were 3 mm in thickness and exhibited similar erosion depths in the race track area. To identify systematic errors such as time-dependent changes in the surface condition of the target, several parameter settings have been measured twice at different times during the variation. The resulting deviation is represented as error bars in the presented measurement results.

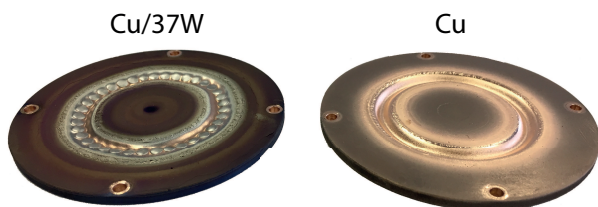


Figure 2: Photograph of the utilized Cu/37W (left) and pure Cu (right) 3 inch targets used in the gas aggregation source. The pure W target is not shown.

III. UTILIZED PROBES

All measurements were performed subsequently with three different kind of probes centered on the chamber and magnetron axis at approximately the same distance to the target. The Langmuir probe measurements were performed using the PTP substrate as a planar Langmuir probe which was biased using a copper wire. The corresponding plasma parameters were primarily calculated to allow an estimation of the energy flux by ions and electrons and are, thus, not discussed in greater detail in this study.

A. Quartz crystal microbalance

For the measurement of the deposition rate, a commercially available quartz crystal microbalance (QCM) *IL150* from *Intelmetrics Global Ltd* with a gold coated 14 mm diameter crystal without water cooling has been used. As described in section II, the QCM was introduced to the chamber using the same mount as used for the PTP. Due to the different probe geometry, the QCM sensor was positioned at a slightly farther distance of 20 mm to the target surface at standard position. Since the QCM detects the change of mass on the quartz crystal, it is necessary to provide material specific constants to allow the calculation of the deposition rate in nm/min ²³. Since, the determined deposition rate calculated from the change of mass is directly proportional to the assumed film density that has been set as an input parameter in the IL 150, it is necessary to obtain realistic densities for the different utilized targets. This was achieved by performing test depositions at different parameters allowing to deduce effective densities from thickness and weight measurements. The resulting densities which were used for the determination of the deposition rates presented in section IV A are summarized in table II. It should be noted that the measured densities are lower as compared to the values of bulk metals which is due to the highly porous character of deposited nanoparticle films.

Although the determined densities from these test depositions showed relatively small errors, later depositions with different substrate holder configurations or substrate material showed strongly deviating results. For this reason, the results of the QCM are only evaluated regarding their relative changes for each investigated target. Here it should be noted, that the change of film density for the different investigated conditions will result in somewhat erroneous deposition rates. However, this effect is expected to be small compared to the general trends and is not further considered for sake of simplicity.

B. Passive thermal probe

For the energy flux measurements inside the aggregation chamber a passive thermal probe was side-mounted

Table I: Experimental parameters used for the parameter variations performed for three different targets, with the varied values printed **bold**. All experiments were performed with argon and the magnetron in was operated in current regulated mode. The standard condition was chosen to be at 16 mm distance to the target, 500 mA current and 60 Pa pressure.

	variation of distance	variation of current	variation of pressure
distance (mm)	16 - 66	16	16
current (mA)	500	50 - 500	500
pressure (Pa)	60	60	20 - 210

Table II: Experimentally determined film densities for the three investigated targets.

target material	density (g/cm ³)	
	bulk	determined
composite (Cu/37W)		11.4 ± 0.9
copper	8.96	7.4 ± 0.6
tungsten	19.3	11.4 ± 0.8

at a distance of 16 mm to the magnetron target and facing the target (see figure 1). A detailed description of this probe and the evaluation of the measurement is presented here as the understanding of the procedure is important for the discussion of the results in section IV. The probe utilized in the experiments consists of a sensor plate (substrate dummy) made of copper with a diameter of 11 mm and a thickness of 70 μm . Spot-welded to the back of it is a Type K thermocouple and an additional copper wire for biasing and current readings²⁴. The sensor plate is surrounded by a metallic shielding to make sure, that only contributions from the upper half-space are considered. A schematic drawing of the PTP design is shown in figure 3.

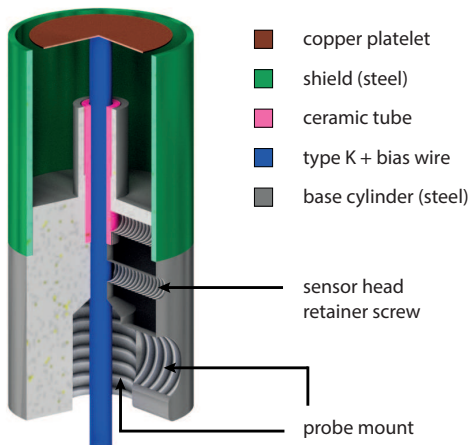


Figure 3: Schematic drawing of the PTP sensor head. The Type K thermocouple and the bias wire are spot-welded to the back of the copper platelet that represents the substrate. The whole sensor is housed in a stainless steel cylinder to shield it from any surrounding influences other than the ones coming from the upper half-space.

It should be noted that the PTP always measures a time-averaged and integrated energy flux that is generated by various energy sources and processes such as charged and neutral particles, surface processes like film formation or radiation from a hot target or chamber walls, respectively. The basic idea of the PTP is to calculate the energy flux from the relation between the time derivative of the enthalpy (\dot{H}) and the time derivative of the temperature (\dot{T}_s) of a well defined substrate dummy. During the heating (T_h - energy source on) and the cooling (T_c - energy source off) of the substrate dummy this relation yields:

$$\text{Heating: } \dot{H}_h = C_s \dot{T}_h = P_{in} - P_{out,h} \quad (1)$$

$$\text{Cooling: } \dot{H}_c = C_s \dot{T}_c = -P_{out,c} \quad (2)$$

Here C_s is the heat capacity of the probe, P_{in} gives the power from the source and $P_{out,h}$ and $P_{out,c}$ denote the power leaving the probe during heating and cooling, respectively. Assuming that the negative cooling terms of equation 1 and 2 are equal for the same substrate temperatures ($P_{out,h}(T_s) = P_{out,c}(T_s)$), the equations for heating and cooling can be combined to calculate the energy flux J_{in} :

$$J_{in} = \frac{P_{in}}{A_s} = \frac{C_s}{A_s} (\dot{T}_h - \dot{T}_c), \quad (3)$$

There are several different methods of evaluating calorimetric temperature curves, however, if the power source is capable of fast switching between off- and on-states, the most desirable method is the so-called *kink method*. The main reason for this is that for the assumption of equal cooling terms during the heating and the cooling phase, any energy flux originating from secondary heat sources has to be constant for the investigated time period. When evaluating with the *kink method*, as described in²⁵, only a short time period of about 2 s around the kinks between the cooling and heating phases are evaluated. This means, that the above-mentioned assumption only needs to apply in this short time frame. Accordingly, any contribution to the energy flux which is relatively constant during this time period does not significantly influence the measured energy flux. Through different measurement procedures, this allows to eliminate certain effects from the measurement results. For example in the case investigated in this study, the contribution from target radiation does not appear in the measurement since the target temperature can be assumed

to be approximately constant during the short measurement time of a few seconds. If instead, the probe would be turned away on plasma shut-off or if a cooled shutter is used to shut off the energy flux, the target radiation would be included in the measurement.

The kink that evolves when switching the power source on from an off-state is referred to as heating kink and the kink that is created when the power source is switched off again, and the next cooling phase starts, is referred to as cooling kink. From both kinks an accurate measurement of the energy flux at these times is obtained and any potential discrepancy between those two results can already be a valuable hint for the stability of the investigated process and the reliability of the measurement method. In figure 4 an exemplary temperature curve with clearly labeled cooling and heating phases as well as evaluated points and corresponding linear fits around the kinks are presented.

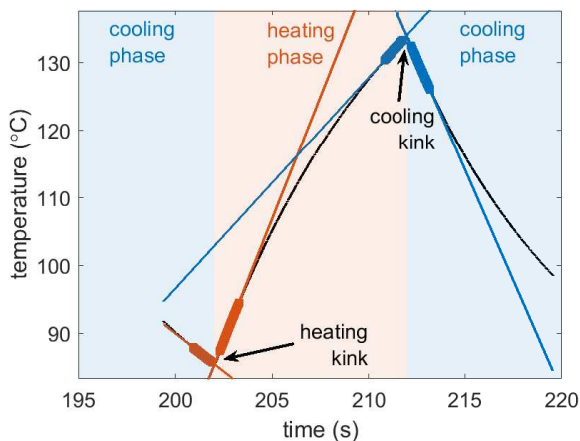


Figure 4: Exemplary evaluation of a PTP curve with heating and cooling kink. The highlighted areas in red and blue denote the data points that were used for the linear fits.

By subtracting the slopes of the two linear fits around the kinks, $\dot{T}_h - \dot{T}_c$ can be easily obtained and the energy flux can be calculated from equation 3, using the heat capacity C_s and surface area A_s of the probe. The heat capacity was determined before and after the measurement campaign using a calibration experiment introduced in²⁴. The obtained values $C_{s,before} = 0.027$ J/K and $C_{s,after} = 0.036$ J/K show a significant deviation which is a result of the film deposited on the probe surface through the course of the measurement campaign. Figure 5 shows a microscopic photograph of the cross section of this film onto the PTP, where the temporal sequence of the measurements are mirrored by the color of the coating; first the copper target was investigated, second the composite target and last the pure tungsten.

To compensate for the gradual increase of the heat capacity, for each variation the value used for the evaluation of the PTP data was approximated by an interpolation taking into account the time the probe was exposed

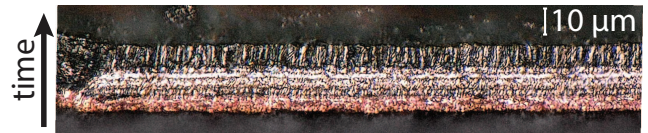


Figure 5: Photograph of the deposited film on the PTP after the measurement campaign. The film was broken off from the probe and investigated under a microscope. Note the copper layer at the bottom exhibiting a somewhat grainy growth structure, followed by the film deposited with the composite target (middle layer) and the top tungsten layer, which exhibits a more columnar growth structure.

to the plasma e.g. for the data from the first variation (distance-Cu) the initial value of 0.027 J/K was used, for the variation in the middle (e.g. pressure-Cu/37W) an adjusted value of 0.030 J/K was used and for the last variation (pressure-W) the final value of 0.036 J/K was used.

IV. RESULTS AND DISCUSSION

A summary of the results obtained with the QCM and the PTP together with the corresponding values of the magnetron power are presented in figure 6. In the following section these complex correlations will be described along the discussion focused on the calorimetric results using QCM and Langmuir data to gain insights into the composition of the energy flux. The SEM images are used to provide a concrete connection between the measured values and the nanoparticle growth and are shortly discussed at the end of this section.

A. Deposition rate

The trends for the deposition rate, which were obtained for the parameter variations introduced in table I, are shown in the second row of figure 6. Here we observe an almost linear trend for the distance- and the magnetron current variation, while the pressure variation exhibits a somewhat more complex dependence.

In a simple model, the deposition rate is mostly defined by two basic processes: (i) the production of sputtered atoms and (ii) the transport of sputtered atoms. The production of sputtered atoms depends on the sputter yield γ_s and the amount of species (energetic ions and neutrals) impinging on the target surface. A characteristic value which can be associated to the latter quantity, is the magnetron current since it is approximately proportional to the amount of kinetic species arriving at the target surface. The sputter yield can be expected to be a function of the mass ratio between target and impinging species as well as of the energy of the impinging particles. This dependence has been investigated and semi-empirically described by many groups, however, especially for the lower energy range, still no universally accepted model is

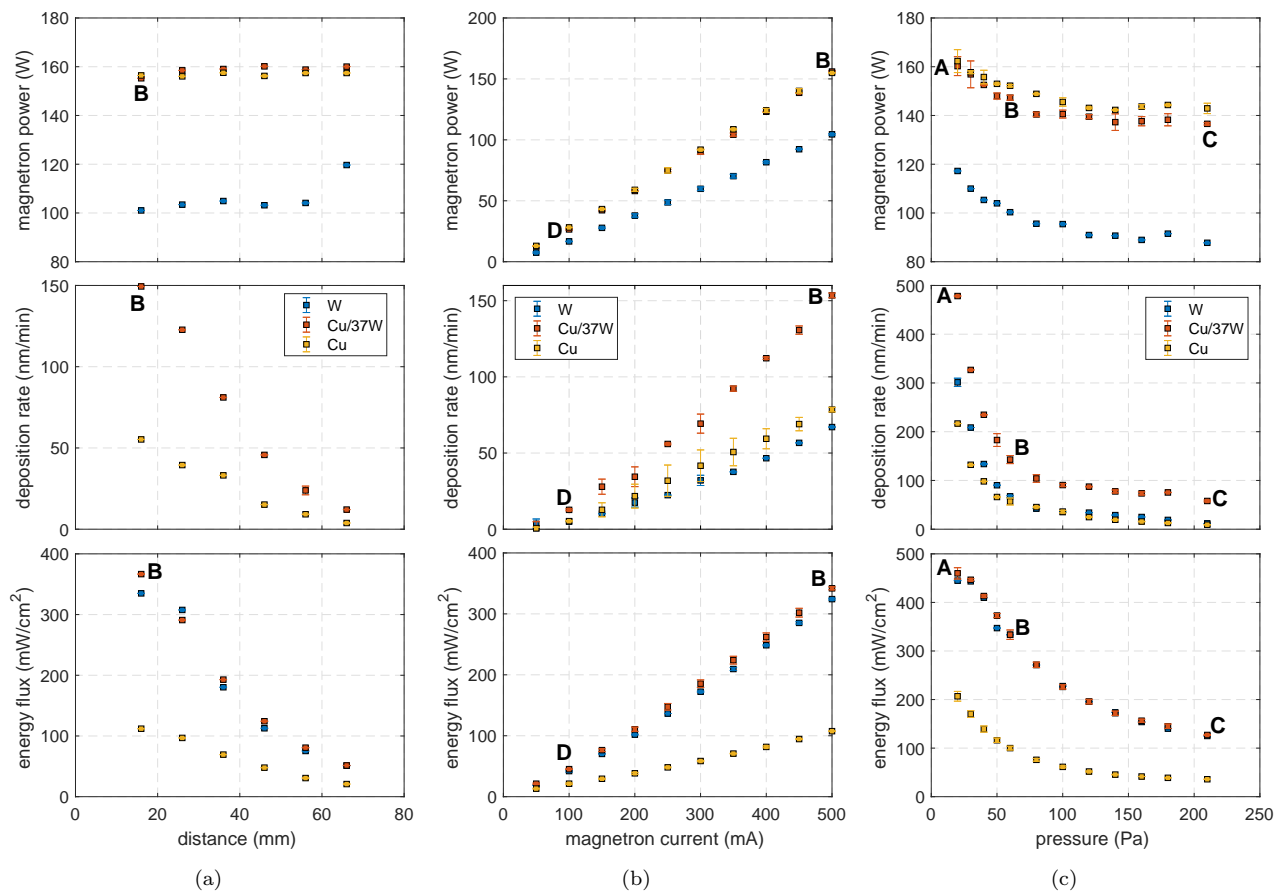


Figure 6: Summary of the deposition rates obtained for the investigated targets and parameter variations. (a) variation of distance between probe and target with 500 mA current and 60 Pa. Unfortunately, no distance variation while measuring the deposition rate for tungsten has been performed. (b) variation of magnetron discharge current at 60 Pa and 16 mm distance, (c) variation of gas pressure with 500 mA current at 16 mm. Error bars obtained from repeated measurements are shown for the variation of magnetron current (b) and argon pressure (c), although in the latter case no repeated measurements were performed with tungsten. For most conditions the energy flux measurements showed a very good reproducibility, making the error bars smaller than the data points. The bold letters mark the data points for the corresponding SEM images (see fig. 9 and 10) in the different conditions.

available^{26,27}. However, qualitatively all studies describe an approximately linear increase with increasing energy of the bombarding species and impinging- to target-mass ratio for the parameter region relevant in this study²⁸. Taking into account the changes of magnetron power presented in the first row of figure 6b, the observed evolution of deposition rate as a function of the magnetron current can be understood directly due to the changes in particle production. For Cu and W we observe an increase of the deposition rate with an approximately linear dependence, while for Cu/37W we observe an above linear increase as a function of the magnetron current. This evolution is mostly driven by the increase of the amount of kinetic atoms arriving at the target cathode which was increased by one order of magnitude. While this would result in a strictly linear dependence, the effect of increased magnetron voltage ($\Delta U_{mdx} \sim 40$ V from 50 mA to 500 mA) provides an additional factor due to the aforementioned

increase in sputter yield.

To explain the results obtained for the variation of distance and pressure (second row figure 6a and 6c), the transport of the species from the target to the probe surface needs to be taken into account as well. In the investigated pressure regime the transport is strongly dominated by collisions with the background gas and with a mean free path in the sub-millimeter range, a diffusion-dominated transport can be expected. Using the common approach based on a Maxwellian gas with collisions described by the Poisson distribution, the mean free path λ_{mfp} for copper and tungsten in argon can be plotted as a function of the background pressure as shown in figure 7²⁹. When comparing this figure to the deposition rate obtained for the pressure variation, the resemblance between the two curves suggests, that the observed dependence is dominantly defined by the collision frequency of the sputtered particles with the background gas. This

trend is additionally amplified by the increase in magnetron power and voltage shown in the first row of figure 6c which leads to an increased sputter yield for lower pressures.

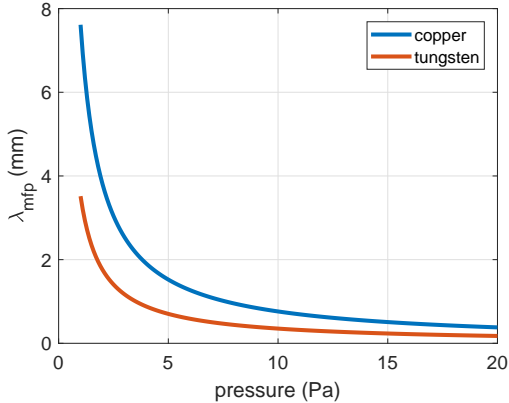


Figure 7: Calculation of the mean free path for copper and tungsten in argon at 300 K according to kinetic gas theory.

The linear decrease for greater distances between target and probe can be directly understood as a result of the linearly increasing number of collisions the sputtered particles undergo as they drift towards the probe. While the axial drift does not result in a decreasing flux, the diffusion perpendicular to the chamber axis and associated losses on the wall result in a decrease of the sputtered flux. For comparable systems with diffusion transport this has been theoretically and experimentally observed by Westwood³⁰ and Ecker et al.³¹.

The conspicuous deviation between the values obtained by the QCM for the compound target compared to the other two targets are not explicable from the data obtained in this study. Since separate determination of the deposition rate by sample deposition and subsequent measurement of the film thickness have not shown a strongly increased deposition rate for Cu/37W, the deviation is likely attributed to some systematic error. Similarly, the absolute QCM values for Cu and W did not match with the values obtained from sample depositions and ex-situ investigations that were performed for selected discharge parameters. The similarity, in spite of different sputtering yields, between copper and tungsten is thus likely attributed to systematic errors as well.

B. Energy flux measurements

As described in section III B, the energy flux obtained with the PTP is a time- and energy integrated quantity which reflects the energy flux originating from a complex set of processes^{29,32}. In the case of magnetron sputtering in the conventional pressure regime of up to a few Pa, important contributions typically arise from the kinetic impact of particles (ions, electrons, energetic neu-

trals), from recombination processes at the surface or from the sublimation enthalpy which is released during film formation on the substrate. In typical DC magnetron sputtering experiments, the contributions originating from the ion-electron recombination and the kinetic flux of ions and electrons to the probe surface only contribute a few percent unless the substrate is biased to voltages significantly different from the floating potential^{33,34}. The Langmuir measurements performed in this study resulted in ion current densities in the range of $10^{-3} - 10^{-1}$ mA/cm², maximum differences between plasma and floating potential of ~ 12 V, approximate electron temperatures of around 2 eV and electron densities of $\sim 10^{15}$ m⁻³. According to the common theory described, e.g. by Kersten et al.³⁵ and Depla et al.³⁶, the contribution due to ions and electrons can be easily calculated to be in the range of only a few mW/cm². Considering the measured energy flux values of up to several 100 mW/cm², the observed trends must, thus, be determined by other contributions like film condensation, kinetic neutral particles or radiation from the plasma or the cathode, respectively.

As the pressure increases and accordingly the mean free paths of ions and neutral particles decreases to values several times smaller than the distance between substrate and cathode, an increasing amount of energy is transferred to the Ar background gas. This transfer of kinetic energy into the gas volume was investigated by Hoffman for a cylindrical magnetron sputtering source and resulted in the concept of 'sputtering wind' which illustrates the directional non-uniform aspect of these energetic fluxes³⁷. Inspired by this work, a detailed study investigating the reduction of the gas density in front of a planar magnetron cathode has been performed by Rosnagel³⁸. Herein, the so called 'rarefaction' of the gas was measured as an apparent pressure reduction and was thoroughly investigated for different combinations of gases and target materials. These investigations revealed a density reduction of up to 85% for high pressure (4 Pa) and high magnetron power and pointed out the sputtered particles as the main driver of the gas rarefaction. Using the Monte Carlo technique, Turner³⁹ calculated similar results which coincided with the observations made by Rosnagel. From these calculations, additional parameters affecting the efficiency of the energy coupling between the sputtered and the background gas atoms have been identified. Besides the sputtering yield, the binding energy of the target material and the collision cross-section and average fraction of energy transferred between sputtered particles and background gas have all been found to produce greater rarefaction for higher values. The corresponding values for the two materials used in this study are summarized in table III.

Although the above-mentioned measurements and simulations were performed in a lower pressure regime (<20 Pa), the same principles apply in the GAS discharge investigated in this study. As mentioned above, due to the short mean free paths, we expect the sputtered flux to

Table III: Relevant parameters for energy transfer from sputtered atoms to the background gas: sputtering yield Y for sputtering ion energy of 300 eV⁴⁰, binding energy E_{bin} , collision cross-section σ ²⁹ and average fraction of energy transferred from the sputtered atom per collision R_{te} ³⁰. The last column gives the energy reflection coefficient R_E of the target material for bombardment by 400 eV argon ions^{41,42}.

	Y	E_{bin} (eV)	σ (nm ²)	R_{te}	R_E
Cu	1.59	3.5	0.54	0.57	0.01
W	0.40	8.8	1.18	0.31	0.12

be thermalized within a short distance from the cathode surface. However, as demonstrated by Urbassek et al. this distance is significantly underestimated if the coupling between the energetic copper particle flow and the argon background gas is neglected⁴³. It is difficult to estimate the exact distance where the gas reaches the highest temperature or to estimate the actual mean free path, however, taking into account the obtained measurement data, we can make the following assumptions for our system:

- I. strong rarefaction with severe reduction of gas density close to the target surface
- II. the rarefaction is dominantly driven by the sputtered metal atoms
- III. due to the rarefaction, the mean free path for reflected Ar neutrals is sufficiently long for them to reach the probe with high energies

Assumptions I. and II. can be directly derived from the recorded magnetron power. A typical signature of rarefaction is the increase of magnetron voltage due to the increased impedance of the plasma³⁸. From the parameters given in table III it can be expected, that the rarefaction is more pronounced and strongest at a position much closer to the target for the cases where copper is present in the system as compared to the case where only tungsten is driving the rarefaction. This can be understood as a result of the shorter mean free path and more efficient energy exchange between the sputtered atoms and the background gas. The resulting reduction of gas density can be observed as an increase in magnetron voltage and power in the first row of figure 6. Here we see almost identical values for the pure copper and the composite target while for tungsten persistently lower values are obtained. Although this could be an effect of different secondary electron yields of copper (1.3) as compared to tungsten (1.0)⁴⁴, this should actually result in a lower required voltage for copper as for tungsten to sustain the same current setpoint. However, figure 6 exhibits higher voltage values for copper which contradicts with this hypothesis and emphasizes the importance of rarefaction for the discharge parameters in this pressure regime. The similarity observed between the composite target and the pure copper target also underlines the dominance of copper as a driver of the rarefaction close to the target and

it indicates that the rarefaction close to the target is already saturated with the amount of copper available from the composite target.

Assumption III. can be derived from the similarity between the energy flux of the composite and the tungsten target which is observed in all measurements in the third row of figure 6 and from an analysis of the possible contributions to the integral energy flux.

From the Langmuir probe measurements it was derived that the energy flux is not strongly affected by the contribution due to electrons and ions and must, therefore, originate from other processes. The plasma radiation can also be eliminated from the list of possible origins, since the typically observed values^{41,45} are too low and the expected changes do not reflect the observed trends. Thus, the energy flux can only be attributed to the sputtered particles, to the reflected particles or to the conduction from the heated gas.

In terms of energy flux, rarefaction can primarily be understood as a loss mechanism. Since the directed energy flux of the sputtered particles is transformed into thermal energy of the gas, the energy is transferred less directly and with losses due to the isotropic nature of the energy flux from the heated gas. In general the maximum of gas temperature can be expected to be close the region where the majority of the sputtered particles are thermalized. For the investigated high pressures we expect this region to be quite close to the target i.e. less than 16 mm away from the target. While the sputtered atoms are expected to be mostly thermalized, the longer mean free path of the fast reflected argon atoms allows them to reach the probe with a significant fraction of their initial energy. The energy flux should, thus, be a composition of the energy released during the film formation, the kinetic energy transferred upon impact of reflected argon and the heat conducted from the hottest point of the gas towards the substrate surface. As mentioned above, this last contribution increases as a result of stronger energy losses of the sputtered atoms and is expected to be strongest for copper, since the most efficient rarefaction is expected for this material. If this effect would be critical for the energy flux we should expect, analogous to the results of the magnetron power, a similar energy flux for the copper- and the composite target. Instead, we observe a strong resemblance between the energy flux of the composite- and the tungsten target. This observation suggests that the energy flux is directly related to the presence of tungsten in the target. From table III it can be seen that tungsten exhibits more than twice the binding energy of copper, which accordingly results in about twice the energy flux from film condensation per deposited atom. However, to achieve energy flux values as high as obtained here solely from the released heat of condensation, deposition rates five times the values observed in the QCM measurements would be required. Therefore, the energy deposited by the reflected argon is assumed to be the dominant contribution to the integral energy flux, especially in the cases of the composite

and the tungsten target. The energy reflection coefficient R_E describes the ratio of energy reflected from the target upon impact of an ion and is given in table III for the case of 400 eV argon ions. Due to the small mass ratio between argon and tungsten, more than 10% of the energy is reflected in the form of fast neutrals, while for copper only about 1% is reflected. From figure 2 it is visible that for the composite target, a high percentage of the racetrack area is made up of tungsten and we can, thus, expect a comparable amount of fast reflected particles as compared to the pure tungsten target. Taking into account the different magnetron powers, a similarly high energy flux between the two target systems can be expected. We conclude that the kinetic energy from the sputtered particles is likely dissipated by the heating of the gas and that conduction of heat through the gas only contributes a relatively small portion to the integral energy flux. The energy released during film formation is expected to contribute a considerable amount. However, it is found to be significantly smaller than the energy flux attributed to the kinetic impact of reflected neutral particles.

Since the energy flux can be understood as power transfer from the target towards the substrate, it is expected that it changes proportionally with the input power of the magnetron. If a strong change in power is present, this usually dominates the change in the energy flux as it is evident in the strong resemblance between magnetron power and energy flux for the variation of the magnetron current (see figure 6b). Eliminating this direct proportional effect, the measurement data allows for better comparison between different systems and emphasizes other, less dominant effects. One way to achieve this is by combining the results obtained for the magnetron power P_{mag} and the energy flux J_s to calculate a value for ratio η of the power transfer with the following equation:

$$\eta = \frac{J_s}{P_{mag}/A_{mag}}, \quad (4)$$

with A_{mag} being the target surface area. Such normalized results are summarized in figure 8.

After taking into account the increased magnetron power for Cu and Cu/37W, tungsten exhibits the highest energy flux values compared to the other two targets in all variation runs (see figure 8). A similar difference in energy flux between Cu and W has been observed by Harbauer et al.⁴⁶ in the conventional lower pressure regime. Although they observed three times higher deposition rates for copper as compared to tungsten, they obtained three times higher values for the energy flux for tungsten, which was argued to likely be a result of the higher heat of condensation (8.8 eV for W, 3.5 eV for Cu⁴⁷). Thornton et al.^{45,48} obtained similar results from their investigations of the energy flux per deposited atom. They found that the energy transfer per deposited particle of tungsten yields about eight times the one obtained for copper. Additional to the aforementioned higher heat of condensation, Thornton points out the importance of

reflected argon atoms with energies up to the cathode potential as an important contribution.

Although these investigations were done at a pressure of roughly 1 Pa, the findings coincide with our results shown in figure 8 and, thus, they further support the assumption that the relevant contributions to the integral energy flux in the higher pressure regime of 20 - 210 Pa are similar to the ones found in the conventional pressure regime.

Albeit, as argued in section III A, the absolute values obtained for the deposition rate likely exhibit a significant systematic error, for sake of comparison we shall use them here to obtain an estimate for the obtained energy per deposited atom. E.g. for the variation of the magnetron current we calculate relatively constant energies per atom of ~ 500 eV for tungsten and ~ 100 eV and ~ 150 eV for pure copper and the composite target, respectively. As argued above, these values are too high to be only a result of film deposition, but are most likely attributed to the impact of reflected neutrals and heat conduction through the gas. Compared to the values obtained by Thornton et al., our values are approximately 5 times higher and compared to Drüsedau et al.⁴¹, they are 2.5 times higher. In agreement with the observations by Drüsedau who observed a linear increase of the energy per atom in the pressure regime from 0.1 - 10 Pa, we observed a comparable increase for pressures below 60 Pa. Taking this trend into account the higher values obtained in this study fit reasonably well with the results obtained by the studies in the conventional pressure regime. Drüsedau also supports the assumption that reflected neutrals play a significant role as a part to the energy flux since they calculated the fast neutrals to account for roughly 75 % of the energy per atom in the case of tungsten (figure 9b in⁴¹).

The observation that the composite target exhibits slightly lower normalized energy flux values than the pure tungsten can be understood as a combination of the smaller contribution from film formation due to the smaller binding energy of copper and a reduction of the contribution from reflected neutrals as a result of the reduced race track area covered by tungsten.

C. SEM investigations

To investigate the effect of the different energy flux values on film formation and to compare them to the well-established structure zone model, additional investigations have been performed by an ex-situ study of four deposited films using the composite target at a substrate distance of 16 mm. Three films were deposited with 500 mA and pressures of $p = 20$ Pa, $p = 60$ Pa and $p = 210$ Pa and one film was deposited with a lower current of 100 mA at 60 Pa. The deposited films have been investigated using a scanning electron microscope (SEM) and are presented in figures 9 and 10.

In figure 9 it can be seen that the sample for the low-

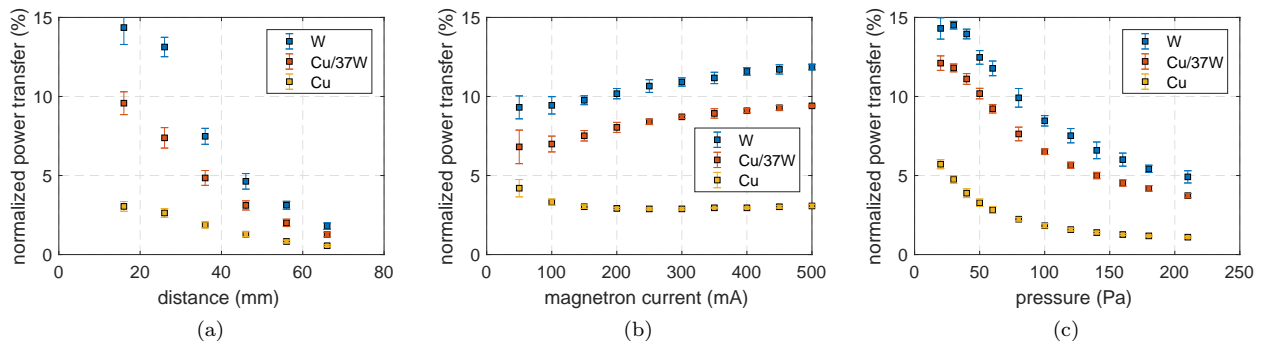


Figure 8: Summary of PTP results normalized with the magnetron power according to equation 4. (a) variation of distance between probe and target with 500 mA current and 60 Pa, (b) variation of magnetron discharge current at 60 Pa and 16 mm distance, (c) variation of gas pressure with 500 mA current at 16 mm.

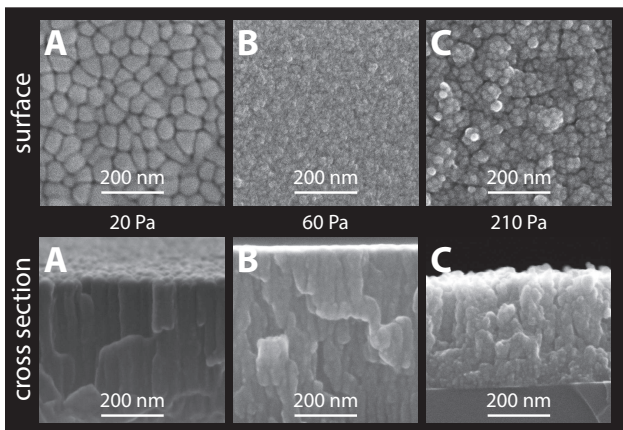


Figure 9: SEM images of deposited film structures using the Cu/37W composite target. The first row shows top view images of the film surface and the second row shows cross sections revealing the growth structure. All depositions were performed at a distance of $d = 16$ mm and a magnetron current of $I_{mag} = 500$ mA. The bold letters correlate to the letters in figure 6, indicating the corresponding magnetron power, deposition rate and energy flux.

est pressure (20 Pa) exhibits a structure as it is known from common film growth. The columnar growth appears to be significantly disrupted by particles and less organized for 60 Pa and at 210 Pa the film appears to be completely composed of bigger particles. Comparing the structure observed for the 20 Pa sample to the structure zone diagram (SZD) by Thornton⁴⁹ or Movchan and Demchishin⁵⁰, we find a zone 1 structure which was observed by Thornton for the highest investigated pressures (~ 4 Pa) or at low substrate temperatures independent of the pressure. The surface exhibits tapered crystallites separated by voids and the structural growth direction is characterized by the incoming particle flux.

Similar to the case for 210 Pa (C), for condition of 100 mA magnetron current and 60 Pa pressure (D) we find a film which is completely composed of particles as

shown in figure 10. However, now the particles exhibit a distinctively different form and size. While in C the film appears to be formed from relatively evenly sized ~ 20 nm particles or clusters of those particles, in D we find a variety of different particles with smooth surfaces and sizes ranging from ~ 20 nm to 100 nm. This difference indicates, that the particles in D were formed at a lower rate by surface growth (attachment of single atoms), whereas the particles in C are likely formed by cluster-cluster collisions. Taking into account the more structured film obtained in B at the same pressure of D but at a significantly higher magnetron current, the role of rarefaction and initial energy of the sputtered atoms for the NP formation becomes apparent.

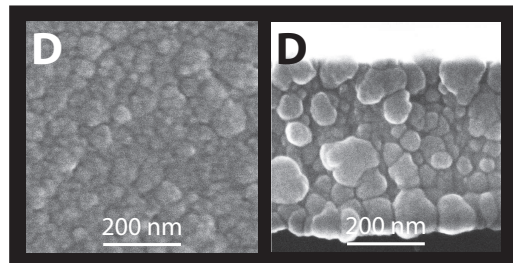


Figure 10: SEM images of deposited film structures using the Cu/37W composite target in 60 Pa at a magnetron current of 100 mA. The left image shows the surface and the right one a cross section of the film. The bold letters correlate to the letters in figure 6, indicating the corresponding magnetron power, deposition rate and energy flux.

V. CONCLUSIONS

Although gas aggregation cluster sources are usually operated in higher pressure regimes than conventional DC magnetron sputtering systems, the basic mechanisms contributing to the integral energy flux are comparable. The current study confirms that contributions from

charged particles (i.e. electrons and ions) and radiation have comparably small influences on the integral energy flux. Similar to the conventional low pressure sputtering regime the integral energy flux is mainly driven by the contribution due to film condensation and reflected neutrals, with the latter being strongly dependent on the mass ratio between gas and target atoms. This was especially evident in the strong resemblance observed in the energy flux between the pure tungsten and the composite target. Gas rarefaction and its accompanying effects were argued to be a significant mechanism in the investigated system as the reduction of the gas density and the associated increase in λ_{mfp} allowed the reflected neutrals to reach the substrate surface with high energies creating a significant contribution to the energy flux.

ACKNOWLEDGEMENTS

This work was partially funded by GACR 17-22016S from the Grant Agency of the Czech Republic.

REFERENCES

- ¹C. Binns, "Nanoclusters deposited on surfaces," *Surface Science Reports*, vol. 44, pp. 1–49, oct 2001.
- ²K. Wegner, P. Piseri, H. V. Tafreshi, and P. Milani, "Cluster beam deposition: a tool for nanoscale science and technology," *Journal of Physics D: Applied Physics*, vol. 39, pp. R439–R459, nov 2006.
- ³C. Cassidy, V. Singh, P. Grammatikopoulos, F. Djurabekova, K. Nordlund, and M. Sowwan, "Inoculation of silicon nanoparticles with silver atoms," *Scientific Reports*, vol. 3, p. 3083, dec 2013.
- ⁴P. Solař, I. Melnichuk, A. Artemenko, O. Polonskyi, O. Kylián, A. Choukourov, D. Slavínská, and H. Biederman, "Nylon-sputtered plasma polymer particles produced by a semi-hollow cathode gas aggregation source," *Vacuum*, vol. 111, pp. 124–130, jan 2015.
- ⁵U. R. Kortshagen, R. M. Sankaran, R. N. Pereira, S. L. Girshick, J. J. Wu, and E. S. Aydil, "Nonthermal Plasma Synthesis of Nanocrystals: Fundamental Principles, Materials, and Applications," *Chemical Reviews*, vol. 116, pp. 11061–11127, sep 2016.
- ⁶K. Sattler, J. Mühlbach, and E. Recknagel, "Generation of Metal Clusters Containing from 2 to 500 Atoms," *Physical Review Letters*, vol. 45, pp. 821–824, sep 1980.
- ⁷H. Haberland, M. Karrais, M. Mall, and Y. Thurner, "Thin films from energetic cluster impact: A feasibility study," *Journal of Vacuum Science & Technology A: Vacuum, Surfaces, and Films*, vol. 10, pp. 3266–3271, sep 1992.
- ⁸T. Takagi, "Ionized cluster beam (ICB) deposition and processes," *Pure and Applied Chemistry*, vol. 60, pp. 781–794, jan 1988.
- ⁹O. Polonskyi, T. Peter, A. Mohammad Ahadi, A. Hinz, T. Strunskus, V. Zaporozhtchenko, H. Biederman, and F. Faupel, "Huge increase in gas phase nanoparticle generation by pulsed direct current sputtering in a reactive gas admixture," *Applied Physics Letters*, vol. 103, p. 033118, jul 2013.
- ¹⁰B. M. Smirnov, I. Shyjumon, and R. Hippler, "Flow of nanosize cluster-containing plasma in a magnetron discharge," *Physical Review E*, vol. 75, p. 066402, jun 2007.
- ¹¹J. Kousal, O. Polonskyi, O. Kylián, A. Choukourov, A. Artemenko, J. Pešička, D. Slavínská, and H. Biederman, "Characterization of nanoparticle flow produced by gas aggregation source," *Vacuum*, vol. 96, pp. 32–38, oct 2013.
- ¹²P. A. Skovorodko, S. A. Brown, and D. Belić, "Gas Dynamic Considerations for Performance of Nanocluster Deposition System," in *AIP Conference Proceedings*, pp. 203–208, 2011.
- ¹³J. Hanuš, M. Vaidulych, O. Kylián, A. Choukourov, J. Kousal, I. Khalakhan, M. Cieslar, P. Solař, and H. Biederman, "Fabrication of Ni@Ti core-shell nanoparticles by modified gas aggregation source," *Journal of Physics D: Applied Physics*, vol. 50, p. 475307, nov 2017.
- ¹⁴A. Caillard, S. Cuynet, T. Lecas, P. Andrezza, M. Mikikian, A.-L. Thomann, and P. Brault, "PdPt catalyst synthesized using a gas aggregation source and magnetron sputtering for fuel cell electrodes," *Journal of Physics D: Applied Physics*, vol. 48, p. 475302, dec 2015.
- ¹⁵M. Benelmekki, J. Vernieres, J.-H. Kim, R.-E. Diaz, P. Grammatikopoulos, and M. Sowwan, "On the formation of ternary metallic-dielectric multicore-shell nanoparticles by inert-gas condensation method," *Materials Chemistry and Physics*, vol. 151, pp. 275–281, feb 2015.
- ¹⁶M. Tchapyguine, T. Andersson, C. Zhang, and O. Björneholm, "Core-shell structure disclosed in self-assembled Cu-Ag nanoalloy particles," *The Journal of Chemical Physics*, vol. 138, p. 104303, mar 2013.
- ¹⁷G. Krishnan, M. A. Verheijen, G. H. ten Brink, G. Palasantzas, and B. J. Kooi, "Tuning structural motifs and alloying of bulk immiscible Mo-Cu bimetallic nanoparticles by gas-phase synthesis," *Nanoscale*, vol. 5, no. 12, p. 5375, 2013.
- ¹⁸A. Vahl, J. Strobel, W. Reichstein, O. Polonskyi, T. Strunskus, L. Kienle, and F. Faupel, "Single target sputter deposition of alloy nanoparticles with adjustable composition via a gas aggregation cluster source," *Nanotechnology*, vol. 28, p. 175703, apr 2017.
- ¹⁹E. Pérez-Tijerina, M. Gracia Pinilla, S. Mejía-Rosales, U. Ortiz-Méndez, A. Torres, and M. José-Yacamán, "Highly size-controlled synthesis of Au/Pd nanoparticles by inert-gas condensation," *Faraday Discuss.*, vol. 138, pp. 353–362, 2008.
- ²⁰V. M. Serdio, M. A. Gracia-Pinilla, S. Velumani, E. G. Pérez-Tijerina, and W. van der Weil, "Synthesis and Characterization of NiCr Self-Assembled Nanorings," *Journal of Nano Research*, vol. 9, pp. 101–108, feb 2010.
- ²¹R. Wang, O. Dmitrieva, M. Farle, G. Dumpich, M. Acet, S. Mejía-Rosales, E. Pérez-Tijerina, M. J. Yacaman, and C. Kisielowski, "FePt Icosahedra with Magnetic Cores and Catalytic Shells," *The Journal of Physical Chemistry C*, vol. 113, pp. 4395–4400, mar 2009.
- ²²P. Solař, D. Nikitin, J. Hanuš, O. Kylián, M. Vaidulych, M. Cieslar, H. Valentova, and H. Biederman, "Production of heterogeneous copper-tungsten particles," in *Proceedings of the Nanocon*, (Brno), 2017.
- ²³Intelmetrics Global Ltd, "Model IL150 Thickness Monitor - Instruction Manual."
- ²⁴M. Stahl, T. Trottenberg, and H. Kersten, "A calorimetric probe for plasma diagnostics," *Review of Scientific Instruments*, vol. 81, no. 2, pp. 1–5, 2010.
- ²⁵S. Gauter, M. Fröhlich, W. Garkas, M. Polak, and H. Kersten, "Calorimetric probe measurements for a high voltage pulsed substrate (PBII) in a HiPIMS process," *Plasma Sources Science and Technology*, vol. 26, p. 065013, may 2017.
- ²⁶P. C. Zalm, "Energy dependence of the sputtering yield of silicon bombarded with neon, argon, krypton, and xenon ions," *Journal of Applied Physics*, vol. 54, pp. 2660–2666, may 1983.
- ²⁷P. Sigmund, "Elements of Sputtering Theory," in *Nanofabrication by Ion-Beam Sputtering*, no. September 2016, pp. 1–40, Pan Stanford Publishing, nov 2012.
- ²⁸P. Sigmund, "Theory of Sputtering. I. Sputtering Yield of Amorphous and Polycrystalline Targets," *Physical Review*, vol. 184, pp. 383–416, aug 1969.
- ²⁹D. Depla and S. Mahieu, eds., *Reactive Sputter Deposition*, vol. 109 of *Springer Series in Materials Science*. Berlin, Hei-

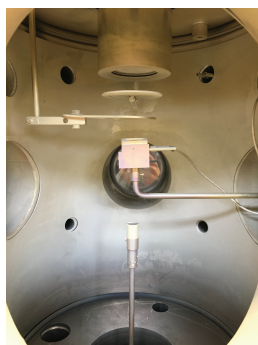
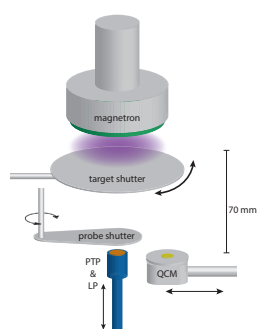
- delberg: Springer Berlin Heidelberg, 2008.
- ³⁰W. D. Westwood, "Calculation of deposition rates in diode sputtering systems," *Journal of Vacuum Science and Technology*, vol. 15, pp. 1–9, jan 1978.
- ³¹G. Ecker and K. G. Emel us, "Cathode Sputtering in Glow Discharges," *Proceedings of the Physical Society. Section B*, vol. 67, pp. 546–552, jul 1954.
- ³²H. Kersten, H. Deutsch, H. Steffen, G. Kroesen, and R. Hippler, "The energy balance at substrate surfaces during plasma processing," *Vacuum*, vol. 63, pp. 385–431, aug 2001.
- ³³R. Wendt, K. Ellmer, and K. Wiesemann, "Thermal power at a substrate during ZnO:Al thin film deposition in a planar magnetron sputtering system," *Journal of Applied Physics*, vol. 82, pp. 2115–2122, sep 1997.
- ³⁴D. Rohde, P. Pecher, H. Kersten, W. Jacob, and R. Hippler, "The energy influx during plasma deposition of amorphous hydrogenated carbon films," *Surface and Coatings Technology*, vol. 149, no. 2-3, pp. 206–216, 2002.
- ³⁵H. Kersten, D. Rohde, H. Steffen, H. Deutsch, R. Hippler, G. H. P. M. Swinkels, and G. M. W. Kroesen, "On the determination of energy fluxes at plasma–surface processes," *Applied Physics A*, vol. 72, no. 5, pp. 531–540, 2001.
- ³⁶D. Depla, S. Heirwegh, S. Mahieu, J. Haemers, and R. De Gryse, "Understanding the discharge voltage behavior during reactive sputtering of oxides," *Journal of Applied Physics*, vol. 101, p. 013301, jan 2007.
- ³⁷D. W. Hoffman, "A sputtering wind," *Journal of Vacuum Science & Technology A: Vacuum, Surfaces, and Films*, vol. 3, pp. 561–566, may 1985.
- ³⁸S. M. Rosnagel, "Gas density reduction effects in magnetrons," *Journal of Vacuum Science & Technology A: Vacuum, Surfaces, and Films*, vol. 6, no. 1, p. 19, 1988.
- ³⁹G. M. Turner, "Monte Carlo calculations of gas rarefaction in a magnetron sputtering discharge," *Journal of Vacuum Science & Technology A: Vacuum, Surfaces, and Films*, vol. 13, pp. 2161–2169, jul 1995.
- ⁴⁰N. Laegreid and G. K. Wehner, "Sputtering Yields of Metals for Ar + and Ne + Ions with Energies from 50 to 600 eV," *Journal of Applied Physics*, vol. 32, pp. 365–369, mar 1961.
- ⁴¹T. P. Dr usedeau, T. Bock, T.-M. John, F. Klabunde, and W. Eckstein, "Energy transfer into the growing film during sputter deposition: An investigation by calorimetric measurements and Monte Carlo simulations," *Journal of Vacuum Science & Technology A: Vacuum, Surfaces, and Films*, vol. 17, pp. 2896–2905, sep 1999.
- ⁴²W. Eckstein and J. P. Biersack, "Reflection of heavy ions," *Zeitschrift f ur Physik B Condensed Matter*, vol. 63, pp. 471–478, dec 1986.
- ⁴³H. M. Urbassek and D. Sibold, "Sputtered atom transport in high-current gas discharges: A self-consistent computer simulation study," *Journal of Vacuum Science & Technology A: Vacuum, Surfaces, and Films*, vol. 11, pp. 676–681, may 1993.
- ⁴⁴R. L. Petry, "Secondary Electron Emission from Tungsten, Copper and Gold," *Physical Review*, vol. 28, pp. 362–366, aug 1926.
- ⁴⁵J. A. Thornton, "Substrate heating in cylindrical magnetron sputtering sources," *Thin Solid Films*, vol. 54, no. 1, pp. 23–31, 1978.
- ⁴⁶K. Harbauer, T. Welzel, and K. Ellmer, "A combined sensor for the diagnostics of plasma and film properties in magnetron sputtering processes," *Thin Solid Films*, vol. 520, no. 20, pp. 6429–6433, 2012.
- ⁴⁷W. M. Haynes, *CRC Handbook of Chemistry and Physics*. Boca Raton, FL: CRC Press, 2014.
- ⁴⁸J. A. Thornton and J. L. Lamb, "Substrate heating rates for planar and cylindrical-post magnetron sputtering sources," *Thin Solid Films*, vol. 119, pp. 87–95, sep 1984.
- ⁴⁹J. A. Thornton, "Influence of apparatus geometry and deposition conditions on the structure and topography of thick sputtered coatings," *Journal of Vacuum Science and Technology*, vol. 11, no. 4, p. 666, 1974.
- ⁵⁰B. A. Movchan and A. V. Demshishin, "Study of the structure and properties of thick vacuum condensates of nickel, titanium, tungsten, aluminium oxide and zirconium dioxide," *Phys. Met. Metallogr. (Engl. Trans.)*, vol. 28, pp. 83–90, jan 1969.

Publication VI

Experimentally unraveling the energy flux originating from a DC magnetron sputtering source

Authors:	S. Gauter, F. Haase, and H. Kersten
Journal:	Journal of Applied Physics (submitted)
Technique:	DC magnetron sputtering (DCMS)
Utilized Probes:	Passive thermal probe (PTP), Quartz crystal microbalance (QCM), Langmuir probe, IR camera
Own contribution:	approx. 40%

Experimental Setup:



Motivation:

This work was aimed at providing a detailed analysis of the energy flux during DCMS and how its main contribution change for different gas-target combinations. Various probe diagnostics paired with visual observation methods like an infrared camera and a scanning electron microscope (SEM) were used.

Main results:

The three main mechanisms that pose a major contribution to the energy flux were identified as the contribution from sputtered particles, reflected neutrals and from a hot target surface. Obviously the sputtered particles have a big influence on the growth structure of the deposited film, reflected neutrals were found to have a great impact as well and can even become the most important contribution to the energy flux depending on the gas-target mass ratio. For target materials with a poor heat conductivity, like titanium, target heat radiation developed a significant influence on the energy flux. The understanding of the driving mechanisms behind the different contributions and on how they transfer the energy to the substrate and the growing film can in principal be used to tailor the composition of the energy flux.

Experimentally unraveling the energy flux originating from a DC magnetron sputtering source

Sven Gauter¹, Fabian Haase¹, and Holger Kersten¹

¹Institute of Experimental and Applied Physics, Kiel University, Kiel, Germany

Abstract

We present investigations of the energy flux in DC magnetron sputtering for 15 different target-gas combinations. The utilized gases were Ar, Kr and He which were studied using targets made of Ag, Al, Cu, Ti and W. The effect of parameter variations (distance, pressure and discharge power) was investigated by calorimetric measurements utilizing a passive thermal probe. For the variation of discharge power, supplementary measurements of plasma parameters and deposition rate were performed using a planar Langmuir probe and a quartz crystal microbalance. The obtained results were used to gain better insight into the different contributions to the integral energy flux. The measurements illustrate clearly that, depending on the target material and on the target gas combination, the main mechanisms generating the energy flux can vary dramatically. For small gas-target mass ratios, reflected neutrals were identified as the main contribution of the energy flux while for combinations with high sputter yield, condensation and kinetic impact of sputtered particles were found to be the most relevant. For thermally poor conducting targets as in the case of titanium, the target can heat up significantly resulting in a strong energy flux from heat radiation which dominates the otherwise modest energy flux.

1 Introduction

One of the major applications present in the large field of plasma technology are plasma-wall interactions such as etching, film deposition and surface modification. In these processes, thermal conditions at the substrate surface are of key interest since they play a dominant role in the final properties of the product. The surface temperature influences elementary processes like adsorption, desorption, diffusion as well as chemical processes like chemical sputtering and surface reactions [1–3]. Especially in the case of thin-film deposition the morphology and stoichiometry of the layers are highly dependent on the thermal surface conditions and on the impact of kinetic particles [1, 4, 5]. As a widespread thin-film deposition technique, magnetron sputtering has been thoroughly investigated and over the years many variations such as reactive sputtering, pulsed DC or high-power im-

pulse magnetron sputtering (HiPIMS) have been developed. In spite of these new developments, the classic metal deposition using DC magnetron sputtering systems is still of high relevance to research and industry alike. Starting from the well noted study by Thornton in 1978 [6] many investigations of the energy flux in these systems have been performed resulting in extensive literature on the topic. Since calorimetric probes provide energy and time integrated values which include a complex mix of different contributions (e.g. from charged particles, neutrals, surface processes, radiation etc.), a persistent point of discussion is the distinction between the several contributions to the integral energy flux. An approved method to obtain more detailed information is the combination of calorimetric measurements with Langmuir probe (LP) and deposition rate measurements. The determined values can be combined to give a simple model of the energy flux and also al-

low the normalization of the measured energy flux on the amount of deposited atoms. Thornton et al. used this procedure in a subsequent study [7] investigating various materials in cylindrical-post and planar magnetron sputtering systems. The same approach was picked up by Drüsedau et al. [8] who additionally combined their experimental results with Monte Carlo simulations. Incorporating the results obtained by Drüsedau, Ekpe et al. [9] developed a sophisticated model to predict deposition rates and calculate the energy per deposited atom. Later, innovative experimental approaches have been presented by e.g. Harbauer et al. [10] who developed a combined sensor of different plasma diagnostics or by Bornholdt et al. [11] who combined energy flux measurements with the bias sweep of a Langmuir probe measurement. Besides the here introduced studies which only represent a small selection and are limited to the area of inert-gas DC magnetron sputtering (DCMS), numerous other studies regarding the energy flux for complex material systems or innovative magnetron sputtering sources have been published, e.g. [12–15]. The work presented here ties in with the basic DCMS studies and seeks to provide a broader overview using a wide range of target-gas combinations investigated for essential parameter variations. Furthermore, the different contributions to the energy flux are analyzed using showcasing examples.

2 Experimental Setup

The experiments were performed in a vacuum vessel (volume of 26 litres) with a top mounted planar DC magnetron sputtering system by *Angstrom sciences* equipped with a water cooled two inch target driven by an *Advanced Energy* MDX 500 power source. The chamber was evacuated by a two stage pumping system consisting of a *Pfeiffer Vacuum* MVP 040-2 membrane pump and a *HiPace* 300 turbo pump which was able to pump the chamber to a base pressure of 10^{-3} Pa. The gas flow was controlled by a *MKS* 647C multi-channel gas flow controller with a pressure control system regulated by a PID controller, which was used for the pressure variations. The pressure was monitored with a Baratron pressure gauge.

For the power and distance variations a constant gas flow value was set. The passive thermal probe (PTP) was mounted on a linear drive inserted at the bottom of the chamber to allow variation of the axial distance between PTP and target. The quartz crystal microbalance (QCM) was introduced from the side through a KF-40 feedthrough mounted on a movable rod (figure 1). The standard distance to the target for all probes was 70 mm, the standard pressure was 2 Pa and the standard magnetron power was chosen to be 50 W. The experimental parameters are summarized in table 1.

For the lower and upper limits in the variations, no stable discharge conditions were reached for He and Kr with some targets and it should be noted that the measurements with helium were performed at a pressure of 2.8 Pa instead of 2 Pa.

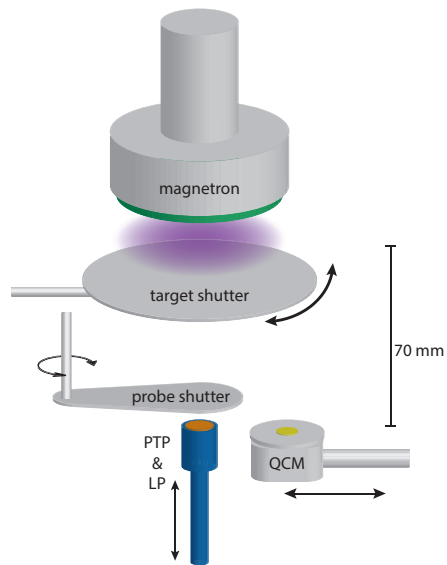


Figure 1: Sketch of the utilized experimental setup with the passive thermal probe, which was also used as a planar Langmuir probe, as well as the QCM which could be moved to the center position.

The magnetron was shut off during the cooling phase of the PTP measurements using the target

Table 1: Experimental parameters used for the parameter variations performed for five targets (Ag, Al, Cu, Ti, W), with the varied values printed **bold**. All experiments were performed with helium, argon and krypton with the magnetron in power regulated mode. The standard condition was chosen to be at 70 mm distance to the target, 50 W power and 2 Pa pressure, however, some extreme values could not be reached when using He or Kr for some targets.

	variation of power	variation of distance	variation of pressure
power (W)	30 - 190	50	50
distance (mm)	70	30 - 160	70
pressure (Pa)	2	2	0.5 - 12

shutter. To minimize the erroneous effect on the calorimetric measurements created by a hot target shutter, an additional shutter close to the probe (probe shutter) was used. Specific test measurements and temperature measurements confirmed that this second shutter remains at a low temperature during the experiments, while a considerable energy flux was detected from the target shutter.

In a subsequent investigation, IR heat camera recordings using an *Optris* PI-D2009-11-A camera were performed to study the effect of target heat radiation. Selected samples of sputter deposited thin films were prepared for analysis with a scanning electron microscope (SEM). A sketch of the discharge chamber is presented in figure 1 illustrating the utilized probes and shutter.

3 Diagnostic tools and simulations

All measurements were performed successively with three different probes (PTP, QCM, LP) centered on the chamber axis at approximately the same distance to the target. For the parameter variations all values were measured twice in a back-and-forth approach to allow a simple estimation of the statistical error and reveal potential effects from e.g. hysteresis. The corresponding plasma parameters and deposition rates were primarily determined to allow an estimation of the energy flux associated with ions, electrons and depositing particles and are, thus, only discussed in these terms.

3.1 Quartz crystal microbalance

For the measurement of the deposition rate, a commercially available quartz crystal microbalance (QCM) IL150 from *Intelmetrics Global Ltd* with a gold coated, 14 mm diameter, 6 MHz crystal has been used without water cooling. Since the QCM primarily detects the change of mass on the quartz crystal, it is necessary to provide material specific constants to allow the calculation of the deposition rate in nm/min [16]. For the different investigated materials, the density and impedance of the bulk material [16] have been used and, thus, the obtained results of the deposition rate may have a tendency to overestimate the actual rate according to the actual density of the deposited film [17].

Deposition rate measurements due to helium sputtering have proven to be difficult since the IL150 was not able to calculate applicable results. Therefore, the deposition rates for helium sputtering were estimated by normalizing the obtained results from argon using the sputter yields for argon and helium obtained from *SRIM* simulations. Later comparison with deposition rates calculated from the sheath thickness measured with the SEM confirmed that this procedure provides reliable values.

3.2 Passive thermal probe

A detailed description of the PTP and the evaluation of the measurement is presented here as the understanding of the procedure is important for the discussion of the results in section 5. The probe utilized in the experiments consists of a sensor plate (substrate dummy) made of copper with a diameter of 11 mm

and a thickness of $70 \mu\text{m}$. Spot-welded to the back of it is a Type K thermocouple and a copper wire for biasing and current readings [18]. For all PTP measurements the probe was not connected to any external potential and was therefore at floating potential. The sensor plate is surrounded by a metallic shielding to make sure, that only contributions from the upper half-space are included in the measurement. A schematic drawing of the PTP design is shown in figure 2.

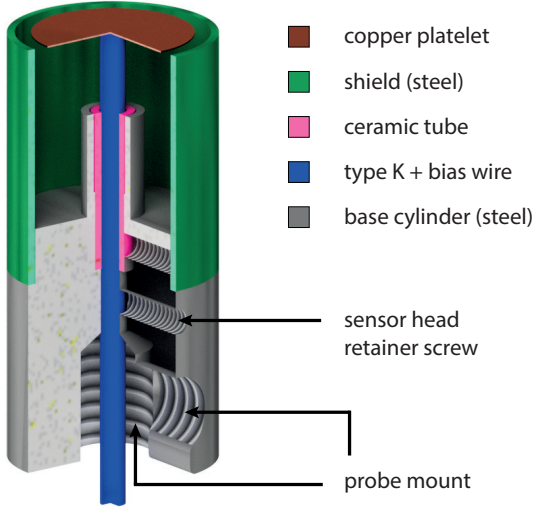


Figure 2: Schematic drawing of the PTP sensor head. The Type K thermocouple and the wire for biasing are spot-welded to the back of the copper platelet that represents the substrate. The whole sensor is housed in a stainless steel cylinder to shield it from any surrounding influences other than the ones coming from the upper half-space.

It should be noted that the PTP measures a time and energy integrated value of the energy flux that is created by various energy sources and processes such as charged and neutral particles, surface processes like film formation or radiation from a hot target or chamber walls, respectively. The basic idea of the PTP is to determine the energy flux from the relation between the time derivative of the enthalpy (\dot{H}) and the time derivative of the temperature (\dot{T}_s) of a well defined substrate dummy. During the heating (T_h - energy source on) and the cooling (T_c - energy source

off) of the substrate dummy this relation yields:

$$\text{Heating: } \dot{H}_h = C_s \dot{T}_h = P_{in} - P_{out,h} \quad (1)$$

$$\text{Cooling: } \dot{H}_c = C_s \dot{T}_c = -P_{out,c} \quad (2)$$

Here C_s is the heat capacity of the probe, P_{in} gives the power from the source and $P_{out,h}$ and $P_{out,c}$ denote the power leaving the probe during heating and cooling, respectively. Assuming that the negative cooling terms of equation 1 and 2 are equal for the same substrate temperatures ($P_{out,h}(T_s) = P_{out,c}(T_s)$), the equations for heating and cooling can be combined to calculate the energy flux J_{in} :

$$J_{in} = \frac{P_{in}}{A_s} = \frac{C_s}{A_s} (\dot{T}_h - \dot{T}_c), \quad (3)$$

There are various methods of evaluating calorimetric temperature curves, however, if the power source is capable of fast switching between off- and on-states or if fast shut-off of the source can be realized due to a shutter system, the most desirable method is the so-called *kink method*, see figure 3. The main reason

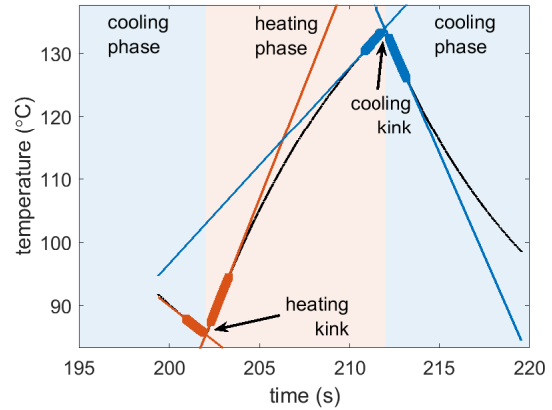


Figure 3: Exemplary evaluation of a PTP curve with heating and cooling kink. The highlighted data points in red and blue denote the data points used for the linear fits.

for this is that for the assumption of equal cooling terms during the heating and the cooling phase, any energy flux originating from secondary heat sources has to be constant for the investigated time period.

When evaluating with the *kink method*, as described in [19], only a short time period of about 2 s around the kinks between the cooling and heating phases are evaluated. This means, that the above-mentioned assumption also only needs to apply in this short time frame. Accordingly, any contribution to the energy flux which is relatively constant during this time period does not significantly influence the measured energy flux. This makes the PTP measurement a truly differential method and efficiently minimizes the influence of parasitical energy flux contributions which change on a slower time scale.

The kink that evolves when switching the power source on from an off-state is referred to as heating kink and the kink the power source is switched off again (start of the next cooling phase) is referred to as cooling kink. From both kinks an accurate measurement of the energy flux at these times is obtained and any potential discrepancy between those two results can already be a valuable hint for the stability of the investigated process and the reliability of the measurement method. In figure 3 an exemplary temperature curve with clearly labeled cooling and heating phases as well as evaluated points and corresponding linear fits around the kinks are presented.

By subtracting the slopes of the two linear fits around the kinks, $\dot{T}_h - \dot{T}_c$ can be easily obtained and the energy flux can be calculated from equation 3, using the heat capacity C_s and surface area A_s of the probe. Since the heat capacity of the probe changes with increasing film thickness, two different PTP probes were used in rotation to minimize the effect of the film which is continuously deposited during the extensive investigations. Using the calibration experiment introduced in [18], the probes were being recalibrated several times throughout the measurements.

3.3 Langmuir probe

The design of the PTP also allows to use the copper plate as a planar Langmuir probe (LP), which is achieved by using an additional wire to apply a bias voltage and measure the resulting current. The measurements were performed using an in-house developed electronics based on a *National Instruments*

USB-6002 card with a sample rate of 50 kHz. A typical measurement takes 4 s, resulting in a total of up to almost 20k data points with a step width of 4.6 mV, depending on the investigated interval. The electron temperature T_e was derived from the slope of the semi-logarithmic current-voltage plot [20]. The plasma potential Φ_{pl} was determined as the intersection between the linear fit used to obtain T_e and the linear fit to the electron saturation regime. In figure 4, two exemplary Langmuir curves are shown for silver in argon and helium, respectively.

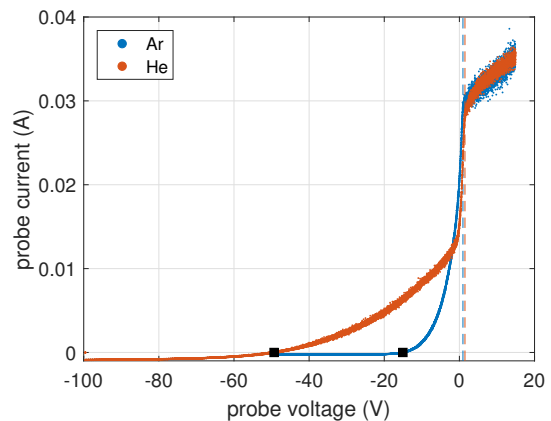


Figure 4: Exemplary Langmuir curves for Ag in Ar (blue data points) and He (red data points) for a discharge power of 90 W at a distance to the target of 70 mm and a gas pressure of 2 Pa and 2.8 Pa for Ar and He respectively. The black square indicates the determined floating potential and the dashed lines the corresponding plasma potentials for Ar and He, respectively.

It can be recognized that for He the LP curve strongly deviates from the typical shape expected for Maxwell distributed electrons, while for Ar a more characteristic planar LP curve is observed. For He, more energetic electrons are present which result in an increase of the current for more negative probe voltages. For argon the floating potential was $\Phi_{fl} = -15.0$ V and the plasma potential $\Phi_{pl} = 1.0$ V, whereas helium exhibited values of $\Phi_{fl} = -49.3$ V and $\Phi_{pl} = 1.5$ V. The more pronounced population of high energy electrons for helium results in a more negative floating potential and a wider gap to Φ_{pl} . The electron temperature T_e was determined for the

population with lower energies as it accounts for the majority of the current, however, it must be noted that this may result in an underestimation of the average electron temperature and correspondingly an underestimation of the calculated electron contribution to the energy flux (see section 4).

3.4 TRIM simulations

TRIM simulations were performed using SRIM-2013 to obtain sputter yields Y_{sp} and the yield of backscattered/reflected particles Y_{refl} as well as the average energy of sputtered and reflected particles E_{sp} and E_{refl} , respectively [21]. The ion acceleration voltage, which is one of the input parameters of TRIM, was derived from averaged values of the recorded power supply readings during the PTP measurements at the standard power setpoint of 50 W. Incident ion angles of 0° up to 30° in a step width of 10° were chosen with 10^5 simulated ions each. The results were corrected by subtracting the surface binding energy of the target material from the energy component of the sputtered particle that is perpendicular to the target since this aspect is not included in the simulation. For further calculations, an average over the values obtained by TRIM simulations for 0° up to 30° was used since we estimate the majority of the incident ions to impact within these angles. Ions with greater incident angles will most likely result in sputtered or reflected particles with such a small angle of emission that they are unlikely to arrive at the substrate (probe) position. We decided to simulate a wider range of incident angles as a method to compensate for the surface roughness. However, it must be noted that the calculated values are taken as a rough estimate only and, therefore, do not claim to quantitatively reflect the real conditions.

From the yields (Y_{sp} and Y_{refl}) and the average energies (E_{sp} and E_{refl}) of the sputtered and reflected particles we also calculated the amount of energy per incident ion which is carried away from the target by sputtered and reflected particles, respectively:

$$\begin{aligned} E_{sp,norm} &= Y_{sp} E_{sp} \\ E_{refl,norm} &= Y_{refl} E_{refl}. \end{aligned}$$

Especially the comparison between these two values can be a useful indicator for the relevance of the sputter or the reflection process for the integral energy flux.

4 Contributions to the energy flux

As described in section 3.2, the energy flux obtained with the PTP is always a time- and energy integrated quantity which reflects the energy flux originating from a complex set of processes [22, 23]. In 1978 Thornton introduced an approximate model to calculate the energy flux for the case of magnetron sputtering with inert gases [24]. This model was based on the contributions from kinetic energy of the sputtered particles J_n , the heat of condensation J_{cond} and the plasma radiation $J_{rad,pl}$. Since then, this model was verified in numerous studies and further refined by additional contributions and sophisticated methods of theoretical calculations. In the following paragraphs the common methods for calculation of the most important contributions relevant for this study alongside some of their limitations are presented. For most of these processes, in reality, certain additional coefficients need to be taken into account. They usually describe the probability or the efficiency of a specific process and range from 0 to 1. The sticking coefficient e.g. describes the probability that a particle sticks to the surface and the energy transfer coefficient describes the percentage of energy transmitted in a collision. For ease of understanding, these coefficients are chosen to be 1 in the following description and also in the absolute calculations presented in this study. As a result, the calculated energy flux represents an 'upper limit estimation' and could, thus, overestimate the actual energy flux. A more generic and detailed description can be found in [22, 23].

4.1 Electrons and ions

The contribution from charge carriers, also called the electric contribution, includes the kinetic energy which is transferred upon impact of electrons or ions on the substrate and the potential contribution which

is released as they recombine. At the floating potential the kinetic contribution is characterized by the equal current densities of ions and electrons j_{fl} and their respective kinetic energies. The kinetic energy of the ions is given by the difference between plasma and floating potential $\Phi_{pl} - \Phi_{fl}$ and in the case of a Maxwellian electron energy distribution function (EEDF) the contribution from electrons can be estimated by the electron temperature T_e . The contribution due to recombination is calculated by the difference between ionization energy Φ_{iniz} and the electron work function Φ_{ewf} . The resulting energy flux can thus be calculated as

$$J_{electric} = \frac{j_{fl}}{e_0} [(\Phi_{pl} - \Phi_{fl}) + 2k_B T_e + (\Phi_{iniz} - \Phi_{ewf})], \quad (4)$$

with the Boltzmann constant k_B and elementary charge e_0 . The variables in equation 4 can be directly obtained from Langmuir measurements and accordingly the errors and uncertainties which are typically associated with Langmuir measurements appear in the calculated electric contribution as well.

4.2 Sputtered particles

Similar to the electric contribution, the contribution from sputtered particles includes a kinetic portion and a potential portion which are both proportional to the flux of sputtered atoms Γ_n . As the sputtered atoms hit the surface of the probe, their kinetic energy E_{kin} is transferred to the probe and as they bind to the film, the surface binding energy E_{bin} is released. The energy flux associated with the sputtered flux can thus be calculated to be:

$$J_{sputter} = \Gamma_n (E_{kin} + E_{bin}). \quad (5)$$

As described in section 3.1, the particle flux can be obtained from QCM measurements. The values for the surface binding energy are taken from literature and are summarized in table 2 for the investigated materials.

The kinetic energy of the arriving sputtered particles is associated with much greater uncertainty. The initial kinetic energy obtained from the sputter process is typically calculated according to the

Table 2: Relevant material properties for the investigated target materials as taken from [25]. E_{bin} gives the surface binding energy, A the atomic mass number, ρ the density of the bulk material and k the thermal conductivity.

	A	E_{bin} (eV)	ρ (g/cm ³)	k (W/(m K))
Ag	108	2.9	10.50	429
Al	27	3.4	2.70	237
Cu	64	3.5	8.96	401
Ti	48	4.9	4.51	22
W	184	8.8	19.30	174

Thompson-formula [26], Monte Carlo simulations or it is determined experimentally [27]. For this study the initial energy is calculated using SRIM [21] as described in section 3.4. The greatest uncertainty, however, arises from the energy loss due to collisions with the background gas which is discussed in section 4.4.

4.3 Reflected neutrals

Reflected neutrals are created as process gas ions get neutralized and reflected from the target cathode. Accordingly, these particles can carry high energies up to the cathode potential, with average energies in the range of ~ 100 eV. The importance of this contribution, especially for the sputtering of heavy targets, was already recognized by Hoffmann and Thornton in 1980 [28] and has since been discussed in numerous works [7–9, 22, 23, 29, 30]. Even though some work has been done to experimentally investigate these fast neutrals by e.g. Rosnagel [31], quantitative measurements are coming with many experimental challenges. Due to this fact, and due to the difficulty of distinction from other energy flux contributions, the effect of reflected neutrals is often neglected or underestimated in the discussion of measured energy flux values. In this work, we consider this contribution by elimination of other contributions which is supported by SRIM simulations as described in 3.4.

4.4 Energy loss due to collisions with the background gas

To understand the energy deposited at the substrate (PTP), one has to take energy losses into account which occur along the way from the target to the substrate surface. These energy losses are governed by the mean free path for collisions between the energetic particles and the background gas λ_{mfp} and by the fraction of energy lost in each collision. The reduction of the initial energy from the sputter process E_{sp} as a function of the distance to the target d can be approximated by

$$E_{kin}(d) = E_{sp} \cdot \exp(-R_{re} d / \lambda_{mfp}), \quad (6)$$

with R_{re} being the remaining fraction of kinetic energy of the colliding particle after one collision. To obtain a rough estimation of this parameter, we calculated an average value as a function of the mass-ratio between impinging sputtered metal atom and the background gas atom. This procedure is inspired by Westwood [32] who integrated the collision equation over all possible collision angles and averaged the result assuming the same probability for each collision angle. However, due to the curvature of the hard sphere, the collision angle does not change linearly with the collision parameter b and, therefore, collision angles close to 90° are overestimated for the assumption made by Westwood. To obtain a more realistic estimation, we calculated the average energy exchange and average angle of deflection for a collision in three dimensions by assuming the probability of the collision parameter to scale with its value. The further from a central collision, the more collision possibilities exist along the radius defined by the collision parameter b . In figure 5 the resulting curves along with calculated values for the gas target combinations investigated in this study are shown together with a small sketch to illustrate the main variables of the collision model. Comparing to Westwood's approach, we obtain the same average angle of deflection and the same values for R_{re} at very uneven masses but smaller energy losses for more similar masses ($0.1 < M_g/M_t < 10$).

Providing a realistic estimation of the mean free path is associated with much greater difficulty and

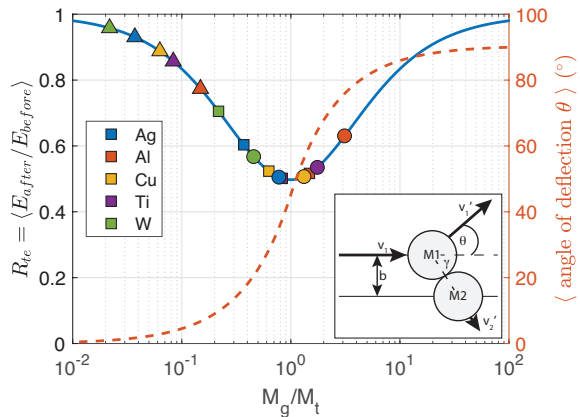


Figure 5: Average remaining energy and average angle of deflection for a collision between two hard spheres as a function of their mass ratio. M_g depicts the mass of the background gas atom and M_t the mass of the sputtered target atom. The values relevant for this study are marked by colored squares (Ar), circles (Kr) and triangles (He) with the different colors representing the different target materials. The values were derived from a simple, elastic 3D hard-sphere collision model.

uncertainty for three principle reasons: (i) as first recognized by Robinson in 1979 [33] the cross section is reduced strongly as a function of the particle energy, (ii) reliable data for cross sections between sputtered atoms and noble gases is rare and usually interpolations from noble gas collision cross sections are used, although one may expect significant discrepancies [29,34,35], (iii) the temperature of the gas can increase strongly as a result of collisions with sputtered particles and reflected neutrals, resulting in a significant increase of the mean free path [36,37]. These points are difficult to resolve experimentally and even though detailed simulations allow to calculate the reduction of the energy of the sputtered atoms and reflected neutrals, they still lack absolute accuracy due to estimated collision cross sections and are furthermore limited to a specific geometry [29]. For our system at standard conditions we estimate that with a pressure-distance product of 140 Pa mm, the sputtered flux is partly thermalized with a smaller fraction of ballistic particles [29,38]. The specific percentage, however, is expected to vary strongly as a

function of the mass ratio i.e. for tungsten in helium the momentum exchange is minimal and almost no deflection of the particles is expected while for silver in argon on average half of the energy is lost in every collision and the direction is changed by 45° , see figure 5.

Although collisions primarily represent a loss mechanism in terms of energy flux, a part of the energy transferred to the gas will also arrive at the substrate as directed background gas atoms - or more isotropic - as thermal energy transferred from the heated gas. As pointed out by Somekh [29] and experimentally shown by Rosnagel [31], the elongated mean free path for faster particles (see figure 6) will also lead to an increased importance of fast reflected neutrals for the energy flux, as they can more efficiently transfer energy from the target to the substrate.

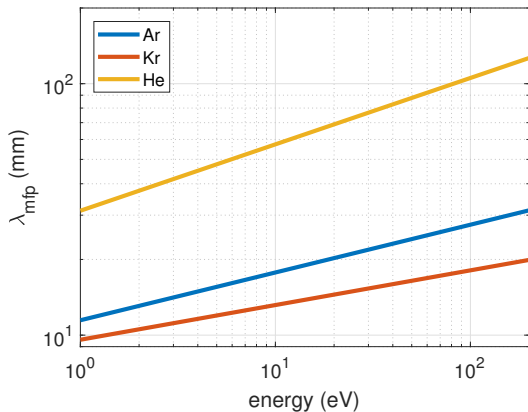


Figure 6: Mean free path for fast noble gas atoms passing through the same noble gas background as calculated according to the Variable Soft Sphere (VSS) model from Koura and Matsumoto [39]. The pressure and temperature used for calculation of the plotted λ_{mfp} are 2 Pa and 350 K.

4.5 Radiation

Energy flux by radiation can principally come from two sources: (i) line radiation from the plasma and (ii) black-body radiation from hot elements in the plasma chamber. Especially the role of line radiation

is difficult to estimate and in most cases it is assumed to be negligible. For our experiment, prior measurements based on the comparison between a modified PTP and OES measurements confirmed that this contribution does not significantly influence our integral energy flux. However, it should be noted that Thornton on the opposite obtained values of several eV per deposited atom from calculations based on the ionization and sputter mechanism [6].

The second source for radiative energy flux is much easier to understand and to investigate. In the case of magnetron sputtering, the primary origin for significant black body radiation is the magnetron target or the anode. In case of poor thermally conducting target materials or insufficient cooling, these parts can get extremely hot and generate a strong energy flux to the substrate. This energy flux can be calculated according to the Boltzmann radiation law:

$$J_{rad} = \nu F_{ts} \sigma (T_t^4 - T_s^4). \quad (7)$$

Here T_t and T_s are the temperatures of the target and the substrate, σ the Stefan-Boltzmann constant, F_{ts} a geometrical factor for parallel discs [40] and ν the radiation exchange rate which compensates for the emissivities being smaller than 1 [41]. In figure 7 an exemplary calculation of the energy flux from a hot magnetron according to equation 7 is shown. Here it is clearly visible that this contribution is small compared to typical integral energy flux values for temperatures below roughly 400°C and can increase to values in the range of 100 mW/cm^2 for high temperatures and higher emissivities.

5 Results

The calorimetric measurements as obtained by the PTP are presented in figure 8. The errors are estimated from repeated measurements obtained by the applied back-and-forth measurement principle.

The first row shows the results for the power, distance and pressure variation in argon. The second row displays the corresponding results for krypton and the third row those for helium. A general order of the energy flux is observed with Ti and W yielding the highest energy flux values, Ag and Cu showing

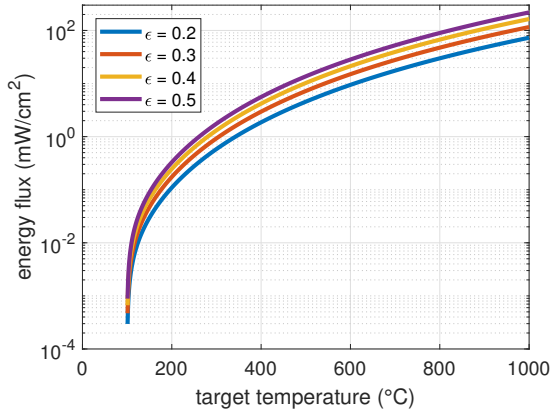


Figure 7: Calculated energy flux according to equation 7 for two parallel discs with diameters $d_t = 5.08$ cm, $d_s = 11$ mm, distance 70 mm and a temperature of 100 °C of the substrate surface. The different graphs are calculated for different emissivities of $\epsilon = 0.2 - 0.5$ for both surfaces.

relatively similar values with moderate energy flux and Al showing the smallest values. Merely in helium there is a more pronounced difference between Ag and Cu and the lightest material aluminum yields a higher energy flux relatively to the other materials. This is likely caused by the more effective sputtering of Al in He resulting from the more akin masses between sputtering gas and target material as compared to the heavier materials. This hypothesis is in good agreement with the SRIM simulations which calculated significantly higher sputter yield for He on Al as compared to Cu.

The power variations show an almost linear increase for all gases and target materials. Since the energy flux can primarily be understood as power transfer from the cathode to the substrate such a linear increase can intuitively be expected. The only outlier regarding this trend is Ti in Ar and Kr which shows a clear deviation as a result of the role of increasing target radiation (see section 6.3). The distance variation shows an expected overall trend for all investigated target-gas combinations with decreasing energy flux values for increasing distance to the target. The observed exponential decrease can be understood as a result of the increased number of collisions

the sputtered and reflected particles undergo as they transit from the target towards the probe. Except for the case of Ti in He, the results of the pressure variation show much less pronounced trends. The energy flux remains relatively constant and in most cases exhibits a weak maximum in the investigated pressure region. The trends can be understood as the result of a balance between the amount of particles being sputtered and reflected from the target and the interaction of these particles with the background gas. For increasing pressure we observed an increase in magnetron current and, accordingly, a decrease of the magnetron voltage due to the constant power mode. In terms of energy flux, the most relevant effect of increased current is the increased amount of sputtered particles and reflected neutrals, while the decrease of the voltage results in a smaller sputter- and reflection yield and smaller kinetic energies of sputtered and reflected particles. In most cases these effects alone would result in an increase of energy flux as the proportional increase with current is not fully compensated by the attenuating effects associated with the decreasing voltage. However, the decreasing mean free path at higher pressures yields another weakening factor for the energy flux as more energy is dissipated in the background gas and, accordingly, less energy flux arrives at the substrate. As observed, these effects mostly balance the integral energy flux in the investigated pressure regime and the observed maximum likely marks the pressure where the attenuating effect of increased collisions start to dominate the energy flux.

6 Discussion

In the following section we will discuss in greater detail three cases where different mechanisms dominate the measured integral energy flux. In figure 9 the different contributions to the integral energy flux at the standard condition are illustrated using a stacked bar plot. Along with the measured energy flux, the calculated values for the electric contribution and the sputter contribution are presented. For the difference to the measured energy flux a placeholder contribution denoted as 'others' is introduced. In the case of small

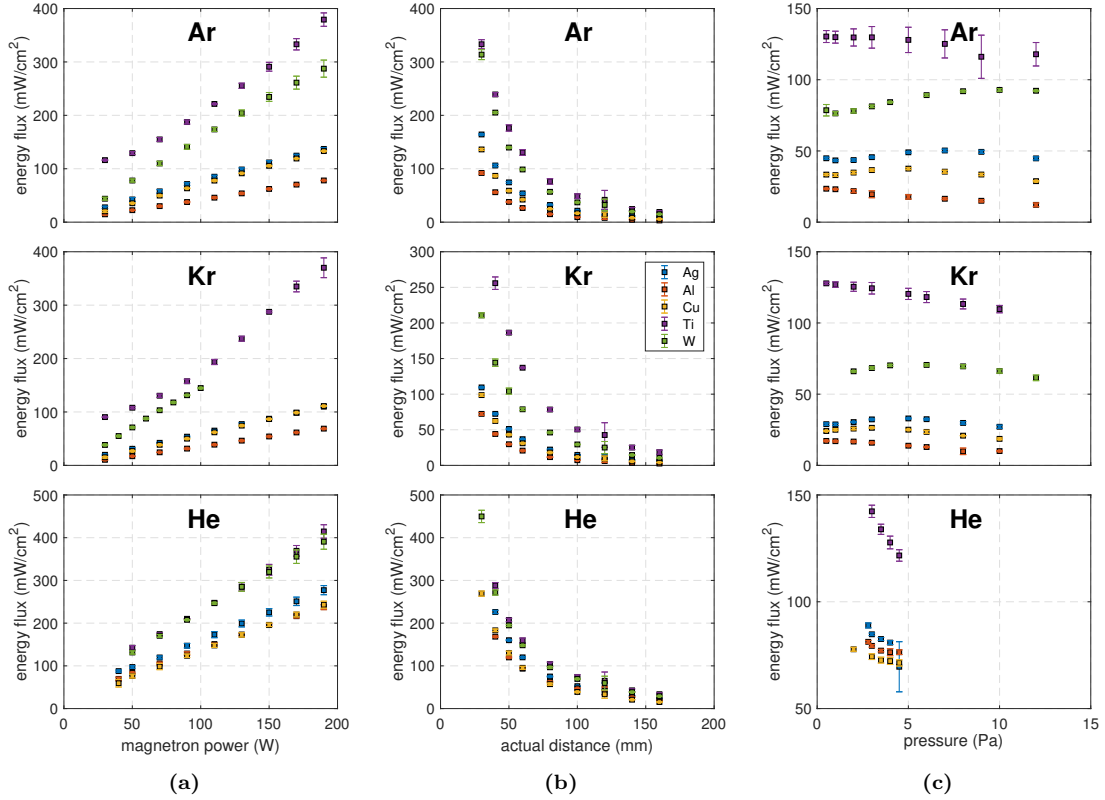


Figure 8: PTP results in argon, krypton and helium for (a) power variation, (b) distance variation and (c) pressure variation. The variations were performed according to the parameters summarized in table 1. The first row shows the results for argon, the second row the investigations for krypton and the last row for helium. While most of the displayed values are obtained as an average from repeated measurements, the results of the power variation with Ti only include the values for the systematic increase of the power from 30 W to 190 W. The values of the systematic decrease of the power from 190 W back to 30 W have been excluded for clarity since a strong hysteresis due to excessive target radiation was detected.

gas-target mass ratios (all He and all W) the contribution from 'others' is expected to be dominated by reflected neutrals which is in good agreement with results obtained from SRIM simulations (plotted in blue). In the case of titanium the target was found to heat up to high temperatures which suggests that the high contribution of 'others' is caused by excessive target radiation. These two extreme cases are discussed in more detail in the last two paragraphs of this section while the first paragraph will focus on the case that the energy flux is dominated by the contribution of thin-film growing particles as observed for

high sputter yield materials like copper or silver.

6.1 Deposition dominated energy flux (Ag, Cu)

For those target materials which exhibit a high sputter yield, usually the contribution from film growing particles dominates the integral energy flux. As an exemplary case, in figure 10 the integral energy flux for a copper target as measured by the PTP during the power variation in argon is presented. In addition, the calculated contributions according to the

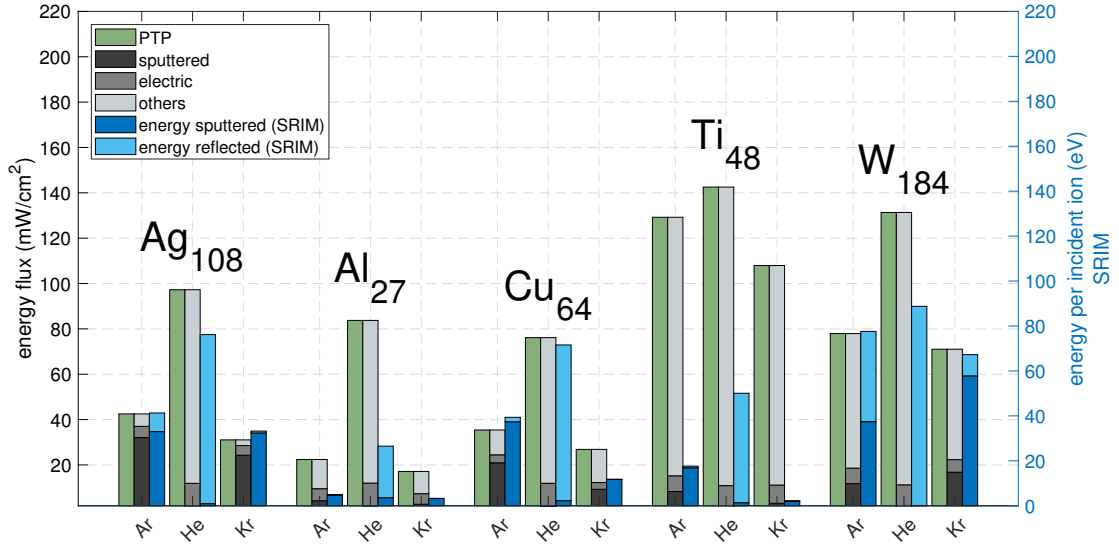


Figure 9: Illustration of the different contributions to the integral energy flux at standard conditions (50 W, 70 mm, 2 Pa) for all investigated target-gas combinations along with simulated data of energy carried away from the target by sputtered and by reflected particles. The values are displayed using a stacked bar graph. The green bar depicts the total energy flux as measured by the PTP (green bar). In three shades of gray, the calculated contributions for the sputtered particles using QCM and TRIM data, the electric contributions by electrons and ions calculated from the Langmuir data and the contributions from 'others' as calculated by subtraction of the combined sputtered and electric contributions from the PTP values. As discussed in the text, the contribution from others can likely be assigned to radiation in the case of titanium and to reflected neutrals in the other cases. The blue bars show the energies calculated from TRIM simulations as described in section 3.4 for sputtered and reflected particles.

equations presented in section 4 and the sum of these calculated values (labeled as 'calc') are shown. Here it can be seen that the neutrals are the biggest contributions to the energy flux as the calculated sum of 'neutr' and 'cond' accounts for ~60 % of the measured energy flux independent of the magnetron power. The 'electric' contribution from ions and electrons on the opposite is relatively small and adds up to only ~10 %. As visible from figure 9, similar percentages are observed for silver with the calculated contribution from neutral particles representing an even bigger portion of the overall energy flux. Due to the aforementioned 'upwards estimation' the percentage of energy flux which is not related to the sputtered particles or electric contribution is expected to be even higher than the calculated difference to the mea-

sured energy flux. In the cases of copper and silver the target surface remained at relatively low temperatures and no significant contribution from radiation was detected (<1 mW/cm²). Therefore, it can be assumed that even in the cases of high sputter yield materials a considerable portion of the energy flux can be attributed to reflected neutrals. This observation is in good agreement with those made by Rosnagel in his study investigating reflected neutrals [31].

6.2 Reflected neutrals dominated energy flux (He, W)

As it is clearly visible in figure 8 the energy flux is persistently among the highest values for all measurements with helium or in the case of tungsten as target

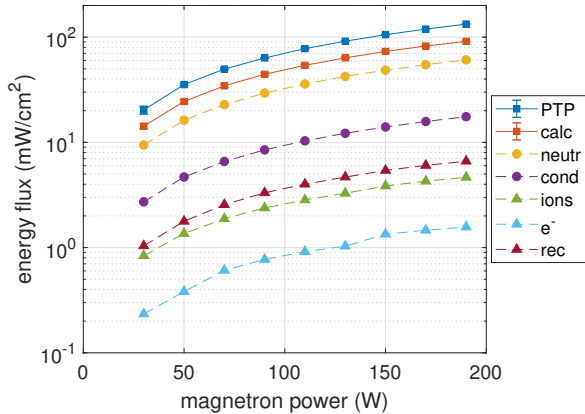


Figure 10: Measured integral energy flux of Cu in Ar during power variation as well as the calculated contributions derived from Langmuir, QCM and SRIM data. The errors presented in the PTP results originate from repeated measurements and the errors displayed in the sum of the calculated contributions ('calc') are obtained by summing up all standard deviations of the individually calculated values.

material. In figure 9 it is shown, that these high energy flux values can not be explained alone by the electric contribution or by that of sputtered atoms. Instead, it is likely a result of the high percentage of particles being reflected from the target. This can be intuitively understood from the simple model of a 2-body collision where we have a high probability for reflection if the incoming particle has a much smaller mass than the other collision partner. However, as shown in [42] even for a gas-target ratio significantly higher than 1, reflection can appear as a result of implanted gas ions in the target material. The results of the SRIM simulations further support the significance of backscattered particles as for almost all cases where He or W is involved we calculate a higher amount of energy being carried away from the target as reflected neutrals compared to that carried away by sputtered particles. Taking into account the more pronounced influence of background gas collisions for the sputtered particles as compared to the reflected ones (see section 4.4), it can be expected that the observed integral energy flux is strongly dominated by reflected neutral particles in these showcasing exam-

ples. As argued in section 6.1, the contribution from reflected neutrals is expected to have a significant influence also in cases where it is much less distinguishable and likely masked by other effects of comparable magnitude and it is further expected to become more relevant for increasing pressure [31].

6.3 Radiation dominated energy flux (Ti)

One striking observation from the various materials studied, is that Ti seems to be the outlier not only in terms of the magnitude of the resulting energy flux but also in terms of the reproducibility of the measurements. Especially in the power variation, Ti exhibited a strong hysteresis of the measurement values obtained at the beginning of the measurement set and the values obtained at the end. For the same parameters we observed a discrepancy in the order of up to ~ 50 mW/cm² and obtained strongly changing values for a repetition of the whole measurement run. Since Ti yields one of the lowest thermal conductivity of all metals (see table 2) one can assume that the heating of the target can have a significant effect. To investigate this, additional measurements were performed using an extended measurement procedure while additionally monitoring the target temperature using an infrared camera. These measurements revealed a direct correlation between the changes in the measured energy flux and the target temperatures. During the measurement, the temperature of the target exceeded the maximum temperature range of 900°C of the IR camera and when the plasma was turned off, a faint orange glow from the target was visible with the naked eye. Following this measurement, the energy flux solely originating from the hot target was measured directly using the PTP. This was achieved by simply shutting off the radiation from the target using the 2-shutter system if the plasma switched off. In figure 11 the resulting energy flux values and the corresponding target temperatures as a function of time along with an exemplary image from the IR camera are presented. Here it can be seen that the target cooled down relatively slow, indicating a weak thermal connection of the target surface to the water-cooled copper holder which remained below 20

°C. Additionally, it can be noted that the measured energy flux values are in good agreement with the calculated values in section 4.5.

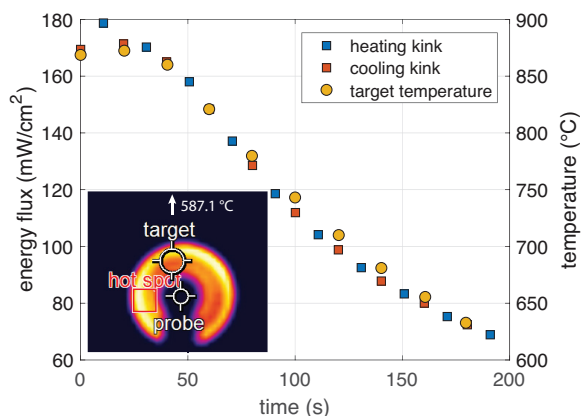


Figure 11: Energy flux due to target radiation as measured with the PTP during cool-down after an extended variation of the magnetron power, along with the corresponding target temperature detected with the IR camera. Additionally an exemplary image obtained with the IR camera indicating the three measurement spots is presented. During the investigations the temperature of the target exceeded 900°C, resulting in a faint orange glow visible to the naked eye.

Since the target temperature changes relatively slow, the energy flux from the plasma excluding the target radiation can be detected using a different switching mechanism for the shut off of the energy flux. By switching off the magnetron voltage instead of closing the shutters, the same background of radiation from the target is present in the small investigated time frame, both during heating and cooling phase. This way, according to the theory presented in section 3.2, the measurement includes all contributions but no target radiation (n.t.r.). In figure 12, measurements for the power variation with Ti using this measurement method alongside with the measurements from figure 8 using the 2-shutter method are presented. The measurements without radiation (source switching) exhibit the same linear dependence as observed for all other metals and show excellent reproducibility. On the other hand, the poor reproducibility for Ti using the shutter system and the resulting increased energy flux values and,

accordingly, the large contribution from 'others' in figure 9 can thus be clearly attributed to the radiation from the target. From the difference between the values obtained from the two measurement methods, a direct determination of the energy flux due to radiation is possible. E.g. for 50 W in argon, the contribution from radiation can be determined to be ~ 100 mW/cm², which correspond to 90 % of the calculated contribution from 'others' in figure 9.

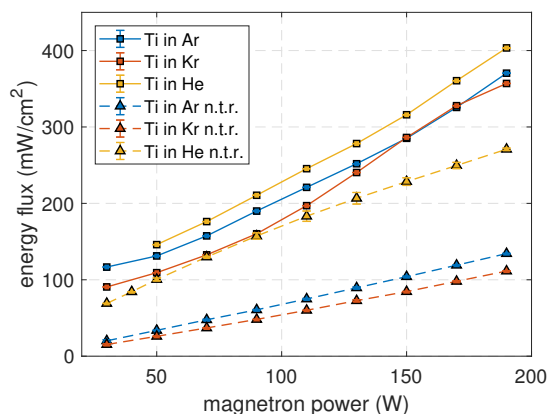


Figure 12: Energy flux measurements of titanium in Ar, Kr and He utilizing two different measurement principles. The data points (squares) connected with the solid lines are produced with the 2-shutter method (see figure 8a), whereas the points (triangles) connected with the dashed lines were obtained using no shutters but instead switching of the power source. Since in the latter case the target radiation is present as a background during both the heating and cooling phase, these measurements are obtained with no target radiation (n.t.r.) contribution in the integral energy flux.

To exclude the possibility of poor thermal conductivity caused by an uneven target backside or improper mounting, we performed additional measurements with a freshly machined target backside to guarantee a smooth surface. This optimization only slightly improved the cooling of the target, so that the obtained results should apply to other comparable systems as well. This is in agreement with recent observations for hot target sputtering of titanium [43,44] or nickel [45] and could also explain high energy flux values observed by Cormier et al. [12]. Additional measurements with gadolinium, which has an

even lower thermal conductivity of $10.5 \text{ W}/(\text{m K})$, exhibited similar characteristics as Ti and, thus, further underline the impact of the targets thermal conductivity. However, it must be noted that the contribution from target radiation is highly dependent on a variety of uncertain factors such as the target history (e.g. how long was the target exposed to high power) or on the efficiency of the target cooling system (e.g. thinner targets would dramatically decrease the target heating).

Although no significant hysteresis during the measurements presented in figure 8 was observed for the other target materials, the same additional investigations were performed with silver, aluminum and tungsten. In all cases the target temperature did not exceed values above 300°C and accordingly, the radiation from the target resulted in energy flux values below $2 \text{ mW}/\text{cm}^2$. It can thus be concluded that the absence of a hysteresis and, accordingly, good reproducibility is a sufficient indicator for a negligible effect of target radiation.

6.4 SEM investigations

The influence of process parameters on the thin film growth can be graphically described by a so called structure zone diagram (SZD). For magnetron sputtering the most referred to SZD is the one introduced by Thornton in 1974 [1] or the updated version presented by Anders in 2010 [46]. For DC magnetron sputtering with no additional substrate heating or biasing, films are typically assigned to the Zone 1 or in some fewer cases to the transition region Zone T. To allow a comparison to these models and, thus, create a connection between the presented energy flux measurements and the actual deposited film, samples were deposited at selected parameter combinations. The copper films were deposited onto silicon substrates placed at a distance of 70 mm to the target surface. For each condition samples were prepared for both, a grounded substrate and an isolated substrate at floating potential. The films were examined using a *Zeiss GeminiSEM* scanning electron microscope (SEM) producing top view images of the surface morphology of the films as well as cross sections revealing the structural growth. Images of the

surface for the floating substrates and cross sections for both the grounded and the floating substrates are summarized in figure 13. Although the substrate is heated much stronger by electrons if it is connected to ground, the images show very similar structures for both the floating and grounded case. Although the substrate is warmer during the deposition on a grounded substrate, the homologous temperature stays within the lower regime as the temperature is not expected to reach a significant fraction of the melting temperature of the material. Therefore no significant effect on the film formation is expected.

In principle, two distinctively different structures, which are best visible in the cross sections, can be observed in figure 13. *A* exhibits a columnar growth structure with clear crystal boundaries which extend throughout the complete film. These crystal boundaries are also visible in the top view image where they create a grain-like structure. The same structure is also visible in the top view of *D*, however, due to the small thickness of the deposited film, the cross section images do not exhibit clear details. Only in a close examination, an indication for domed crystallites with bigger diameter compared to the ones seen in *A* is present. In both cases the bombardment by reflected neutrals is comparatively low and while the depositing atoms are expected to be partly thermalized for 2 Pa, they are likely completely thermalized in the case of 12 Pa. For samples *B*, *C* and *E* the clear columnar structure is disrupted in favor of a more dense growth pattern with smaller crystallites which do not extend through the complete film thickness. The disruption of the columnar morphology is somewhat comparable to that observed for biased sputtering [47, 48]. Here the kinetic impact of highly energetic ions disrupts the columnar growth which is typically attributed to resputtering and additional nucleation sites. In the same way, in our case the formation of smaller crystallites can be associated to the increased energy of reflected neutrals and depositing atoms arriving at the substrate. In the case of the increased discharge power (*B*) the energy increases mostly as a result of stronger rarefaction and increased magnetron voltage. For the significantly reduced pressure (*C*), the dominant parameter is the increased mean free path which directly results in fewer collisions and, accord-

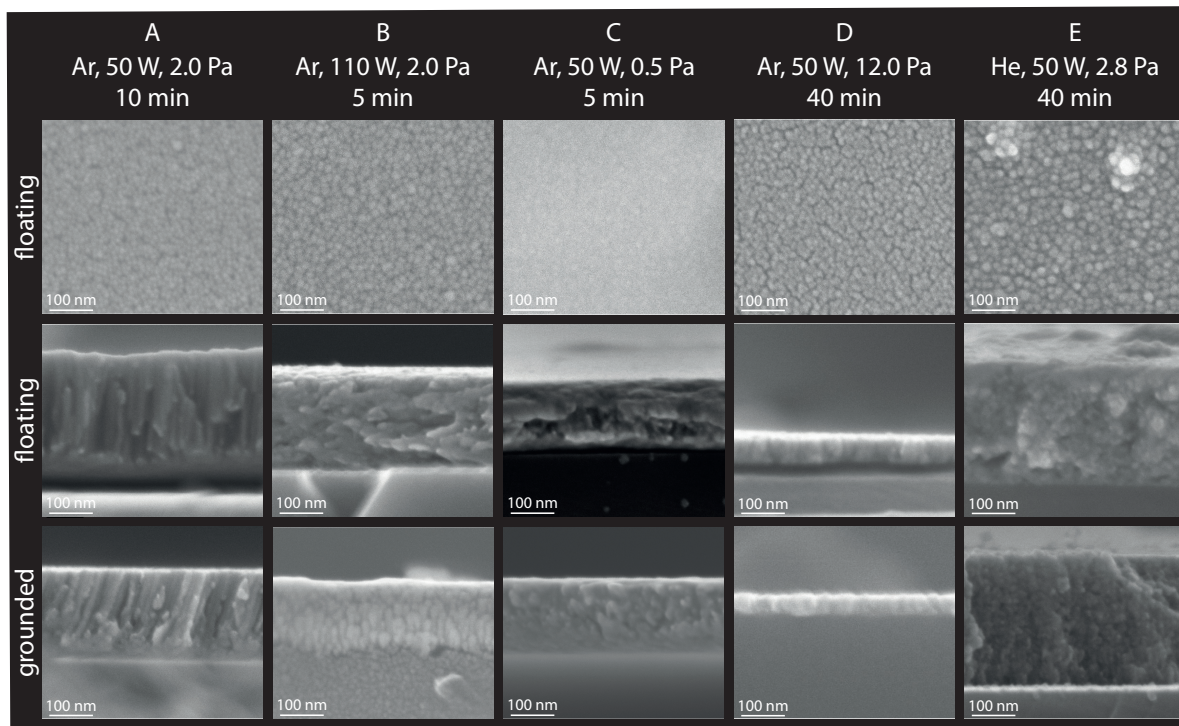


Figure 13: SEM images of a copper film deposited on a silicon wafer in Ar and He at selected discharge parameters. The top row shows the surface morphology for films deposited on a floating substrate, the second and third row show cross sections of the corresponding films with a floating and grounded substrate, respectively.

ingly, higher energies. The extreme case with helium as a sputter gas (*E*) results in a strong neutral bombardment combined with a low deposition rate. The strong neutral bombardment could explain the finely grained structure visible in the cross sections and the comparatively rough surface observed in the top view is likely a result a resputtering.

7 Conclusions

Detailed investigations of the energy flux in DC magnetron sputtering with fifteen gas-target combinations examined for essential parameter variations have been presented. Additional measurements using Langmuir probe, QCM and IR imaging combined with SRIM simulations were used to allow a more detailed analysis of the different contributions to the

integral energy flux. In spite of the apparent simplicity of the investigated system (DCMS of metals using inert gases), fundamentally different compositions of the integral energy flux were observed. The three dominant mechanisms were identified as the energy flux originating from sputtered particles, from reflected neutrals and from a hot target surface. While the first mechanism is of essential nature to the film deposition process and is especially dominant for materials with a high sputter yield, the mechanism attributed to reflected neutrals was found to be of equal importance. In the case of a small gas-target mass ratio the energy flux from reflected neutrals can even be the leading factor. For target materials with a low thermal conductivity, such as titanium, the target surface can heat up to high temperatures resulting in a significant radiative energy

flux which can easily surpass the contribution from other mechanisms. However, in systems with a biased substrate the contribution of charged particles becomes more and more significant and in many cases dominates the energy flux.

The understanding of the driving mechanisms behind the different contributions and on how they transfer the energy to the substrate and the growing film can in principal be used to tailor the composition of the energy flux. While the energy flux from radiation, condensation or electrons represents a relatively anisotropic contribution, the kinetic impact of ions, sputtered particles and especially reflected neutrals dissipates energy much more localized into the film. Changing e.g. the gas-target mass ratio by using a different background gas could, thus, be used to change the amount of highly kinetic particles impinging on the film during deposition. The copper samples investigated by SEM illustrated the principal changes of the film structure from columnar growth to a more dense film with smaller crystallites. In spite of the expected increase in energy flux associated with electron heating, no clear difference of the film structure for samples deposited at floating potential compared to those using a grounded substrate were observed.

Acknowledgements

The authors would like to thank Dr. Oleksandr Polonskyi from the Technical Faculty of the Christian-Albrechts-University in Kiel, Germany, for his dedicated work in acquiring the SEM images.

References

- [1] J. A. Thornton, "Influence of apparatus geometry and deposition conditions on the structure and topography of thick sputtered coatings," *Journal of Vacuum Science and Technology*, vol. 11, no. 4, p. 666, 1974.
- [2] H. Deutsch, H. Kersten, S. Klagge, and A. Rutscher, "On the Temperature Dependence of Plasma Polymerization," *Contrib. Plasma Phys.*, vol. 28, pp. 149–155, 1988.
- [3] H. Deutsch, H. Kersten, and A. Rutscher, "Basic Mechanisms in Plasma Etching," *Contributions to Plasma Physics*, vol. 29, no. 3, pp. 263–284, 1989.
- [4] H. Kersten, H. Deutsch, H. Steffen, G. M. W. Kroesen, and R. Hippler, "The energy balance at substrate surfaces during plasma processing," *Vacuum*, vol. 63, pp. 385–431, aug 2001.
- [5] H. Kersten, R. J. M. M. Snijkers, J. Schulze, G. M. W. Kroesen, H. Deutsch, and F. J. De Hoog, "Energy transfer from radio frequency sheath accelerated CF+3 and Ar+ ions to a Si wafer," *Applied Physics Letters*, vol. 64, no. 12, pp. 1496–1498, 1994.
- [6] J. A. Thornton, "Substrate heating in cylindrical magnetron sputtering sources," *Thin Solid Films*, vol. 54, no. 1, pp. 23–31, 1978.
- [7] J. A. Thornton and J. L. Lamb, "Substrate heating rates for planar and cylindrical-post magnetron sputtering sources," *Thin Solid Films*, vol. 119, pp. 87–95, sep 1984.
- [8] T. P. Drüsedau, T. Bock, T.-M. John, F. Klabunde, and W. Eckstein, "Energy transfer into the growing film during sputter deposition: An investigation by calorimetric measurements and Monte Carlo simulations," *Journal of Vacuum Science & Technology A: Vacuum, Surfaces, and Films*, vol. 17, pp. 2896–2905, sep 1999.
- [9] S. D. Ekpe and S. K. Dew, "Theoretical and experimental determination of the energy flux during magnetron sputter deposition onto an unbiased substrate," *Journal of Vacuum Science & Technology A: Vacuum, Surfaces, and Films*, vol. 21, no. 2, p. 476, 2003.
- [10] K. Harbauer, T. Welzel, and K. Ellmer, "A combined sensor for the diagnostics of plasma

- and film properties in magnetron sputtering processes,” *Thin Solid Films*, vol. 520, no. 20, pp. 6429–6433, 2012.
- [11] S. Bornholdt and H. Kersten, “Transient calorimetric diagnostics for plasma processing,” *The European Physical Journal D*, vol. 67, p. 176, aug 2013.
- [12] P.-A. Cormier, A. Balhamri, A.-L. Thomann, R. Dussart, N. Semmar, J. Mathias, R. Snyders, and S. Konstantinidis, “Measuring the energy flux at the substrate position during magnetron sputter deposition processes,” *Journal of Applied Physics*, vol. 113, p. 013305, jan 2013.
- [13] M. Čada, J. W. Bradley, G. C. B. Clarke, and P. J. Kelly, “Measurement of energy transfer at an isolated substrate in a pulsed dc magnetron discharge,” *Journal of Applied Physics*, vol. 102, p. 063301, sep 2007.
- [14] F. Haase, D. Lundin, S. Bornholdt, and H. Kersten, “On the Impact of Electron Temperature in Magnetron Sputtering Benchmarked with Energy Flux Measurements,” *Contributions to Plasma Physics*, vol. 55, pp. 701–713, dec 2015.
- [15] D. Lundin, M. Stahl, H. Kersten, and U. Helmersson, “Energy flux measurements in high power impulse magnetron sputtering,” *Journal of Physics D: Applied Physics*, vol. 42, no. 18, p. 185202, 2009.
- [16] Intelmetrics Global Ltd, “Model IL150 Thickness Monitor - Instruction Manual.”
- [17] M. Samuelsson, D. Lundin, J. Jensen, M. A. Raadu, J. T. Gudmundsson, and U. Helmersson, “On the film density using high power impulse magnetron sputtering,” *Surface and Coatings Technology*, vol. 205, pp. 591–596, oct 2010.
- [18] M. Stahl, T. Trottenberg, and H. Kersten, “A calorimetric probe for plasma diagnostics,” *Review of Scientific Instruments*, vol. 81, no. 2, pp. 1–5, 2010.
- [19] S. Gauter, M. Fröhlich, W. Garkas, M. Polak, and H. Kersten, “Calorimetric probe measurements for a high voltage pulsed substrate (PBII) in a HiPIMS process,” *Plasma Sources Science and Technology*, vol. 26, p. 065013, may 2017.
- [20] R. Hippler, *Low Temperature Plasmas : fundamentals, technologies, and techniques. Volume 2*. Weinheim: WILEY-VCH Verlag, 2008.
- [21] J. F. Ziegler, M. Ziegler, and J. P. Biersack, “SRIM – The stopping and range of ions in matter (2010),” *Nuclear Instruments and Methods in Physics Research Section B: Beam Interactions with Materials and Atoms*, vol. 268, pp. 1818–1823, jun 2010.
- [22] H. Kersten, H. Deutsch, H. Steffen, G. Kroesen, and R. Hippler, “The energy balance at substrate surfaces during plasma processing,” *Vacuum*, vol. 63, pp. 385–431, aug 2001.
- [23] D. Depla and S. Mahieu, eds., *Reactive Sputter Deposition*, vol. 109 of *Springer Series in Materials Science*. Berlin, Heidelberg: Springer Berlin Heidelberg, 2008.
- [24] J. A. Thornton, “Magnetron sputtering: basic physics and application to cylindrical magnetrons,” *Journal of Vacuum Science and Technology*, vol. 15, pp. 171–177, mar 1978.
- [25] W. M. Haynes, *CRC Handbook of Chemistry and Physics*. Boca Raton, FL: CRC Press, 2014.
- [26] M. W. Thompson, “II. The energy spectrum of ejected atoms during the high energy sputtering of gold,” *Philosophical Magazine*, vol. 18, pp. 377–414, aug 1968.
- [27] A. Goehlich, D. Gillmann, and H. Döbele, “Angular resolved energy distributions of sputtered atoms at low bombarding energy,” *Nuclear Instruments and Methods in Physics Research Section B: Beam Interactions with Materials and Atoms*, vol. 164-165, pp. 834–839, apr 2000.
- [28] D. W. Hoffman and J. A. Thornton, “Compressive stress and inert gas in Mo films sputtered

- from a cylindrical-post magnetron with Ne, Ar, Kr, and Xe,” *Journal of Vacuum Science and Technology*, vol. 17, pp. 380–383, jan 1980.
- [29] R. E. Somekh, “The thermalization of energetic atoms during the sputtering process,” *Journal of Vacuum Science & Technology A: Vacuum, Surfaces, and Films*, vol. 2, pp. 1285–1291, jul 1984.
- [30] R. Wendt, K. Ellmer, and K. Wiesemann, “Thermal power at a substrate during ZnO:Al thin film deposition in a planar magnetron sputtering system,” *Journal of Applied Physics*, vol. 82, pp. 2115–2122, sep 1997.
- [31] S. M. Rossnagel, “Energetic particle bombardment of films during magnetron sputtering,” *Journal of Vacuum Science & Technology A: Vacuum, Surfaces, and Films*, vol. 7, pp. 1025–1029, may 1989.
- [32] P. Sigmund, “Theory of Sputtering. I. Sputtering Yield of Amorphous and Polycrystalline Targets,” *Physical Review*, vol. 184, pp. 383–416, aug 1969.
- [33] R. S. Robinson, “Energetic binary collisions in rare gas plasmas,” *Journal of Vacuum Science and Technology*, vol. 16, pp. 185–188, mar 1979.
- [34] D. Lundin, C. Vitelaru, L. D. Poucques, N. Brenning, and T. Minea, “Ti–Ar scattering cross sections by direct comparison of Monte Carlo simulations and laser-induced fluorescence spectroscopy in magnetron discharges,” *Journal of Physics D: Applied Physics*, vol. 46, p. 175201, may 2013.
- [35] Y. Yamamura and M. Ishida, “Monte Carlo simulation of the thermalization of sputtered atoms and reflected atoms in the magnetron sputtering discharge,” *Journal of Vacuum Science & Technology A: Vacuum, Surfaces, and Films*, vol. 13, pp. 101–112, jan 1995.
- [36] D. W. Hoffman, “A sputtering wind,” *Journal of Vacuum Science & Technology A: Vacuum, Surfaces, and Films*, vol. 3, pp. 561–566, may 1985.
- [37] S. M. Rossnagel, “Gas density reduction effects in magnetrons,” *Journal of Vacuum Science & Technology A: Vacuum, Surfaces, and Films*, vol. 6, no. 1, p. 19, 1988.
- [38] I. Petrov, I. Ivanov, V. Orlinov, and J. Sundgren, “Comparison of magnetron sputter deposition conditions in neon, argon, krypton, and xenon discharges,” *Journal of Vacuum Science & Technology A: Vacuum, Surfaces, and Films*, vol. 11, pp. 2733–2741, sep 1993.
- [39] K. Koura and H. Matsumoto, “Variable soft sphere molecular model for air species,” *Physics of Fluids A: Fluid Dynamics*, vol. 4, pp. 1083–1085, may 1992.
- [40] F. P. Incropera, D. P. DeWitt, T. L. Bergman, and A. S. Lavine, *Fundamentals of Heat and Mass Transfer*. Hoboken, NJ, USA: John Wiley & Sons, Inc., 2007.
- [41] Massachusetts Institute of Technology, “Radiation Heat Transfer Between Planar Surfaces,” <http://web.mit.edu/16.unified/www/FALL/thermodynam/>, 2018.
- [42] R. Feder, C. Bundesmann, H. Neumann, and B. Rauschenbach, “Ion beam sputtering of germanium – Energy and angular distribution of sputtered and scattered particles,” *Nuclear Instruments and Methods in Physics Research Section B: Beam Interactions with Materials and Atoms*, vol. 334, pp. 88–95, sep 2014.
- [43] A. A. Komlev, E. A. Minzhulina, V. V. Smirnov, and V. I. Shapovalov, “Influence of argon pressure and current density on substrate temperature during magnetron sputtering of hot titanium target,” *Applied Physics A*, vol. 124, p. 48, jan 2018.
- [44] E. A. Minzhulina, V. I. Shapovalov, V. V. Smirnov, A. V. Zav’aylov, and V. S. Levitskiy, “Thermal processes during reactive sputtering of

hot titanium target,” *Journal of Physics: Conference Series*, vol. 857, p. 012031, may 2017.

- [45] A. Caillard, M. El’Mokh, N. Semmar, R. Dus-sart, T. Lecas, and A.-L. Thomann, “Energy Transferred From a Hot Nickel Target During Magnetron Sputtering,” *IEEE Transactions on Plasma Science*, vol. 42, pp. 2802–2803, oct 2014.
- [46] A. Anders, “A structure zone diagram including plasma-based deposition and ion etching,” *Thin Solid Films*, vol. 518, no. 15, pp. 4087–4090, 2010.
- [47] D. M. Mattox and G. J. Kominiak, “Structure Modification by Ion Bombardment during Deposition,” *Journal of Vacuum Science and Technol-ogy*, vol. 9, pp. 528–532, jan 1972.
- [48] J.-W. Lim, Y. Ishikawa, K. Miyake, M. Ya-mashita, and M. Isshiki, “Influence of Substrate Bias Voltage on the Properties of Cu Thin Films by Sputter Type Ion Beam Deposition,” *MATERIALS TRANSACTIONS*, vol. 43, no. 6, pp. 1403–1408, 2002.

5 Conclusion and Outlook

Albeit every publication presented in the last section already contains a conclusion on its own, a general summary is given here in order to create a complete image and to present all the different findings obtained in the different projects.

- Evidence of secondary electrons during plasma-immersion ion implantation was found using a calorimetric probe (publication [I]). Although, the PTP's measurement principle does not allow for time resolved measurements during one single pulse, it was still able to pick up changes in the system over the time of several high voltage pulses. Angle variations have proven the detected energy flux to be a directed phenomenon originating from the substrate. Further investigations, including the variation of pulse voltage, pulse frequency, pulse length and distance to the substrate, as well as the variation in substrate materials (Al, Cu, stainless steel) all support the proposition of secondary electrons to be the main cause for the recorded energy flux.
- Energy flux measurements were performed during plasma-immersion ion implantation of seven different substrate materials (publication [II]). The substrates have preliminarily been treated in a hot furnace creating an oxide layer on the substrate surfaces. The oxidized substrates were sputtered with argon with intermittent short calorimetric measurements determining the energy flux. For all target materials, the higher secondary electron yield of the oxidized surface resulted in a higher energy flux, decreasing with decreasing oxide layer due to sputtering of argon ions. In the case of Mg and AZ91, the transition from an oxidized to a metallic surface was completed within a short period of sputtering, visible as an abrupt change in the energy flux. Using a simple model and combining the energy flux values with the recorded PIII current, secondary electron yields could be calculated.

The same measurement principle was applied when exposing the substrates and their metallic surfaces to a nitrogen plasma with the high voltage pulses turned on. In almost every case, except Mg, the secondary electron yield was smaller when exhibiting a (partly) nitrided surface as compared to the metallic surface.

- Detailed investigations of the energy flux during reactive magnetron sputtering of titanium were performed in publication [III] where two different power source modes (DC and HiPIMS) were compared. In contrast to PIII (publications [I] and [II]) where the fast high voltage pulses are applied to the substrate, HiPIMS applies fast pulses to the magnetron target (cathode). Again, the PTP was able to obtain valuable information, albeit the fast nature of the pulses. Generally, the HiPIMS process exhibits higher energy flux values as compared to DCMS, however, with increasing O₂ reactive gas flow the energy flux decreases for both systems as the target surface transitions from a pure metal to a poisoned mode. Accompanying this process is a decrease in deposition

rate for both DCMS (factor 10) and HiPIMS (factor 14). Further, the discrepancy between the higher energy flux of HiPIMS compared to DCMS is shrinking with increased target poisoning. However, when transitioning from a metal to a poisoned mode, the energy flux of DCMS does not decrease on a significant level and changes in HiPIMS were below 20%. Using Langmuir probe diagnostics during DCMS it was found that the particle fluxes of electrons and ions increase on the other hand, which explains the rather unaffected energy flux.

- The choice of process gas and its influence on the electron temperature during DCMS was studied with calorimetric probe, Langmuir probe and quartz crystal microbalance using a titanium target (publication [IV]). Argon, neon and krypton were used as process gas and the plasma parameters were obtained at two positions (close to the target and at a typical substrate distance) using the Langmuir probe. Close to the target, neon exhibits considerably higher electron temperatures as compared to the other two gases, leading to a decreased mean free path for ionization. In turn, the probability of ionizing neutrals is higher when using neon, which opens up new ways of tailoring the deposition process. However, drawbacks in deposition rates were also observed.

Further, with the help of Langmuir probe data and deposition rate values, the integral energy flux as measured by the PTP could be broken down into its main contributions. At ground potential, the main contribution to the energy flux originates from neutrals and film formation, however, when biasing the substrate the contribution of charged particles may exceed those values and become dominant. This will result in different film properties.

- Given that conventional DCMS is performed at low pressures of up to a few pascals, the calorimetric probe was put to the test at higher pressures in publication [V] where a gas aggregation source was studied, operating at pressures several tens of pascals up to a few hundreds of pascals. Typically, the DC magnetron equipped chamber does produce nanoparticles that exit the aggregation chamber through an exit orifice. Detailed investigations inside the aggregation chamber using three different targets (Cu, W, Cu/37W) were performed, while obtaining energy flux and deposition rate values as well as plasma parameters. Results revealed the higher pressure system comparable with conventional low pressure DCMS in terms of dominant contributions of the energy flux. Like in conventional DCMS, reflected neutrals and the contribution due to film formation are the major influences that dictate the energy flux. The influence of reflected neutrals was highly dependent on the gas-target mass ratio. Gas rarefaction and its accompanying effects were argued to be a significant mechanism in the investigated system as the reduction of the gas density and the associated increase in λ_{mfp} allowed the reflected neutrals to reach the substrate surface with high energies creating a significant contribution to the energy flux.
- Returning to conventional DCMS, publication [VI] offers a detailed look at the capabilities of the PTP. Fifteen gas-target combinations were extensively studied and different dominant contributions to the energy flux were found depending on the gas-target combination. In the case of target materials with high a sputter yield (like

Ag or Cu), film forming neutral particles dominate the energy flux. However, in the case of uneven gas-target mass ratios reflected neutrals rise strongly in significance and can become the main contribution to the integral energy flux, as was the case for all investigations with He. In case of target materials with poor heat conductivity like titanium, excessive target heating results in a major contribution by target heat radiation. Those different driving mechanisms are also present in the deposited film in terms of growth structure as investigated with SEM. Here, textbook like columnar growth is observed for 'low power' deposition processes and as the particles gain more energy more dense and grain structured films were found.

Summarizing it can be concluded that the passive thermal probe is a versatile tool and can be applied to a wide variety of different plasma processes. Even fast processes with short pulses (e.g. PIII or HiPIMS) can be investigated. The knowledge about the energy flux provides deeper insights into the interaction between complex plasma processes and the surrounding walls (i.e. the substrate). If energy flux measurements are paired with Langmuir probe diagnostics and deposition rate measurements, a detailed picture of the particle mechanisms during plasma processing can be obtained. That information is crucial for controlling and optimizing industrial coating processes.

Following topics as well as mechanical challenges may be addressed in future investigations:

- A sophisticated shutter system capable of fast switching, or a rotor shutter with the right frequency in front of the PTP, which is triggered to the pulsed system (PIII, HiPIMS) might allow for time resolved calorimetric measurements. Using this technique, the PTP would still measure over several pulses to detect a sufficient temperature rise but always during the same time in the pulse. For example if the pulse is set to last 15 μs and the shutter opens after a delay of 5 μs for an additional 5 μs , the PTP records only bits of pulses that occur in its middle. The result is an integration of all those same time points during the pulses. A delay generator would also enable to consider a time of flight of the particles generated at the source to the probe, depending on the distance.
- The studies with the PTP during sputtering of an oxide layer or nitriding a metallic surface in a PIII system (publication [II]) would be more comparable if argon was used in both cases. The substrates need to be nitrided beforehand and then sputtered with argon until they exhibit a metallic surface. This would also enable a quick surface observation after the surface preparation to make sure the surface is truly covered with a nitride (which was not entirely clear in the investigations), which should also be done after preparing the oxide layer in the furnace. Additionally, it would also be interesting to create an oxide layer with additional oxygen gas admixture during pulsing with intermittent PTP measurements, as is done with nitrogen.
- Time resolved Langmuir measurements in HiPIMS should be done using the same setup as in publication [III]. Obtaining the plasma parameters during the pulses would allow for a real comparison between the mechanisms present in DCMS and HiPIMS. Energy flux contributions should be calculated according to publication [VI].

- Unfortunately, no further experiments using the acquired high-speed camera during PIII were performed. To gain insights into the processes, especially the ion movement during the pulse, small levitating dust particles should be used as visual probes. When illuminated by a laser and observed by the camera, the ion drag during acceleration onto the substrate surface might create a dust particle movement detectable with the camera.

Bibliography

- [1] H. K. Raut, V. A. Ganesh, A. S. Nair, and S. Ramakrishna, “Anti-reflective coatings: A critical, in-depth review,” *Energy & Environmental Science*, vol. 4, no. 10, p. 3779, 2011.
- [2] G. Franz, *Low Pressure Plasmas and Microstructuring Technology*. Berlin, Heidelberg: Springer Berlin Heidelberg, 2009.
- [3] G. W. Goward, “Progress in coating for gas turbine airfoils,” *Surface and Coatings Technology*, vol. 108-109, pp. 73–79, 1998.
- [4] N. P. Padture, “Thermal Barrier Coatings for Gas-Turbine Engine Applications,” *Science*, vol. 296, no. 5566, pp. 280–284, 2002.
- [5] X. Chen and H. J. Schluesener, “Nanosilver: A nanoparticle in medical application,” *Toxicology Letters*, vol. 176, no. 1, pp. 1–12, 2008.
- [6] L. Zhao, P. K. Chu, Y. Zhang, and Z. Wu, “Antibacterial coatings on titanium implants,” *Journal of Biomedical Materials Research Part B: Applied Biomaterials*, vol. 91B, pp. 470–480, oct 2009.
- [7] M. Geetha, A. Singh, R. Asokamani, and A. Gogia, “Ti based biomaterials, the ultimate choice for orthopaedic implants – A review,” *Progress in Materials Science*, vol. 54, pp. 397–425, may 2009.
- [8] “Iceland Nordic Visitor, <https://www.nordicvisitor.com/images/iceland/winter/northern-lights-lake-thingvellir-national-park-iceland.jpg>.”
- [9] F. Chen, *Introduction to Plasma Physics and Controlled Fusion*. Berlin, Heidelberg: Springer, 2016.
- [10] I. P. B. Editors, I. P. E. G. C. an Co-Chairs, I. J. C. T. Unit, and Physics, “Chapter 1: Overview and summary,” *Nuclear Fusion*, vol. 39, pp. 2137–2174, dec 1999.
- [11] Sugawara, *Plasma Etching Fundamentals and Applications*. Oxford University Press, 1998.
- [12] J. A. Thornton, “Substrate heating in cylindrical magnetron sputtering sources,” *Thin Solid Films*, vol. 54, no. 1, pp. 23–31, 1978.
- [13] K. Ellmer and R. Mientus, “Calorimetric measurements with a heat flux transducer of the total power influx onto a substrate during magnetron sputtering,” *Surface and Coatings Technology*, vol. 116-119, pp. 1102–1106, sep 1999.

- [14] H. Kersten, D. Rohde, J. Berndt, H. Deutsch, and R. Hippler, “Investigations on the energy influx at plasma processes by means of a simple thermal probe,” *Thin Solid Films*, vol. 377-378, pp. 585–591, 2000.
- [15] M. Čada, J. W. Bradley, G. C. B. Clarke, and P. J. Kelly, “Measurement of energy transfer at an isolated substrate in a pulsed dc magnetron discharge,” *Journal of Applied Physics*, vol. 102, p. 063301, sep 2007.
- [16] D. Lundin, M. Stahl, H. Kersten, and U. Helmersson, “Energy flux measurements in high power impulse magnetron sputtering,” *Journal of Physics D: Applied Physics*, vol. 42, p. 185202, sep 2009.
- [17] P. A. Cormier, M. Stahl, A. L. Thomann, R. Dussart, M. Wolter, N. Semmar, J. Mathias, and H. Kersten, “On the measurement of energy fluxes in plasmas using a calorimetric probe and a thermopile sensor,” *Journal of Physics D: Applied Physics*, vol. 43, no. 46, p. 465201, 2010.
- [18] S. Bornholdt, T. Peter, T. Strunskus, V. Zaporojtchenko, F. Faupel, and H. Kersten, “The method of conventional calorimetric probes — A short review and application for the characterization of nanocluster sources,” *Surface and Coatings Technology*, vol. 205, pp. S388–S392, jul 2011.
- [19] S. Bornholdt and H. Kersten, “Transient calorimetric diagnostics for plasma processing,” *The European Physical Journal D*, vol. 67, p. 176, aug 2013.
- [20] S. Bornholdt, N. Itagaki, K. Kuwahara, H. Wulff, M. Shiratani, and H. Kersten, “Characterization of the energy flux toward the substrate during magnetron sputter deposition of ZnO thin films,” *Plasma Sources Science and Technology*, vol. 22, p. 025019, apr 2013.
- [21] R. Wiese, H. Kersten, G. Wiese, and R. Bartsch, “Energy influx measurements with an active thermal probe in plasma-technological processes,” *EPJ Techniques and Instrumentation*, vol. 2, no. 1, p. 2, 2015.
- [22] S. Gauter, M. Fröhlich, W. Garkas, M. Polak, and H. Kersten, “Calorimetric probe measurements for a high voltage pulsed substrate (PBII) in a HiPIMS process,” *Plasma Sources Science and Technology*, vol. 26, p. 065013, may 2017.
- [23] I. Langmuir, “Oscillations in Ionized Gases,” *Proceedings of the National Academy of Sciences*, vol. 14, pp. 627–637, aug 1928.
- [24] A. Piel, *Plasma Physics*. Berlin, Heidelberg: Springer Berlin Heidelberg, 2010.
- [25] D. Bohm, “The Characteristics of Electrical Discharges in Magnetic Fields,” ch. 3, p. 77, New York, NY: McGraw-Hill, 1949.
- [26] I. Langmuir, “The Interaction of Electron and Positive Ion Space Charges in Cathode Sheaths,” *Physical Review*, vol. 33, pp. 954–989, jun 1929.

- [27] J. A. Thornton, "Influence of apparatus geometry and deposition conditions on the structure and topography of thick sputtered coatings," *Journal of Vacuum Science and Technology*, vol. 11, no. 4, p. 666, 1974.
- [28] A. Anders, "A structure zone diagram including plasma-based deposition and ion etching," *Thin Solid Films*, vol. 518, no. 15, pp. 4087–4090, 2010.
- [29] H. Kersten, D. Rohde, H. Steffen, H. Deutsch, R. Hippler, G. H. P. M. Swinkels, and G. M. W. Kroesen, "On the determination of energy fluxes at plasma–surface processes," *Applied Physics A*, vol. 72, no. 5, pp. 531–540, 2001.
- [30] M. Wolter, I. Levchenko, H. Kersten, S. Kumar, and K. Ostrikov, "Disentangling fluxes of energy and matter in plasma-surface interactions: Effect of process parameters," *Journal of Applied Physics*, vol. 108, p. 053302, sep 2010.
- [31] D. Depla and S. Mahieu, eds., *Reactive Sputter Deposition*, vol. 109 of *Springer Series in Materials Science*. Berlin, Heidelberg: Springer Berlin Heidelberg, 2008.
- [32] G. Federici, C. Skinner, J. Brooks, J. Coad, C. Grisolia, A. Haasz, A. Hassanein, V. Philipps, C. Pitcher, J. Roth, W. Wampler, and D. Whyte, "Plasma-material interactions in current tokamaks and their implications for next step fusion reactors," *Nuclear Fusion*, vol. 41, pp. 1967–2137, dec 2001.
- [33] J. Roth, E. Tsitrone, A. Loarte, T. Loarer, G. Counsell, R. Neu, V. Philipps, S. Brezinsek, M. Lehnen, P. Coad, C. Grisolia, K. Schmid, K. Krieger, A. Kallenbach, B. Lipschultz, R. Doerner, R. Causey, V. Alimov, W. Shu, O. Ogorodnikova, A. Kirschner, G. Federici, and A. Kukushkin, "Recent analysis of key plasma wall interactions issues for ITER," *Journal of Nuclear Materials*, vol. 390-391, pp. 1–9, jun 2009.
- [34] A. Kirschner, V. Philipps, J. Winter, and U. Kögler, "Simulation of the plasma-wall interaction in a tokamak with the Monte Carlo code ERO-TEXTOR," *Nuclear Fusion*, vol. 40, pp. 989–1001, may 2000.
- [35] B. A. Movchan and A. V. Demshishin, "Study of the structure and properties of thick vacuum condensates of nickel, titanium, tungsten, aluminium oxide and zirconium dioxide," *Phys. Met. Metallogr. (Engl. Trans.)*, vol. 28, pp. 83–90, jan 1969.
- [36] M. J. Druyvesteyn and F. M. Penning, "The Mechanism of Electrical Discharges in Gases of Low Pressure," *Reviews of Modern Physics*, vol. 12, pp. 87–174, apr 1940.
- [37] H. Kersten, H. Deutsch, H. Steffen, G. M. W. Kroesen, and R. Hippler, "The energy balance at substrate surfaces during plasma processing," *Vacuum*, vol. 63, pp. 385–431, aug 2001.
- [38] S. Kadlec, C. Quaeyhaegens, G. Knuyt, and L. Stals, "Energy distribution of ions in an unbalanced magnetron plasma measured with energy-resolved mass spectrometry," *Surface and Coatings Technology*, vol. 89, no. 1-2, pp. 177–184, 1997.

- [39] K. Ellmer, “Magnetron sputtering of transparent conductive zinc oxide: relation between the sputtering parameters and the electronic properties,” *Journal of Physics D: Applied Physics*, vol. 33, pp. R17–R32, feb 2000.
- [40] K. Ellmer and T. Welzel, “Reactive magnetron sputtering of transparent conductive oxide thin films: Role of energetic particle (ion) bombardment,” *Journal of Materials Research*, vol. 27, pp. 765–779, mar 2012.
- [41] H. E. Roosendaal and J. B. Sanders, “On the energy distribution and angular distribution of sputtered particles,” *Radiation Effects*, vol. 52, pp. 137–143, jan 1980.
- [42] G. Betz and K. Wien, “Energy and angular distributions of sputtered particles,” *International Journal of Mass Spectrometry and Ion Processes*, vol. 140, pp. 1–110, dec 1994.
- [43] D. Rosenberg and G. K. Wehner, “Sputtering Yields for Low Energy He + -, Kr + -, and Xe + -Ion Bombardment,” *Journal of Applied Physics*, vol. 33, pp. 1842–1845, may 1962.
- [44] N. Laegreid and G. K. Wehner, “Sputtering Yields of Metals for Ar + and Ne + Ions with Energies from 50 to 600 ev,” *Journal of Applied Physics*, vol. 32, pp. 365–369, mar 1961.
- [45] J. F. Ziegler, M. Ziegler, and J. P. Biersack, “SRIM – The stopping and range of ions in matter (2010),” *Nuclear Instruments and Methods in Physics Research Section B: Beam Interactions with Materials and Atoms*, vol. 268, pp. 1818–1823, jun 2010.
- [46] T. Trottenberg, A. Spethmann, V. Schneider, M. Stahl, M. Giesenhagen, and H. Kersten, “Non-Electrostatic Diagnostics for Ion Beams,” *Contributions to Plasma Physics*, vol. 52, pp. 584–592, aug 2012.
- [47] T. Trottenberg, V. Schneider, and H. Kersten, “Measurement of the force on microparticles in a beam of energetic ions and neutral atoms,” *Physics of Plasmas*, vol. 17, no. 10, pp. 774–780, 2010.
- [48] M. Stahl, T. Trottenberg, and H. Kersten, “A calorimetric probe for plasma diagnostics,” *Review of Scientific Instruments*, vol. 81, no. 2, pp. 1–5, 2010.
- [49] J. B. Hudson, *Surface science : an introduction*. New York: J. Wiley & Sons, 1998.
- [50] H. Kersten, H. Deutsch, H. Steffen, G. Kroesen, and R. Hippler, “The energy balance at substrate surfaces during plasma processing,” *Vacuum*, vol. 63, pp. 385–431, aug 2001.
- [51] M. Knudsen, “Die molekulare Wärmeleitung der Gase und der Akkommodationskoeffizient,” *Annalen der Physik*, vol. 339, no. 4, pp. 593–656, 1911.
- [52] M. Knudsen, “Radiometerdruck und Akkommodationskoeffizient,” *Annalen der Physik*, vol. 398, no. 2, pp. 129–185, 1930.

- [53] O. V. Sazhin, S. F. Borisov, and F. Sharipov, "Accommodation coefficient of tangential momentum on atomically clean and contaminated surfaces," *Journal of Vacuum Science & Technology A: Vacuum, Surfaces, and Films*, vol. 19, pp. 2499–2503, sep 2001.
- [54] R. Piejak, V. Godyak, B. Alexandrovich, and N. Tishchenko, "Surface temperature and thermal balance of probes immersed in high density plasma," *Plasma Sources Science and Technology*, vol. 7, pp. 590–598, nov 1998.
- [55] H. Kersten, E. Stoffels, W. W. Stoffels, M. Otte, C. Csambal, H. Deutsch, and R. Hippler, "Energy influx from an rf plasma to a substrate during plasma processing," *Journal of Applied Physics*, vol. 87, no. 8, pp. 3637–3645, 2000.
- [56] E. Hotston, "Threshold energies for sputtering," *Nuclear Fusion*, vol. 15, pp. 544–547, jun 1975.
- [57] B. Chapman, *Glow Discharge Processes: Sputtering and Plasma Etching*. New York: Wiley, 1980.
- [58] A. Piel, *Plasma Physics*. Berlin, Heidelberg: Springer Berlin Heidelberg, 2010.
- [59] M. A. Lieberman and A. J. Lichtenberg, *Principles of Plasma Discharges and Materials Processing*. Hoboken, NJ, USA: John Wiley & Sons, Inc., apr 2005.
- [60] E. Husain and R. S. Nema, "Analysis of Paschen Curves for air, N₂ and SF₆ Using the Townsend Breakdown Equation," *IEEE Transactions on Electrical Insulation*, vol. EI-17, pp. 350–353, aug 1982.
- [61] W. H. Miller, "Theory of Penning Ionization. I. Atoms," *The Journal of Chemical Physics*, vol. 52, no. 7, p. 3563, 1970.
- [62] D. Maczka, A. Meldizon, W. Żuk, and A. Latuszyński, "Penning ionization in a plasma ion source," *Nuclear Instruments and Methods in Physics Research*, vol. 186, pp. 335–342, jul 1981.
- [63] J. A. Thornton, "Magnetron sputtering: basic physics and application to cylindrical magnetrons," *Journal of Vacuum Science and Technology*, vol. 15, pp. 171–177, mar 1978.
- [64] P. Kelly and R. Arnell, "Magnetron sputtering: a review of recent developments and applications," *Vacuum*, vol. 56, pp. 159–172, mar 2000.
- [65] T. Welzel, S. Naumov, and K. Ellmer, "Ion distribution measurements to probe target and plasma processes in electronegative magnetron discharges. I. Negative ions," *Journal of Applied Physics*, vol. 109, p. 073302, apr 2011.
- [66] A. E. Delahoy, S. Y. Guo, C. Paduraru, and A. Belkind, "Reactive-environment, hollow cathode sputtering: Basic characteristics and application to Al₂O₃, doped ZnO, and In₂O₃:Mo," *Journal of Vacuum Science & Technology A: Vacuum, Surfaces, and Films*, vol. 22, pp. 1697–1704, jul 2004.

- [67] K. Ishii, “High-rate low kinetic energy gas-flow-sputtering system,” *Journal of Vacuum Science & Technology A: Vacuum, Surfaces, and Films*, vol. 7, pp. 256–258, mar 1989.
- [68] S. Aisenberg and R. Chabot, “Ion-Beam Deposition of Thin Films of Diamondlike Carbon,” *Journal of Applied Physics*, vol. 42, pp. 2953–2958, jun 1971.
- [69] J. M. HARPER, “Ion Beam Deposition,” in *Thin Film Processes*, pp. 175–206, Elsevier, 1978.
- [70] D. B. Chrisey and G. K. Hubler, eds., *Pulsed laser deposition of thin films*. New York: Wiley, 1994.
- [71] A. Anders, *Cathodic Arcs*, vol. 50 of *Springer Series on Atomic, Optical, and Plasma Physics*. New York, NY: Springer New York, 2008.
- [72] I. Svadkovski, D. Golosov, and S. Zavatskiy, “Characterisation parameters for unbalanced magnetron sputtering systems,” *Vacuum*, vol. 68, pp. 283–290, dec 2002.
- [73] B. Window and N. Savvides, “Charged particle fluxes from planar magnetron sputtering sources,” *Journal of Vacuum Science & Technology A: Vacuum, Surfaces, and Films*, vol. 4, pp. 196–202, mar 1986.
- [74] D. A. Golosov, “Balanced magnetic field in magnetron sputtering systems,” *Vacuum*, vol. 139, pp. 109–116, may 2017.
- [75] R. Howson, H. J’Afer, and A. Spencer, “Substrate effects from an unbalanced magnetron,” *Thin Solid Films*, vol. 193-194, pp. 127–137, jan 1990.
- [76] C. Christou and Z. H. Barber, “Ionization of sputtered material in a planar magnetron discharge,” *Journal of Vacuum Science & Technology A: Vacuum, Surfaces, and Films*, vol. 18, pp. 2897–2907, nov 2000.
- [77] V. Kouznetsov, K. Macák, J. M. Schneider, U. Helmersson, and I. Petrov, “A novel pulsed magnetron sputter technique utilizing very high target power densities,” *Surface and Coatings Technology*, vol. 122, pp. 290–293, dec 1999.
- [78] U. Helmersson, M. Lattemann, J. Bohlmark, A. P. Ehiasarian, and J. T. Gudmundsson, “Ionized physical vapor deposition (IPVD): A review of technology and applications,” *Thin Solid Films*, vol. 513, pp. 1–24, aug 2006.
- [79] D. Lundin and K. Sarakinos, “An introduction to thin film processing using high-power impulse magnetron sputtering,” *Journal of Materials Research*, vol. 27, pp. 780–792, mar 2012.
- [80] A. Anders, “Self-sputtering runaway in high power impulse magnetron sputtering: The role of secondary electrons and multiply charged metal ions,” *Applied Physics Letters*, vol. 92, p. 201501, may 2008.

- [81] J. Andersson and A. Anders, “Gasless sputtering: Opportunities for ultraclean metalization, coatings in space, and propulsion,” *Applied Physics Letters*, vol. 92, p. 221503, jun 2008.
- [82] P. Poolcharuansin, B. Liebig, and J. Bradley, “Plasma Parameters in a Pre-Ionized HiPIMS Discharge Operating at Low Pressure,” *IEEE Transactions on Plasma Science*, vol. 38, pp. 3007–3015, nov 2010.
- [83] J. Hirvonen, C. Carosella, R. Kant, I. Singer, R. Vardiman, and B. Rath, “Improvement of metal properties by ion implantation,” *Thin Solid Films*, vol. 63, pp. 5–10, oct 1979.
- [84] O. Hubler and F. Smidt, “Application of ion implantation to wear protection of materials,” *Nuclear Instruments and Methods in Physics Research Section B: Beam Interactions with Materials and Atoms*, vol. 7-8, pp. 151–157, mar 1985.
- [85] S. T. Picraux, “Ion implantation metallurgy,” *Physics Today*, vol. 37, pp. 38–44, nov 1984.
- [86] J. R. Conrad, J. L. Radtke, R. A. Dodd, F. J. Worzala, and N. C. Tran, “Plasma source ion-implantation technique for surface modification of materials,” *Journal of Applied Physics*, vol. 62, no. 11, pp. 4591–4596, 1987.
- [87] M. A. Lieberman, “Model of plasma immersion ion implantation,” *Journal of Applied Physics*, vol. 66, no. 7, p. 2926, 1989.
- [88] C. D. Child, “Discharge From Hot Cao,” *Physical Review (Series I)*, vol. 32, pp. 492–511, may 1911.
- [89] C. G. Abbot, “The silver disk pyrhelimeter (with one plate),” *Smithsonian miscellaneous collections*, vol. 56, no. 19, 1911.
- [90] R. Gardon, “An Instrument for the Direct Measurement of Intense Thermal Radiation,” *Review of Scientific Instruments*, vol. 24, pp. 366–370, may 1953.
- [91] H. Steffen, H. Kersten, and H. Wulff, “Investigation of the energy transfer to the substrate during titanium deposition in a hollow cathode arc,” *Journal of Vacuum Science & Technology A: Vacuum, Surfaces, and Films*, vol. 12, pp. 2780–2783, sep 1994.
- [92] H. Kersten, D. Rohde, H. Steffen, H. Deutsch, and R. Hippler, “Die Bestimmung von Energieflüssen bei Plasmaoberflächenprozessen,” *Galvanotechnik*, vol. 96, no. 12, pp. 2996–3007, 2005.
- [93] M. Stahl, “Energiestrommessungen in Prozessplasmen,” *Diplomarbeit*, 2009.
- [94] R. Wendt, K. Ellmer, and K. Wiesemann, “Thermal power at a substrate during ZnO:Al thin film deposition in a planar magnetron sputtering system,” *Journal of Applied Physics*, vol. 82, pp. 2115–2122, sep 1997.

-
- [95] B. Koch, W. Bohmeyer, G. Fussmann, P. Kornejew, and H.-D. Reiner, “Energy flux measurements in a steady-state discharge at PSI-2,” *Journal of Nuclear Materials*, vol. 290-293, pp. 653–657, mar 2001.
- [96] H. M. Mott-Smith and I. Langmuir, “The Theory of Collectors in Gaseous Discharges,” *Physical Review*, vol. 28, pp. 727–763, oct 1926.
- [97] I. H. Hutchinson, “Principles of Plasma Diagnostics,” *Plasma Physics and Controlled Fusion*, vol. 44, no. 12, p. 2603, 2002.
- [98] K. Jacobsen, J.-E. Wahlund, and A. Pedersen, “Cassini Langmuir probe measurements in the inner magnetosphere of Saturn,” *Planetary and Space Science*, vol. 57, pp. 48–52, jan 2009.
- [99] D. Lundin, U. Helmersson, S. Kirkpatrick, S. Rohde, and N. Brenning, “Anomalous electron transport in high power impulse magnetron sputtering,” *Plasma Sources Science and Technology*, vol. 17, p. 025007, may 2008.
- [100] A. Ganguli, B. B. Sahu, and R. D. Tarey, “A new structure for RF-compensated Langmuir probes with external filters tunable in the absence of plasma,” *Plasma Sources Science and Technology*, vol. 17, p. 015003, feb 2008.
- [101] G. Sauerbrey, “Verwendung von Schwingquarzen zur Wägung dünner Schichten und zur Mikrowägung,” *Zeitschrift für Physik*, vol. 155, pp. 206–222, apr 1959.

Curriculum Vitae

Personal Data

Name: Fabian Haase
Date of birth: 04.08.1987
Place of birth: Itzehoe
Citizenship: German

Education

1994 - 1998 Elementary School Hohenlockstedt
1998 - 2007 Secondary School: Kaiser-Karl-Schule Itzehoe
2007 Abitur
2008 - 2012 Bachelor of Science at Kiel University in Physics
2012 Bachelor Thesis: *Einfluss der elektrischen Leitfähigkeit auf die Aufladung von Staub in Plasmen*
2012 - 2014 Master of Science at Kiel University in Physics
2014 Master Thesis: *Kombination von Kalorimetrischer und Langmuir-Sonde für den Einsatz in der Plasmadiagnostik*
2014 - 2018 PhD student at Kiel University in the Plasmatechnology Group

Civilian

2007 - 2008 Civilian Service, Sozialpsychiatrische Initiativen, Lohbarbek

Acknowledgments

Foremost, I would like to thank my supervisor Prof. Dr. Holger Kersten for giving me the opportunity to work on such interesting and fascinating topics in his Plasmatechnology Group. I have always felt supported by him, no matter if it was trying out new things, needing help and getting some new ideas in a fruitful discussion or presenting results in front of international colleagues. The freedom and support I have experienced in the last years is highly appreciated.

This obviously extends throughout his whole working group, which I would like to thank each member of. The scientific exchange, countless coffee breaks and resulting pleasant work environment made it easy to come to work every day. Further I would like to thank Micheal Poser and Volker Rohwer for their tireless support in planning and creating new electronics and finding solutions for countless mechanical challenges. For the many hours spent in the lab and the office, his untiring and infectious drive to get to the bottom of things and fruitful discussions and ideas I would especially like to thank my colleague Sven Gauter.

I would also like to thank Dr. Stephan Mändl and Dr. Darina Manova from the IOM in Leipzig, who it was a pleasure to work with during our collaborative project.

For the many things he taught me about magnetron sputtering and his cheerful way of work, I thank Dr. Daniel Lundin from the Université Paris-Sud.

Many experimental investigations would not have been possible without the necessary tools and hardware, which is why I would like to thank Michael Brix, Frank Brach and the whole crew of the 'Zentralwerkstatt', as well as Jürgen Holz.

I would also like to thank Tim Riedel of the working group Surface Physics at the Kiel University for enduring our countless visits to his office and workshop to be able to build our PTPs and his support during said works.

As a closing statement, I would like to extend my deepest gratitude to my friends and family, especially my parents, for their dedicated support throughout all those years.

Thank you very much!

Eidesstattliche Erklärung

Hiermit versichere ich an Eides statt, dass ich die vorliegende Arbeit selbstständig und ohne fremde Hilfe angefertigt habe. Ausschnitte, welche wörtlich oder sinngemäß aus Arbeiten anderer Autoren beruhen, sind als solche klar gekennzeichnet. Ich versichere außerdem, dass ich keine andere als die angegebene Literatur verwendet habe. Diese Versicherung schließt alle in dieser Arbeit enthaltenen Skizzen, Grafiken und bildlichen Darstellungen ein.

Die Arbeit als Ganzes wurde bisher keiner anderen Prüfungsbehörde vorgelegt. Teile dieser Arbeit wurden bereits in begutachteten wissenschaftlichen Fachzeitschriften veröffentlicht und sind als solche gekennzeichnet. Die in den Veröffentlichungen angeführten Quellenverweise sind in den Veröffentlichungen selbst und nicht zusätzlich im Literaturverzeichnis dieser Arbeit aufgeführt.

Abschließend erkläre ich, dass diese Arbeit unter Einhaltung der Regeln guter wissenschaftlicher Praxis der Deutschen Forschungsgemeinschaft entstanden ist.

Kiel, Mai 2018

